ABSTRACT

Title of Dissertation: AERODYNAMIC SEPARATION OF FRAGMENTED BODIES IN HIGH-SPEED FLOW

Thomas J. Whalen
Doctor of Philosophy, 2021

Dissertation Directed by: Professor Stuart Laurence
Department of Aerospace Engineering

Atmospheric entry of meteoroids poses danger to humans in the form of blast-wave overpressure, impact craters, tsunamis, and other assorted threats. The relative risks of each are highly dependent on the details of the unavoidable structural disruption that occurs and the subsequent aerodynamic separation sequence, so accurate prediction of fragment trajectories is required for threat mitigation. However, the physics of aerodynamic separation immediately following meteor fragmentation are virtually uncharacterized, allowing for only low confidence in threat assessment projections.

The present work endeavors to constrain the separation behavior of fragmenting bodies by examining the model problem of close-packed sphere clusters and, to a lesser extent, clouds of dusty debris. Free-flight experimentation in UMD HyperT-ERP, a Mach-6 shock tunnel, is conducted to provide a foundation for both statistical and aerodynamic analyses, while coupled inviscid CFD/FEA provides complementary insight into the mechanisms driving fragment separation. First, computations

of equal-sized sphere pairs reveal a previously unidentified phenomenon wherein two bodies in continual mechanical contact oscillate about a stable angle-of-attack equilibrium and achieve anomalously high lateral velocities. Proceeding to higher cluster populations, separation procedure can be divided into two stages: mutual repulsion from a common center and subsequent subcluster interactions dictated by the influence of an upstream body. The degree of repulsion induced by the former demonstrates close correlation with the initial angular position of a fragment, whereas the lateral velocities resulting from the latter appear to be normally distributed about a slightly positive value. The transverse separation characteristics of equal-sphere clusters numbering from 2 to 115 bodies are used to constrain a power-law fit between the lateral extent of a disrupted swarm and its population, providing a significant improvement to existing models of aerodynamic separation following fragmentation. Furthermore, experiments of unequal-sphere clusters, whose compositions are governed by realizations of truncated power laws, reveal a systematic underestimate in the equal-sphere correlation, resulting largely from massive subclusters suppressing high expulsion. A unified model of fragment separation, based on both the aforementioned power-law fit and a combined Rayleigh—exponential distribution, is then proposed. Finally, the dynamics of dusty debris clouds are discussed, with implications for mass depletion and energy deposition of rubble-pile-type impactors highlighted.

AERODYNAMIC SEPARATION OF FRAGMENTED BODIES IN HIGH-SPEED FLOW

by

Thomas J. Whalen

Dissertation submitted to the Faculty of the Graduate School of the
University of Maryland, College Park in partial fulfillment
of the requirements for the degree of
Doctor of Philosophy
2021

Advisory Committee:
Associate Professor Stuart Laurence, Co-Chair/Advisor
Assistant Professor Christoph Brehm, Co-Chair
Associate Professor Johan Larsson, Dean's Representative
Professor Richard Mushotzky
Professor Kenneth Yu

Acknowledgments

I first thank my advisor, Prof. Dr. Stuart Laurence, for his ceaseless wisdom, meticulous copy editing, and eagerness for me to develop and explore my own ideas. His guidance was invaluable in my growth as a researcher. I also thank my committee, Profs. Christoph Brehm, Johan Larsson, Richard Mushotzky, and Kenneth Yu, for providing insightful critiques on this comparatively hefty work, undoubtedly making it more effective and impactful.

I am grateful for the assistance of Prof. Ralf Deiterding of University of Southampton for furnishing his powerful AMROC/DYNA3D code and for his ever-rapid correspondence, which allowed me to quickly master and implement said computational tools. I would also like to acknowledge the contributions of my official (and unofficial) NASA (and ex-NASA) mentors, Mr. Gregory Buck, Dr. Eric Stern, Dr. Joseph Brock, and Dr. Jason Rabinovitch, whose interest in and encouragement of my research always provided extra motivation.

The past six years would have been quite dull without my HAPL labmates, whose high spirits imbued JMP and MANUF with a liveliness unrivaled. And, in particular, a special thanks to my fellow generation of HAPLonians (Alvin, Cam, Rich, Andrew): it was a pleasure to tackle the trials and tribulations of graduate school together. I would be remiss were I not to acknowledge the essential support of

Chick-fil-A, Taco Bell, 7-Eleven, and Dunkin' Donuts; your spicy deluxe combo #2's, hot sauce packets, buffalo chicken taquitos, and medium regulars w/ cream/sugar are really the stuff that PhDs are made of.

I am eternally grateful to Bill and Liz Egan for welcoming me as an intermittent tenant over the past ten months. I could not ask for better (future) parents-in-law.

To MaBoiz, Boston, Dartmouth, DC, and in between.

None of this would have been possible without a lifetime of support from my parents, Mark and Lisa, and sister, Sami. Seriously, I couldn't have done this without you.

The biggest thanks of all goes to my loving and lovely fiancé, Molly.

Thos. J. Whalen was supported by a NASA Space Technology Research Fellowship under grant 80NSSC18K1188.

Table of Contents

Acknowledgements ii

Table of Contents iv

List of Tables vi

List of Figures vii

Nomenclature x

Chapter 1: Introduction 1
- 1.1 Motivation . . . 1
- 1.2 Review of Related Works . . . 2
  - 1.2.1 Meteor Events . . . 2
  - 1.2.2 Free-Flight Separation Aerodynamics . . . 6
- 1.3 Scope of Work . . . 12
  - 1.3.1 Definition of Model Problem . . . 13
  - 1.3.2 Objectives and Strategy . . . 20
- 1.4 Important Definitions and Concepts . . . 25
- 1.5 Structure of Dissertation . . . 29

Chapter 2: Experimental Approach 31
- 2.1 Facility . . . 32
- 2.2 Stereoscopic Visualization . . . 36
- 2.3 Model Suspension and Release . . . 40
- 2.4 Body Tracking Routines . . . 45
  - 2.4.1 Edge Detection . . . 45
  - 2.4.2 Synthetic Image Fitting . . . 47
- 2.5 In Situ Camera Calibration . . . 50
- 2.6 Three-Dimensional Reconstruction . . . 55
- 2.7 Experimental Reliability Considerations . . . 60
- 2.8 Cluster Configurations . . . 63

Chapter 3: Computational Modeling 68
- 3.1 Numerical Methodology . . . 68
- 3.2 Model Verification . . . 74
- 3.3 Experimental Validation . . . 80

3.4 Simulation Parameters . . . 88

Chapter 4: Equal Spheres: Small Clusters 93
4.1 Two-Sphere Simulation Survey . . . 93
4.2 Four-Sphere Experiments . . . 105
4.3 Four-Sphere Simulation Survey . . . 111
4.4 Conclusions . . . 127

Chapter 5: Equal Spheres: Intermediate Clusters 128
5.1 Eight-Sphere Experiments . . . 128
5.2 Eleven-Sphere Experiments . . . 134
5.3 Thirteen-Sphere Simulation Survey . . . 140
5.4 Conclusions . . . 160

Chapter 6: Equal Spheres: Populous Clusters and Statistics 162
6.1 General Observations . . . 163
6.1.1 Primary Separation Attributes . . . 166
6.1.2 Cluster-Core Collisions . . . 172
6.1.3 Highly Expelled Spheres . . . 174
6.1.4 Isotropy . . . 177
6.2 Aggregate Statistics . . . 180
6.2.1 Primary Separation Range and Duration . . . 180
6.2.2 Lateral Velocity Distributions . . . 183
6.3 Conclusions . . . 192

Chapter 7: Unequal-Sphere Clusters 194
7.1 Cluster Parameters and Sizing Considerations . . . 196
7.2 General Observations . . . 201
7.3 Aggregate Statistics . . . 209
7.4 Separation Modeling . . . 224
7.5 Conclusions . . . 228

Chapter 8: Dusty Debris 230
8.1 General Observations . . . 231
8.2 Mass Depletion . . . 239
8.3 Energy Deposition Modeling . . . 243
8.4 Hybrid Separation . . . 247
8.5 Conclusions . . . 250

Chapter 9: Conclusions 252

Appendix A: Power-Law Fragmentation 259

Bibliography 264

List of Tables

2.1 Experimental freestream flow conditions 35
2.2 Compendium of experimental configurations 67

3.1 Grid refinement study 76
3.2 Numerical freestream flow conditions 89
3.3 Simulation Parameters 92

7.1 Exponential fits to unequal-sphere lateral velocity 225

List of Figures

1.1 Damage zones of Chelyabinsk and Pułtusk events . . . 4
1.2 Fallen trees from Tunguska site . . . 6
1.3 Basic aerodynamic phenomena for sphere pairs . . . 8
1.4 Parameterization of model problem . . . 23
1.5 Definition of polar/alignment angle . . . 28

2.1 HyperTERP schematic . . . 33
2.2 Reservoir pressure traces . . . 35
2.3 Stereoscopic camera arrangements . . . 38
2.4 Camera setup photograph . . . 39
2.5 Suspension/release model . . . 42
2.6 Shell separation sequence . . . 43
2.7 Rotated shell separation sequence . . . 44
2.8 Generation of synthetic sphere image . . . 49
2.9 Example synthetic image fit . . . 51
2.10 Grid calibration . . . 52
2.11 Reconstructed camera arrangement . . . 54
2.12 Sphere identification fit . . . 55
2.13 Projection error for arrangement C1 . . . 57
2.14 Projection error for arrangements C2 and C3 . . . 59
2.15 Experimental repeatability of predetermined cluster arrangements . . . 62

3.1 AMROC mesh refinement strategy . . . 71
3.2 DYNA3D mesh structure and body contact demonstration . . . 72
3.3 Protocol for data flow between AMROC and DYNA3D . . . 73
3.4 Graphical comparison of all grid refinement cases . . . 78
3.5 Grid refinement flowfield . . . 79
3.6 Coarse simulation velocity and force errors . . . 81
3.7 Graphical comparison of simulation with validation experiment . . . 84
3.8 Free-flight validation error . . . 86
3.9 Sample computational sphere clusters . . . 90

4.1 Sphere pair separation from $\theta_0 = 90°$ . . . 95
4.2 Sphere pair separation from $\theta_0 = 120°$ . . . 96
4.3 Sphere pair separation from $\theta_0 = 135°$ . . . 97
4.4 Sphere pair separation from $\theta_0 = 172.5°$ . . . 98

4.5 Polar trajectories and lateral velocities of two-sphere survey 100
4.6 Alignment angle phase space of contacting sphere pairs 103
4.7 Lift-to-drag ratio of contacting sphere pairs 104
4.8 Lateral velocities of shot 4A in different reference frames 106
4.9 Reconstruction of shot 4B 108
4.10 Lateral velocity profiles of shot 4B 109
4.11 Phase-space behavior of rolling pair in shot 4B 111
4.12 Separation sequence for 36°-pitch/18°-yaw four-sphere cluster 113
4.13 Force coefficients for 36°-pitch/18°-yaw four-sphere cluster 114
4.14 Binned lateral velocities for four-sphere clusters 116
4.15 Polar and azimuthal angle correlations for four-sphere clusters 118
4.16 Example clusters under four-sphere geometric parameterization . . . 122
4.17 Separation properties under tetrahedron reduced parameterization . . 124
4.18 Geometric dependencies of four-sphere clusters 125

5.1 Three-dimensional reconstruction and lateral velocities of shot 8A . . 130
5.2 Trajectories, lateral velocities, and lateral forces of shot 8B 133
5.3 Separation sequence of shot 11B 135
5.4 Reconstruction and velocities of shots 11A and 11B 136
5.5 Cluster geometry for thirteen-sphere simulations 142
5.6 Thirteen-sphere cluster trajectories, forces, and velocities: 136.8° pitch, 141.1° yaw 143
5.7 Thirteen-sphere cluster trajectories, forces, and velocities: −0.1° pitch, 8.6° yaw 147
5.8 Primary separation statistics for thirteen-sphere survey 148
5.9 Polar angle correlation for thirteen-sphere survey 151
5.10 Example thirteen-sphere clusters illustrating various bluntness indices 155
5.11 Geometric dependencies of thirteen-sphere clusters 157
5.12 Internal sphere separation properties of thirteen-sphere clusters . . . 159
5.13 Aerodynamic energy deposition of thirteen-sphere clusters 161

6.1 Separation sequence of shot 115D 164
6.2 Separation sequences of shots 27E and 52E 167
6.3 Computational and experimental shock structures of populous clusters 168
6.4 Flattening ratio analysis of primary separation for shot 36A 171
6.5 Cluster-core collisions of shot 115E 173
6.6 Lateral velocities of most ejected spheres 175
6.7 Azimuthal variance of separation in shots 52A and 115A 178
6.8 Primary separation statistics with cluster population 182
6.9 Collective lateral velocity with equal cluster population 185
6.10 Lateral velocity distribution fits for equal clusters 189
6.11 Center-of-mass lateral offset with equal cluster population 192

7.1 Unequal-cluster mass fractions and radius-ratio probabilities 198
7.2 Separation sequence of shot 2E-U 203

7.3 Separation sequence of shot 5E-U . . . 205
7.4 Reconstruction and velocities of shot 3A-U . . . 206
7.5 Lateral velocities of most ejected unequal spheres . . . 209
7.6 Collective lateral velocity with power-law index . . . 210
7.7 Relation between collective lateral velocity, subcluster mass, and power-law index . . . 213
7.8 Radius-ratio dependence of mass entrainment . . . 215
7.9 Example decomposed Rayleigh distributions and exponential fit at $\alpha = 3$ . . . 219
7.10 Decomposed Rayleigh and exponential fits for all unequal-cluster types 220
7.11 Rayleigh–exponential fitting model for unequal clusters . . . 223
7.12 Sample lateral velocities generated from statistical separation model . 228

8.1 Shadowgraph sequence of shot PB . . . 233
8.2 Zoomed shadowgraph sequence of shot PE . . . 237
8.3 Surrogate sphere fitting method . . . 241
8.4 Dusty debris exponential mass loss . . . 243
8.5 Comparison of energy deposition models for dusty debris impactor . . 245
8.6 Sensitivity of dusty debris energy deposition to variable inputs 248
8.7 Separation sequence of shot 15P . . . 249

A.1 Fragment-size distribution for meteorites . . . 262

Nomenclature

Acronyms

AMR	Adaptive Mesh Refinement
AMROC	Adaptive Mesh Refinement in Object-oriented C++
CFD	Computational Fluid Dynamics
CFL	Courant-Friedrichs-Lewy
FEA	Finite Element Analysis
FOV	Field-Of-View
FSD	Fragment Size Distribution
HyperTERP	H*yper*sonic Tunnel for Educational and Research Purposes
PDF	Probability Density Function
UMD	University of MarylanD

Variables

a	Exponential fit coefficient OR acceleration
A	Asymmetry index OR Scaling constant
A_s	Frontal area of surrogate sphere
b	Exponential fit exponent
B	Bluntness index
C	Aerodynamic separation coefficient
C_D	Drag coefficient
C_F	Total force coefficient
C_T	Lateral force coefficient
d	Diameter
D	Drag
E	Specific total energy OR Elastic modulus
f_r	PDF of Rayleigh distribution
f_{re}	PDF of Rayleigh–exponential distribution
g	Gravitational acceleration
h	Altitude
L	Lift/lateral force
m	Mass
M	Mach number
$\hat{n}$	Unit-normal vector
N	Cluster population
p	Pressure OR Probability

r	Radius
S	Material strength
t	Time
t_0	Cluster release time
T	Temperature
u	Fluid velocity
v	Object streamwise velocity
V	Impactor speed
V_T	Lateral sphere velocity
$\overline{V_T}$	Collective lateral velocity of cluster
w	Summation weight
$\vec{x}$	Position vector
x	Streamwise coordinate
x_{sep}	Edge-to-edge distance between spheres
y	Vertical coordinate
z	Spanwise coordinate
α	Power-law index for generating unequal clusters
α_s	Strength-scaling parameter
β	Power-law index for curve fitting
β_q	Fit parameter for meteorite FSD
γ	Ratio of specific heats
ϵ	Reprojection error of 3D reconstruction in pixel coordinates
ε	Error of specified quantity
θ	Polar/alignment angle OR meteor flight angle
ν	Poisson's ratio
ρ	Density
$\sigma_{[\ ]}$	Uncertainty of selected quantity
σ_r	Rayleigh scale parameter
σ_{ab}	Ablation coefficient
τ_d	Mass depletion timescale
τ_s	Characteristic separation timescale
υ_s	Characteristic separation velocity
ϕ	Azimuthal angle

Subscripts and Superscripts

c	Cluster-referenced quantity
com	Center-of-mass-related quantity
l	Leading-sphere-reference quantity
E	Earth-referenced quantity
m	Meteoroid-related quantity
max	Maximum quantity
min	Minimum quantity
N	Population-referenced quantity

p	Primary-separation-related quantity
proj	Camera-projected quantity
r	Radius-referenced quantity
rel	Relative quantity
s	Scaled quantity
sph	Sphere-referenced quantity
sub	Subcluster quantity
0	Stagnation OR Initial quantity
1	Primary-sphere-reference quantity OR Quantity after primary separation
2	Secondary-sphere-reference quantity OR Quantity after secondary separation
12	Sphere-pair-related quantity
∞	Freestream quantity
$\perp$	Perpendicular quantity
$'$	Nondimensional quantity

Chapter 1: Introduction

1.1 Motivation

The omnipresent threat of meteoroid and asteroid strikes has both captivated and perturbed the public imagination throughout recorded history. In modern times, impact events have caused injury to the ground populace and localized property damage (Popova et al., 2013), while ancient craters of tremendous scale implicate major collisions as a source of mass extinction (Alvarez et al., 1980). Most frequently, astronomical bodies entering Earth's atmosphere are of limited size (Bland and Artemieva, 2003) and explode at high altitude rather than producing an impact crater (Bronshten, 2012). Predominately generated by objects less than 50 meters in diameter, hundreds of such airbursts have been reported (Halliday et al., 1996), with events like Tunguska (Chyba et al., 1993) illustrating the potential scale of destruction. It is these such objects, rather than the kilometer-scale dinosaur killers, that constitute the greatest hazard over relevant timescales (hundreds of years, Brown et al. (2013)). The multifold consequences of airbursts hold high importance for the threats posed by impact events. While airbursts can prevent the passage of a principal body to the ground, thereby hindering the formation of massive craters, the resulting cluster of fragments may be spread great distances (Passey and Melosh,

1980), effectively expanding the range of potential damage. Furthermore, disruption events transfer much of the impactor's kinetic energy to the atmosphere, which, in turn, carries a damaging blast wave over great distances (Mathias et al., 2017). Other hazards including tsunami (Rumpf et al., 2017) and thermal radiation (Johnston and Stern, 2019) have also been identified as capable of catastrophe.

All hazards posed by disrupted meteors are tightly coupled to the physics of fragmentation (McMullan and Collins, 2019), which occurs when the exceptionally high pressures encountered by the astronomical object within Earth's atmosphere exceed its material strength. The resulting separation of the fragment swarm is primarily dictated by aerodynamic interactions between nearby bodies (Passey and Melosh, 1980) and determines both the pattern and form of potential damage. Numerous existing models predict the dispersal of a fragmented impactor (Chyba et al., 1993; Hills and Goda, 1993; Svetsov and Nemtchinov, 1995; Wheeler et al., 2017), but, unfortunately, none are founded on physically consistent laws of aerodynamic separation. In fact, very few studies have even endeavored to characterize the behaviors of fragment swarms at high speed, leaving the risks posed by airburst impact events wholly unconstrained.

1.2 Review of Related Works

1.2.1 Meteor Events

We now present accounts of selected airburst events with relevance to the current problem of aerodynamic separation following catastrophic fragmentation.

The Chelyabinsk event of 2013 was a well-documented airburst that highlighted humanity's vulnerability to impacts from smaller scale objects (Brown et al., 2013). Both video recordings of and the extensive property damage resulting from the airburst (see Figure 1.1(a)) have helped constrain the entry and fragmentation properties of the impactor. The $\sim$ 20-m-diameter meteoroid entered the atmosphere at $\sim$ 19 km/s and began fragmenting at an altitude above 80 km before suffering a major disruption at $\sim$30 km, manifested in the radiation lightcurve (Popova et al., 2013). The resulting elliptical strewn field registered fragments which were spread several kilometers cross-range and tens of kilometers downrange (Borovička et al., 2013a), including a $\sim$ 500 kg primary fragment, while glass shattered by the blast-wave was recorded out to a distance of 120 km. While the airburst did not result in any causalities, hundreds of residents reported injury in the form of eye damage, 'sunburns', and cuts from flying glass (Popova et al., 2013). Despite the comparatively modest scale of the initial impactor, such objects strike Earth with far greater frequency than the 100-meter-plus asteroids that induce widespread calamity, which effectively enhances the hazards constituted by airburst events (Brown et al., 2013).

The Morávka and Košice meteorite falls caused far less damage than Chelyabinsk but, given the abundance of fragments spawned, highlight the inadequacies of the existing depiction of mass dispersal following disruption. Several video recordings captured the fireball and fragment spreading caused by the airburst of the 1.25-m-diameter Morávka meteoroid over the Czech Republic (Borovička et al., 2003); here, fragmentation into 10 primary bodies at an altitude of $\sim$ 45 km was observed, followed by further disruption of these 10 bodies between 37 and 29 km (Borovička

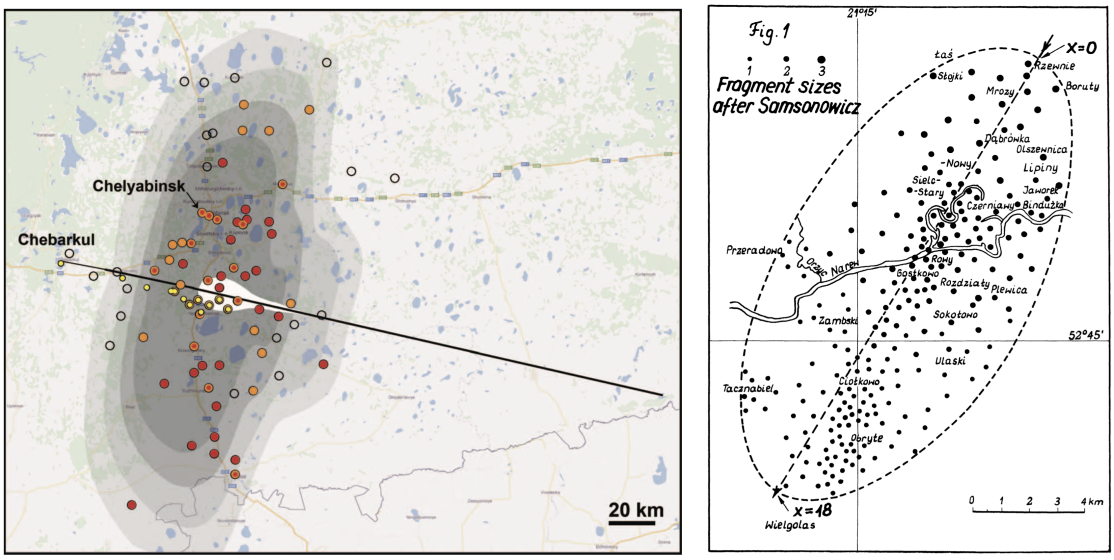

(a) (b)

Figure 1.1: (a) Map of villages damaged by Chelyabinsk airburst event (colored by extent of destruction) and overlaid contours of predicted blast-wave overpressure (Popova et al., 2013). (b) Map of scatter ellipse from Pułtusk event (Lang and Kowalski, 1971).

and Kalenda, 2003). While the extent of break-up displayed was not in itself exceptional, the imaged fragments reached velocities of 300 m/s, which surpasses by an order of magnitude the speeds predicted by standard models of aerodynamic separation (Borovička and Kalenda, 2003), suggesting that uncharacterized aspects of fragmentation may have contributed significantly to the ultimate trajectories of the separating mass. Similarly, the Košice airburst, produced by the 15 km/s entry of a $\sim$ 1 m chondrite into Earth's atmosphere, scattered meteorites over an area of tens of square kilometers in eastern Slovakia (Borovička et al., 2013b). The strewn field revealed that a number of medium-to-large fragments landed at cross-range positions several kilometers away from their expected positions, again signaling the need for a more accurate representation of the physics of aerodynamic separation.

Several older impact events relied on eyewitness accounts to inform the details of atmospheric entry but nonetheless exhibited fragmentation into impressive swarms. The Pułtusk meteorite shower, which fell over Poland in 1868, broke up catastrophically and spread stony meteorites over a 127 km^2 area (Lang and Kowalski, 1971), as shown in Figure 1.1(b). The 'Pułtusk peas', as they are known, ranged from a half gram to 9 kg in mass and are estimated to number close to 100,000. Repelled by such a calamitous airburst, it is no surprise that meteorites spanned a cross-range width of 9 km. As evidenced by the Sikhote-Alin impact of 1947, large-scale fragmentation is not limited to just stony-type meteoroids. According to witnesses, the nickel-iron Sikhote-Alin meteor fragmented at heights of 58, 34, 16, and 6 (Svetsov and Nemtchinov, 1995), with the final break-up altitude much lower than those attained by stony meteors. The meteorites, over 3,000 in number, were recovered from a set of several scatter ellipses corresponding each to a discrete fragmentation event (Krinov, 1974) and span an area of 12×4 km (Tsvetkov, 1987). Together, these examples demonstrate the sheer magnitude of fragments which can be generated by an airburst, indicating that a two-body model of separation aerodynamics (such as will be discussed in Section 1.2.2) is highly unlikely to accurately predict the landing zones of fragment swarms.

Finally, one of the most well-known impact events is the 1908 Tunguska explosion, which caused widespread damage but left no discernible crater, rendering it of a different class of airburst than those already presented. Chyba et al. (1993), presenting an analysis of the geological composition and aerodynamics of the Tunguska object, found that a 15 Mton stony asteroid is consistent with the putative

Figure 1.2: Fallen trees from Kulik's photograph of the region affected by the Tunguska event (Farinella et al., 2001).

9-km-altitude explosion estimated from tree-fall patterns. Other works have posited that the impactor was of cometary origins (see Kresak (1978), for example), but, regardless of its provenance, the low-altitude burst generated a strong blast-wave and intense radiation that, together, felled and scorched trees (as in Figure 1.2) far from its epicenter (Johnston and Stern, 2019). Had such an event occurred over a populous area, the consequences would have been dire; thus, the uncertainty surrounding the meteoroid's material composition and fragmented motion is problematic and highlights the need for a better understanding of the aerodynamic separation physics.

1.2.2 Free-Flight Separation Aerodynamics

Aerodynamic separation of free-flying objects has largely been studied in the context of sphere pairs, so, to acquaint the reader with the basic physics of free-flight separation, we review the driving mechanisms identified through the works of Lau-

rence et al. (2011; 2007; 2012), among others. In the diagrams of Figure 1.3 (Marwege et al., 2018), a principal large sphere in a hypersonic flow generates a bow shock and wake structure through which a secondary small sphere travels. Note that, in this discussion, we use the term 'wake' loosely to describe any area behind the primary body but inside of the bow shock. In panel (a), if the secondary sphere is positioned near the bow shock, or alongside the primary (not shown), a strong repulsive force causes severe lateral acceleration and expulsion from the shock-bounded region, after which the spheres fly independently. If, on the other hand, the secondary lies within the shock but offset from the system's primary axis (panel (b)), an outwardly directed stagnation pressure gradient yields attractive lateral forces, commonly referred to as entrainment. For secondary spheres of size comparable to the primary, a negative relative streamwise acceleration tends to arise, whereas smaller bodies continue to accelerate downstream; the transition between the two behaviors depends on the ratio of sphere radii and the exact position of the secondary within the primary's wake. Moving into the wake's core (panel (c)), the dynamic pressure of the flow decreases considerably, and the relative drag of the secondary invariably becomes negative. In combination with the vanishing lateral forces in this arrangement, the secondary sphere may rapidly approach (or draft behind) the primary, typically leading to collision between the two. Finally, for a precise set of kinematic conditions, the secondary experiences can travel directly along the path of the primary's bow shock in a phenomenon known as shock surfing (panel (d)), which can greatly enhance the lateral separation velocity of the pair. In this configuration, the post-shock flow angularity and reduced stagnation pressure

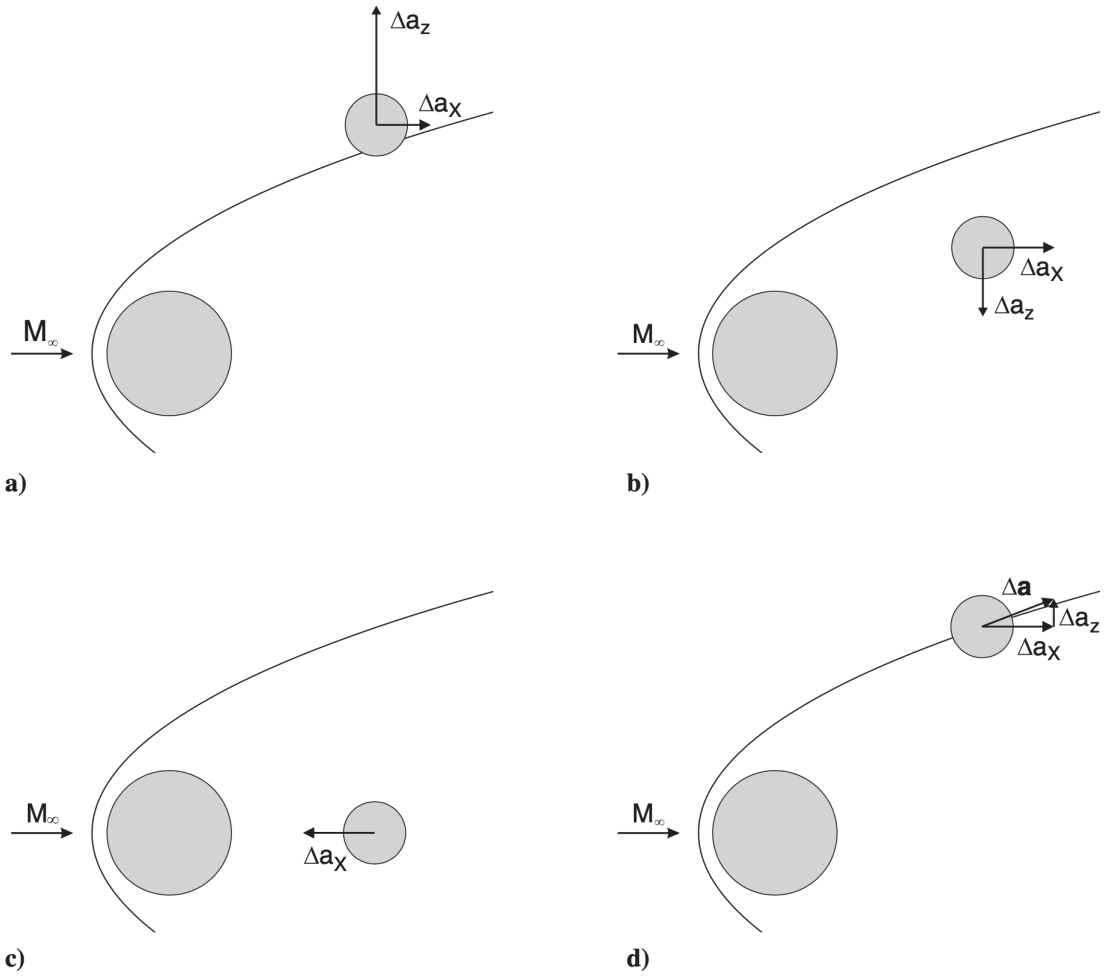

Figure 1.3: Aerodynamic phenomena exhibited by sphere pairs: (a) expulsion, (b) entrainment, (c) drafting, and (d) shock surfing (Marwege et al., 2018).

losses on the secondary's inboard region provides a moderate repulsive force that is balanced by the drag-only dynamics of its outboard side to yield a lift-to-drag ratio equivalent to the tangent of the local shock angle. While this discussion represents only a simplified account of the governing mechanics, the general depiction of repulsion near the bow shock and attraction in the region it encompasses is sufficient for comprehension of the attributes exhibited in more complex scenarios.

Meteoroid fragmentation events are generally categorized into one of two classes with distinct aerodynamic properties: those that spawn a limited number of bodies and those that catastrophically break up into a fluid swarm-like mass (Register et al., 2017), although a transition regime is posited to exist in between (Svetsov and Nemtchinov, 1995). Considering the former scenario, Passey and Melosh (1980) conjectured that, when a body fractures into two spherical fragments encompassed by a common bow shock, the aerodynamic repulsion would result in the smaller fragment achieving a lateral velocity, V_T, determined by a separation constant, C, estimated to lie between 0.03 and 2.25, and the radius ratio, r_2/r_1 (with $r_1 \geq r_2$):

$$V_T = \sqrt{C \frac{r_1}{r_2} \frac{\rho_a}{\rho_m}} V, \tag{1.1}$$

where ρ_a and ρ_m are the atmospheric and meteoroid densities, respectively, and V represents the meteoroid's transit speed at fragmentation. Later studies sought to establish a physical basis for the notion of a governing constant, with Artemieva and Shuvalov (1996) obtaining a value of 0.2 from numerical simulations of separating hemicylinders. Laurence et al. (2011; 2007; 2012), however, provide detailed expo-

sitions of the effects of shock-wave surfing, in which they find that the separation characteristics are highly sensitive to the particular alignment angle and fragment radius ratio considered, obfuscating the meaning of a unique 'constant'. Li et al. (2015) extend the discussion of shock-wave surfing to nonspherical fragments and note that rotational motion of a secondary body can prolong shock surfing.

In contrast to the discrete-fragment case, studies of debris-cloud separation have generally been rooted in characterization of the energy deposition resulting from bodies in atmospheric transit, wherein the aerodynamic spreading rate is a critical parameter. Hills and Goda (1993) introduce the so-called pancake model of continuous fragmentation, in which a swarm of fragments disperses with a separation constant of 7/2. Chyba et al. (1993), on the other hand, model debris-cloud dispersion using the analogy of a face-on deforming cylinder with a well-defined interior pressure, but, while cognizant of the analogy's breakdown at some critical radius, they do not attempt to estimate a governing aerodynamic constant. Svetsov and Nemtchinov (1995) conducted hydrodynamic simulations, noting a cross-range spread of particles in agreement with the above analytical models and a tendency towards conical forms that render the swarm more resistant to spreading and deceleration. Other studies have examined agglomerations with more than two bodies but do not quite replicate the liquid-like dispersion embodying this class of aerodynamic separation. For instance, Artemieva and Shuvalov (2001) numerically simulated the separation of thirteen- and twenty-seven-cube clusters, which each achieved a C value of approximately unity. Park and Park (2020), based on experimental observations of three-, four-, and six-sphere rings, suggested an amended scaling of

the final lateral velocity with dependence on the number of bodies, N (essentially $C \rightarrow CN$), but the noncompact arrangements examined are not typical of realistic entry bodies.

In addition to the repulsive behavior observed immediately after break up, fragmentation events are characterized by strong wake effects. Artemieva and Shuvalov (1996) noted the attractive fluid properties of a fragment's wake, manifested in numerical simulations, for example, by streamwise-aligned columns of cubes bound for collision. Laurence et al. (2007) further explored this effect by applying the hypersonic blast-wave analogy to fragment separation; they found that a stagnation pressure gradient directly behind the primary bow shock was largely responsible for the observed 'collimation' into the primary wake. Finally, Register et al. (2020) identified configurations in which far-wake entrainment is realizable and describe the possibility of protected fragments for a radius ratio of 1/6.

Despite progress in understanding the physics of meteoroid break up, many questions about fragmentation aerodynamics still linger. Only a limited number of studies have investigated the separation of agglomerations with more than two equal-sized, discrete fragments (Artemieva and Shuvalov, 1996, 2001; Park and Park, 2020), none of which considered spherical bodies originating from compact clusters, leaving the effect of a fragmented cluster's population on its separation velocity mostly uncharacterized. Allowing for populous clusters with unequal bodies is expected to further complicate the resultant behavior, with near-wake, far-wake, shock-surfing, and independent trajectories all achievable, but such scenarios have not been examined experimentally or computationally. Extending any of the extant

two-body aerodynamic models (Laurence and Deiterding, 2011; Marwege et al., 2018; Prevereaud, 2014; Register et al., 2020) to this setting may produce reliable trajectory estimates if one fragment dominates the forces on all others; however, the general applicability of two-body modeling across fragmentation scenarios has not been assessed. Additionally, fragment nonsphericity may enhance lateral velocities for shock-surfing bodies (Li et al., 2015), but it is unclear whether it plays a significant role in the bulk separation of clusters. Finally, the current understanding of debris cloud dispersion is mainly rooted in simplistic physical arguments (Chyba et al., 1993; Hills and Goda, 1993), and much of the governing flow physics remains to be constrained. Of course, all of these questions are inherently tied to uncertainties in the internal structure of meteoroids, which remains unanswerable at present.

1.3 Scope of Work

In short, the central objectives of the present work are given by the following five tasks:

- Establish a complementary experimental/computational platform for the study of fragmented meteor analogs in controlled settings.
- Characterize the fluid-structure physics of aerodynamic separation for scenarios with more than two discrete fragments.
- Understand the relationship between fragment dispersal and the population/size-distribution attributes of the disrupted body.

- Construct statistical models of the fragment spread resulting from meteor fragmentation for use in risk assessment tools.

- Constrain the atmospheric energy transfer of dusty debris swarms.

More detailed expositions of the so-called model problem of meteor fragmentation and the strategies undertaken to accomplish the aforementioned objectives are thus given in the following sections.

1.3.1 Definition of Model Problem

Meteor fragmentation is a complex process dependent on the detailed structural properties of an impacting body. While recent explorations of kilometer-scale asteroids have yielded some insight regarding the surface composition and bulk porosity of selected potentially hazardous objects (Fujiwara et al., 2006; Sugita et al., 2019), essentially confirming the rubble pile hypothesis for the largest potential impactors (Walsh, 2018), the accompanying aerodynamics of such agglomerations are poorly constrained. Meanwhile, the attributes of the less massive objects that comprise the majority of documented airburst events are virtually uncharacterized. It can be inferred, however, that these more prevalent small bodies possess some degree of internal strength, as ascertained from their penetration to the lower atmosphere before disruption, while the various chemical compositions determined from recovered meteorites imply a range of formation processes and, therefore, fragmentation tendencies. It is the latter scenario that receives the bulk of our attention in this work, with only a short segment dedicated to strengthless rubble-pile dynamics.

Instead of considering the aerodynamic fragmentation of intricately constructed (and likely unrealistic) impactors with the full breadth of pertinent physics, we find it prudent to examine the problem in a simplified setting to compose a consolidated knowledge base and inform later investigation of more complex scenarios. Thus, we restrict the scope of this work to focus on the following idealized scenario: **1)** following disruption, all bodies are perfect spheres; **2)** these spheres are initially packed in a compact agglomeration bounded by a well-defined circumscribing sphere; **3)** fragmentation occurs instantly; **4)** no regolith (or dusty debris) is released at fragmentation; **5)** no strain energy is freed upon disruption (i.e., the fragments are stationary relative to their common center-of-mass following the moment of disruption); **6)** no further fragmentation of spheres occurs before bodies are aerodynamically independent; **7)** the cluster is rotationally stationary; **8)** all dynamics occur under perfect gas flow conditions; and **9)** inflow properties are constant. Overall, this strategy focuses on simplified geometries and neglects the structural mechanics of material failure prior to fragment release.

We note that certain aspects of the model fragmentation problem represent more significant deviations from realistic meteor disruption than others. Therefore, for the sake of understanding both the inaccuracies introduced by the idealized scenario and the suitability of such assumptions (with many commonly employed in related studies), we will discuss the implications of each constraint individually:

(1) The most significant simplification in this work is that of fragmentation into perfect spheres, which drastically reduces the permissible parameter space by removing the dependence of body rotations and enables the study of aerodynamic

separation in a methodical manner. Despite the magnitude of the simplification, such an assumption is common in the study meteor fragmentation (Laurence et al., 2007; Marwege et al., 2018; Prevereaud, 2014; Register et al., 2020). Indeed, recovered meteorites, as proxies for airborne fragments, commonly exhibit irregular morphologies (Popova et al., 2013) and would be expected demonstrate aerodynamic behaviors distinct from those of a perfect sphere. Relative to the spherical base case, the consequence of the presence of nonspherical fragments, however, has received less attention. Artemieva and Shuvalov (1996, 2001) considered separating hemiclyinders and cubes respectively, but, suppressing the rotational nature of such geometries, they found behaviors quite similar to those of separating spheres. Li et al. (2015), on the other hand, simulated the complete dynamics of sphere-cube pairs and posited that certain fragment geometries may experience extended periods of shock surfing, potentially increasing the lateral range of a disrupted cloud. Additionally, provided a stable angle-of-attack arrangement exists for a particular irregular fragment, it could feasibly develop a natural lifting behavior, which would similarly be expected to enhance the effective lateral velocity of the disrupted impactor. The results of the model problem may thus be considered a lower limit on the fragment dispersal attained during realistic disruption events.

(2) As with distinct meteor fragments, the shape of a progenitor body can range from the highly peculiar (Fujiwara et al., 2006) to the quasi-spherical (Sugita et al., 2019), and the ultimate separation behavior should be very sensitive to the particular combination of morphology and entry attitude encountered. Nevertheless, spherical clusters may be expected to occupy an intermediate regime between the

behaviors of the more oblate and prolate meteoroid geometries.

(3) Structurally, an actual fragmentation event likely involves the failure of pre-existing fault lines above a critical stagnation pressure and internal incubation of the energetic flow through the newly opened fissures (Park and Brown, 2012). In the framework of Park and Brown (2012), the incubation time (that is, the time between incipient structural failure and the onset of aerodynamic separation) may be several times longer than the characteristic separation timescale, which would tend to decrease a body's rate of fragmentation over its flight. On the contrary, the rheological explosion experiments of Gorazdovskij (1976) seem to suggest nearly instantaneous disruption into numerous fragments. Considering the uncertainty surrounding the exact physics of fragmentation, in this work we exclude the investigation of the structural mechanics governing rock-breaking and focus only on the dynamics of the discrete bodies subjected to hypervelocity flow. While the assumption of sudden fragmentation is employed in nearly all investigations of atmospheric energy deposition (Chyba et al., 1993; McMullan and Collins, 2019; Register et al., 2017; Wheeler et al., 2017), future works may seek to unify what now forms a distinct set of physical regimes.

(4) While monolithic impactors likely do not retain regolith in the standard sense (owing to their low surface gravity), they do spawn an abundance of dusty particulate upon structural fracture, evidenced by the enduring dust cloud generally left in a disrupted meteor's wake (Borovi$\hat{c}$ka and Kalenda, 2003; Ceplecha et al., 1998; Gorkavyi et al., 2013; McCord et al., 1995; McIntosh and Douglas, 1968). The presence of this material seems inevitable, but, to the author's knowledge, no

comprehensive exploration of the mass lost to dusty fragmentation debris has been conducted, leaving the primary effect of this assumption unknown. We will, albeit briefly, relax this constraint at the conclusion of this work to allow for a limited investigation of its role in separation aerodynamics.

(5) The structural deformation brought about by aerodynamic loading can result in considerable strain energy, which would grant the fragments some initial kinetic energy upon their release (Laurence and Deiterding, 2011). The degree of momentum conferred for typical meteoroid materials, however, is comparable only to that accrued aerodynamically for sphere pairs and would not present a substantial modification to the terminal fragment trajectories of more populous clusters. Employing the strain energy conversation framework of Laurence and Deiterding (2011), for example, an 15 km/s impactor with an elastic modulus of 200 GPa (typical of iron) bursting into two fragments of radius ratio of 0.2 at an altitude of 16 km will exhibit a maximum dimensionless lateral velocity of 0.18 immediately after disruption, less than the minimum value attained for sphere pairs of equal size.

(6) Fragmentation is initiated whenever the stress distribution somewhere within a body exceeds its material strength, so it is conceivable that a shed fragment could itself break up while still under the aerodynamic influence of the swarm. This is particularly likely for bodies subjected to shock impingement, which produces high heat-flux and dynamic pressure loading near the shock-shock intersection line, and energetic collisions. However, from Weibull strength-scaling considerations (Weibull, 1939), objects resulting from a disruption event are expected to be stronger than the parent body, which may suppress, to some extent, continuous break-up in favor

of discrete fragmentation.

(7) Typical meteoroid rotation periods (minutes, see, for example, Scheirich et al. (2010)) are orders of magnitude longer than the luminous atmospheric transit of an impactor (seconds, see Popova et al. (2013), for instance), so the assumption of an initially nonrotary body for the spatial scales of interest should not affect the fidelity of the results obtained herein.

(8) In a realistic entry setting, the flow around a body of interest is chemically reactive and undergoing radiative processes, leading to significant modification of the temperature and density distributions, especially near the body's stagnation point. The surface pressure distribution over a sphere, however, is only mildly altered relative to the perfect gas scenario (Vincenti and Kruger, 1965), yielding aerodynamic forces that can be closely approximated with more basic physics. We do note that the shock structure of a chemically reactive flow is compressed, effectively lying closer to the generating body. Thus, for a cluster of fragments, the exact bow shock pattern would then differ from the perfect gas case and might be expected to encourage augmented separation of bodies due to shock impingement at locations further inboard. However, Sousa et al. (2021) note that, for bodies in contact, a reduction to the specific heat ratio diminishes the separation impulse, so the overall impact of high-temperature aerodynamic effects is currently unclear.

(9) Because of the exponential density profile of Earth's atmosphere, a meteor's inflow conditions are continually changing along its trajectory. This is, however, at odds with the standard nondimensionalizations of cluster separation properties, which assume constant fluid density and velocity, leaving the equivalence

between measurements acquired using the model problem and real-scenario predictions uncertain. As a demonstration of this quandary, we present a rough calculation of sample fragmentation scenario: a 20-m-radius meteoroid traveling vertically at 20 km/s fragments at an altitude of 30 km and, based on the accepted nondimensionalization with the appropriate density, the aerodynamic disruption timescale is 0.3 seconds, by which time the swarm has descended by 7 km; the density at this lower altitude is 3 times higher than at the initial fragmentation height, leading to a characteristic timescale roughly half of that previously calculated. Repeating this exercise for a more probable entry angle of 45°, swarm descends by $\sim$ 5 km over one characteristic timescale, whereupon the ambient density has risen by a factor of 2.4 and the timescale diminished by 68%, reinforcing the magnitude of the problem over a range of entry conditions. The nondimensionalization inconsistency likewise propagates to velocity predictions, as the resultant collective lateral velocity of a separating cluster is a integrated quantity scaled by the dynamic pressure of the inflow. Using nondimensionalized correlations directly to predict separation properties will inevitably lead to an underestimate in the range of the fragmented swarm, with the exact magnitude of the error dependent on body size and velocity. We do note, however, that methods for translating constant-inflow results to realistic entry scenarios can likely be constructed by modeling the temporal lateral force profiles of separating fragments using, for example, results obtained in this work.

1.3.2 Objectives and Strategy

Having established the physical scope and limitations of the model problem, we will now detail the objectives of the present study and the means by which we hope to accomplish them. The primary variable whose effects we seek to investigate is the fragment composition of a freshly disrupted meteoroid. In particular, the population of the swarm and its fragment size distribution are parameters that have been shown by other authors (Artemieva and Shuvalov (1996), Park and Park (2020), Laurence et al. (2007), etc.) to strongly influence the aerodynamic separation properties of a fragmented body. As is outlined in Section 1.2, the available data beyond a handful of bodies is mostly nonexistent, inhibiting accurate prediction of impact events, so we endeavor to explore the physics and statistical behavior of more populous clusters with the goal of informing meteor risk-assessment modeling.

We begin our explorations of aerodynamic sphere separation with the most basic scenario, clusters of equal-sized fragments. In this particular setting, variation of a single parameter, the population of the cluster, N, can provide insight into changes in the governing physics with increasing cluster size and associated measurements can provide a basis for theoretical predictions of meteor fragmentation. The case of two-sphere separation, studied extensively in the related literature and revisted here with focus on previously unexplored aspects of the problem, serves as springboard into more complex cluster configurations. Progressively increasing the number of bodies present in the agglomeration, we select certain populations to investigate in greater depth and test other cluster populations several times to

promote statistical convergence of our results (as cluster attitude can influence terminal kinematics, particularly for less populous configurations). We impose a ceiling of 115 spheres, set in part by limitations in data processing; this approximates catastrophic breakup events but lies well below the range of dusty debris resulting from a rubble pile impactor. We would like to stress that increasing the number of bodies by no means enhances the fidelity of the results obtained, but rather captures a range of behaviors from a variety of breakup scenarios. For example, the Wabar (Gnos et al., 2013) and Chelyabinsk (Popova et al., 2013) events are characterized by a small number of dynamically relevant bodies (in addition to the numerous small bodies of negligible contribution to the total cluster mass), whereas impacts at Pułtusk (Lang and Kowalski, 1971) and Sikhote-Alin (Krinov, 1974) spawned scores of massive fragments and thousands of meteorites overall. Keeping mindful of the obvious inaccuracies in the model problem of meteor fragmentation, we may cautiously extrapolate the findings from this survey of equal-sphere clusters to inform more realistic configurations.

Clearly, meteoroids do not fragment into clouds of equal-sized bodies, so the second portion of this work concerns the more realistic scenario of clusters composed of unequal spheres. Approaching this problem in a reducible manner, however, requires parameterization of the methods by which sphere sizes are chosen. Meteorite size distributions (assessed from recovered fragments following an airburst) are generally reputed to adhere to a power-law distribution (Hartmann, 1969); while this problem is not quite identical to the distribution of fragment sizes produced at the moment of meteor disruption, one might expect the fragmented distribution to

follow similar trends. Therefore, we determine the composition of unequal-sphere clusters by generating sets of predetermined sphere sizes from randomized realizations of power laws with varying indices. Specifically, a truncated power law defined by $p(r) \propto r^{-\alpha}$ defines the probability of selecting spheres of a certain radius, and the power-law indices explored (α values of integers $1 \rightarrow 5$) are likely to provide a closer approximation to an actual entry event than equal fragments. This class of problem and the survey of equal-sphere clusters together thus form a fundamental two-dimensional space of separation behaviors, which is illustrated by contours of the collective lateral velocity (to be defined precisely in Section 1.4) in Figure 1.4. Due to the vastness of the two-dimensional parameter space and the need for many realizations of each point in the plane, we only examine the separation of power-law clusters for one choice of sphere population, providing an intersection with the equal-sphere survey at 52 bodies.

Finally, a small portion of this work will detail the response of an agglomeration of dusty debris to breakup under hypersonic flow as a proxy for the atmospheric entry of rubble-pile-type impactors. With emphasis on a qualitative assessment of hypersonic particulate separation generally and its patent deviation from accepted models, we describe the implications for the atmospheric energy deposition of these objects and present a new mathematical representation.

To study the separation of equal- and unequal-sphere clusters, we employ a twofold approach with the hope of maximizing the fidelity of the conclusions deduced: experiments in a hypersonic wind tunnel and coupled fluid-structural numerical simulations. The two investigative methods are essentially complementary

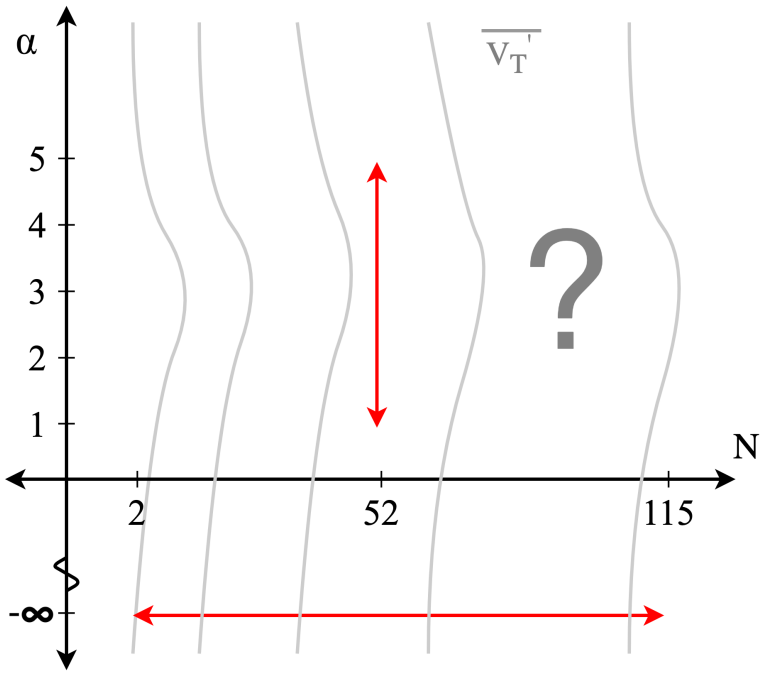

Figure 1.4: Parameter space of aerodynamic separation for model problem with hypothetical contours of separation velocity in gray and cases explored highlighted in red. Note that a power-law index of negative infinity effectively corresponds to a cluster of equal-sized spheres.

in nature, as the simulations allow precise control of attitude parameters (and truly instantaneous release), whereas experiments are more a efficient way to explore a large parameter space, especially with varying fragment sizes and large numbers. All experiments consist of free-flying bodies released from a spherical cluster into a Mach-6 freestream and nonintrusive optical diagnostics that yield measurements of sphere motions. The rapid onset of steady flow in a short-duration facility enables close approximation of an instantaneous breakup, while the (mostly) randomized cluster arrangements signal the need for multiple experiments at each condition to encourage statistical convergence of the terminal kinematics. We note that our experimental framework allows for straightforward testing of arbitrarily populous clusters with any fragment size distribution, although, in practice, we limit ourselves to the aforementioned N–α parameter space. On the other hand, numerical simulations modeling the coupled inviscid computational fluid dynamics (CFD) and finite element analysis (FEA) afford a method for examining in depth the dependence of separation properties on the initial attitude of a cluster. Subjected to variations in the bulk pitch and yaw of the agglomeration, the spheres are instantaneously released from well-defined initial positions into a Mach-20 freestream, and access to fluid state, surface pressure, and forces (in addition to kinematics, of course) provide a greater level of insight into the exact mechanics dictating the aerodynamic separation observed. Computational cost considerations limit this component of the study to surveys of 2, 4, 13, and 57 equal-sphere clusters.

Application of this complementary experimental-computational approach to the model problem allows us to address several outstanding questions impeding ade-

quate characterization and prediction of meteor fragmentation events: what happens when a meteor breaks up into more than two bodies? Are new physical mechanisms introduced as the population of a fragmented cluster increases? How does surface contact between bodies affect terminal trajectories? Do varying fragment size distributions lead to disparate aerodynamic separation trends? Can statistical models of meteor fragmentation be developed? Will they lead to improved separation velocity and atmospheric energy deposition predictions? Do clouds of dusty particulate actually behave as flattening 'pancakes' in high-speed flows, as suggested by previous authors? Obtaining answers to these points serves as the primary objective of this work and will hopefully enhance our common understanding of impact events.

1.4 Important Definitions and Concepts

Several important quantities and assumptions arise repeatedly in this work; we define them now for the reader's recollection. Comparative measurements of cluster separation require a common nondimensionalization to provide a basis for interpreting data obtained under differing flow/flight conditions. The standard time- and velocity-scales found throughout related literature follow from dimensional analysis:

$$\tau_s = \sqrt{\frac{\rho_{\text{sph}}}{\rho_\infty}}\frac{r_{\text{sph}}}{u_\infty}, \qquad \upsilon_s = \sqrt{\frac{\rho_\infty}{\rho_{\text{sph}}}}u_\infty, \tag{1.2}$$

where u_∞ is the freestream velocity, r_{sph} is the radius of the equal spheres, and ρ_{sph} and ρ_∞ refer to the sphere and freestream densities, respectively. The relation

of Passey and Melosh (1980), for example, gives (for equal spheres)

$$V_T = \sqrt{C} v_s, \tag{1.3}$$

where, in their two-body nomenclature, V_T is the final lateral velocity of the smaller body and C their separation coefficient.

For sphere clusters, however, it makes sense to slightly redefine some of these quantities. First, we find it prudent to reference the characteristic time-scale to the radius of the initial cluster, r_c:

$$\tau_s = \sqrt{\frac{\rho_{\text{sph}}}{\rho_\infty}} \frac{r_c}{u_\infty}. \tag{1.4}$$

Furthermore, all calculations of individual lateral separation velocities are referenced to the kinematics of the nonstationary center-of-mass (subscript com) of the cluster:

$$\begin{aligned} \overrightarrow{x_{\text{rel},i}} &= \left(\vec{x}_i - \vec{x}_{\text{com}}\right) - \left(\vec{x}_i - \vec{x}_{\text{com}}\right)_{\hat{x}}, \\ V_{T,i} &= \left(\vec{V}_i - \vec{V}_{\text{com}}\right) \cdot \frac{\overrightarrow{x_{\text{rel},i}}}{||\overrightarrow{x_{\text{rel},i}}||}, \end{aligned} \tag{1.5}$$

where $(\cdot)_{\hat{x}}$ represents the streamwise component of a sphere's relative position. We then define the collective lateral velocity of an N-sphere cluster as the mass-weighted mean of all cluster-centric lateral velocities:

$$\overline{V_T} = \sum_i^N \frac{m_i V_{T,i}}{m_c}. \tag{1.6}$$

Finally, we arrive at the nondimensional quantities,

$$t' = t/\tau_s, \quad V_T' = V_T/v_s, \quad \text{and} \quad \overline{V_T'} = \overline{V_T}/v_s, \tag{1.7}$$

the latter of which essentially equates the separation coefficient, C, with the nondimensional collective lateral velocity:

$$\overline{V_T'} = \sqrt{C}. \tag{1.8}$$

Given that $\overline{V_T'}$ is the more intuitively understood quantity of this identity, in this work we give all collective lateral velocities in terms of this variable. Furthermore, all velocity measurements are implicitly recognized to be dimensionless throughout this work.

For experiments without idealized release of spheres into the freestream flow, the release timescale is not negligible compared to sphere dynamical timescales, and the proper reference time of an experiment, t_0, is not well-defined. To establish a common standard for identifying time-zero in free-flight experiments, we estimate t_0 using two different methods, which are dependent on the properties of the cluster of interest. For clusters whose positions are tracked to early times ($N < 14$, typically), we define t_0 as the time at which an extrapolation of a linear fit to $\overline{V_T}$ reaches zero. For more populous (and unequal) clusters with sphere motions only tracked later in their flight, we instead extrapolate a linear fit to the mean streamwise velocity of the swarm.

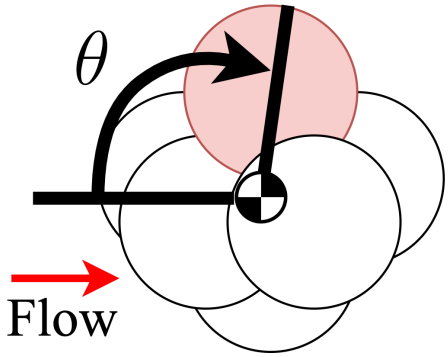

Figure 1.5: Definition of polar/alignment angle used in this work.

At several points in this work we reference the polar/alignment angle, θ, of a sphere/pair. For individual bodies, we adopt a convention wherein θ represents the angle between the upstream direction and a vector connecting the cluster's center of mass to the centroid of the sphere of interest, with an angle of 180° indicating that the body is located at the aft of the agglomeration. For sphere pairs, on the other hand, the alignment angle of the duo is simply set to the polar angle of the downstream body. Figure 1.5 provides a simple illustration of the angular definition used throughout the present study.

In the discussion of experimental results, we adopt a naming convention to clearly and succinctly identify the type and chronological appearance of a particular experiment. For equal-clusters, the number of spheres is followed by the chronologically ordered letter of the test; the second experiment with eleven spheres, for example, would be labeled shot 11B. For unequal-clusters, the power-law index and chronological letter are followed by '-U' to avoid ambiguity with equal-cluster tests, as in shot 2D-U for the fourth experiment of the $\alpha = 2$ clusters. Finally, we replace the population/index character with 'P' for dusty debris clouds.

1.5 Structure of Dissertation

The structure of this dissertation has been formulated to gradually build a foundation of understanding for the reader, highlighting trends in aerodynamic cluster separation and generalizing the most elemental findings in simple statistical forms. The presentation of our work is thus composed as follows.

As hypersonic wind tunnel tests form the primary investigatory thrust of this work, we begin, in Chapter 1.5, by giving a comprehensive account of the experimental methods employed, which constitutes a mixture of novel diagnostic methods and established techniques that have been tailored for this particular problem. Furthermore, we explore the reliability of the current experimental apparatus and detail its fidelity to the model problem described in Section 1.3. The computational methodology is then described in Chapter 3. Here, the details of the coupled numerical scheme are accompanied by grid-refinement and experimental validation studies to verify the validity of the chosen computational model and its implementation.

Following establishment of the methodologies utilized, we recount the details of the results obtained therein. Aiming to slowly construct a cumulative comprehension of the governing physics, we divide each topic into digestible segments, beginning with the smallest ($N \leq 4$) equal-sphere clusters (Chapter 4). The findings of relevant computational surveys are relayed, while certain representative experiments are analyzed in depth. Next, we advance to equal clusters of intermediate size (between 5 and 19 spheres) in Chapter 5, which adheres to a similar structure as its predecessor. The final chapter in the realm of equal-sized spheres (Chapter 6)

examines the separation of the largest clusters encountered (between 20 and 115), which are probed almost exclusively through experiments. Furthermore, we conduct statistical analyses over all equal-cluster populations to derive a basic description of cluster separation kinematics. We note that the exact selection of population subdivisions is somewhat arbitrary, but it does represent approximate delineations in both data processing capabilities and the influence of the physical mechanisms observed.

Increasing the complexity of the problem further in Chapter 7, we expand our purview to the separation of unequal power-law clusters, for which aerodynamic trends are highlighted exclusively through detailed investigations of selected experiments. Beyond the elucidation of the driving mechanics, the statistics of unequal-sphere separation and the extension of the equal-sphere prediction methodology comprise a central role. We relax our constraints on the model problem in Chapter 8 and review experiments of dusty-debris clusters, which serve as an approximate analog to rubble-pile astronomical bodies. This analysis, mostly qualitative in nature, draws a contrast between the wind tunnel observations and existing models of high-speed debris-cloud dynamics, and we posit an alternative model for the atmospheric energy deposition of such configurations. Finally, in Chapter 9, we close with a discussion of the contributions of this work to the state-of-the-art and other assorted concluding remarks.

Chapter 2: Experimental Approach

As detailed in Chapter 1, we endeavor to characterize the aerodynamic aspects of meteor fragmentation by studying the model problem of close-packed equal- and unequal-sphere clusters released instantaneously into a hypersonic freestream, and experimentation in a hypersonic wind tunnel serves as an indispensable approach for addressing this objective. With a suitable methodology, short-duration hypersonic wind tunnels can enable experiments involving arbitrarily complex cluster compositions on rapid timetables, which stands in contrast to the relatively limited set of configurations attainable under the present computational framework (Chapter 3). The randomly configured initial cluster arrangements are well-suited to our interest in the terminal statistical outcomes of the various fragmentation classes, though exploration of the governing fluid mechanics is possible for smaller sphere populations.

Thus, in this chapter, we develop a novel methodology for multi-body free-flight experimentation that enables experiments closely approximating the model problem of meteor fragmentation defined in Chapter 1 and allows for the effective investigation of the aerodynamic separation trends that arise when spheres are released instantaneously into hypersonic flow. While the efficacy of these methods has only been demonstrated in one particular facility, they are applicable to free-

flight experimentation in any short-duration hypersonic wind tunnel, and certain components of the diagnostic techniques can be utilized in long-duration testing as well. We additionally detail the wind tunnel and operating conditions chosen, and describe any observed deviations from the idealized release process. Finally, we recount the parameters of the experiments conducted in this work.

2.1 Facility

The facility utilized for all experiments in this study was the Hypersonic Tunnel for Educational and Research Purposes (HyperTERP) at the University of Maryland (Butler and Laurence, 2019), with labeled schematic provided in Figure 2.1. HyperTERP is a reflected-shock tunnel equipped with an axisymmetric contoured nozzle supplying a Mach number of 6 at its 220-mm-diameter exit plane. The nozzle exhausts into a cylindrical test section measuring 305 mm in diameter, with optical access provided by four 152-mm-diameter windows on the top, bottom, and sides. The driver section of the upstream shock tube measures 5.4 m in length with a 100 mm inner diameter and adjoins the 10-m-long driven section by means of a double-diaphragm, enabling precise control over test initiation. To operate the tunnel, the entire facility is evacuated to near-vacuum conditions, whereupon the driven section is filled with a desiccated test gas (either air or nitrogen) to modest pressure (roughly half atmospheric); the driver section is pumped with a mixture of the test gas and helium to much higher pressure. The precise set of pressures is dictated by the desired stagnation pressure, the selected gas species ratio, and the

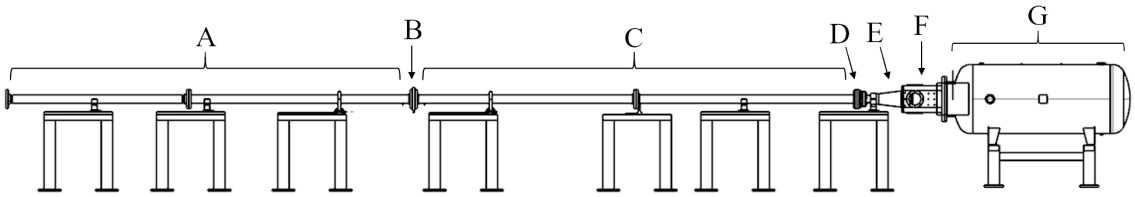

Figure 2.1: Schematic of HyperTERP hypersonic wind tunnel with (A) driver section, (B) double-diaphragm, (C) driven section, (D) secondary diaphragm, (E) Mach 6 nozzle, (F) test section, and (G) dump tank

shock-tube tailoring conditions needed to maximize the steady test time. The test is commenced by rupturing the double-diaphragm, and the ensuing shock advances towards a secondary diaphragm located immediately upstream of the nozzle. This thinner mylar sheet bursts upon reflection of the incident shock, permitting test gas from the high-pressure and -temperature reservoir to pass through the nozzle and begin the test. The steady test time concludes when the expansion from the primary diaphragm rupture reaches the reservoir after reflecting off the opposite end of the shock tube.

During the first tunnel entry of this work, we operated at one test condition with target fill parameters of 56.0 kPa driven pressure, 2.05 MPa driver pressure, and $\sim$0.22 air–helium driver gas ratio, which yields a stagnation pressure of 1.35 MPa and stagnation temperature of 866 K. To match the observed flight time with the nominal steady test duration, the fill pressures (and thus freestream dynamic pressure) were reduced in a subsequent experimental campaign: 52.0 kPa of dried nitrogen and 1.90-MPa driver-gas mixture instead produced a stagnation pressure and temperature of 1.33 MPa and 877 K, respectively. In our notation, Condition A refers to the lower-pressure condition of the second tunnel entry and Condition B

to the higher-pressure flow of the initial campaign (freestream flow conditions are provided in Table 2.1). Note that, because the aerodynamic interference between nearby fragments can be roughly approximated as an inviscid interaction (Laurence et al., 2007), differences in the freestream flow are not expected to modify the characteristics of the separation phenomenon, and, indeed, all pertinent kinematic quantities are nondimensionalized by the dynamic pressure of the freestream.

Exact reservoir conditions are estimated on a run-to-run basis by measuring the propagation speed of the incident shock, as well as the resultant pressure rise, using high-speed PCB pressure transducers mounted in the shock-tube walls. From the sample reservoir pressure traces provided in Figure 2.2, the measured pressures exhibit some degree of overshoot beyond their steady values during the first $\sim$4 ms and Condition A typically shows a brief pressure spike (likely due to the presence of diaphragm shrapnel near the reservoir region), but, because freestream pressure variations do not alter sphere trajectories and only mildly affect the velocities, we consider the steady test duration to extend from flow arrival until the $\sim$13 ms drop-off. Additionally, the swift establishment of steady flow, which is typical of shock tunnel facilities, is crucial for achieving the proper test conditions over the duration of the sphere flight. For Condition A, the stagnation pressure deviates from its mean by a standard deviation of 3.4% over this nominal steady test time, while the variability in mean stagnation pressure over the entire campaign is 0.5%. Condition B, on the other hand, exhibits 3.1% stagnation-pressure unsteadiness during an experiment and 1.9% run-to-run variability. We note, however, a systematic uncertainty of $\sim$1.6% associated with the pressure sensors resulting from intrinsic calibration

	Condition A	Condition B
M_∞	6.0	6.05
P_∞ [Pa]	790	847
T_∞ [K]	110	112
ρ_∞ [kg/m^3]	0.0249	0.0263
u_∞ [m/s]	1264	1275

Table 2.1: Freestream flow quantities for both run conditions

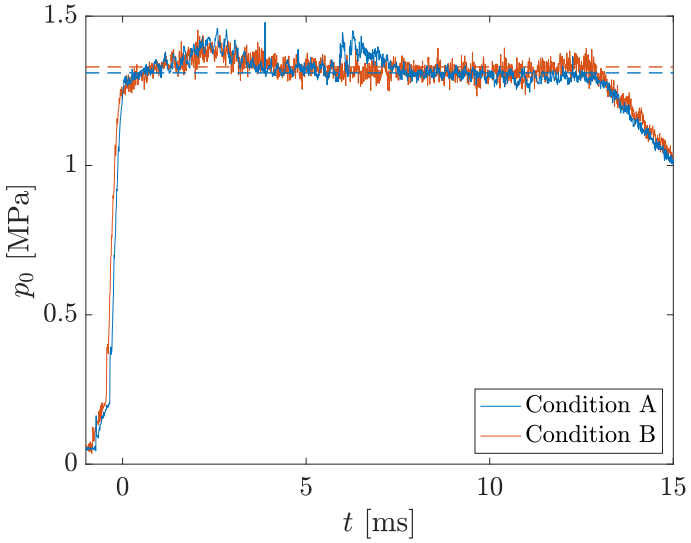

Figure 2.2: Sample reservoir pressure traces where dashed line indicates mean value for each run condition.

errors. Although we cannot directly monitor the unsteadiness in stagnation temperature during an experiment (it is expected to be of lower magnitude than pressure unsteadiness, in any case), we do find a run-to-run variability of $\sim$1.6% in mean temperature based on shock-speed measurements for both conditions.

We note that the shock tunnel is essentially operated as a cold-flow facility, where the fluid physics are limited to the perfect-gas domain. While high-temperature gas effects such as dissociation and ablation are important for understanding energy exchange processes between the atmosphere and a transiting body, pressure, and thus aerodynamic forces, is only slightly modified under such conditions (Laurence and Deiterding, 2011); therefore, replication of the thermal

flow environment is not required to achieve scenarios with representative separation mechanics. Also, meteoroids enter Earth's atmosphere with Mach numbers much higher than that considered here (typically $M_\infty > 40$), but, by virtue of the Mach-number independence principle (Anderson, 2000), we do not expect much deviation in the fragmentation aerodynamics.

2.2 Stereoscopic Visualization

All measurements of sphere motions are performed nonintrusively by means of optical methods. In our setup, two approximately orthogonal camera views were employed to reconstruct the three-dimensional positions from projected visualizations, with three variations of the apparatus used throughout. A schematic of all camera arrangements is provided in Figure 2.3. In the first arrangement, C1 in our notation, a z-type focused shadowgraph arrangement captured the sphere outlines on the horizontal imaging plane and essentially functioned as a schlieren system without a cut-off (although the knife-edge was inserted for selected runs to obtain schlieren images); the reduced presence of flow features prevented compromising the tracking accuracy while allowing some insight into the aerodynamics. Imagery for the focused shadowgraph was obtained with a Vision Research Phantom v2512 (and Nikon 70-300 mm lens at 300 mm) paired to an illuminating Cavitar Cavilux HF laser with a 40 ns pulse length. A second view of the experimental volume was acquired from below the test section by another Phantom v2512 with a Tamron 16-300 mm lens at $\sim$ 150 mm; back-lighting was provided by an array of DC-powered

Luminus 460 ± 10 nm LEDs with several layers of photography diffuser sheeting, which produced a uniform imaging background. The synchronized cameras were operated in either 704×1024 or 608×896–pixel resolution modes, resulting in frame rates of either 32 or 44 kfps, respectively. The exposure time of the second camera varied between 10 and 15 μs; for the given level of illumination, the corresponding noise level fell between 2.1% and 1.4% of the maximum pixel intensity, compared to 1.8% for the shadowgraph system. The Tamron 16-300 mm and Nikon 70-300 mm lenses used herein exhibit pincushion distortion levels of 1.5% and 1.1%, but such effects were not corrected for in setup C1.

Improvements to the apparatus were implemented to ensure higher quality images during the follow-on wind tunnel entry. The presence of a coherence-borne interference pattern in the laser-illuminated shadowgraph system introduced optical artifacts that decreased the signal-to-noise ratio of the acquired data. To remove such undesirable features from the images in the second configuration, C2, we instead placed a single LED (Luminus, 537 ± 15 nm) at the focus of the 1.5-m shadowgraph mirror; a ∼0.5-mm pinhole reduced the effective emission area of the light source, thereby maintaining suitable depth-of-field. The previous shadowgraph camera was replaced with a Phantom v2640, which operates in both 4-Mpx standard mode and the faster 1-Mpx binned mode. Most experiments were conducted at 35-kHz/0.8-μs in binned mode, with both cameras at 768×896-pixel resolution, while several runs utilized a 1552×1792-pixel-resolution shadowgraph at 9.4 kHz. Furthermore,

https://www.lenstip.com/405.6-Lens_review-Tamron_16-300_mm_f_3.5-6.3_Di_II_VC_PZD_MACRO_Distortion.html

https://www.lenstip.com/537.6-Lens_review-Nikon_Nikkor_AF-P_DX_70-300_mm_f_4.5-6.3G_ED_VR_Distortion.html

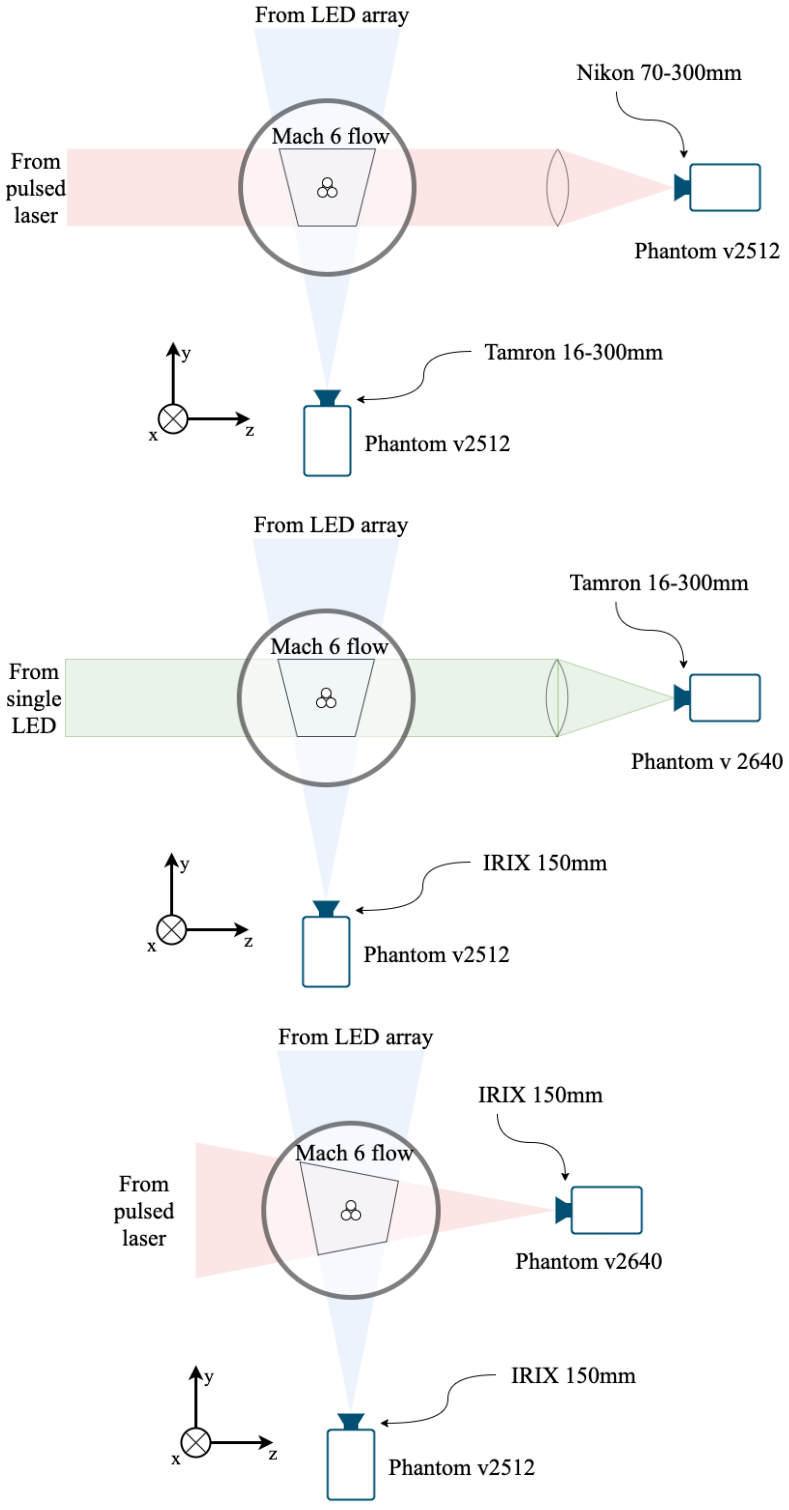

Figure 2.3: Downstream view of stereoscopic camera arrangements and effective viewing volumes with coordinate system orientation. Camera setups (top) C1, (middle) C2, and (bottom) C3 are pictured.

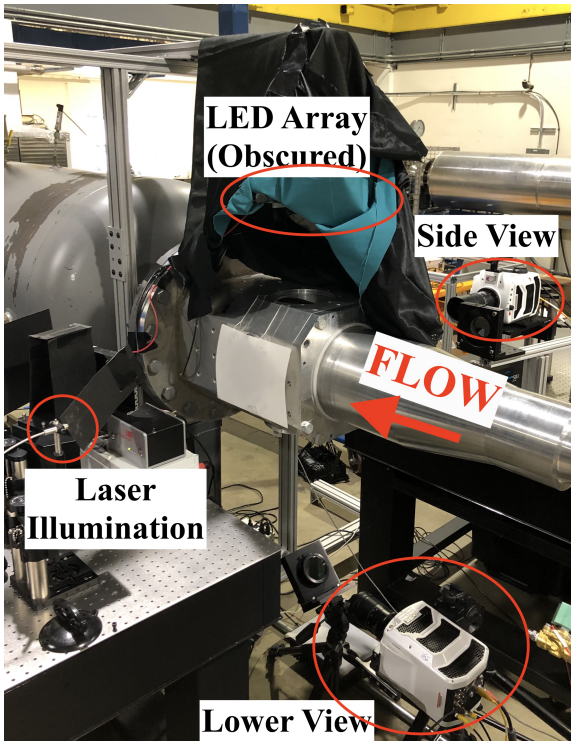

Figure 2.4: Photograph of camera setup C3 with relevant details highlighted.

the camera lenses were reorganized to use an IRIX 150 mm lens, which is virtually aberration-free, for the standard view. Finally, to minimize errors produced by refractive index disturbances in the flowfield, an additional standard camera with IRIX 150 mm lens replaces the shadowgraph in the third visualization apparatus, C3, a photograph of which is shown in Figure 2.4. As the LED of arrangement C2 provided inadequate illumination, the pulsed laser was reintroduced to the horizontal viewing plane, and three layers of diffuser sheeting was deemed sufficient to mitigate the influence of speckle interference in the back lighting. A longer pulse length of duration 400 ns was required. The noise levels of the shadowgraph and standard cameras in these arrangements are ∼1.4% and ∼1.1% of the mean background pixel value, respectively.

https://www.lenstip.com/556.6-Lens_review-Irix_150_mm_f_2.8_MACRO_1:1_Dragonfly_Distortion.html

2.3 Model Suspension and Release

All experiments in this investigation utilize spheres released into the freestream flow as test models, with both random and predetermined clusters designated as initial configurations. A principal difficulty associated with free-flight experimentation is suspending a test model at the correct orientation prior to a test and achieving rapid, nondisruptive release after flow establishment. Previous studies have employed frayed dental floss severed by impulsive flow startup (Laurence et al., 2012), mechanically actuated cut-down of cotton threads (Mudford et al., 2015), and electromagnetic control systems (Tanno et al., 2012) in the suspension/release procedure, but such methods are infeasible when considering large collections of bodies. Instead, we rely on aerodynamically informed models enabled by three-dimensional printing methods, which helps to transfer much of the design complexity away from manual setup processes.

The foundation of the new configuration is a pair of hemispherical shells that enclose the spheres and, following flow arrival, separate cleanly and rapidly by aerodynamic means. Figure 2.5 presents a representative depiction of a single shell. Before the test, the shells are held together by two dowel/hole pairs located on tabs forward and aft of the cavity; a small degree of misalignment is introduced to subject the shells to structural loading, impeding their natural tendency to separate when hanging before a test. For predetermined sphere arrangements, the inner diameter of the encasing cavity is assigned a value 98% that of the cluster's circumscribing sphere and molded spherical caps are subtracted from the interior surfaces to guide

the test bodies into the chosen positions. On the other hand, when a random agglomeration of spheres is desired, one can simply fill the assembled shells through a 9.5-mm aperture. Each shell is additionally fitted with a set of flaps to promote aerodynamic separation from the initial formation. The forward flaps are angled at 30° to the freestream flow, which was deemed a suitable inclination to achieve a strong opening moment over a range of yaw angles; to reduce mass these flaps are printed as frames which are canvassed with Kapton tape. The rear flaps are aligned with the freestream and are extruded from the upper and lower surfaces of the shells to avoid the wakes of the forward flaps. As the shells yaw outward, the rear flaps are increasingly exposed to the flow and provide an increase in the lateral momentum of the shells, precluding recontact with the spherical test bodies. Suspension anchor points are aligned with the center-of-mass of the modeled system, with a small streamwise correction due to the presence of the Kapton tape. Once assembled, the model is hung oriented directly into the freestream flow.

The shells must be lightweight to ensure that they break apart from the initial configuration quickly, imparting minimal impulse to the interior spheres and leaving them undisturbed in the freestream. The size of the shells varies with cluster configuration (ranging between diameters of 13 mm and 18 mm), but a shell/flap thickness of 0.5 mm and a mean mass of 0.45 g regularly results in separation times of less than 1.5 ms. We note that the shell design is not rigorously optimized by means of, for instance, coupled CFD/FEA simulations but was rather established after incremental improvements to its separation performance as observed by experimentation. All 3D-printed models are fabricated on a Formlabs Form 2 stereolithography printer,

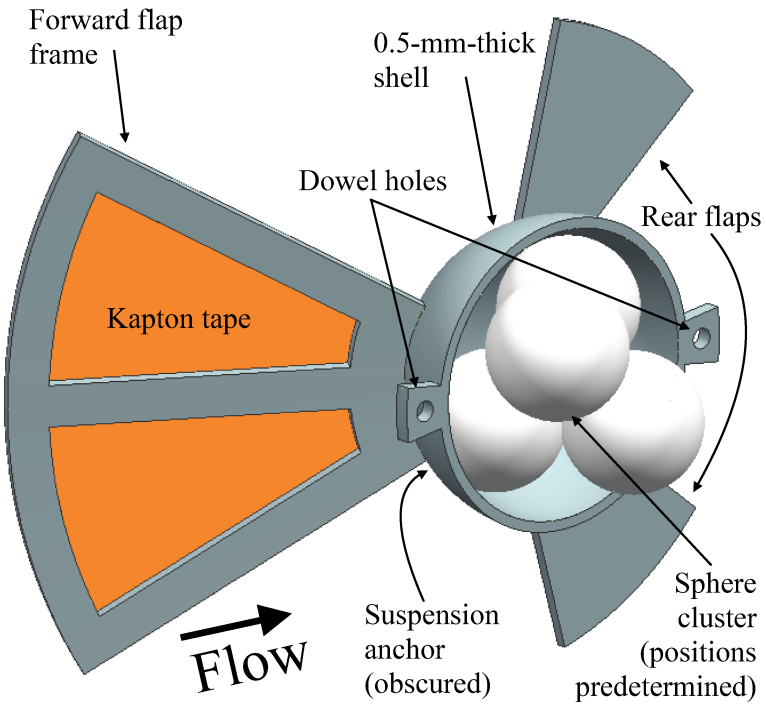

Figure 2.5: Computer-aided design of suspension/release model for a predetermined four-sphere cluster. Opposing shell not shown.

which, with a layer thickness of 50 μm, is capable of resolving fine model details. After the models are cleaned of the inevitable layer of print residue, they are cured under 405-nm light for 30 minutes at 60 C to improve structural properties such as elastic modulus and total tensile strength. The mildly adhesive finish of the resin-based models is detrimental to facilitating a smooth breakup process, so all shells and spheres are coated with a thin layer of cornstarch powder to mitigate disturbance of the test configuration.

In Figure 2.6, we present a synchronized sequence of images from below and the side of the test section illustrating the experimental initiation process. At pre-test quiescent conditions (column 1), two threads of dental floss, each frayed to a single strand below a piece of tape, suspend the entire formation from hooks mounted in

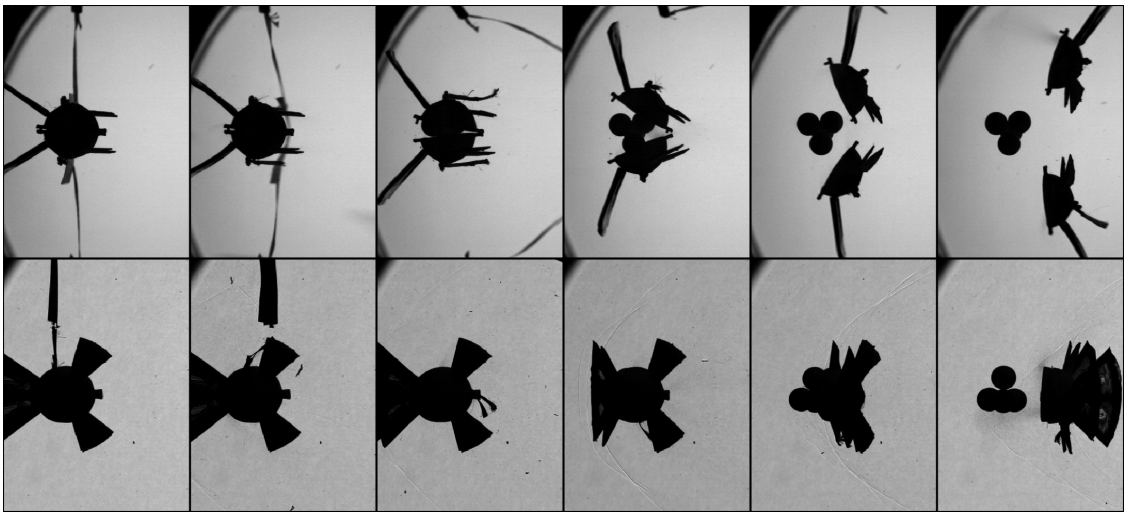

Figure 2.6: Separation sequence of hemispherical shells enclosing sphere cluster. Images taken from (top row) below and (bottom row) the side of the test section shown in 0.33 ms intervals. Flow arrival occurs in second column.

the test-section roof. At flow arrival (column 2), the sudden acceleration of the tape causes the floss to break, while in columns 3 and 4, the high inboard pressures on the forward flaps cause the shells to open about the rear dowel/hole pair. By column 5, the shells have rotated far enough that the trailing flaps provide some degree of lateral acceleration. Finally, in column 6, the cluster has developed its own bow shock and none of the spheres are obscured by the shells, so we consider the valid portion of the free-flight experiment to have commenced.

From Figure 2.6, it is clear that the cluster is fully visible in the shadowgraph view much later than in the standard view ($\sim$0.5 ms), which is undesirable for configurations in which we seek to extract motions from early portions of the spheres' flights. To obviate this limitation, we additionally introduce a variant of the shell design with both forward and rear flaps rolled 45° about the primary axis of the apparatus. In this configuration, the cluster becomes visible in both camera views simultaneously, allowing for three-dimensional position estimation before the spheres

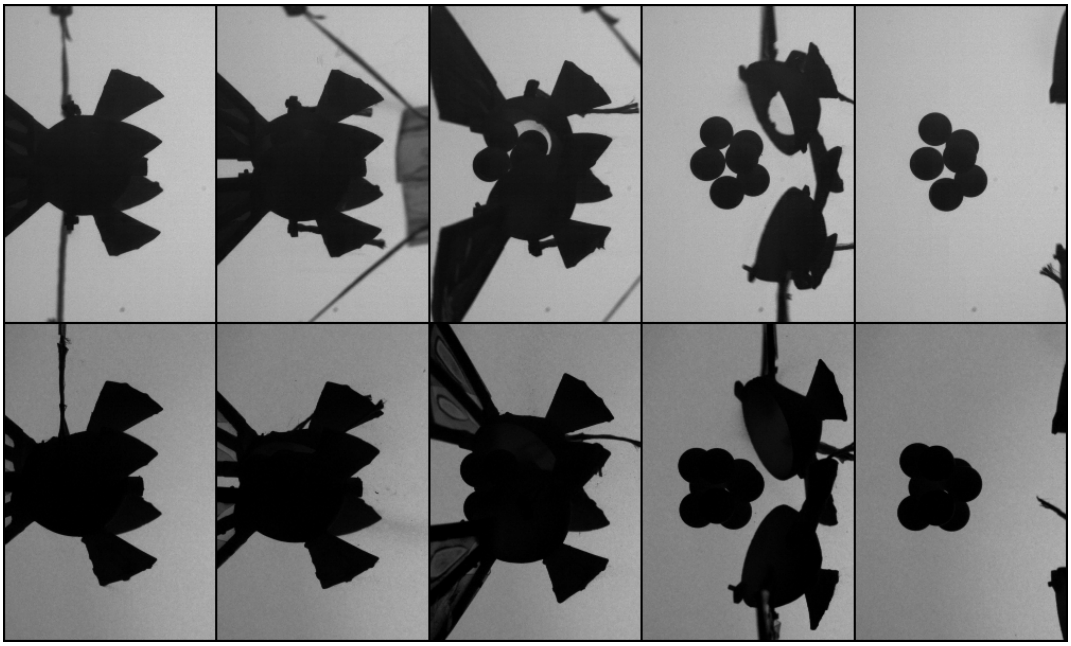

Figure 2.7: Separation sequence for suspension shells with flaps rolled by 45° for (top) vertical and (bottom) horizontal camera standard views (arrangement C3). Images show in intervals of 0.4 ms.

progress too far from their initial locations in the cluster. Indeed, in Figure 2.7, we see that, prior to flow arrival, the shells appear identical in projection and, by a time of ∼1 ms (frame 4), the cluster is unobstructed in both camera views, verifying the efficacy of the rotated shell setup. We additionally make use of this shell design for experiments of dusty debris, as a shell junction aligned with the vertical camera view will occasionally leak onto the lower window, obscuring the visualization path.

Due to the combination of sphere size constraints (shell opening transients may overwhelm the trajectories of especially small spheres) and the limited field-of-view (FOV) allowed by the test section windows, the streamwise separation length-scale is estimated to be slightly larger than the streamwise extent of the viewing volume. As characterization of the terminal separation properties is a central goal of this work, we conduct a majority of the experiments with the agglomeration

suspended upstream of the FOV, which promotes the aerodynamic independence of constituent spheres before they exit the FOV. All other tests, such as those shown in Figures 2.6 and 2.7, feature a cluster initially located within the FOV. The number of tests conducted in each suspension position is noted in Table 2.2 at the end of the chapter.

2.4 Body Tracking Routines

Every test case in this experimental series features an initially close-packed cluster of spheres that quickly breaks apart, transitioning into a number of well-spaced bodies on independent trajectories. We thus begin tracking bodies as they leave the field-of-view and process the image set in reverse order. However, line-of-sight obscuration is virtually guaranteed for this class of testing, and the degree of overlap dictates the selection of body tracking routines employed during image processing. Working backwards, we begin with an edge-detection algorithm (Section 2.4.1), as the spheres are adequately separated, and progress to synthetic image fitting (Section 2.4.2) when the bodies approach their initial cluster.

2.4.1 Edge Detection

When only minor silhouette overlap is present, we estimate the position of a sphere in an image using the edge-detection routine detailed extensively by Laurence and various co-authors (Laurence and Karl, 2010; Laurence, 2012; Laurence and Hornung, 2009). We will, therefore, present only briefly the operating principles of

this algorithm along with any modifications needed for the present application.

For each sphere, we begin by identifying a sub-image region consisting of the $2d_{\text{sph}}$-pixel region centered about the expected sphere centroid. This sub-image is subjected to a Canny edge detector (Canny, 1986), which identifies sets of connected edges in an image, expressed as a binary representation of the input. At this point, user input is required to identify the start and end points of the circular arcs corresponding to the sphere outline of interest. With moderate overlap present even at later test stages, the use of multiple segments to define an interrupted sphere edge is not uncommon. The identified pixel-resolution edge points are then refined to subpixel accuracy through examination of the sub-image's gradient-magnitude distribution (Laurence and Karl, 2010). A linear least-squares fit of a circle to these subpixel-resolution arcs then yields the sphere's projected coordinates and radius. For reference, Laurence and Karl (2010) observed positional uncertainties of $\sim$0.001 pixels for a sphere of radius 25.4 pixels using this technique.

In testing scenarios with large numbers of spheres, we include a slight modification to the above edge-detection process to reduce the extent of manual labor by eliminating the need for clicking start/end points of every edge segment. Beginning with a circular Hough transform of the input image, we obtain approximate centroid locations of the spheres within the field-of-view and compute the Canny edge image as before. Given a set of estimated circle radii, $r_{\text{sph,proj}}$, we collect all edge points within $1.05r_{\text{sph,proj}}$ of the Hough centers and assign edge directions based on their relative positions. We then perform least-squares fits of the subpixel-corrected edges to achieve a new estimate of the circle centroids. We iterate through the

edge acquisition and fitting process thrice more, utilizing only edge points located between 0.98 and $1.02r_{\mathrm{sph,proj}}$ from the current centers, which has been observed to achieve convergence. To prevent the accumulation of tracking errors, some logic is implemented: if a calculated sphere position lies more than one radius away from its predicted location (computed from a six-point quadratic fit), we instead assign to its trajectory the quadratic prediction. Furthermore, a manual input stage can be activated if severe discrepancies between the predicted and Hough-transformed centroids are detected. We note that a small degree of error is incurred during sphere overlap due to the edge selection range of 0.98–$1.02r_{\mathrm{sph,proj}}$, but this effect is offset by an orders-of-magnitude reduction in the manual labor requirements.

2.4.2 Synthetic Image Fitting

Towards the beginning of an experiment, the significant amount of sphere edge occultation precludes the use of edge detection as a viable method for positional tracking, as the least-squares fit quality decreases with the reduction in available arc length; furthermore, the identity of edges tends to become unclear under manual examination, and the Canny routine encounters difficulties near silhouette intersections. To account for these changes in the visualization environment, we instead employ a newly developed synthetic-image-fitting routine to more accurately estimate the pixelwise centroids of the spheres. At the basis of this algorithm is the idea that a set of spheres can be represented in a noise-free artificial image using basic computer vision techniques. In contrast to more complex free-flight geome-

tries studied in stereoscopic systems (Starshak et al., 2018; Starshak and Laurence, 2021), determining the projected shape of a sphere is a trivial task. However, in our implementation, distortion in the optical system (which is possibly compounded by that arising from flow features) led us to select an unrotated ellipse, rather than a circle, as a suitable proxy for the appearance of a sphere.

The generation of a synthetic image is divided into subsidiary tasks by producing one image for each individual sphere before merging all into a composite frame. The parameters needed to create an elemental sub-image are the $x-$ and $y-$pixel coordinates of a sphere's projected centroid, the elliptical semi-major and semi-minor axis values, and a smoothing parameter. The image then is produced in several stages that seek to replicate the effects of blurring and pixelation inherent in the acquisition optics. First, we construct a high-resolution binary image by examining whether test subpixels fall within the bounding zone of a given ellipse. The increase in resolution relative to the baseline image varies inversely with the standard deviation of the camera noise; for example, a camera noise level of 1.6% of the mean background pixel intensity would equate to a 8×8 grid of subpixel sampling points for fitting purposes. The grayscale range of this image is then scaled such that the obscured and background subpixels match their respective mean values in the wind tunnel images. Next, we model blurring by passing the high-resolution image through a Gaussian filter with width determined by the input smoothing parameter, generally equating to a full-width half-max in the range of 0.5 to 1.5 pixels. The single-sphere artificial image is then obtained by averaging the subpixel intensity within each proper pixel, as in the example presented in Figure 2.8. Finally, the

Figure 2.8: Construction sequence of a single artificial ellipse image with (left) 8×8 super-resolution image, (center) applied blurring, and (right) final pixelated result.

complete synthetic image is composed by a pseudo-ray-tracing process in which we stack the individual ellipse images and retain the minimum pixel value along each slice. The routine can be conducted in parallel until this final operation, which considerably reduces the computation time on multiprocessing-enabled machines.

With this synthetic image generation routine established, we are now able to estimate the two-dimensional locations of the N spheres in camera coordinates. Minimization of the difference between an experimental image and modeled artificial images is undertaken using the Nelder–Mead algorithm (Nelder and Mead, 1965) for a non-linear least-squares fit of the $5N$ free parameters: centroid position, elliptical axis lengths, and smoothing magnitude for each sphere. The Nelder–Mead algorithm does not require gradient evaluations, which is useful for our current setting with a potentially large number of variables, and takes a scalar functional output, in this case the 2-norm of the image residual, to survey the parameter space. For the sake of computational cost, we prime the global optimization process by first attaining an approximate fit for each sphere individually. The global minimization

problem is subsequently allowed to run for $20 \times 5N$ iterations, which has been observed to provide suitable convergence. For example, we provide in Figure 2.9 a typical image displaying severe overlap, the best-fit residual image, and the cost curve attained during the minimization process. Note that flow features present in shadowgraph images do increase the residual error but often appear sufficiently distant from ellipse edges as to limit influence on the fit quality. Occasionally, spheres will experience periods of complete occlusion or near alignment, preventing accurate tracking altogether. Under these circumstances, which mostly occur near the beginning of an experiment, we correct for obvious errors by replacing the affected portion of the trajectory with a second-order or, occasionally, a third-order polynomial curve-fit, omitting from the fit data obviously unreliable timesteps. From a limited error estimation study of this method considering artificially generated images of three overlapping ellipses with 1.6% added noise, we find a characteristic positional uncertainty of 0.012 pixels. While this marks a considerable increase from the edge-detection method, achieving higher positional accuracy is most necessary when computing sphere velocities (as differentiation amplifies errors), which are not a major concern earlier in an experiment.

2.5 In Situ Camera Calibration

Calibration of the optical apparatus is an essential step in determining the three-dimensional positions of the free-flying spheres. Arrangements C1 and C2 necessitate the use of two distinct camera models to describe projection from a point

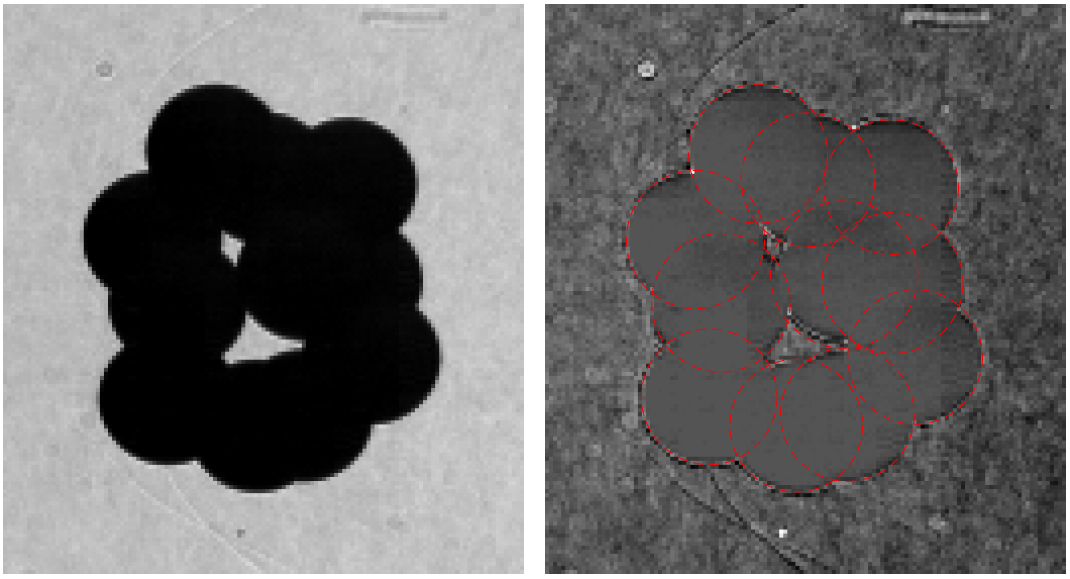

(a) (b)

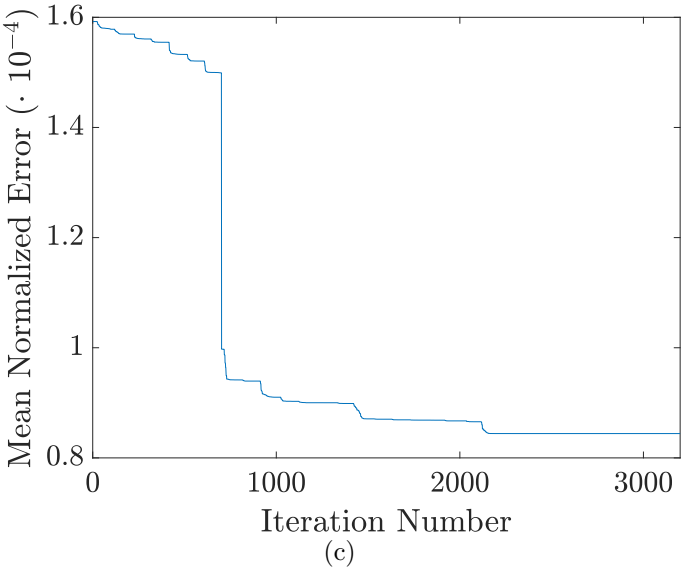

(c)

Figure 2.9: (a) Experimental shadowgraph image of 11 spheres, (b) best-fit residual image with sphere edges from initial kinematic-derived guess, and (c) optimization cost curve.

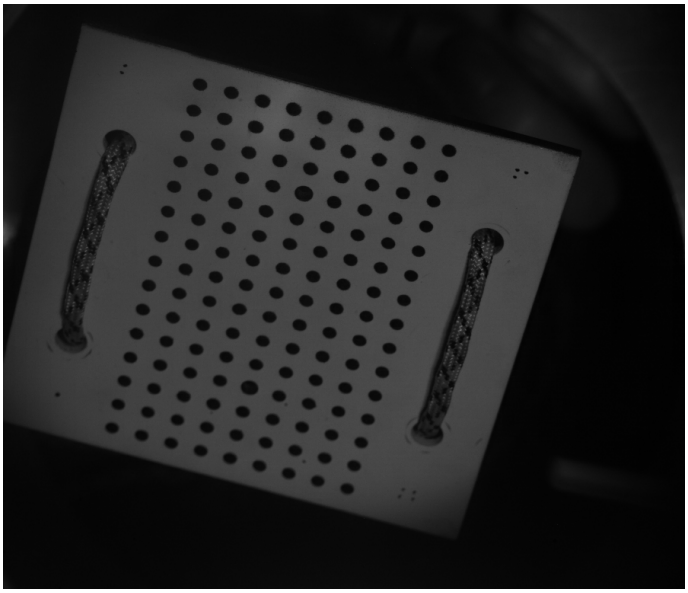

Figure 2.10: Sample internal calibration image of 9 × 15 grid of markers.

in three-dimensional space to locations on the image planes: a standard pinhole model suffices for the vertical view, whereas the parallel light of shadowgraph warrants an orthographic projection model. For setup C3, on the other hand, a camera model consisting of two pinholes will suffice. The first stage of calibration involves determination of the cameras' internal parameters (i.e., scale and projective center), which was accomplished by imaging a 9×15 grid of markers on a suspended plate at various orientations inside the test section and jointly solving for the plate and camera properties that minimize the projected error of the markers.

As a consequence of a sensitive mounting system with occasional misalignment occurring between runs, determination of relative camera positions and orientations (i.e., the second stage of calibration) was conducted on a run-to-run basis by means of a novel in-situ self-calibration technique that effectively allows the experimental sphere positions to double as calibration data. Our method is enabled by the fact that a point in three dimensional space projects to a four-coordinate set when

imaged by two cameras, which effectively allows for one free parameter per realization. Thus, using the edge-detection method of Section 2.4.1 on a subset of camera frames without significant projection overlap, we compute the subpixel-accurate two-dimensional positions of each sphere to form a set of constraints. Next, we achieve best fits to both three-dimensional sphere positions and camera positional/rotational parameters by minimizing the projection error dictated by the selected camera models, a process known as bundle adjustment (Triggs et al., 2000). In our implementation of bundle adjustment, we place the pinhole camera at the origin and, due to the lack of depth information in orthographic projection, constrain the shadowgraph camera to lie at a position 1 m away from the test section. We additionally utilize at least 1,000 pairs of sphere pixel locations to prevent overfitting. On certain occasions, it is clear that the cameras' focal and first-order distortion values have shifted between runs, so we fit those parameters during the calibration process when appropriate. The estimated position and orientation of the shadowgraph camera relative to the primary pinhole camera thus serves as the basis for reconstructing the sphere positions for the remainder of images in a given experiment.

In certain circumstances, establishing consistent sphere identities between camera views may not be an obvious process, but, because self-calibration relies on an accurate sphere-pair mapping, we must devise a method for labeling the bodies without knowledge of the true camera arrangement. We first begin with an approximately correct camera calibration, generally taken from a previously processed experiment, and accordingly compute the reprojection errors of all $\binom{N}{2}$ sphere-pairing combinations. The two-dimensional profile of the reprojection error thus encodes

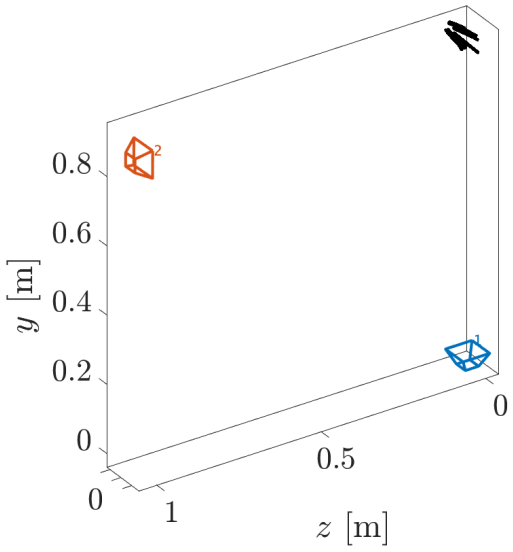

Figure 2.11: Reconstructed camera arrangement for an experiment conducted in setup C2 with jointly-optimized sphere locations shown in the upper right.

information regarding inaccuracies in the assumed camera calibration that should be common only to those errors acquired using the correct sphere labels, that is, all correct sphere pairings exhibit similar spatial error profiles, whereas an inconsistent labeling shows drastically different errors. Therefore, we perform a sixth-order polynomial fit to the reprojection error profile and select the combinations of sphere pairings that minimize overall deviation from the fit, an example of which is shown in Figure 2.12. For comparison, an incorrect pairing can result in errors spanning hundreds of pixels, as opposed to the $\sim$ 4-pixel deviation illustrated here. As this procedure requires an acceptable error profile to attain an initial fit, we identify one body of known identity, either the first or last sphere to exit the field-of-view, and update the polynomial fit after adding each pair mapping. Once all spheres are suitably labeled, self-calibration can proceed as above.

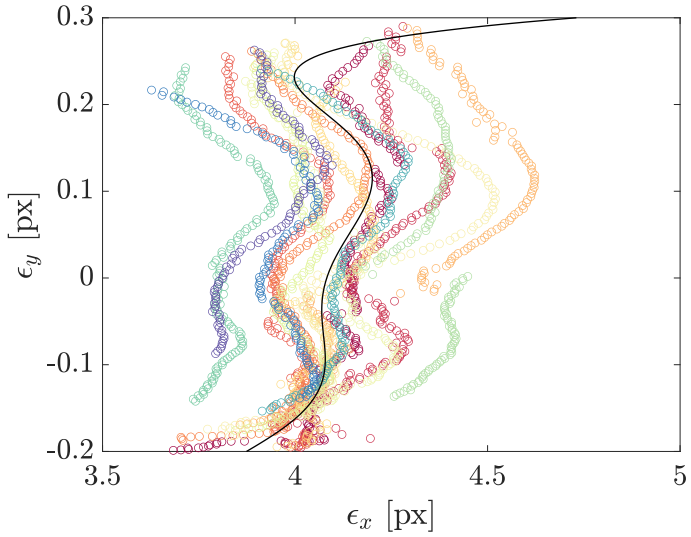

Figure 2.12: Preliminary reprojection error profiles used to derive consistent sphere labels in 14-sphere experiment. Circular markers indicate error for each sphere observation, while solid black line is sixth-order polynomial fit to stacked error profile.

2.6 Three-Dimensional Reconstruction

After tracking a set of spheres in two-dimensional pixel coordinates and establishing a camera calibration, one can estimate the three-dimensional positions of the constituent bodies. In general, a camera model establishes a method for defining the equivalence between a point in the camera's intrinsic two-dimensional frame and a line in the global coordinate system. Therefore, two points in different camera views corresponding to the same object spawn projection lines that intersect precisely at the object's three-dimensional location. Realistically, errors in both sphere positional estimation and camera calibration preclude the intersection of the skew projective lines. Instead, three-dimensional triangulation of a point is computed by solving for the coordinates along the projective lines for which the distance between the two is minimized by means of linear least-squares fitting. The corresponding

three-dimensional point is defined as the midpoint of the minimizing coordinates, and the projection error is taken as minimum distance between the projective lines. While not a rigorous form of uncertainty estimation, the projection error combines the uncertainties of sphere tracking with those of camera calibration and yields an approximate sense of the scale of errors accrued. Three-dimensional reconstruction can easily be extended to an arbitrary number of cameras to better constrain sphere positions.

Characteristic uncertainties in the reconstructed three-dimensional positions for this work are estimated based on the projection errors derived from representative tests. In Figure 2.13, for example, we provide errors for experiments in the C1 campera arrangement with four and eleven spheres, respectively. The four-body experiment, consisting of spheres of 6.35-mm diameter, utilizes edge-detection tracking exclusively. A spell of elevated uncertainty afflicts one body near the beginning of the test, possibly arising from refractive index disturbances caused by the wake structure generated by spheres further upstream. Furthermore, projection errors increase for all bodies near the conclusion of the experiments, which is likely a consequence of increased distortion near the edge of the field of view. Over the complete test time, we observe a mean error of 0.033 mm ($0.0052 d_{\mathrm{sph}}$), which serves as a characteristic positional uncertainty for spheres of this size using edge-detection methods.

The eleven-body test (Figure 2.13(b)), featuring 4.76-mm-diameter spheres, employs a combination of synthetic image fitting and edge detection, with the $t = 3.4$ ms transition point marked by a vertical dashed line. The projection errors, as well

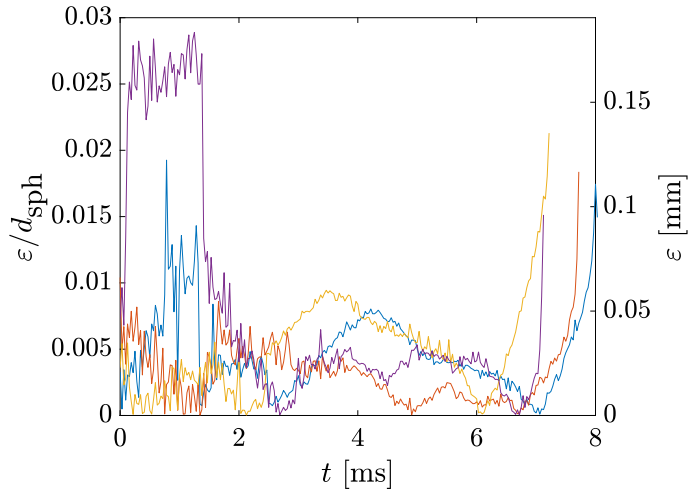

(a)

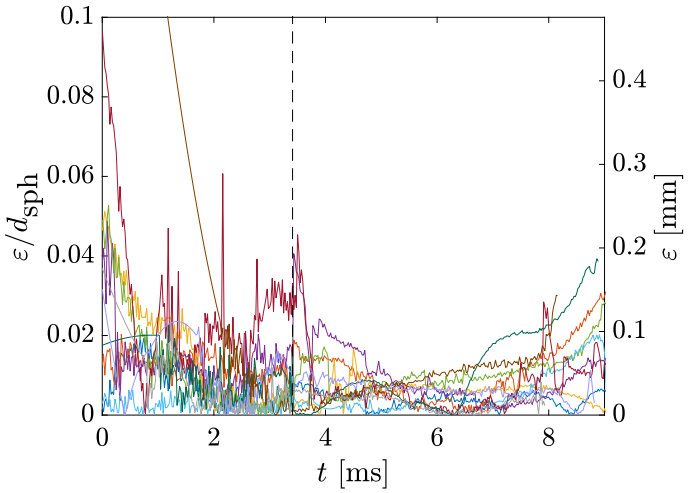

(b)

Figure 2.13: Representative projection errors in the C1 camera arrangement for (a) four spheres of diameter 6.35 mm and (b) eleven spheres of diameter 4.76 mm. Synthetic image fitting was employed to the left of the dashed line and edge detection to the right.

as the point-to-point scatter, of the former method are clearly enhanced relative to those of edge detection. While these difference are partly due to the accuracy limitations of synthetic image fitting, the increasing proximity of spheres towards their initial positions diminishes the amount of information available to constrain sphere positions. Indeed, one of the spheres (colored in brown) was completely obscured before $t = 2$ ms, and extrapolation of a second-order polynomial curve fit contributed to the high errors observed for this body. Synthetic image fitting for this test thus exhibited mean projection errors of 0.060 mm (0.089 mm) without (and with) inclusion of the obscured trajectory, corresponding to $0.013d_{\text{sph}}$ ($0.019d_{\text{sph}}$). This compares with 0.037 mm, or $0.008d_{\text{sph}}$, for edge detection.

Uncertainties for the improved camera configurations, C2 and C3, are much reduced, as expected. As in Figure 2.14, projection errors from a 4.76-mm-diameter, 14-sphere test in the C2 arrangement exhibit maxima of $\sim 0.01d_{\text{sph}}$, with a mean error of $0.0044d_{\text{sph}}$, or 0.022 mm, over the full test time. This 33% uncertainty decrease in the edge-tracking method can likely be attributed to the augmented signal-to-noise levels, as well as the use of a zoomless camera lens (oriented in the vertical direction) that minimizes optical distortion. A representative experiment in setup C3 employed both edge-tracking and synthetic-image fitting routines to track 8 bodies of diameter 5 mm. Exchanging the shadowgraph for a second standard camera effectively halved the measured projection errors, as mean uncertainties of $0.0019d_{\text{sph}}$, or 0.0095 mm, were observed over the full test duration. While the standard camera setup allows for more accurate assessment of sphere trajectories, it lacks the qualitative flowfield information afforded by shadowgraph, which can be

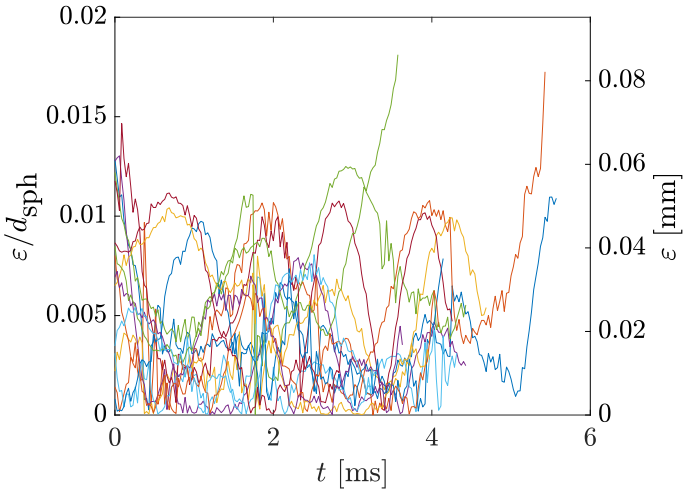

(a)

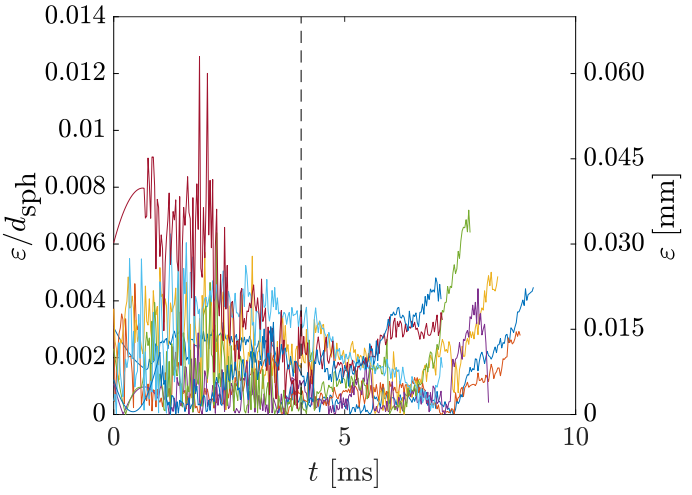

(b)

Figure 2.14: Representative projection errors in the (a) C2 and (b) C3 camera arrangements. Synthetic image fitting was employed to the left of the dashed line and edge detection to the right in panel (b).

beneficial when interpreting separation behaviors.

Sphere velocities are computed by differentiating their positions with a three-point central-difference scheme and applying successive moving-average filters of 7 and 5 data points. Following the smoothing operations, the characteristic uncertainty in velocity for a particular configuration is given by (see, e.g., Altman and Bland (2005)):

$$\sigma_v = \frac{1}{\sqrt{70}} \frac{\sigma_x}{\Delta t}, \tag{2.1}$$

where σ_x refers to the error resulting from positional tracking and three-dimensional reconstruction. For the 4.76-mm-diameter C2 case, for example, this would equate to 0.092 m/s or, in terms of the nondimensional lateral velocity introduced in Section 1.4, $0.017 v_s$; we consider this sufficiently low for confidence in the extracted velocity profiles.

2.7 Experimental Reliability Considerations

Now that we have established the workings and capabilities of the implemented experimental methodology, we briefly discuss the feasibility of trajectory replication compared to our idealized scenario of spheres originating from well-defined initial positions and instantaneously released into a well-established flow. Possible dynamic influences arising from the free-flight testing framework that might lead to deviations from this scenario are flow startup transients, disruption of spheres due to surface contact with the separating shells, aerodynamic interference between shells and spheres, and, in the context of predetermined sphere positions, misalignment of the

initial assembly.

To assess the impact of the potential error sources, we analyze the trajectories of two 4-sphere tests with the same nominal orientation, which is quite sensitive to the initial attitude and was selected specifically to examine the experimental repeatability. We find in both cases that, once stereoscopic tracking begins (slightly following proper aerodynamic release), the most upstream sphere exhibits a $\hat{z}$-velocity of $> 25\%$ of its terminal lateral velocity, whereas the remainder of the bodies possess lateral velocities consistent with zero. From Figure 2.15, examination of the leading spheres' motions in the vertical camera view (that is, before they are visible from the side) reveals that they are nearly stationary after surface contact with the shells has ceased, which indicates that premature aerodynamic forces is a more likely origin of any nonzero initial kinematics than mechanical contact. Although one might not expect unsteady flow startup (limited to ~ 0.5 ms) to directly influence the dynamics of the spheres (which are only partially exposed to the flow before $t \approx 0.5$ ms), such transients could affect the shell release and their resultant positions relative to the spheres, thereby possibly modifying the aerodynamic interference that appears to drive the divergence from the idealized testing scenario.

Analysis of the initial positions of the spheres shows differences in the cluster pitch and yaw angles of 2° and 5°, respectively, which can be roughly discerned in the upper panels of Figure 2.15. While this represents only a minor deviation in the arrangement's initial attitude and closely conforms to expectations from the model design, the modified post-release shock and wake structures, possibly coupled with shell aerodynamic interference, result in obvious trajectory discrepancies. In par-

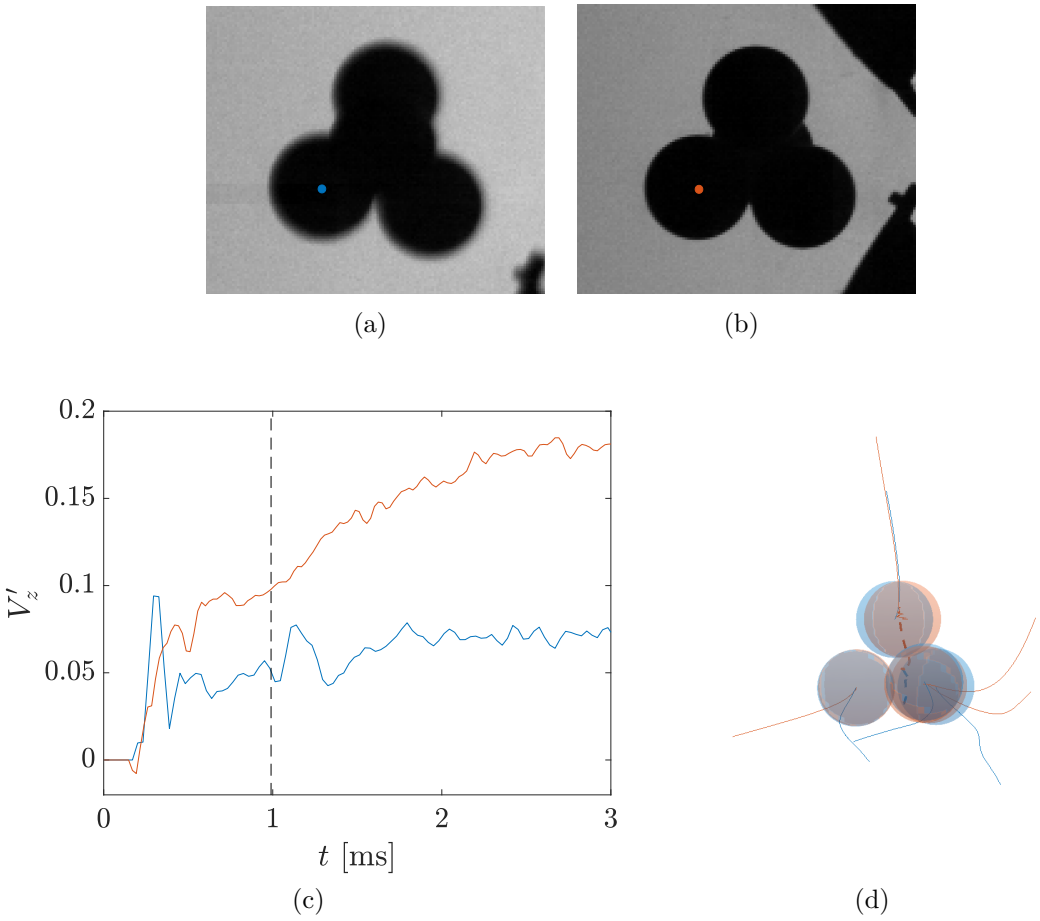

Figure 2.15: (a,b) Cluster visualization at $t = 0.99$ ms from below test section for repeated experiments of condition 4B, (c) spanwise nondimensional velocities of the leading spheres taken from vertical view only, and (d) overplotted initial positions and trajectories in downstream projection.

ticular, as is visible in the trajectory reconstruction visualization of Figure 2.15(d), the 'rolling' motion of the cluster leader and its immediate downstream neighbor (SE of center) is oriented slightly differently in the repeated tests, inducing wake entrainment of a third body (SW of center) in one experiment and shock surfing of the same body in the other. Additionally, the fourth body (N of center) undergoes shock surfing in both cases, but the duration of this arrangement is differs, resulting in slight deviations in its trajectory. In any case, achieving exactly repeatable results for highly sensitive predetermined test arrangements is rather elusive, but, as the primary goal of this work is to examine the behavior of random arrangements of spheres, the inconsistency observed here is ultimately inconsequential. Instead, we consider aerodynamic interference from the shell the primary source of error, but, because sphere kinematics are only mildly affected over this portion of the experiment, we deem our testing procedure capable of producing results characteristic of the model problem.

2.8 Cluster Configurations

In the experimental component of this work, we examine the separation of clusters consisting of equal-sized spheres, unequal spheres, and, to a lesser extent, dusty debris, with principal parameters provided in Table 2.2. All spheres are fabricated from Delrin acetal plastic ($\rho = 1400 \pm 40$ kg/m^3) or higher-density PTFE ($\rho = 2320 \pm 45$ kg/m^3), the latter of which is used in scenarios in which the beginning of the experiment is of increased interest. According to the manufacturer's

specifications, spheres of both materials exhibit <%1 deviation from sphericity. The precise selection of equal-sphere cluster populations was determined as follows: a four-sphere agglomeration served as the least populous multi-body cluster, while eight spheres was deemed an appropriate baseline for more complex scenarios, whose numbers (14, 27, 52, 99) were determined by successive population increases of 90%. Some intermediate values (11, 15, 36, 115) were admitted to encourage completeness of the resulting dataset and eschew undue focus on scenarios in which deviation from overall cluster sphericity was noted. The limiting cluster population of 115 bodies was established with regard to the extensive labor requirements associated with kinematic data extraction. The unequal-sphere clusters, on the other hand, were formed by selecting sphere sizes from realizations of a power law distribution with index, α, varying between 1 and 5. We use a ratio of four for the range (maximum to minimum) of sphere diameters and, for compatibility with the equal-sphere survey, fix the population of the unequal clusters at 52 bodies, judged to be large enough that the statistics of sphere kinematics would be roughly independent of any outliers in the randomized selection process. A more detailed accounting of the unequal-cluster compositions will be presented in Chapter 7.

Most sphere clusters in this work represent a close approximation to the most compact cluster of a given population (i.e., their bounding geometry is also spherical), although certain configurations (14 and 99 equal spheres, for example) seem to be slightly underpacked. For each cluster population, we attempt to conduct at least four experiments to achieve an approximate estimate of the separation statistics, although certain intermediate population conditions (11 and 36, for instance)

receive less attention as a result of their proximity to other well-studied cases. In addition to the tests with clusters of plastic spheres, we perform several experiments with an agglomeration of cornstarch-based baby powder (see Chapter 8).

The selection of sphere sizes constitutes a trade-off between aerodynamic interaction length-scale, flight time, and disruption from shell separation, with the selected sphere diameters, d_{sph}, generally decreasing as the number of bodies in the configuration increases: for equal-sphere clusters, this varies between 6.35 mm for 4 bodies and 2.38 for 115. The inner diameters of the suspension/release shells, d_c, for randomly packed equal-sphere clusters are chosen by consulting the optimal packing efficiency tables of Huang and Yu (2012) for the sphere-sphere packing problem and applying a 10% reduction to the listed value. Conversely, the optimal shell diameter for an unequal-sphere cluster is determined by randomly (and repeatedly) initializing the positions of bodies of a selected sample population and finding the smallest circumscribing diameter that achieves negligible contact stress following a rearranging relaxation process. Owing to the randomized selection process of the unequal-sphere clusters, however, the effective circumscribing volume differs for each cluster, so we introduce some degree of consistency by enforcing that 'valid' clusters fall within 5% of the mean packing efficiency as determined by numerous iterations of this sizing process.

As terminal separation properties are of critical interest in this work, the majority of tests are conducted with the upstream suspension position, but at least one experiment in the downstream location is included for many cluster arrangements. For spheres of such modest scale and density, gravitational acceleration is roughly

three orders of magnitude less than that caused by aerodynamic forces and thus entirely negligible. In total, 67 wind tunnel tests were conducted, with 37 investigating equal-sphere clusters, 25 unequal clusters, and 5 dusty debris.

N	d_{sph} [mm]	d_c [mm]	Material	Flow Config.	# Upstream Runs	# Downstream Runs	Camera Config.
4	5.0 / 6.35	11 / 13.9	PTFE / Delrin	A / B	0	5	C3 / C1
8	5.0 / 5.56	13 / 15.2	PTFE / Delrin	A	3	2	C3 / C2
11	4.76	13.9	PTFE	B	0	2	C1
14	4.76	15.2	Delrin	A	4	0	C2
15	5.0	15.3	PTFE	A	0	4	C3
27	4.0	15.2	Delrin	A	4	1	C2
36	3.18	13.9	Delrin	B	0	1	C1
52	3.18	15.2	Delrin	A	4	1	C2
52	$\alpha = 1$	17.5	Delrin	A	4	1	C2
52	$\alpha = 2$	14.4	Delrin	A	4	1	C2
52	$\alpha = 3$	17.9	Delrin	A	4	1	C2
52	$\alpha = 4$	15.2	Delrin	A	4	1	C2
52	$\alpha = 5$	13.6	Delrin	A	4	1	C2
99	2.38	13.9	Delrin	A	1	0	C2
115	2.38	13.9	Delrin	A	4	1	C2
$\gg$115	—	13.9	Cornstarch Powder	A	2	3	C2

Table 2.2: Compendium of experimental configurations

Chapter 3: Computational Modeling

While experiments may serve as the primary thrust of this work, numerical simulations of sphere separation also form a crucial foundation for characterization of equal-sphere aerodynamics. In particular, a computational approach affords the capabilities of selecting initial configurations not easily attained in an experimental setup and systematically varying a cluster's governing parameters. Additionally, the volumetric flowfield information available from simulations, more so than the qualitative density disturbances present in a shadowgraph, can assist in deciphering the mechanisms driving the observed sphere trajectories. Furthermore, the idealized release of spheres into a quasi-steady hypersonic freestream provides a perfect representation of the model problem of meteor fragmentation. Thus, in this chapter, we detail the numerical methodology employed, assess its performance under relevant circumstances, and describe its specific usage in this study.

3.1 Numerical Methodology

In correspondence with the model problem defined in Section 1.3, the simulation scenario of interest is the release of a close-packed sphere cluster into a high-speed flow, and the basic mechanics of governing the motions of the discrete

bodies illuminate the choice of simulation strategy. A foremost task is determining the flow field generated by the presence of the obstructing bodies; the fluid pressure distributions over the spheres, in turn, dictate the aerodynamic forces experienced by each. However, the complete dynamical behavior of the bodies relies on the surface contact that they inevitably experience at the commencement of a simulation, as well as the potential later periods of collision and sustained contact. The separation of spheres from their initial positions within a cluster thus forms a multi-physics problem which must be solved by means of a coupled simulation suite. In this work, we accordingly couple inviscid computational fluid dynamics (CFD) to a finite element analysis (FEA) software in order to simulate sphere motions.

A primary challenge of simulating the flow around a set of free-flying spheres is appropriately modifying the topology of the fluid mesh while maintaining high accuracy in the flowfield solution. To this end, previous studies of computational free-flight sphere separation (Butler et al., 2021; Laurence et al., 2012) have implemented codes specifically designed to handle complex embedded boundaries robustly and adaptively refine the simulation mesh in regions of the flow field identified to harbor features such as shock waves. Because many of the dynamically relevant features in the flow over a sphere at hypersonic conditions tend not to be viscous in nature, we can model the physics approximately with the equations of inviscid flow to reduce computational cost. Such a selection, however, comes at the expense of accuracy in the wake region of the a sphere, but, as will be shown throughout this work, the contribution of wake dynamics to the overall separation behavior of equal-sphere clusters is minimal.

The fluid solver chosen to numerically compute the flows governing the separation dynamics of clustered spheres is Adaptive Mesh Refinement in Object-Oriented C++, or AMROC (Deiterding, 2009), which solves the Euler equations for inviscid flow:

$$\begin{aligned} \partial_t \rho + \nabla \cdot (\rho \vec{u}) &= 0, \\ \partial_t (\rho \vec{u}) + \nabla \cdot (\rho \vec{u} \otimes \vec{u}) + \nabla p &= 0, \quad \text{and} \\ \partial_t (\rho E) + \nabla \cdot ((\rho E + p)\vec{u}) &= 0. \end{aligned} \tag{3.1}$$

Here E represents the specific total energy, and pressure is determined from the polytropic equation of state, $p = (\gamma - 1)(\rho E - \frac{1}{2}\mathbf{u}^T\mathbf{u})$. All solid features are treated as embedded boundaries within a Cartesian mesh, while spatial discretization is formulated in a finite-volume flux-splitting scheme. The MUSCL-Hancock reconstruction method with a Minmod limiter is implemented by Van Leer flux vector splitting for estimation of numerical flux at cell interfaces. Away from shocks and discontinuities, this semi-discrete formulation provides second-order accuracy, and reverts to first-order near embedded boundaries across which a ghost-fluid-based interpolation scheme mirrors primitive variables. An explicit Euler time-marching scheme is conducted for all fluid simulations.

The central advantage of AMROC is its use of a fully parallelized adaptive mesh refinement (AMR) scheme that permits the effective capture of transient flow features associated with moving boundaries. The patch-based approach divides the underlying Cartesian mesh into refinements subsets which are evaluated recursively and with relative iteration count imposed by a prescribed target Courant–Friedrichs–Lewy (CFL) number. The refinement process itself is controlled

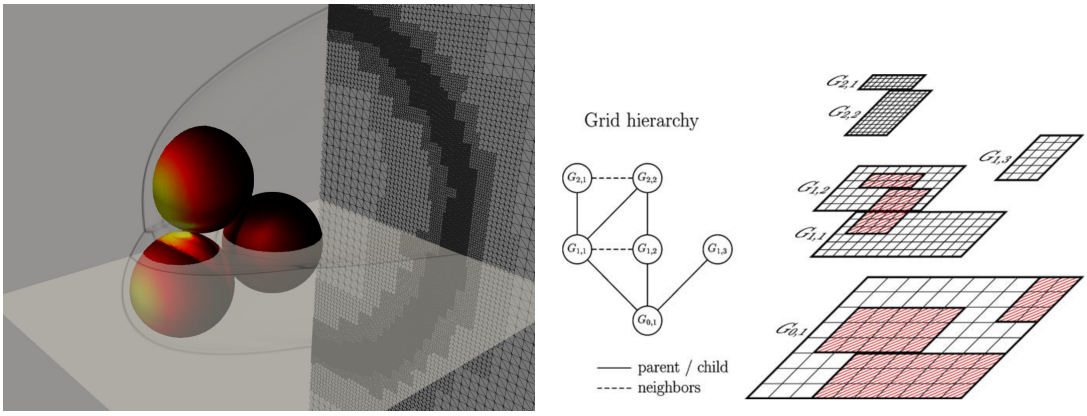

(a) (b)

Figure 3.1: (a) Representative computational mesh with three fluid refinement levels showing surface pressure, numerical schlieren, and automatically refined mesh capturing the shock. (b) Schematic of AMROC's mesh refinement hierarchy from Deiterding (2009).

by user-defined gradient thresholds of selected state variables (typically density) and by wall proximity as determined by the level-set function. The parallelized AMR method is equipped with both load-balancing and repartitioning to account for evolving mesh topologies. Figure 3.1 provides a demonstration of AMROC's mesh refinement capabilities with a schemetic of its hierarchical refinement approach.

The structural modeling component of the numerical framework is accomplished using the DYNA3D solver. DYNA3D is an explicit, nonlinear finite-element code commonly used to capture high-speed structural phenomena, and allows for a range of material models and contact physics (Hallquist and Jin, 2005). A structured grid of regular hexahedral elements is required for the current simulation setting, and we employ a three-dimensional butterfly mesh with relaxation of the external cell blocks to ensure the reliability of execution for a spherical structural domain, as is illustrated by the touching spheres of Figure 3.2. A critical strength of DYNA3D is its robust contact detection algorithm; a global search for proximity

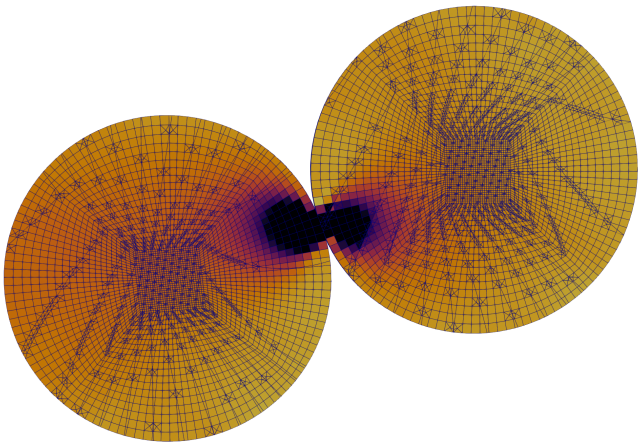

Figure 3.2: Collision of two spheres demonstrating the mesh structure employed and multi-body contact capabilities of DYNA3D with cells colored by principal stress in horizontal direction. Note that slicing plane is slightly skewed to nominal cell orientation, leading to notch-like artifacts.

between principal surfaces and subsidiary nodes, supported by a detailed contact-checking routine, provides proper treatment of nodal penetration and directional pushback for multi-body impacts in dynamic simulation settings. Furthermore, automatic surface-definition instructions render the code agnostic of input geometry and applicable to more complex scenarios featuring self-contact and material failure. Sliding surface dynamics are computed using standard friction laws, with kinematic and static friction coefficients held constant at 0.5 and 0.7, respectively, in our implementation. We use only the elastic material model in this work, although material failure capabilities present a natural extension of our methodology to body fragmentation along predefined fault lines. We note, however, that the publicly available installment of DYNA3D does not implement parallel execution and therefore limits the scale of problems attainable.

Coupling the fluid and structural solvers is accomplished by transmitting

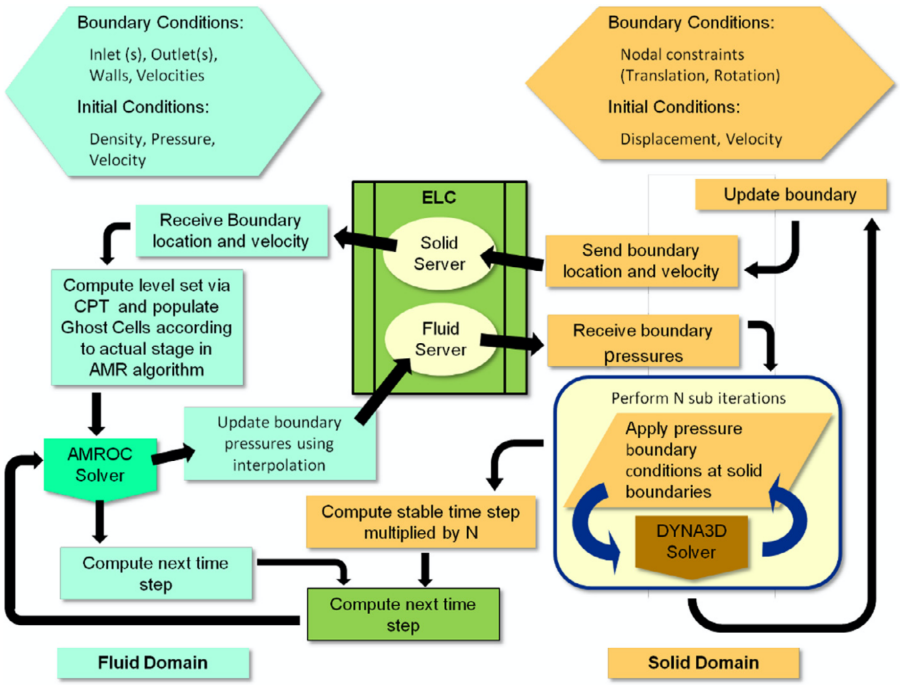

Figure 3.3: Data transmission protocol for coupled execution of AMROC/DYNA3D from Deiterding and Wood (2013).

to DYNA3D the pressure boundary conditions, to which the principal stresses of boundary cells are equated, and to AMROC the updated geometric boundaries, which determine the kinematics of embedded fluid ghost cells (Deiterding and Wood, 2013). Boundary-condition transfer between solvers is updated serially, which increases computational cost in comparison to parallel execution but ensures a higher degree of numerical stability (Deiterding and Wood, 2013). Computation of the level-set function is performed by applying to the triangulated surface mesh the Closest Point Transform of Mauch (2003), an efficient algorithm designed specifically for this coupled solver. Solid and fluid meshes are constructed such that nodal spacing is roughly equivalent on the finest grid level, while the global time-stepping parameter is determined by selecting the minimum of the stress-wave transmission

and target CFL timescales. In this study, DYNA3D is run on a single core, whereas AMROC is parallelized across a larger number of processors. See Figure 3.3 for an illustration of the coupled execution procedure.

We note that the fully elastic separation problem without notable feedback from structural deformations into the flowfield does not truly require treatment of the material response with a finite element analysis, as less complex models (such as the discrete element method of Mishra and Rajamani (1992)) may produce similar results. The FEA-based approach was nevertheless chosen for a mixture of historical and practical reasons: initial intentions included the extension of our work to fluid-structure problems with material failure, while AMROC had already been coupled to DYNA3D, thereby circumventing the need for the development of new coupled computational tools. Future studies, particularly those simulating unequal-sphere clusters, may seek to reformulate the coupled numerical model with the implementation of a more appropriate structural approach.

3.2 Model Verification

To assess the computational reliability of the present numerical model, we perform a grid-refinement study of sphere separation from a chosen initial arrangement at Mach 20 (simulation inflow properties will be described in full in Section 3.4). The configuration of interest here comprises four spheres with centers positioned at the vertices of regular tetrahedral which has been rotated some distance away from its principal attitude. The chosen geometry exhibits several behaviors char-

acteristic of small-cluster separation (which will be presented in Chapter 4) and, therefore, was deemed a suitable case for verifying the convergence of the coupled fluid/solid solver. The verification study consists of four simulations of successively refined fluid and structural domains, each with spheres of 0.1 m radius on a domain measuring 2.0 m $\times$ 1.2 m $\times$ 1.2 m. In our nomenclature, the numeric simulation labels refer to the increasing degree of overall refinement in each case. The base grid resolution varied with the overall refinement level, as both meshes of dimension $160 \times 96 \times 96$ and $106 \times 64 \times 64$ were used: in the coarsest simulation (i.e., case 1), the finer base mesh was refined just once by a factor of two, yielding a minimum edge distance, Δx_{min}, of $0.063 r_{\text{sph}}$, while case 2 achieved a Δx_{min} value of $0.047 r_{\text{sph}}$ with two refinement passes of the coarse base mesh. The incremental refinement scheme was devised to explore the numerics of configurations with 75%, 150%, and 200% of the overall refinement of the intended mesh arrangement, case 2. The solid meshes employed in each case were constructed to match the size of the finest fluid cells, and time-step sizes were automatically adjusted to match a CFL condition of 0.8. All computations were run on a 56-core Dell Precision T7820 workstation; the coarsest simulation required $\sim$1,000 CPUh of computation to complete, while the finest simulation, at $\sim$18,000 CPUh, was significantly more expensive. Details of the grid dimensions and refinement strategies can be found, along with execution statistics, in Table 3.1.

Before quantifying the differences between runs of various resolution, we will detail the general behaviors exhibited by the spheres. The selected cluster arrangement, presented before release in the uppermost row of Figure 3.4, features one

Case No.	Grid (Structure)	Base Grid (Fluid)	Refinement Factors	$\Delta x_{\min}$ ($\cdot\ 1/r_{\text{sph}}$)	Steps	Cores	CPU [h]
1	$16 \times 16 \times 20$	$160 \times 96 \times 96$	[2, 0, 0]	0.063	44 314	56	1 064
2	$20 \times 20 \times 20$	$106 \times 64 \times 64$	[2, 2, 0]	0.047	55 620	28	1 307
3	$30 \times 30 \times 20$	$160 \times 96 \times 96$	[2, 2, 0]	0.031	83 932	56	7 300
4	$40 \times 40 \times 20$	$106 \times 64 \times 64$	[2, 2, 2]	0.023	111 984	56	18 200

Table 3.1: Grid refinement study parameters

body furthest upstream (sphere 1), which generates a bow shock that impinges on two bodies downstream of it (spheres 2 and 3), while a fourth sphere (sphere 4) is nearly aligned with sphere 1 in the streamwise direction and is therefore mostly shielded from the Mach-20 inflow. Following the graphics associated with case 4 (the rightmost column), we see that the region of elevated surface pressure on sphere 3 resides a considerable distance inboard of its centroid, fostering immediate lateral repulsion and a prompt transition to aerodynamic independence, as it travels beyond the bounds of the bow shock of sphere 1. Sphere 2, on the other hand, experiences a broader band of high pressure passing directly over its center, as well as a more concentrated pressure peak near its point of contact with sphere 1. As sphere 2 is repelled from the cluster, the irregular impingement pattern develops into the more standard Type-IV shock-shock interaction footprint (including even a secondary pressure band, Chu and Lu (2012)), which persists and broadens as sphere 2 shock-surfs downstream. Finally, spheres 1 and 4 engage in the paired travel representative of streamwise-aligned spheres (to be described in detail in Chapter 4); sphere 4 remains in the aerodynamic shadow of its leader for $\sim 2\tau_s$ before the streamwise momentum accrued by sphere 1 is transmitted to sphere 4, pushing it laterally outward from their mutual contact point and commencing a

shock-surfing sequence cut short by the termination of the simulation.

Now, expanding the scope of our inspection to cases of all resolution, we find minor discrepancies in the sphere trajectories as presented in the columns of Figure 3.4. While the motions of spheres 1 and 3 remain nearly identical across the grid refinement survey, modifications to the paths traveled by spheres 2 and 4 are apparent. Indeed, the most notable inconsistency is the persistence of the shock-surfing behavior observed in case 4. Focusing on the final timestep of the graphical comparison, it is clear that the band of augmented pressure on sphere 4 proceeds further inboard with increasing resolution, signaling a transition from entrainment to shock surfing. The cause for the discrepancy, then, must be ascertained from a more detailed examination of the surface pressure at the start of the simulation. Figure 3.5 thus presents a comparison between cases 2 and 4, with centerline flow-structures (via pseudo-schlieren) and surface pressure displayed. Both simulations capture the shock-shock interaction arising near the conjunction of spheres 1 and 3, although, judging from the surface pressure distribution, the interaction extends further laterally on the finer mesh. However, the most significant difference between coarse and fine seems to arise in the magnitude of the elevated pressure regions on the leeward side of sphere 1 and the exposed side of sphere 2; the pressure of the approximately stagnant flow near the sphere 1–2 tangency point depends strongly on the path of the influencing streamlines, which may not be sufficiently resolved, especially in the presence of a swept shock-shock interaction. Accordingly, case 2 demonstrates a reduced leeward pressure relative to case 4, which decreases its separation laterally and gives way to the wake-entrainment process initiated at the

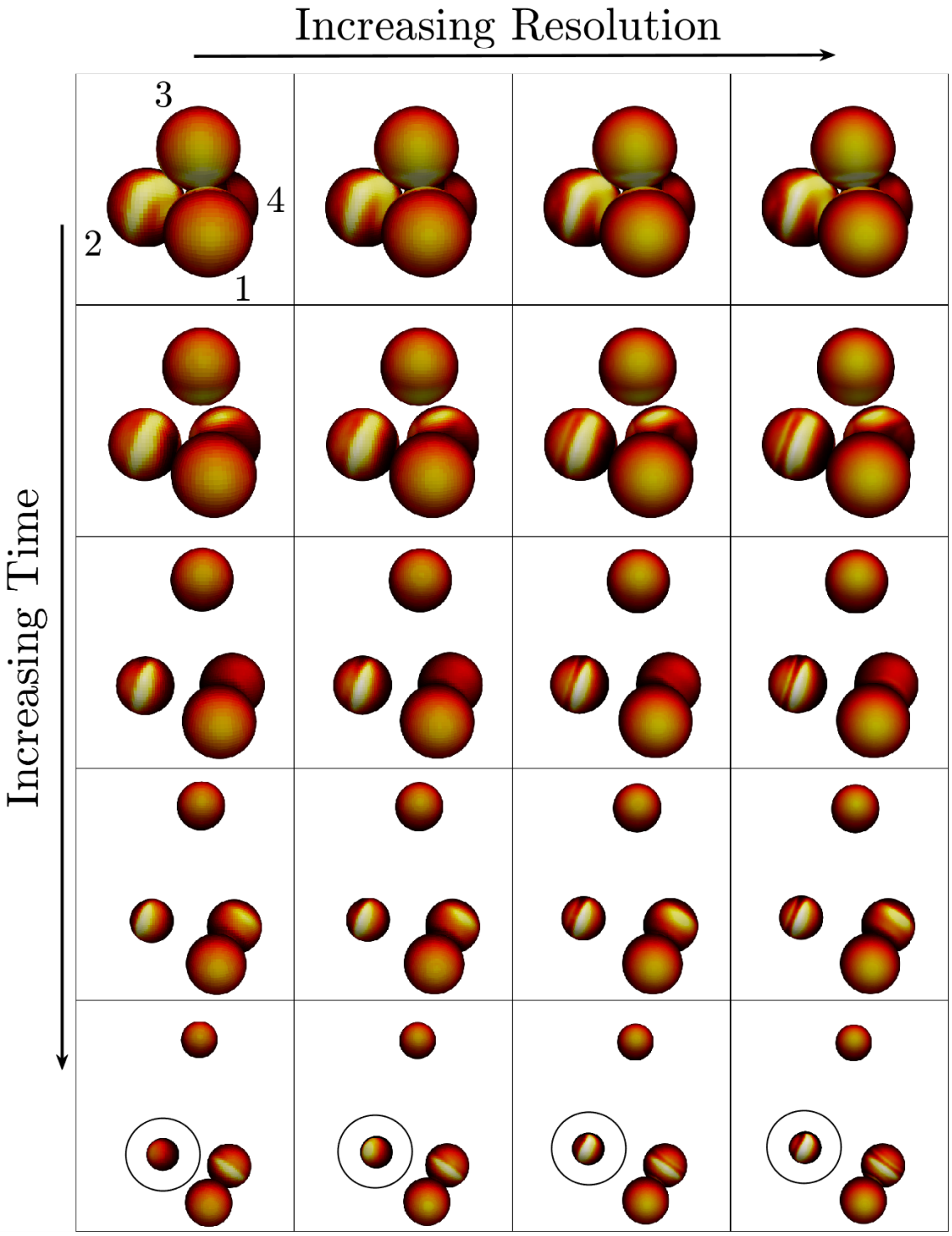

Figure 3.4: Downstream graphical comparison of all grid refinement cases with sphere surfaces shaded by pressure and trajectory discrepancy of sphere 4 highlighted in bottom row. Rows show positions in increments of τ_s, with left-to-right columnar progression from coarsest to finest.

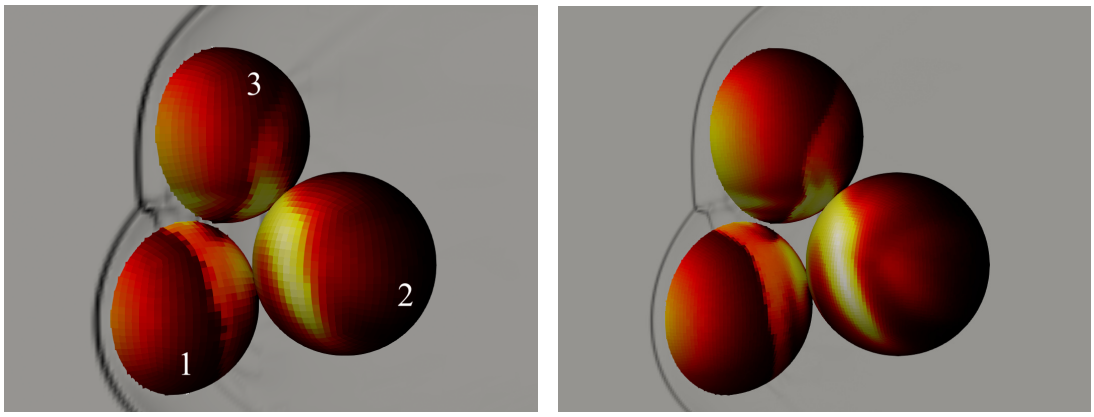

Figure 3.5: Centerline pseudo-schlieren with surface pressure at sphere release for cases (a) 2 and (b) 4 from model verification simulations.

end of the simulation. Thus, while the pressure distributions in cases 2 and 4 are qualitatively very similar, the integrated nature of the sphere separation problem, as well as the high sensitivity of shock-surfing to its effective initial conditions generally, allows for accumulated errors to prompt the observed trajectory divergence.

Keeping in mind the details of the divergence between sphere trajectories, we now examine the exact errors accrued in the mean lateral velocity of the cluster, as well as those from mean lateral force coefficients, which are presented in Figure 3.6. Examining the error in mean lateral velocity suggests that the spheres of case 3 follow trajectories almost identical to those in the finest simulation, remaining within 1% error for the majority of their flight. Cases 1 and 2, on the other hand, show elevated errors which are somewhat obfuscated by the residual resulting from the collision series between spheres 1 and 4. Prior to complete trajectory divergence at $\sim 2.5\tau_s$, errors are limited to $\sim$3%, with no obvious differentiating trends between cases 1 and 2, although the lateral velocity errors for case 1 deviate more sharply thereafter. Inspecting the errors in mean lateral force coefficient instead elucidate

the differences in the governing aerodynamics in the absence of structural contributions to the extracted trajectory errors. Here, the refinement level of each simulation is well-correlated to overall error experienced; following the positive peak in force error (induced by delayed abatement of repulsive forces on sphere 3), we observe approximately constant errors of 1.0% for case 1, 0.6% for case 2, and 0.1% for case 3. As with the lateral velocity evaluation, however, diverging trajectories for the coarser simulations give rise to highly augmented errors. Despite the apparent incompatibility of the various refinement cases after $\sim 2.5\tau_s$, the dynamical regime of interest for the sphere cluster simulations is that which arises when the bodies are in close proximity. As will be described in Chapter 4, this so-called primary separation stage ends at $t' = 2.15$ for the present scenario, and we will correspondingly restrict our appraisal of the fidelity of the simulations to this period. Clearly, the sphere trajectories are very nearly converged in case 3, but the six-fold increase in computation time over case 2 renders this refinement selection (and even more so for case 4) infeasible for parametric survey purposes. Instead, we find that the modest force errors offered by refinement case 2 ($< 2\%$ over the primary separation), coupled with its rapid computation time, make it a suitable choice for our numerical investigation.

3.3 Experimental Validation

To provide a basis for the validity of the coupled numerical methodology, we present a comparative assessment of a selected experiment of separating free-flight

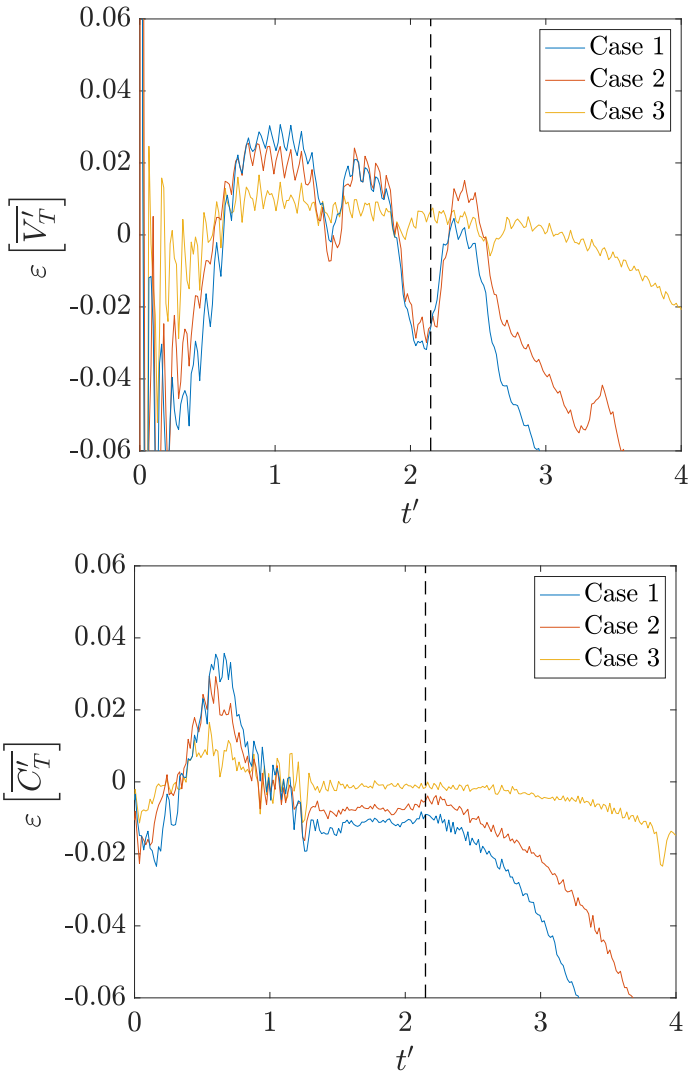

Figure 3.6: Error in (a) mean lateral velocity and (b) mean lateral force coefficient relative to finest simulation for cases 1–3. End of primary separation stage indicated with dashed black line.

spheres and a corresponding simulation with fully matched conditions. The chosen experiment features four spheres of diameter 6.35 mm arranged into a tetrahedron (as in the grid-refinement study of Section 3.2), with two leading spheres at approximately similar streamwise locations and a pair of roughly aligned trailing spheres. Simulations of spheres at a similar orientations reveal that this arrangement is expected to produce extended shock surfing, a scenario highly sensitive to relative sphere positions and a sensible benchmark test of the resultant computational aerodynamics. In Figure 3.7, a sequence of images taken from below and from the side of the test section depict the sphere trajectories, along with a three-dimensional reconstruction of the extracted positions, where time-zero represents the point at which the counterpart numerical simulation draws its initial kinematics. Shocks, though faint, are visible in the central column, which helps provide some degree of information about the underlying fluid dynamics. As shown in the $t = 1.40$ ms frame, the two leading spheres experience strong repulsive forces and almost immediately separate laterally, at which point the trailing spheres are no longer shielded from the freestream flow. Indeed, in the shadowgraph visualization of $t = 2.80$ ms, impingement of the shock from sphere 1 on sphere 4 is apparent and the resulting drag augmentation is reflected in the increased positional separation between the two. Note that sphere 3 likely also receives the bow shock from sphere 1, but the associated flow features are not visible because the density disturbance is far removed from its tangency point with the pulsed beam. In any case, it appears that spheres 1 and 2 have ceased aerodynamic interaction by frame $t = 2.80$ ms, while 3 and 4 remain under the influence of sphere 1 for an extended period of time. From the

three-dimensional reconstruction, sphere 3 has begun to fall into the wake of sphere 1, while the shock-shock interaction on sphere 4 moves further towards its inboard side (see central frames of $t = 4.20$–7.00 ms), indicating an eventual expulsion trajectory. The trailing spheres have left the stereoscopic viewing volume by $t = 7.00$ ms, and the leading spheres continue on undisturbed trajectories until completion of the experiment.

The complementary simulation exhibits qualitatively similar behavior, as evidenced in the projected numerical sphere positions in the left and center columns of Figure 3.7. While we do commence sphere tracking before time-zero in the experiment, at this time the suspension shells have not yet separated far enough from the spheres. Instead, at the selected t_0, the cluster has established its own bow shock and the sphere dynamics are unlikely to be influenced much by the shells, so any discrepancy between simulation and experiment is considered to be independent of the suspension/release mechanism. Note also that the spheres possess nonzero initial velocities resulting both from contact forces as the shells break apart and from pressure forces before the spheres achieve aerodynamic independence from the shells. These initial velocities are limited to $0.0015u_\infty$ and are achieved in the simulation by applying brief impulses to the spheres synchronous with the commencement of the coupled portion of the computation.

As a quantitative measure of the agreement between experiment and simulation, we present a comparison of positional errors relative to the sphere radius in Figure 3.8(a) and nondimensional lateral velocity errors in Figure 3.8(b). Most spheres follow the same general paths in both experiment and simulation, remain-

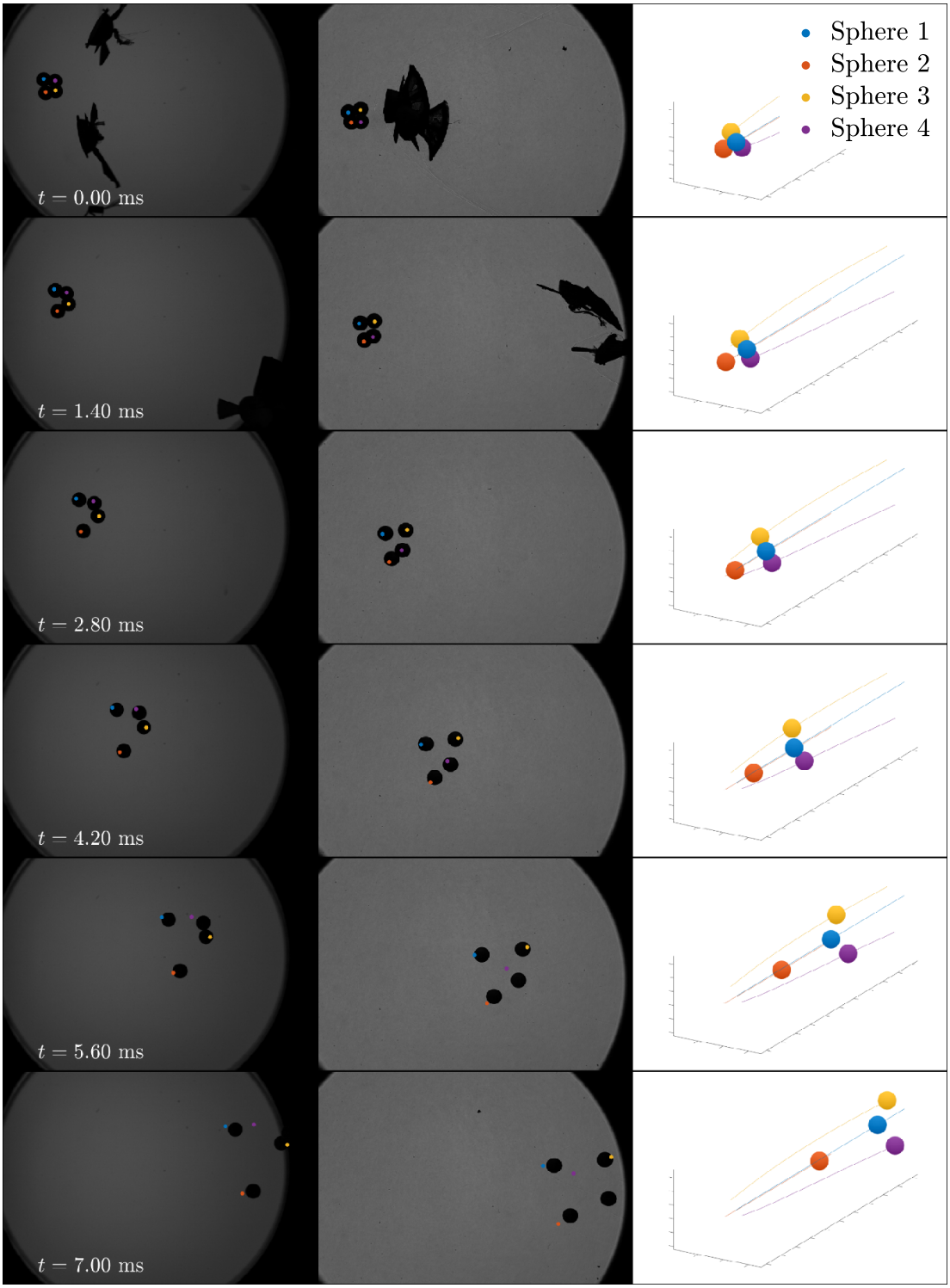

Figure 3.7: Separation sequence of four-sphere validation experiment in camera arrangement C1 with (left) vertical standard camera, (center) horizontal shadowgraph camera, and (right) positional reconstruction. Markers in the left and center columns indicate numerical sphere positions.

ing within one sphere-diameter of their experimental positions, but sphere 4 shows significant deviation beginning at roughly $t = 4$ ms. Relative to the experiment, this sphere exhibits reduced displacement in the streamwise direction, while the lateral motion follows that of sphere 1, indicating that it begins to follow a wake-entrainment trajectory (in agreement with visualization of computational flowfield results). The other major discrepancy in the results of the numerical modeling is the streamwise positions of the leading spheres. As might be expected in a setting that neglects viscosity, the drag forces on the spheres will be reduced compared to experimental results, particularly for those bodies exposed to unimpeded freestream flow. Despite the positional differences of the other bodies and the complex interaction to which it is subjected, sphere 3 surprisingly exhibits very low deviation from its experimental trajectory. Furthermore, spheres 1, 2, and 3 accrue positional errors as the simulation progresses, but their lateral velocities do not diverge from the experimental results, with errors of $0.038v_s$, $0.099v_s$, and $0.040v_s$ for spheres 1, 2, and 3, respectively, at $t = 5$ ms; this can be considered adequately low for confidence in the equivalence between the simulated and experimental realizations of the separation process for this cluster.

The major discrepancies observed between the experimental and computational trajectories are likely to stem directly from the difference in the nominal drag coefficient for viscous and inviscid spheres. In the numerical interaction between spheres 1 and 4, the streamwise distance between bodies is greater due to the reduced drag on the primary. As a result, the bow shock has spread further laterally at the streamwise position of the secondary sphere and impinges further towards its

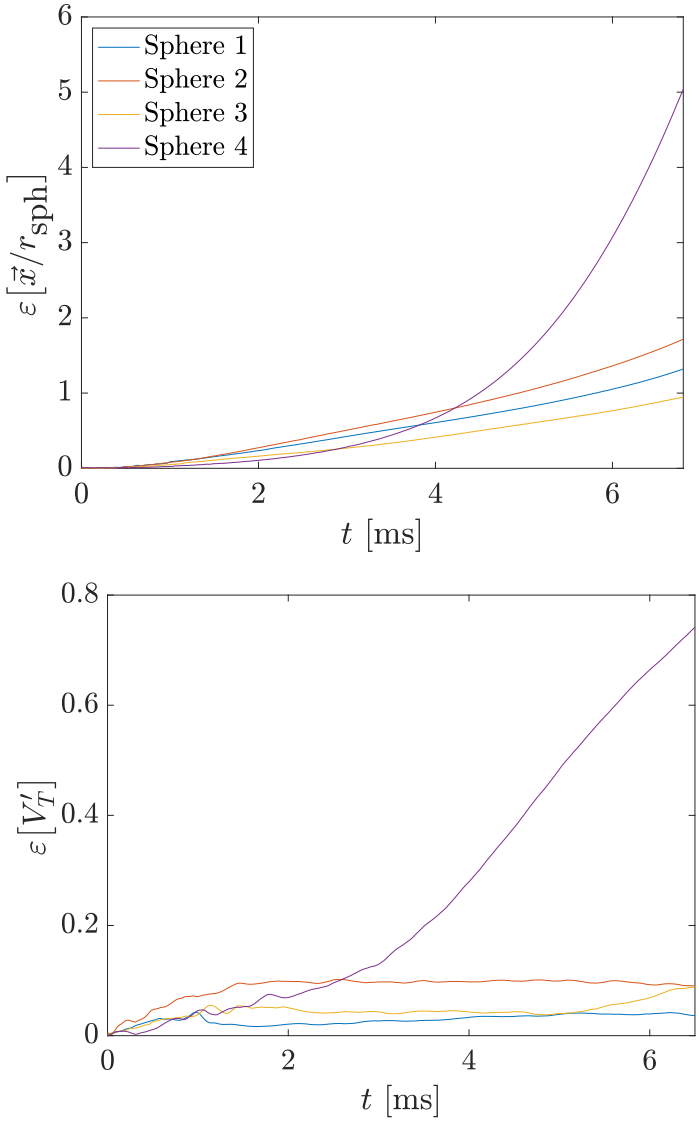

Figure 3.8: (a) Positional error between computation and experiment relative to sphere radius and (b) error in nondimensionl lateral velocity.

outboard flank, which, in turn, reduces the lateral force. When the lateral-force-to-drag ratio of the secondary body (which is already following the shock) falls below the tangent of the local shock angle, it will become entrained in the wake of the primary, which is evidently what occurs in the simulation of interest. Based on the trajectory discrepancy of sphere 4 in this particular scenario, we might expect a systematic underestimate of sphere separation velocities under the current numerical methodology.

One rather surprising finding in Figure 3.8 is the minor positional errors associated with sphere 3, which is entrained in the wake of the leading body, the region expected to be the most susceptible to the omission of viscosity. Of course, the contribution of viscosity to force coefficients is greatest along the centerline of the wake (Register et al., 2020), and this body is removed laterally from the primary axis during much of its flight, slightly reducing the expected modifications to the aerodynamic forces; nevertheless, we do observe a mild increase in velocity error as it draws nearer to the centerline after 5 ms. Additionally, the increased distance between spheres 1 and 3 in the simulations is roughly consistent with neglected viscosity, as the streamwise force coefficients would be reduced (see, e.g., Register et al. (2020)). In any case, the terminal trajectories achieved from flight through this region are generally less sensitive to the exact forces experienced than in a shock-surfing configuration, so the resultant sphere kinematics for simulations of wake-entrained bodies are considered to be characteristic of the actual fluid dynamics even if viscosity is not treated. Overall, all bodies besides sphere 4 remain within one sphere diameter of their experimental positions for the entire simulation and ex-

hibit low deviation in lateral velocity, so we deem the numerical model of coupled AMROC/DYNA3D well-suited for reproducing the general behaviors exhibited by spheres separating from clusters.

3.4 Simulation Parameters

Aside from the validation study of Section 3.3, the freestream flow for all cluster configurations possessed a Mach number of 20. This selection of Mach number is considerably less than that of a meteoroid entering Earth's atmosphere (likely above Mach 40), but as discussed earlier, as dictated by the Mach number independence principle for a perfect gas, the resultant aerodynamics should be roughly equivalent. The density of freestream flow was set to 0.01% of that selected for the spheres (8×10^3 kg/m^3 to approximate iron meteors), and the freestream temperature was constrained by choice of velocity (15,000 m/s, typical of meteors) and Mach number. Given that AMROC solves the Euler equations under a perfect-gas equation of state, the unphysically high freestream temperatures (1400 K) and pressures (321.4 kPa) experienced here will not cause the sphere dynamics to deviate from that attained in a standard inviscid flow. Furthermore, all results are presented in nondimensional form, and, because perfect-gas flow is self-similar, the exact dimensional flow conditions and sphere dimensions are not of high importance. In any case, we note that the primary influence of real-gas effects in this setting would be to alter the shock stand-off distance near the stagnation streamlines and would not be expected to modify separation trends appreciably. Structurally, we employ a fully

Parameter	Value
M_∞	20.0
P_∞ [kPa]	321.4
T_∞ [K]	1400.0
ρ_∞ [kg/m^3]	0.80
u_∞ [m/s]	15000
r_{sph} [m]	0.1
ρ_{sph} [kg/m^3]	8000
E_{sph} [GPa]	200
ν_{sph}	0.28

Table 3.2: Inflow and structure properties

elastic material model with a Young's modulus of 200 GPa and a Poisson ratio of 0.28 (again, both matching that of iron) for the 0.1-m-radius spheres. Details of inflow and structural properties can be found in Table 3.2.

All numerical simulations in this work examine the separation of equal-sphere clusters of limited population. AMROC/DYNA3D is theoretically capable of computing the dynamics of arbitrary cluster compositions, but several architectural conditions limit the range of truly achievable scenarios. First, the serialized implementation of the DYNA3D component of the suite constitutes a bottleneck in the code's execution. While the increased computational cost of a large sphere population can be compensated for in the fluid domain by dividing the load over a commensurate number of processors (provided access to a high-performance computing cluster), the wall-time of the finite-element problem will scale directly with the number of bodies considered. Additionally, to ensure the stability and accuracy of the simulations, we match the minimum length scales of the structural and fluid meshes. In the case of unequal-sphere clusters, matching the fluid length scale with structural geometry of the smallest body will result in an intractably large fluid

mesh with correspondingly reduced time-stepping, precluding timely computation of the simulation. Cluster arrangements with both many and unequal spheres do represent a keen problem of interest in this work, but the sheer computational magnitude of even comparatively simple simulations of these classes justifies our focus on less populous equal-sphere clusters alone (with experiments as the chosen means for investigating unequal and more populous clusters).

The geometries of interest are sphere cluster arrangements at various attitudes for four population selections shown in Figure 3.9: two, four, thirteen, and fifty-seven spheres. For the sphere pair simulations, the bodies are initially in contact and rotated about their common center-of-mass by a variety of pitch (or equivalently, polar alignement angle) values. For more populous clusters, we maintain close-packed sphere configurations and vary both the pitch and yaw angles of the cluster from its principal attitude (the exact details of the selected parameter values in each survey will be given in the appropriate subsections of later chapters). Four-sphere clusters are thus formed by positioning the sphere centers at the vertices of a regular tetrahedron, thirteen spheres by constructing two layers of a face-centered

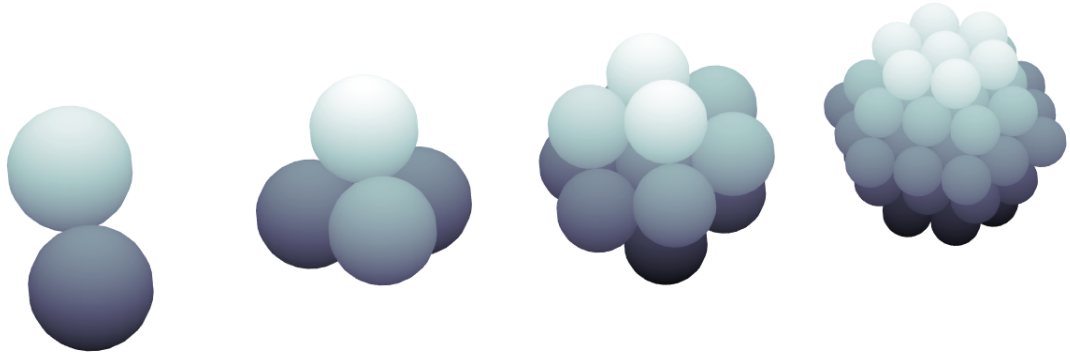

Figure 3.9: General geometric appearance of 2-, 4-, 13-, and 57-sphere close-packed clusters.

cubic lattice, and fifty-seven spheres by assembling three layers of a hexagonal close-packed lattice. In accordance with the model verification study of Section 3.2, each structural mesh for the two- and four-sphere clusters contains 2400 surface elements, and the refinement levels of the solid and fluid domains are matched such that the maximum stable time-step size in DYNA3D roughly equates to a target CFL number of 0.8 for time-stepping control in AMROC. Due to the drastically increased computational demands of the thirteen- and fifty-seven sphere cluster simulations, in these cases we employ coarsened meshes similar to that of case 1 in the grid-refinement study. Additionally, reduced CFL targets of 0.7 and 0.6 were employed in the thirteen- and fifty-seven-sphere simulations, respectively, to promote the stability of the computations. During a simulation, a period of 3 ms is allotted to establish quasi-steady flow over the stationary spheres, at which point, they are allowed to fly freely until program termination. The exact spatial scales of the fluid domain varies between cluster populations, as does the simulation duration, and both can be found in Table 3.3 along with the utilized refinement factors, which are invoked based on density-gradient threshold and wall proximity criteria. Typical computational times increased from ∼700 CPUh for two bodies to ∼19,000 CPUh for the fifty-seven sphere agglomeration on a 56-core Dell Precision T7820 workstation. In total, 13 runs were conducted for two spheres, 38 for four, 36 for thirteen, and just one for fifty-seven.

N_{sph}	Grid (Structure)	Base Grid (Fluid)	Domain Size ($\cdot\ 1/r_{\mathrm{sph}}$)	Refinement Factors	Δx_{min} ($\cdot\ 1/r_{\mathrm{sph}}$)	Duration ($\cdot\ 1/\tau_s$)	Cores	CPU [h]	Total Runs
2	$20 \times 20 \times 20$	$126 \times 50 \times 50$	$25 \times 10 \times 10$	[2, 2, 0]	0.050	9.0	9	700	13
4	$20 \times 20 \times 20$	$106 \times 64 \times 64$	$20 \times 12 \times 12$	[2, 2, 0]	0.047	5.4	28	1 300	38
13	$16 \times 16 \times 12$	$160 \times 80 \times 80$	$40 \times 20 \times 20$	[2, 2, 0]	0.063	6.0	56	4 000	36
57	$16 \times 16 \times 10$	$104 \times 80 \times 80$	$42 \times 32 \times 32$	[2, 2, 2]	0.05	1.4	56	19 100	1

Table 3.3: Simulation parameters

Chapter 4: Equal Spheres: Small Clusters

We first begin our examination of the model problem of aerodynamic meteor fragmentation with clusters of equal spheres numbering fewer than ten bodies. The results of experiments and computations will be both presented, beginning with a reexamination of the simplest possible arrangement, two equal spheres, with the physics of surface contact modeled. Following an increase to the populations of four spheres, we will draw conclusions regarding the physics governing the separation of the least populous fragmentation scenarios.

4.1 Two-Sphere Simulation Survey

The simplest nontrivial scenario of sphere separation is two equal-sized initially-touching spheres at various alignment angles. The aerodynamics of this configuration have been well characterized in previous studies (Laurence and Deiterding, 2011; Laurence et al., 2007; Register et al., 2020), but the effects of surface contact between the pair have not yet been systematically investigated. In particular, the terminal behavior of spheres arranged into a streamwise-aligned formation (i.e., no immediate separation) is still unknown despite the relatively fundamental nature of the problem. To ascertain the trajectories of and elucidate the physics governing

sphere pairs at various alignment angles, we undertake a computational survey using the coupled fluid-structural numerical methodology and simulation conditions described in Chapter 3. In accordance with the definitions of Section 1.4, we adopt the convention wherein θ represents the alignment angle between the upstream direction and a vector connecting the pair's center of mass to the center of the downstream body, with an angle of 180° indicating that the secondary sphere is directly behind the primary. The simulation configurations span initial alignment angles, θ_0, of 90° and 180°, and are simulated at increments of 7.5°, allowing for identification of the various aerodynamic tendencies of the pair.

To acquaint the reader with the most basic aspects of sphere separation, we present qualitatively several representative cases that demonstrate typical sphere-pair behaviors, some of which arise in more populous clusters. First, Figure 4.1 illustrates the trajectories resulting from a well-studied arrangement, two bodies positioned at the same streamwise coordinate (i.e., $\theta_0 = 90°$). From both the centerline pseudoschlieren and surface pressure of the first frame, the spheres are clearly subjected to high pressures, of similar magnitude to the stagnation value, on their inboard regions as a result of their common bow shock. As expected, they exhibit spanwise separation in the subsequent frames, which causes the common bow shock to bifurcate along with an associated reduction in the extent of the elevated inboard pressures. By the fourth frame, the intersecting shock structures lie an appreciable distance from the spheres' surfaces and appear to have no influence on the surface pressure distributions; the bodies thus travel independently for the remainder of their flight.

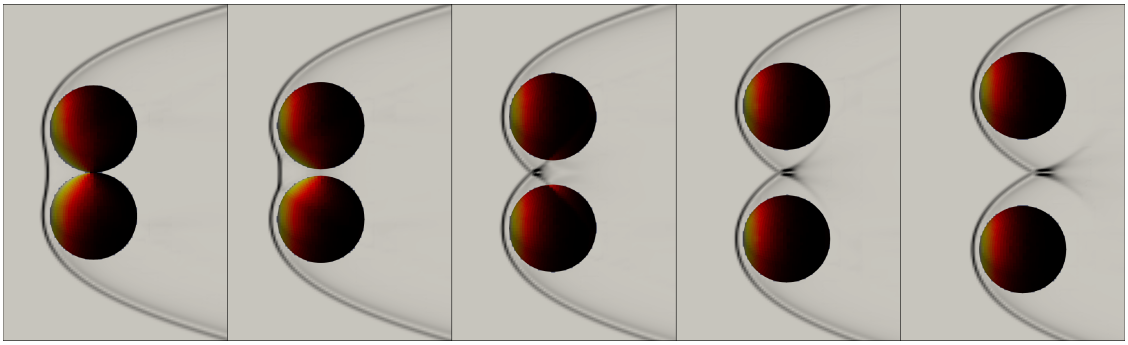

Figure 4.1: Separation sequence from initial alignment angle of 90° with coloring by surface pressure and centerline pseudo-schlieren. Frames shown in increments of $0.61\tau_s$ ($\sim$0.81 ms).

Rotating the pair to an alignment angle of 120°, we find that the separating action of the common bow shock gives way to dynamics dictated by shock impingement, as demonstrated in the sequence of Figure 4.2. Here, the secondary (or downstream) body initially receives the bow shock of the primary (or upstream) slightly below its stagnation point, producing a band of enhanced pressure that generally occurs in Type-IV shock-shock interactions, while a terminal shock propagates from the intersection point to the leeward region of the primary body. Together, the pressure footprints of the shock structures induce immediate separation of the bodies in both the streamwise and lateral directions. The primary body quickly becomes independent of the secondary, whereas the secondary continues to surf the shock of the primary (Laurence and Deiterding, 2011) until the final frame, which considerably augments its lateral velocity. Thus, the 90° and 120° scenarios yield the same general terminal behaviors despite obvious differences in the intervening aerodynamic mechanisms.

From the trajectory visualization of Figure 4.3, a dramatic change in the spheres' motions occurs for the $\theta_0 = 135°$ arrangement. As in the 120° configuration,

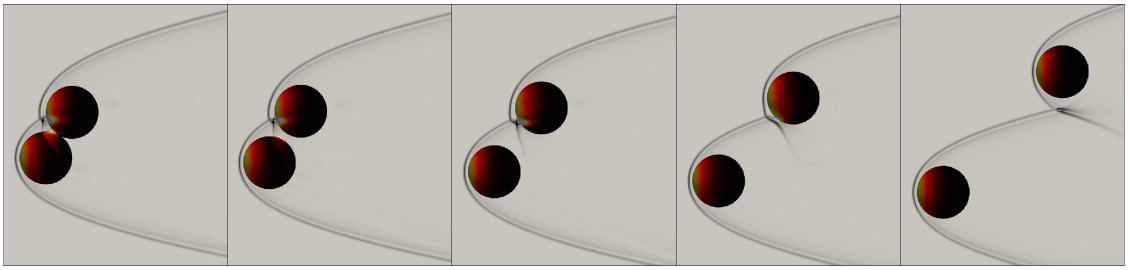

Figure 4.2: Separation sequence from initial alignment angle of 120° with coloring by surface pressure and centerline pseudo-schlieren. Frames shown in increments of $1.20\tau_s$ ($\sim$1.60 ms).

the secondary sphere is subjected to the bow shock of the primary, but shock impingement occurs above the stagnation point in the present scenario, which instead promotes prolonged contact between the bodies. Indeed, the bodies travel downstream in tandem, maintaining mechanical contact, and, due to an effective moment provided by the shock impingement, begin to rotate in the $+\theta$ direction about their common center of mass. The alignment angle of the pair reaches a maximum in the fourth frame and, as evidenced by the reappearance of the high-pressure impingement region, decreases thereafter, suggesting stable cyclical behavior. At the same time, the effective angularity of the tandem bodies results in a common lift force which drives the pair in the lateral direction. In contrast to the previously explored scenarios, this potentially stable lifting behavior relies on both the aerodynamics and structural mechanics of the constituent bodies and may prove an important mechanism for enhancing the lateral momentum of more populous clusters.

Finally, in Figure 4.4 we examine a sphere pair with near alignment in the streamwise direction. The configuration, angled at 172.5° to the freestream, displays high drag on the primary body with modest surface pressure visible on the secondary, which yields a destabilizing moment. Because the effective moment arm

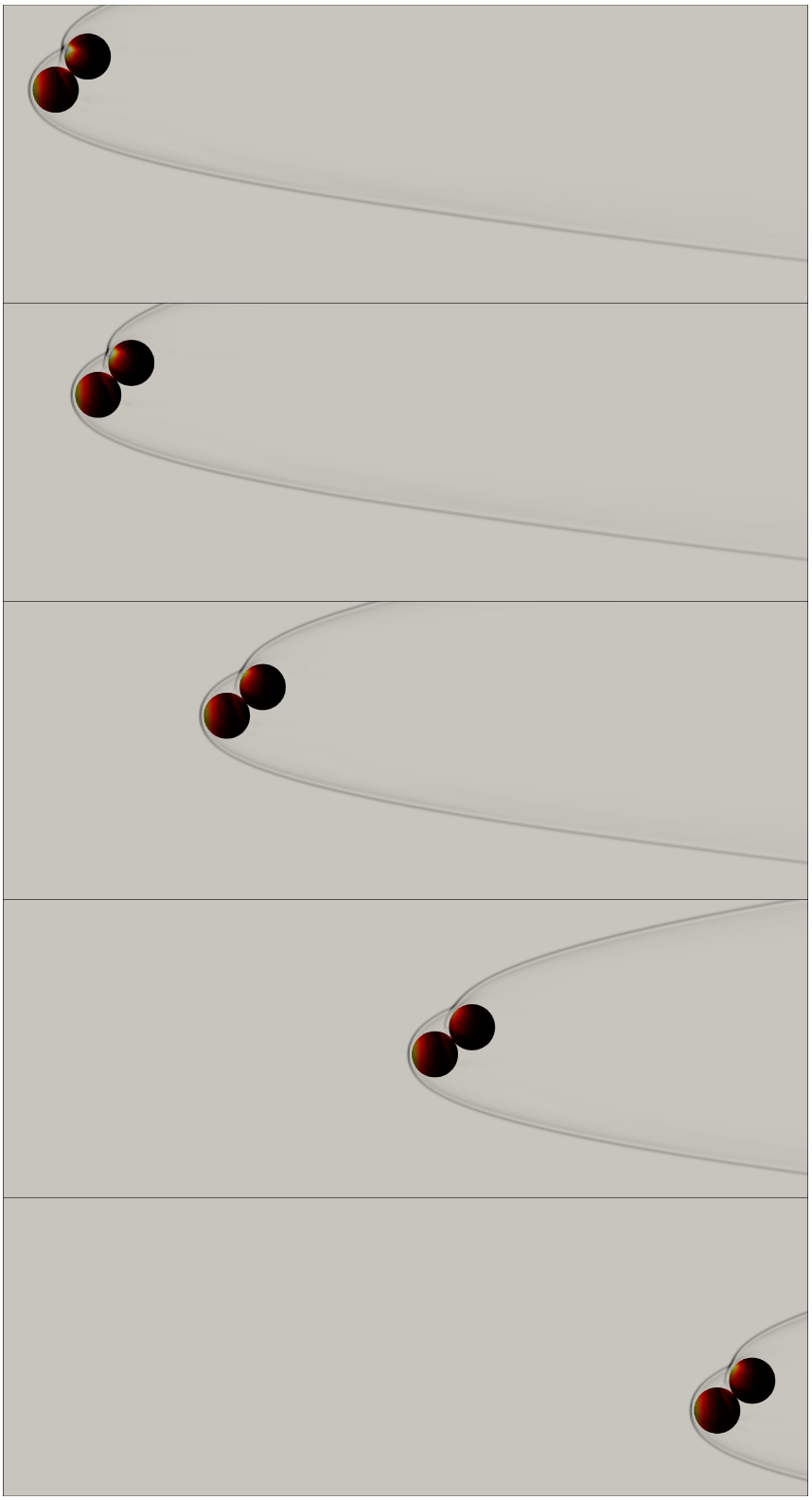

Figure 4.3: Separation sequence from initial alignment angle of 135° with coloring by surface pressure and centerline pseudo-schlieren. Frames shown in increments of $1.83\tau_s$ ($\sim$2.45 ms).

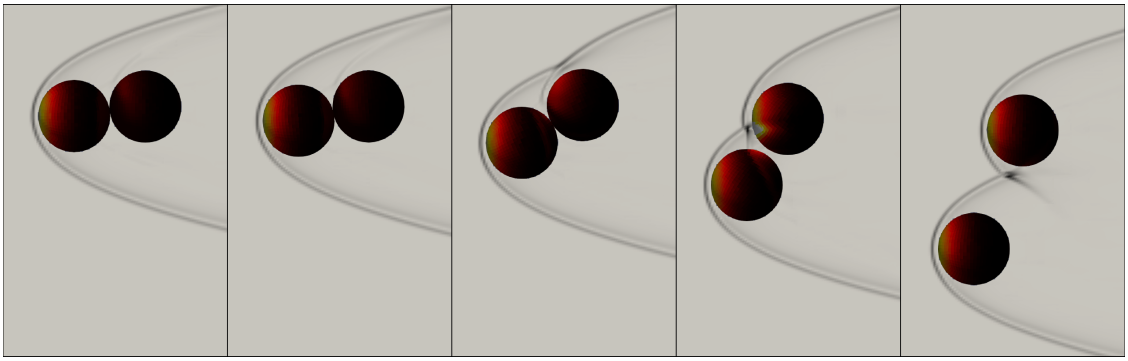

Figure 4.4: Separation sequence from initial alignment angle of 172.5° with coloring by surface pressure and centerline pseudo-schlieren. Frames shown in increments of $2.11\tau_s$ (∼2.81 ms).

is minimal immediately after release, the 'rolling' motion of the spheres is initially imperceptible but accelerates as the spheres' inclination to the freestream grows. In the fourth frame, the secondary sphere ceases surface contact with the primary, indicating that angular momentum of the pair was sufficient enough to overcome the restorative effects of shock impingement observed at 135°. The secondary body rapidly passes through the shock of the primary, before the spheres achieve aerodynamic independence in a manner similar to the lower θ_0 arrangements. However, in contrast to the 120° case, the primary sphere accrues more lateral momentum than the secondary, which remains nearly stationary laterally over the simulation, and signifies opposing trends for the motion of the system's center of mass.

Having established the general trends associated with sphere-pair aerodynamics, we now present in Figure 4.5(a) the trajectories of all secondary (downstream) spheres in the polar coordinate system of the primary (where the radial coordinate represents the edge-to-edge separation of the spheres), as well as time histories and final values of the lateral sphere velocities from the system's center of mass in Figures 4.5(b) and 4.5(c). The behavior near alignment angles of $\theta_0 = 90°$ closely

conforms to expectations of mutual repulsion examined earlier: the spheres separate laterally under the influence of high inboard pressures, achieving separation velocities of $\sim$0.2 over their $\sim 1.7\tau_s$ interacting flight duration. As evidenced by the post-release increase in alignment angle for higher θ_0, the transition from mutual repulsion to shock-surfing-induced separation occurs gradually between alignment angles of 90° and 120° and causes an appreciable enhancement to the lateral spread of the bodies, with V_T' values rising monotonically from 0.2 to 0.25 and the separation timescale extending to $\sim 4\tau_s$. At 127.5°, the secondary sphere exhibits brief surfing before becoming entrained in the wake of and then colliding with the leading sphere. This simulation, however, as well as a repeated computation with duration extended to $t' = 11$, do not resolve the eventual trajectories of the spheres, indicating that a prolonged series of (relatively) energetic collisions is a potentially sustainable configuration.

Spheres initially positioned in 135° and 142.5° arrangements, on the other hand, remain in contact for the duration of the simulations; as in Figure 4.3, examination of surface pressures on the trailing sphere reveals that, in both cases, restorative moments drive the angular alignment of the pair about a posited equilibrium θ. Indeed, for these cases, the surface separation of the spheres remains consistent with zero, as does the lateral velocity of the system, with low- and high-frequency residual oscillations respectively representing the bulk rotational oscillations and the elastic mechanical vibrations from surface contact. As the initial orientation is rotated further towards alignment with the freestream, the trailing sphere tends to 'roll' along the surface of the primary until surface contact is lost and the bodies begin to sep-

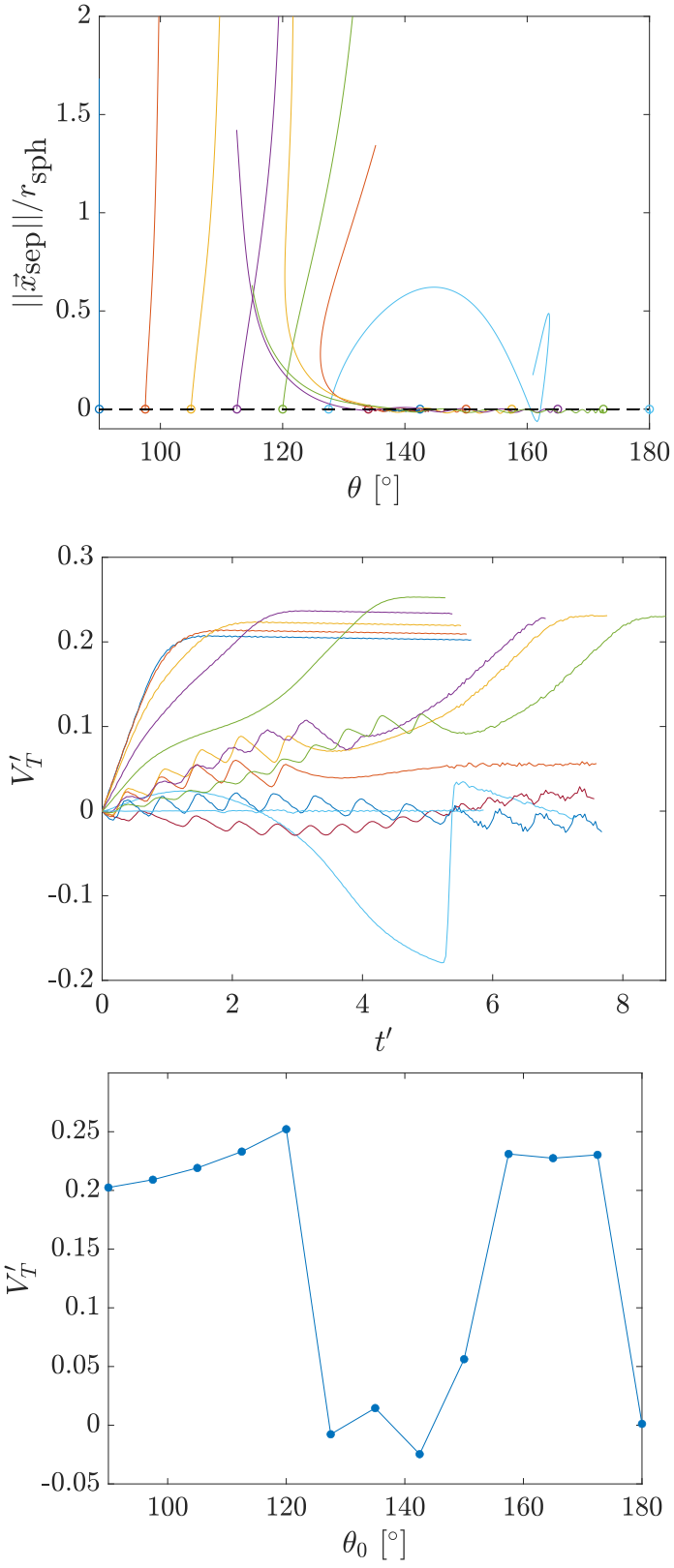

Figure 4.5: (a) Polar trajectory map, (b) lateral velocity of two-sphere survey, and (c) final lateral velocity with initial alignment angle.

arate by aerodynamic means, such as is demonstrated in Figure 4.4. The 150° case features a secondary sphere that remains on a persistent shock surfing trajectory, albeit without much enhancement to its lateral velocity. We note that closure of the final trajectories was not attained for this case, even with the computation time extended to $11\tau_s$ in a subsequent simulation. On the other hand, limited shock-surfing, which more than doubles the lateral velocity of the system, and subsequent aerodynamic independence follow the loss of surface contact for cases 157.5°–172.5°, as the angular momentum accrued by the pair has endowed the secondary sphere with enough lateral momentum to transit the impinging shock. The duration of contact is somewhat dependent on the initial angle, ranging from ~ 4 to $6\tau_s$ (Figure 4.5(b)), while the loss of contact in all cases appears to occur near 130° (Figure 4.5(a)). For an initial alignment angle of 180°, no discernible change in the pair's attitude was recorded, suggesting the presence of an (unstable) equilibrium position. Noticeably absent in Figure 4.5(a) are secondary spheres that persist in the wake of the primary, which follows from the reduced drag and subsequent collisions that occur in such arrangements. This seems to signify three permitted trajectories: immediate separation, delayed separation following a period of contact, and indefinite contact, with sphere pairs in the former two categories achieving lateral velocities between 0.2 and 0.25 (with the notable exceptions of the 127.5° and 150° cases). Indeed, this bi-modal behavior is manifest in the two distinct sets of final lateral velocities in Figure 4.5(c).

To gain further insight into the apparent stability behavior of the sphere pairs at $\theta_0 = 135°$ and 142.5°, we model the motions of both spheres as a single rigid

body and extract from the simulations a database of forces and moments for use in simulating the dynamics of the single-body system. Based on the computed forces on each sphere, the bodies will remain in contact for polar angles above 132°, and thus the rigid-body assumption remains valid only for alignment angles above this limit. We compare this simplified model with computational trajectories in a phase space constructed from the polar alignment angle, θ, in Figure 4.6 and observe qualitatively similar behavior. It should be noted, however, that, while the positional coordinates follow very similar trajectories, the elastic spheres move much more quickly than the two-lobed rigid body as a result of frictional surface sliding, so we have scaled $\dot{\theta}_{CFD}$ by an empirical correction of 1/6 to roughly match the ordinate limits of the simulation methods. The encouraging agreement between CFD/FEA and the rigid-body model validates the use of the latter method for qualitative prediction of sphere kinematics while subject to surface contact, with identification of the stable oscillation range of particular interest. Choosing initial coordinates of $(\theta_0 = 132°, \dot{\theta'}_0 = 0)$, we trace, as shown in gray, the phase loop delimiting the regions of stable rotations and rolling-separation. This bounding locus, centered about $\sim 140°$, contains stationary initial alignment angles of 132° and 145.7° and permits a maximum nondimensional rotational speed of ∼4. Although this represents a narrow stability band in highly specialized circumstances, the implications of a binary body resisting breakup during atmospheric transit are significant for energy deposition considerations — as the effective retention of inertia will allow the body to penetrate deeper into the atmosphere — and ground-footprint prediction, which will be discussed shortly. Contact stability for bodies of smaller radius ratios caused by

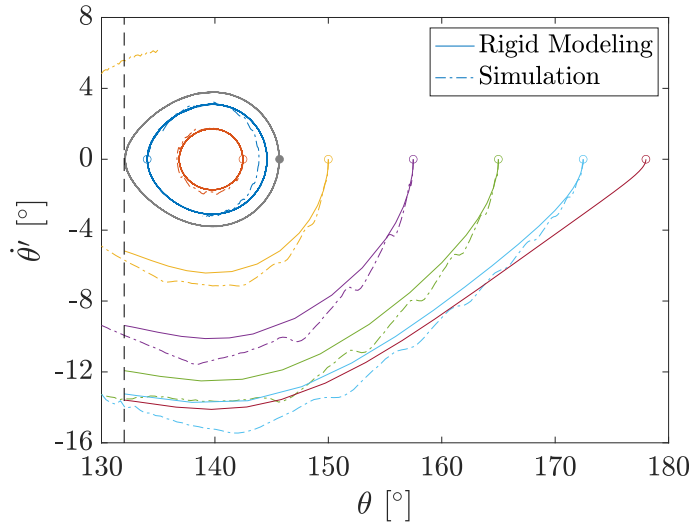

Figure 4.6: Polar alignment angle phase space of spheres that initially remain in contact, with bounding stability locus shown in gray and assumed 132° separation limit in dashed black.

aerodynamic shielding has been noted by Register et al. (2020), and its persistence to bodies of equal size suggests that a stable regime exists for a wide range of relative sphere sizes.

A particularly important consequence of stable sphere contact is the effective lifting characteristics resulting from the pair's angularity. Thus, retaining the framework of a binary rigid body and utilizing force coefficients from CFD simulations, we compute the lift-to-drag ratio experienced mutually by the sphere pair, which is given in Figure 4.7 (note that the region between 172.5° and 180° is linearly interpolated). We find a maximum L/D of 0.22 at $\theta = 141.5°$ followed by an approximately linear decrease. While the mean L/D of 0.197 within the stability region is comparatively quite low for hypersonic aerodynamics (Anderson, 2000), unlimited enhancement to the lateral velocity of the system should be theoretically possible. However, more likely is the occurrence of limited contact (that is, behavior

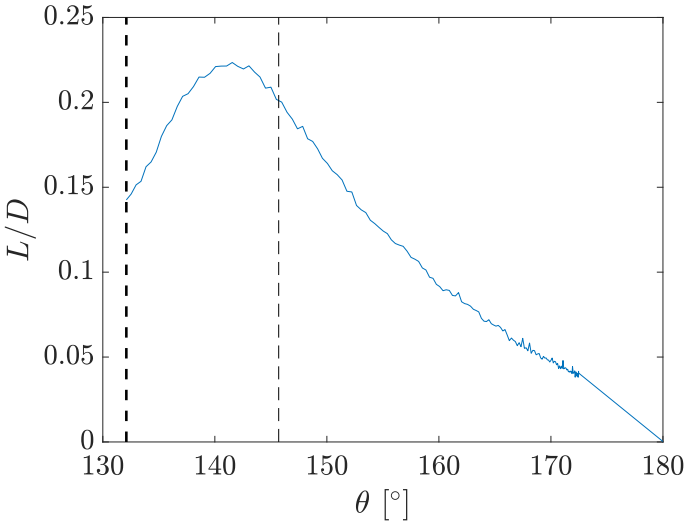

Figure 4.7: Lift-to-drag ratio of contacting sphere pairs, with the 132° separation limit in bold dashed black and the 145.7° upper stability limit in lighter relief.

located outside of the phase-space stability locus), during which significant mutual momentum can still be accumulated. In such scenarios, the reduced angularity of the pair yields lower lift, and the overall acceleration of the system's center of mass is highly dependent on the initial conditions. For instance, pairs commencing travel closer to the stability limit will remain in high-lift configurations for longer than those beginning towards 180°, which will quickly transit the high-lift zone. As expected, the dependency of final center-of-mass offset velocity on initial alignment angle forms a monotonically decreasing relationship, with center-of-mass V_T' values of 0.42, 0.32, and 0.28 attained for θ_0 of 150°, 157.5°, and 172.5°, respectively. As the mutual motion of these sphere pairs is greater than the lateral spread of the fragments themselves, this lifting contact mechanism may constitute an important facet of sphere separation in more populous settings, with sphere pairs comprising a set of highly expelled fragments.

4.2 Four-Sphere Experiments

While the aerodynamic separation of binary spheres is a well-studied process, it lacks the complexity of fragmentation events likely to occur during the atmospheric entry of meteoroids. As an initial exploration of the separation characteristics of more populous fragment swarms, we conduct experiments with four equal-sized spheres positioned such that their centers are located on the vertices of a regular tetrahedron. The two pre-determined cluster orientations examined here are selected as scenarios that exhibit behaviors representative of four-sphere separation, with a detailed examination using numerical simulations presented in the following subsection..

An example image sequence of shot 4A with reconstructed three-dimensional trajectories can be found in experimental validation analysis of Figure 3.7 in the previous chapter. Shot 4A features two upstream (or leading) spheres initially located at similar streamwise coordinates (a difference of $0.2d_{\text{sph}}$) and a second downstream (or trailing) pair partially shielded from the freestream flow by the leading spheres. In this particular case, the motions of the bodies are best understood in the context of two distinct, noninertial reference frames: a coordinate system centered about the cluster's center of mass and one established by the kinematics of the most upstream sphere. From the lateral separation velocities of the spheres in both systems (Figure 4.8), the center-of-mass frame adequately captures a quasi-linear velocity profile during the initial separation process (hereafter designated the 'primary' separation stage). On the other hand, the leading-sphere-referenced velocities, $V'_{T,l}$, showing

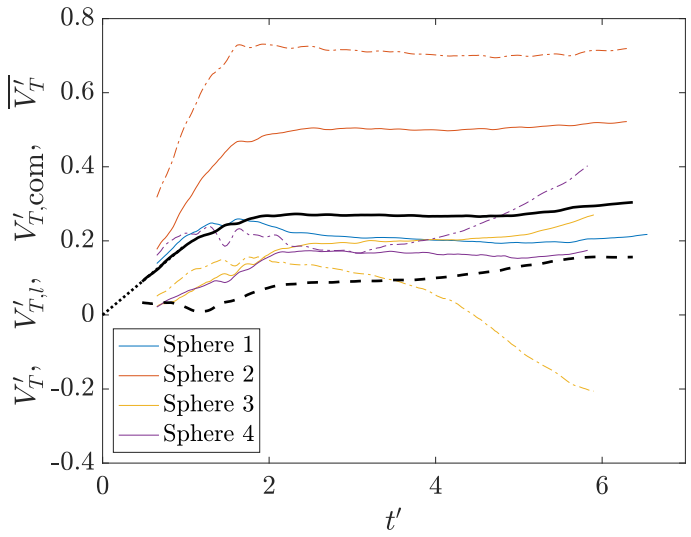

Figure 4.8: Transverse velocities for all spheres in shot 4A in center-of-mass (colored solid) and leading-sphere-centric (dash-dot) reference frames (V'_T and $V'_{T,l}$, respectively), along with lateral motion of the center of mass (dashed black) and collective lateral velocity (solid black) extrapolated to time-zero (dotted black).

much greater variation later in the test, demonstrate the importance of a 'secondary' separation stage in which individual, rather than bulk-cluster, interactions are dominant.

In the center-of-mass frame, we see that the leading spheres are quickly repelled from one another under the influence of a common bow shock. The lateral forces on the foremost spheres diminish rapidly as the cluster moves apart, while the trailing spheres experience weaker impulses, delayed somewhat by the initial flow shielding provided by spheres 1 and 2. These trailing bodies (spheres 3 and 4) lie further in the aerodynamic shadow of sphere 1 than 2, consequently forcing them in the approximate direction of travel of sphere 1; this contributes somewhat to the reduced cluster-centric lateral velocity of sphere 1 (~ 0.25) compared to sphere 2 (~ 0.5). Sphere 2 then proceeds through the remainder of the test volume without further aerodynamic interference, and the flowfield generated by sphere 1 largely governs

the trajectories of the bodies trailing it. Based on the time elapsed before the V_T' measurements plateau, the primary separation stage of this configuration persists for approximately $2.3\tau_s$.

The secondary dynamical regime marks a transition towards trajectories increasingly determined by positions relative to the furthest upstream body. The radially repelled agglomeration establishes a subcluster in which spheres 3 and 4 are aerodynamic receivers of the shock/wake structure generated by sphere 1. The leading-sphere-referenced transverse velocity of sphere 3 decreases as the experiment progresses, becoming negative at $t' \approx 4.1$, indicating that it has become entrained in the wake of sphere 1. Sphere 4, on the other hand, is accelerated further away from the lateral position of sphere 1, likely a result of shock-surfing behavior. By the time the spheres leave the visualization volume, secondary-stage interactions have caused the collective lateral velocity of the cluster to increase from ~ 0.27 to ~ 0.30, a value typical of this class of formation, as will be shown in Section 4.3.

Shot 4B, rotated approximately 50° in pitch and 30° in yaw from the previous cluster's attitude, is shown reconstructed in Figure 4.9 and exhibits separation characteristics quite distinct from those in shot 4A. The initial formation is composed of an obvious leading body (sphere 1) shielding an axially aligned trailing body (sphere 2) and two spheres (3 and 4) positioned at similar streamwise coordinates near the axial center of the formation. Following shell separation, spheres 3 and 4 experience severe repulsion from the center of the cluster (see Figure 4.10); as a result of their shock-receiving initial positions, they appear to follow shock-surfing trajectories for 3.4 and $4.3\tau_s$, respectively, whereafter they exhibit center-of-mass-referenced lateral

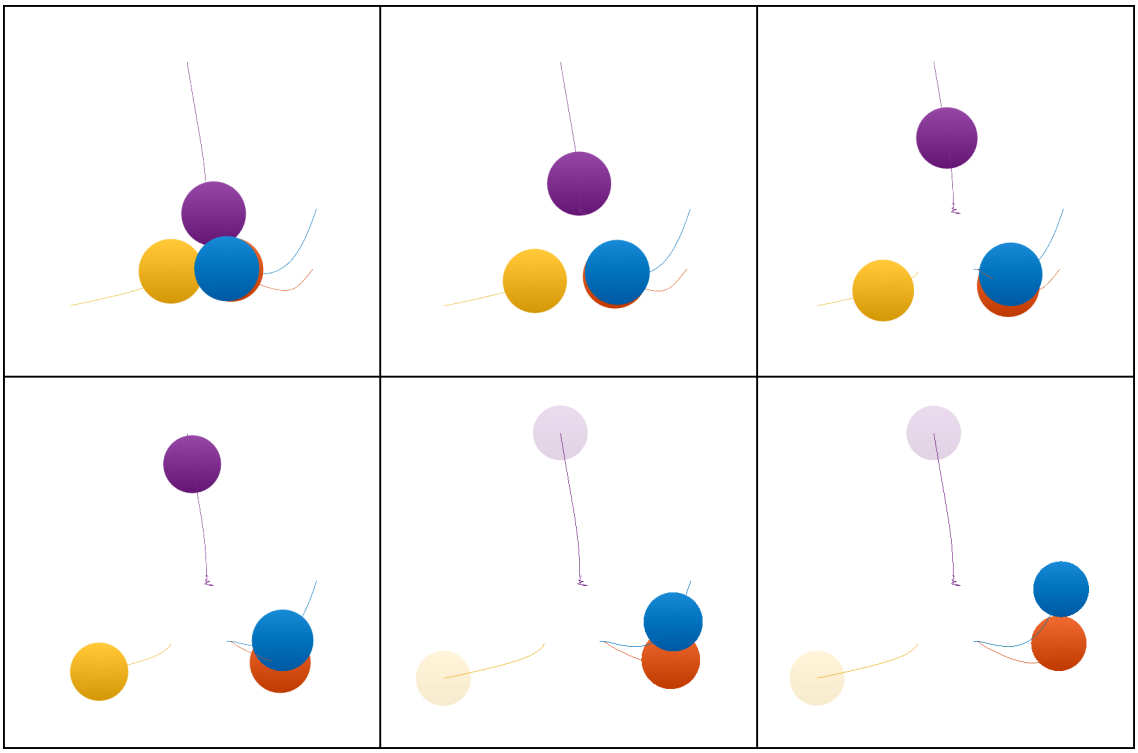

Figure 4.9: Downstream-projected reconstruction of shot 4B, with frames shown in increments of $1.49\tau_s$ (1.89 ms). Sphere coloring by number: 1, blue; 2, red; 3, yellow; 4, purple.

velocities of ~ 0.45. Meanwhile, spheres 1 and 2 are given a milder lateral push from the cluster's center of mass, throughout which sphere 2 maintains surface contact with and lies almost directly behind sphere 1. As detailed in the inviscid sphere-pair simulations of Section 4.1, this constitutes an unstable arrangement in which the high drag on sphere 1 produces a moment that causes the bodies to 'roll' about a common center while experiencing a mutual lifting force.

As in shot 4A, the secondary separation regime greatly influences the individual trajectory characteristics of the cluster, even if the collective lateral velocity remains largely unaltered. The lateral velocities of shot 4B spheres show the greatest increases in the first $\sim 4\tau_s$ before exhibiting more moderate changes thereafter.

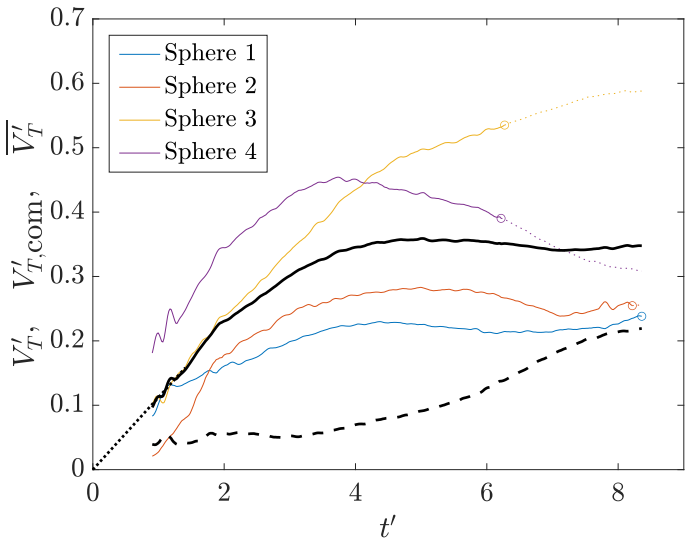

Figure 4.10: Center-of-mass-referenced transverse velocities (colored solid) for shot 4B with global-frame extrapolation (colored dotted), collective lateral velocity (solid black) with extrapolation to t_0' (dotted black), and center-of-mass lateral offset (dashed black)

Because spheres 3 and 4 are aerodynamically independent when exiting the viewing volume, we can estimate the center-of-mass trajectory and extrapolate their cluster-centric transverse velocities, leading to the extended collective lateral velocity and center-of-mass offset measurements in Figure 4.10. Immediately, we see that the collective lateral velocity (shown in solid black) rises during the primary separation phase to an approximately constant value of ~ 0.35, higher than that achieved in shot 4A. On the other hand, the lateral offset of the center-of-mass from the initial primary axis of the cluster (dashed black) appears to accelerate only during the second half of the test; this delayed onset in the center-of-mass motion results directly from the lifting dynamics of the 1–2 sphere pair. The effects of center-of-mass acceleration propagate into the relative motions of spheres 3 and 4: the lift of the 1–2 pair pushes it further towards sphere 4 and away from sphere 3, accounting for the observed velocity trends. In the context of meteoroid entry, the movement

of a cluster's center of mass during flight may prove deceptive for interpretation of possible strewn field patterns (involving limited cluster populations). Despite the approximately equal lateral velocities of spheres 3 and 4 in the global frame, sphere 3 ultimately exhibits a much higher value of V_T' and would appear a far outlying fragment upon examination of the expected ground footprint.

Returning to the rolling behavior of spheres 1 and 2, we quantify the system kinematics in terms of the polar alignment angle, θ_{12}, between the trailing sphere and contact point, as measured from the upstream direction. Obtaining the sphere's angular velocity by means of finite differencing and scaling by the inverse characteristic timescale, $1/\tau_s$, we provide a phase representation of the pair's rotation in Figure 4.11 to elucidate some aspects of the phenomenon. While the spheres begin at $\theta_{12,0} = 176°$, the initial aerodynamic impulse modifies the alignment line slightly, with the polar angle decreasing from a maximum value of 178°. Once the dynamics of pair are no longer influenced by the other two bodies, an approximately constant negative moment drives θ_{12} to a value of 145°, at which point it decreases with a constant angular velocity, indicating a region of near-zero rotational forces. Finally, at 132°, the spheres lose surface contact and begin to separate. From the Section 4.1, such contact binary rotations can be modeled by extracting force coefficients from inviscid simulations and assuming the spheres form a conjoined rigid body. Indeed, comparison of experimental results with rigid-body modeling shows good agreement in both the phase trajectory and 132° separation point. Thus, the rolling behavior of spheres 1 and 2 in shot 4B provides indirect evidence for persistent contact pairs in viscous flow, which, in addition to shock-surfing, could provide a mechanism for

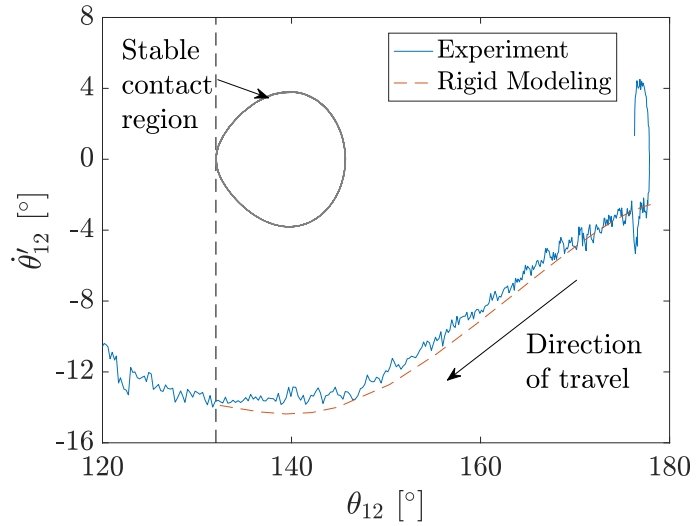

Figure 4.11: Alignment angle phase-space depiction of contact rolling behavior exhibited by spheres 1 and 2 in shot 4B. Separation point at 132° shown in dashed black and stable contact locus circled in gray.

extreme outlying fragments in crater fields.

4.3 Four-Sphere Simulation Survey

The four-equal-sphere experiments of Section 4.2 illustrate through a small number of representative cases the division of sphere dynamics into distinct regimes, as well as the continued influence of lifting sphere pairs in a more populous setting. We now conduct a simulation survey of the same geometry (that is, spheres with centroids placed on regular tetrahedron vertices) to extract a more detailed description of sphere separation from this configuration. Assuming a standardized formation rather than a random agglomeration allows for systematic variation of the governing parameters, in this case the pitch and yaw angles of the cluster (note that separation behavior is degenerate under roll transformations). Although the definition of the principal orientation is arbitrary in this setting, we adopt a convention for

0°-pitch/0°-yaw in which three spheres form a streamwise-normal plane behind a single leading sphere. The simulated parameter space spans angles of $-36°$ to $54°$ in pitch and $0°$ to $90°$ in yaw at intervals of $18°$, with several additional tests performed to capture the full extent of separation behaviors. In total, 38 simulations were performed following the methodology outlined in Chapter 3.

First, to highlight some of the governing dynamics of the four-body separation scenario, we review the features of a typical separation sequence of spheres initially placed in a tetrahedron, while noting that the general character of the phenomenon is not expected to differ from that detailed in Section 4.2. In Figure 4.12, we present a set of snapshots visualizing instantaneous sphere positions colored by surface pressure and the associated primary shock structures on the first refinement level from an initial orientation of 36°-pitch/18°-yaw, as well as lateral velocities and force coefficients in Figure 4.13. Note that this is the same simulation used for verification of the numerical model of Chapter 3. In the cluster's initial state, an encompassing bow shock generated principally by sphere 1 impinges on spheres 2 and 3, while sphere 4 is shielded in its wake. The shock-shock interaction on the inboard side of sphere 3 results in a region of high surface pressure on both spheres 1 and 3 ($C_T \approx 0.45$), promoting immediate lateral repulsion. Consequently, sphere 3 is aerodynamically independent from the rest of the cluster by $t' = 2$.

Sphere 2 resides at a location further downstream in the cluster and so is subjected to both shock impingement from sphere 1 and the swept shock-shock interaction between spheres 1 and 3. Both occur towards the front of the body, which induces augmented drag and increases the initial impulse in the streamwise

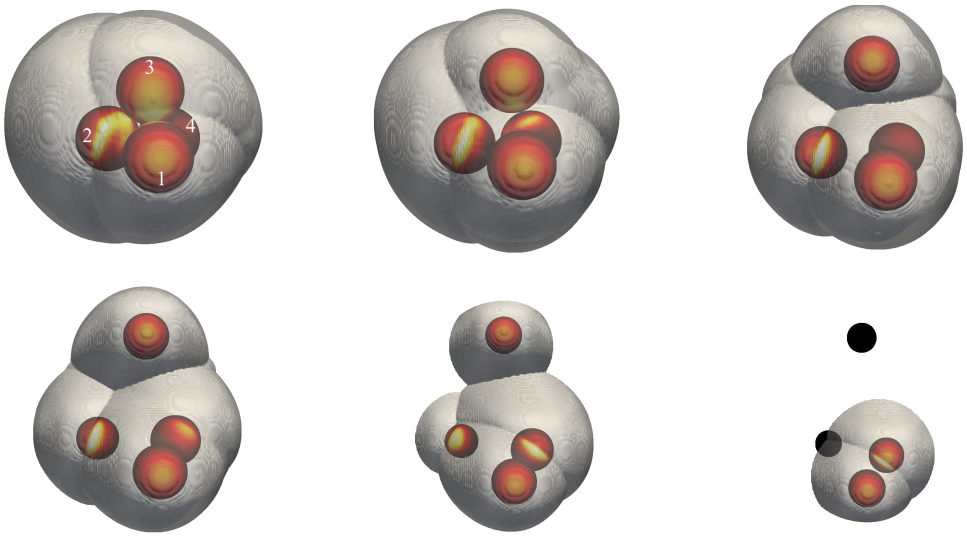

Figure 4.12: Trajectories of spheres separating from 36°-pitch/18°-yaw cluster with surfaces colored by pressure and primary shock structure visualized in gray. Images in steps of $t' = 0.94$.

direction. As in the visualization of Figure 4.12, sphere 2 remains in a shock surfing trajectory for an extended period of time before beginning to follow an entrainment trajectory in the wake of sphere 1. On the other hand, sphere 4, located initially in the wake of the leading sphere, experiences highly reduced drag which initiates a prolonged series of collisions between the two before 'rolling' away from sphere 1, as in Section 4.1. Due to the delayed onset of repulsive forces on sphere 4, it trails sphere 1 laterally and eventually exhibits separation that brings it further towards the cluster center than sphere 1. The primary separation phase lasts until $t' = 1.65$, as inferred from the mean lateral force coefficient, at which point the collective lateral velocity reaches 0.27, while the final value is roughly equivalent. While the spheres have not all reached their final aerodynamic state before exiting the computational domain, we find this simulation illustrative of the variety of behaviors observed in the survey.

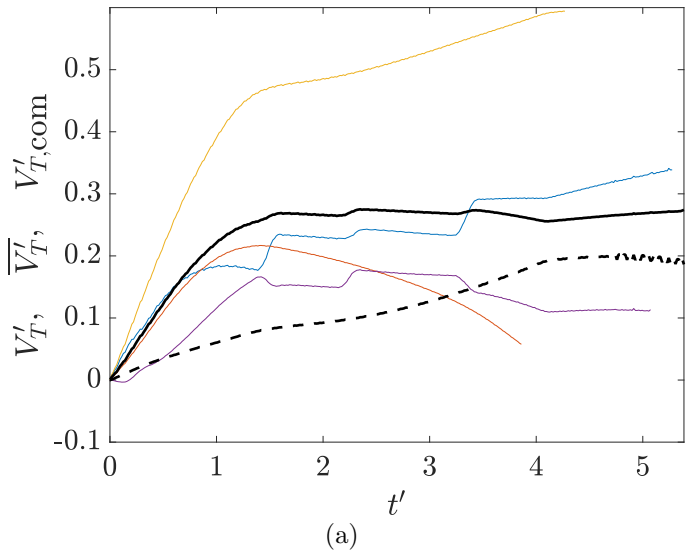

(a)

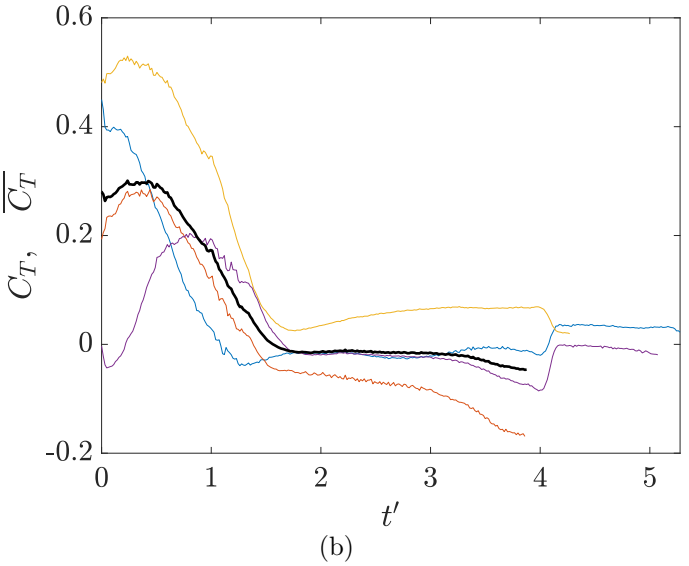

(b)

Figure 4.13: (a) Lateral velocities and (b) lateral force coefficients for four-sphere cluster at 36°-pitch/18°-yaw.

In the case of two equal-sized spheres separating, the parameter governing the resultant dynamics is the initial polar alignment angle, and we might likewise expect the behavior of the individual spheres in a tetrahedron cluster to be highly sensitive to their initial positioning. As such, we now investigate the dependence of ensemble separation behaviors on θ_0 by conducting the following procedure. First, considering all spheres in the survey independent of the other bodies present in their constituent simulations, we bin the spheres into groups, each of width 15°, by initial polar angle. Next, we compute the lateral velocity of all bodies relative to their cluster's center of mass. Note that the number density distribution vanishes towards θ_0 values of 0° and 180°, so bins towards the extremes of the range are less populated than those nearer the center. In Figure 4.14, the stacked timeseries of grouped lateral velocities shows a clear dependence of trajectory on initial polar angle. Spheres positioned towards the front of the formation (0° – 30°) tend to experience mild separation velocities, likely because the downstream spheres are largely incapable of influencing their dynamics, while those located slightly upstream of the flank (60° – 90°) are subject to immediate expulsion or shock surfing, reaching mean lateral velocities of 0.68.

At intermediate forward positions (30° – 60°), the separation characteristics seem dominated by collisions with other spheres, which are manifested as discontinuous jumps in V_T' that seem to occur after only a small degree of repulsion. This category is mainly occupied by the leader of a sphere pair repelled in tandem (as in spheres 1 and 4 in Figure 4.12), and the enhancement in V_T' through the two-sphere subcluster interaction can reach values of ~ 0.2, which is consistent which

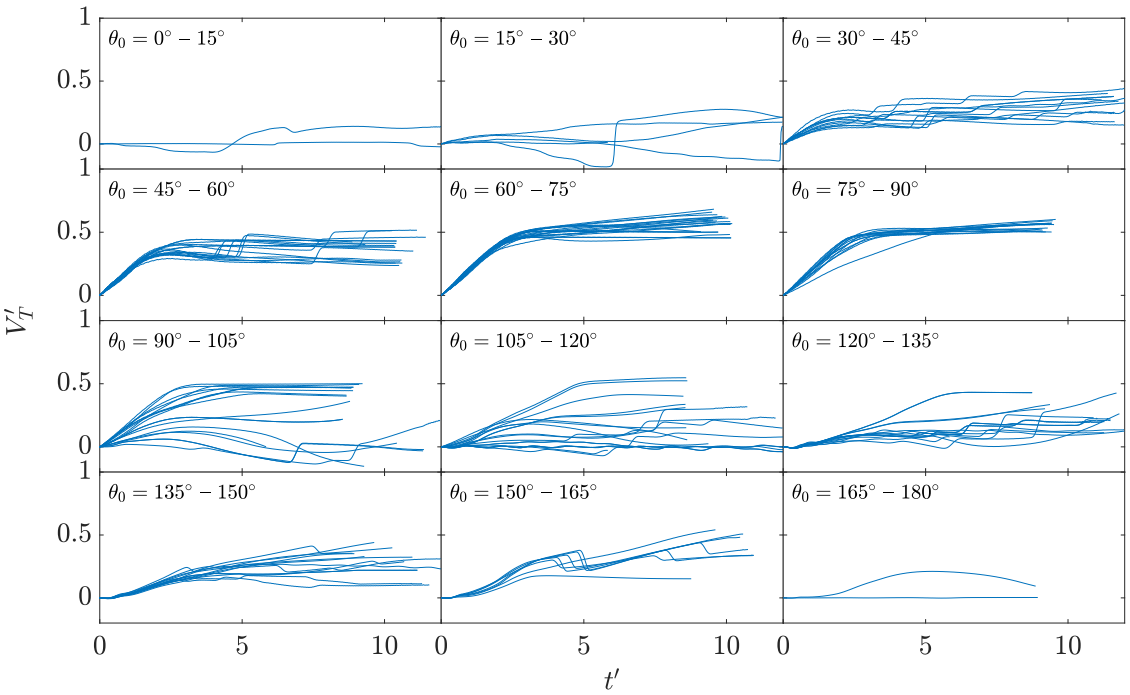

Figure 4.14: Timeseries of lateral velocity binned by initial polar angle.

the results of Section 4.1. Polar angles above 90° mark a transition from expulsion to entainment trajectories, although the notable variation in separation velocities at $\theta_0 = 90° - 120°$ indicates some level of dependence on geometry-specific properties. Note that, while some bodies seem not to have leveled off to a final lateral velocity, the distribution of kinematics at simulation termination is likely a fairly accurate representation of the true range of values. Just as bins 30° – 60° constitute the upstream (primary) bodies in a sphere pair, the spheres in bins 120° – 165° represent their downstream (secondary) counterparts in the same manner as described in Section 4.1; these, too, are marked by collisions and a delayed increase in lateral velocity typical of the 'rolling' trajectories. Finally, in the rear of the formation, rotational symmetry keeps the lateral separation velocities modest in scale.

Using the final lateral velocities of each sphere, we can create a basis for

estimating separation velocities based on initial polar angle alone. Defining the final velocity as that attained when a sphere reaches the limits of the computational domain or when the simulation ends, we present the mean lateral velocity of each binned group, along with error bars denoting one standard deviation, in Figure 4.15(a). The lateral separation velocity increases nearly linearly from initial polar angles of 0° to $\sim$ 70°, the latter marking the angle at which extended shock surfing is probable. At the lower end of this linear separation regime, the lateral forces on the sphere of interest are minimal, but the dynamical influence of other bodies grows towards higher polar angles where they will be more closely aligned in streamwise positioning and more inclined to generate a common bow shock. The brief plateau between $\sim$ 70° and $\sim$ 90° is consistent with the high sensitivity of shock surfing to initial positioning and represents the highest degree of expulsion observed in the survey. The lateral velocities of 0.6 achieved here are roughly consistent with the measurements of Laurence et al. (2012) of the shock surfing behavior of secondary spheres with radius ratio 0.625 from approximately the same range of initial alignment angles.

A substantial reduction in separation velocity occurs thereafter as a result of the increasing number of entrainment events, although a wide spread in the data is apparent. Above $\theta_0 = 120°$, we again observe a roughly linear rise in the separation velocity; these bins represent spheres that are initially shielded from the freestream flow by an upstream body and remain in the wake of that body until a nominal two-sphere interaction can commence, so it is not entirely surprising the trends here seem to mirror those at lower θ_0 values. Based on the geometric properties of a regular

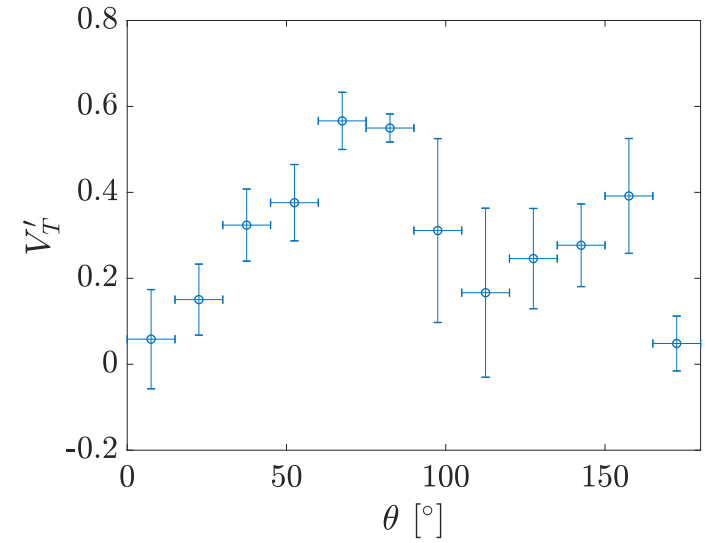

(a)

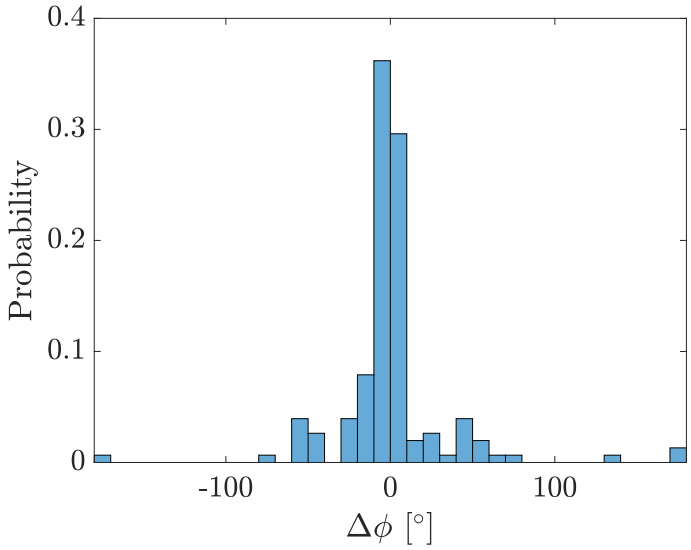

(b)

Figure 4.15: Ensemble statistics examining (a) terminal lateral velocity binned by initial polar angle and (b) difference between final and initial azimuthal angle.

tetrahedron, secondary spheres at larger polar angles are shielded by spheres on the higher angle end of the primary linear regime, resulting in positive linear slopes in both instances. In general, the response of secondary spheres to repulsion is delayed (see Figure 4.14), which causes the 'rolling' action to occur towards the cluster's center of mass and consequently accounts for a reduced separation velocity relative to that of the primary sphere. Close to 180°, tetrahedron symmetry appears to keep the separation velocity low, but the two-sphere sample size is too small to draw any reliable conclusions. Because most of the variation in separation velocity seems to be captured by the polar angle, it is plausible that reduced-order statistical modeling of separation could accurately predict the terminal trajectory of constituent fragments without specifically treating the geometrical intricacies of the initial cluster.

Existing models of the aerodynamic separation of fragmenting bodies (the pancake model of Hills and Goda (1993), for example) assume pure radial expansion of the free-flying bodies. Such a simplification has not been verified, however, using high fidelity methods. As a simple test of this assumption, we investigate the difference in azimuthal angle, ϕ, over the course of a simulation, where ϕ is referenced to the position of the cluster center of mass. Figure 4.15(b) shows that the majority of spheres do not experience much change in their azimuthal positions: 75% remain with 20° of their initial positions, while a handful of entrained bodies have passed through the wake of a primary sphere to achieve $\Delta\phi$ values of ±180°. A moderate number of bodies have moved further from their initial azimuthal positions, though tetrahedral symmetries are likely a contributing factor, as such cases tend to occur with pairs of trailing spheres near initial yaw angles of 0°. Despite some variation in

azimuthal angle as a result of a separation event, we find that the preponderance of bodies expand nearly laterally from their initial positions, justifying to some extent the use of that assumption in simplified aerodynamic modeling of fragmentation events with equal-sized bodies.

Now that we have established some broad conclusions regarding the separation behavior of spheres based only on initial positioning in a cluster, we can examine the detailed characteristics of the clusters as determined by their orientations. The survey parameters subject to variation were the pitch and yaw of the tetrahedral arrangement; while these parameters do drive the range of behaviors achieved, they do not possess an underlying physical correlation with the separation characteristics of a given cluster. Instead, we derive a set of reduced parameters that are functionally independent of the specific configuration considered and better capture the geometric features that one might expect to be significant for the resulting aerodynamics and, thus, the separation behavior. First, we define a bluntness parameter, B, which effectively describes whether the primary bow shock is generated by multiple spheres, thus creating a region of high pressure between the bodies and promoting separation. For a given tetrahedron orientation, B is determined by computing the unit normals for all external faces (i.e., planes through any three sphere centroids) and finding the maximum projection onto the upstream direction:

$$B = \max(\hat{n}_i \cdot \langle -1, 0, 0 \rangle). \tag{4.1}$$

The geometry of a tetrahedron limits the bluntness index to [1/3, 1], where larger

values indicate a higher proclivity for immediate repulsion and the smallest values denote a single leading sphere.

The second parameter is the asymmetry index, which represents the lateral mass offset between the aerodynamically relevant bodies and the system's center of mass, i.e., this parameter takes a large value when a lone shock-generating body is not located along the centerline. To compute this quantity, we determine the initial lateral distance of each sphere from the center of mass and assign a summation weight based on its streamwise position; a quadratic weighting is utilized upstream of the center of mass, while downstream spheres are assigned a value of zero. The set of weights is normalized to unity, and the 2-norm of the summation is scaled by the radius of the virtual circumscribing sphere:

$$
\begin{aligned}
A =& ||\Sigma_i w_i' \left(\vec{x}_{i,l} - \vec{x}_{\mathrm{com},l}\right)||/r_v, \quad \text{where} \\
w_i =& \begin{cases} (x_i - x_{\mathrm{com}})^2 & , x_i < x_{\mathrm{com}} \\ 0 & , x_i \geq x_{\mathrm{com}} \end{cases} \quad \text{and} \quad w_i' = \frac{w_i}{\Sigma_j w_j}.
\end{aligned}
\tag{4.2}
$$

Here, the l subscript refers to the lateral component the position vector and r_v is the virtual sphere radius. The asymmetry index takes values between 0 and ∼0.32 for a tetrahedron, where the aerodynamic offset from the primary axis is greatest at larger values. To provide an intuition for the appearance of clusters at certain points in A–B space, we present in Figure 4.16 illustrative agglomerations that exhibit slender, blunt, symmetric, asymmetric, and mixed attributes. The locus of points in the A–B plane is highly dependent on the cluster geometry and appears much more

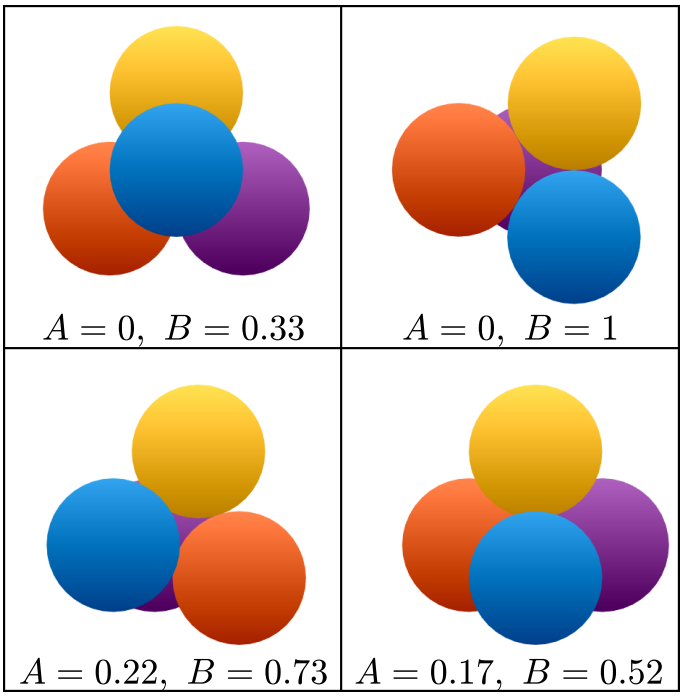

Figure 4.16: Downstream view of sample clusters labeled according to geometric parameterization.

irregular in form than does the rectangular pitch-yaw space explored for survey purposes. Furthermore, we note that this set of parameters maps roll-degenerate states to the same coordinates in A–B space.

In Figure 4.17, we present maps of the surveyed cluster separation properties under the reduced parameterization. With the boundary derived from a random sampling of cluster orientations and simulation points noted in red, the vertex-centered tessellations give the collective separation velocity of the cluster, $\overline{V'_T}$, the lateral velocity of its center of mass, $V'_{T,\mathrm{com}}$, and the maximum lateral velocity, $V'_{T,\mathrm{max}}$. The map of $\overline{V'_T}$ demonstrates a clear correlation of the collective separation velocity with the bluntness index. Near B values of 1/3 (i.e., more streamlined cases), the cluster approaches separation velocities of zero; by extrapolation of the results of Section 4.1, one might expect a lower limit of $\sim$0.2, but certain arrange-

ments possess symmetries that render them somewhat resistant to separation. In Figure 4.18(a), for example, increased outboard pressures on the rear spheres due to shock impingement are balanced by contact forces, allowing the cluster to translate downstream without any perceptible disruption. Such behavior may not be characteristic of actual entry events, however. Towards higher values of B, $\overline{V_T'}$ increases to ∼0.5, which tends to occur when all spheres are immediately repelled. While one might expect little dependence of the collective separation velocity on the asymmetry index, we find that a larger aerodynamic offset can enhance separation compared to initially blunter clusters with high symmetry. In Figure 4.18(b), the presence of one trailing sphere along the primary axis reduces the overall lateral velocity of the cluster ($\overline{V_T'} = 0.39$), while all spheres (including a primary/secondary pair) are repelled from the center of mass in Figure 4.18(c) ($\overline{V_T'} = 0.56$). There is clearly a high degree of variation in the collective separation velocities experienced by a tetrahedral cluster of spheres, but we attempt to estimate a characteristic $\overline{V_T'}$ for comparative purposes. Weighting each simulation by its normalized cell area in Figure 4.17(a), we find a value of ∼0.35, which represents a marked increase from the sphere-pair value (~ 0.22).

From Figure 4.17(b), the cluster center of mass can deviate significantly from the initial primary axis; the area-weighted mean of the tesselation in Figure 4.17(b) yields a value of ∼0.13, large enough to meaningfully alter the trajectory and location of energy deposition due to a body entering the atmosphere. Surprisingly, the correlation with the asymmetry index is not so clear here. Highly symmetrical cases (see Figures 4.18(a) and 4.18(b)) do tend towards a laterally stationary center of

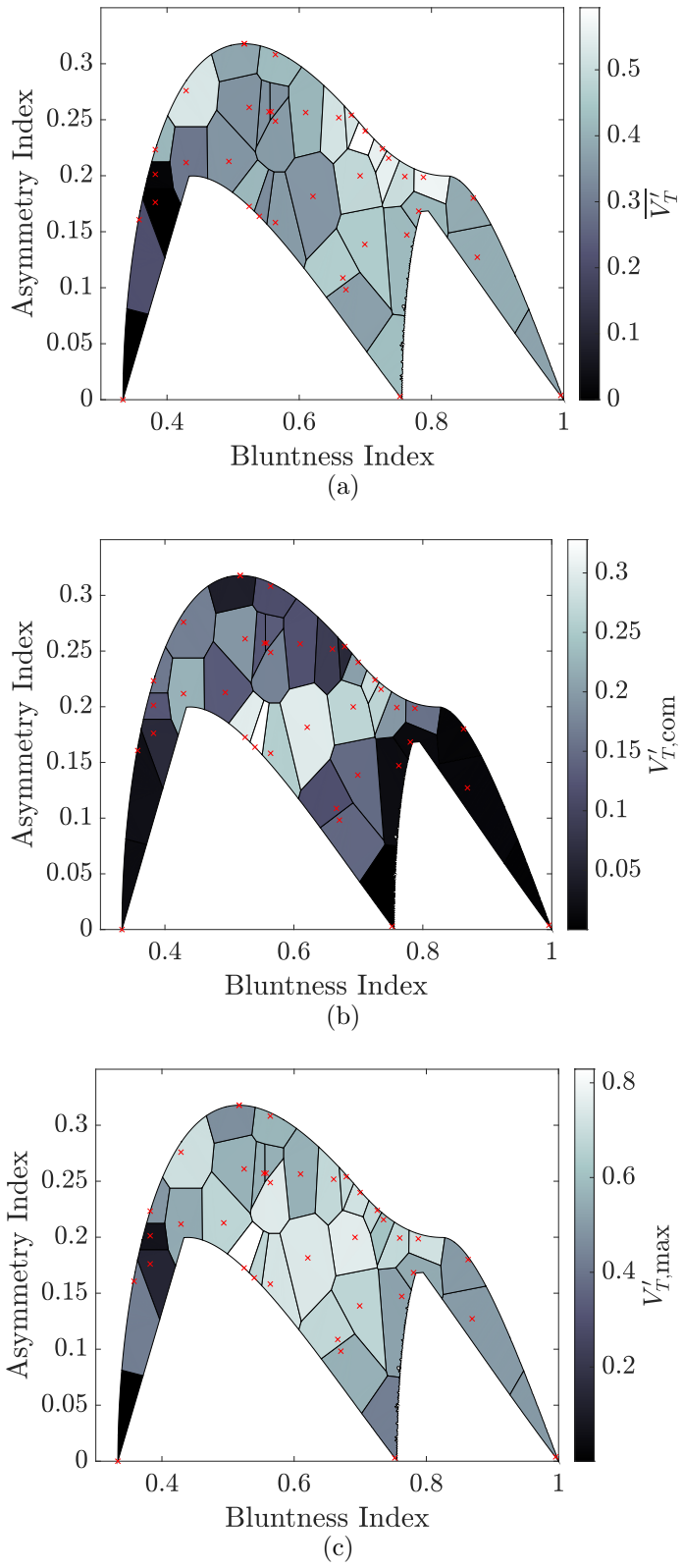

Figure 4.17: Maps of (a) collective separation velocity, (b) lateral center-of-mass velocity, and (c) maximum lateral velocity under the reduced parameterization.

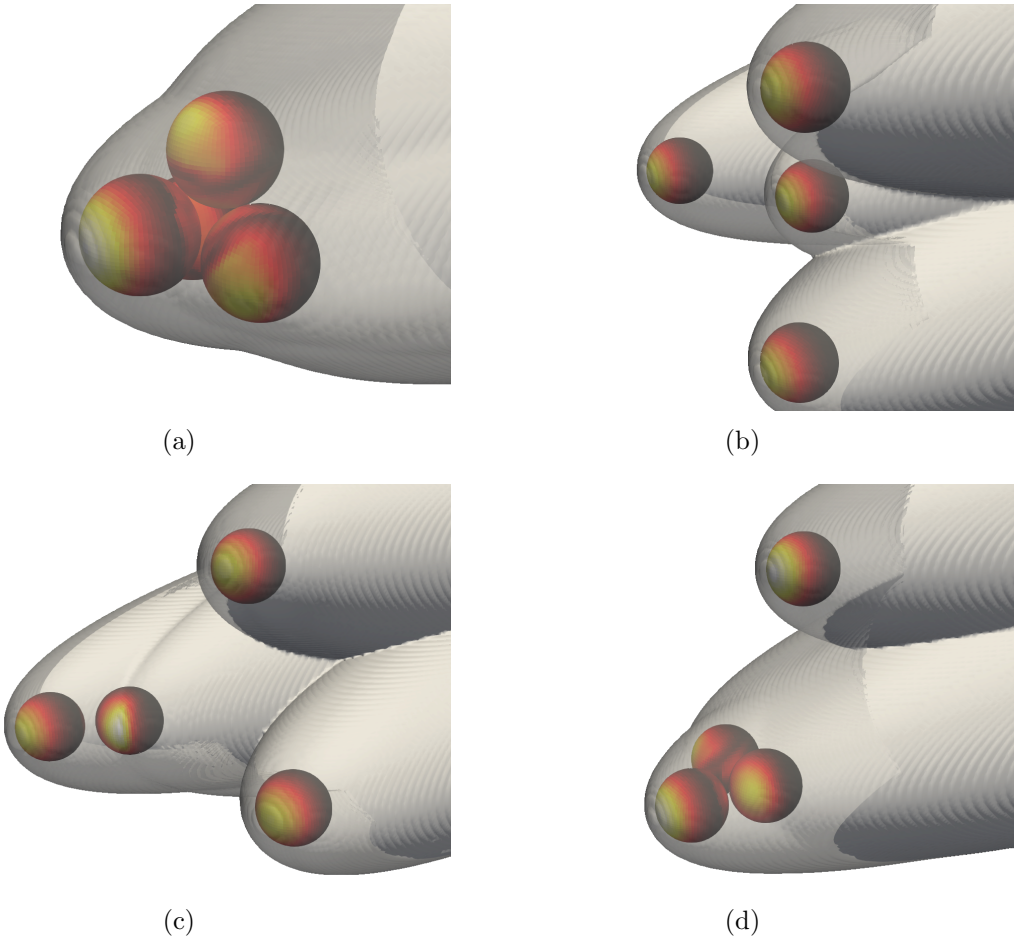

(a) (b)

(c) (d)

Figure 4.18: Snapshots of cases with asymmetry–bluntness indices of (a) 0–0.33, (b) 0–1, (c) 0.22–0.73, and (d) 0.17–0.52 demonstrating the dependence of separation characteristics on cluster geometry/attitude. Selection of cluster attitudes is identical to that in Figure 4.16.

mass, but the most severe instances of center of mass repulsion occur for only moderately asymmetric agglomerations. For instance, Figure 4.18(d) shows a quasi-stable subcluster of three spheres that skews the center of mass sharply away from its initial position. At higher A values (Figure 4.18(c)), primary/secondary sphere pairs can generate transient lifting configurations before eventually separating, although, at $A = 0.31,\ B = 0.52$, the lateral forces induced by a streamwise-aligned sphere pair are small enough that their lateral momentum is almost completely offset by two bodies initially expelled from the cluster. The acute shift of mass away from the nominal trajectory axis may be a peculiarity of the tetrahedral geometry chosen here. Indeed, as the number of spheres is increased, one might expect more uniform spreading of the constituent bodies in a cluster with little offset to the center of mass location. As we will see in Chapter 5, such a situation would equate with reducing the extent of the explorable asymmetry–bluntness space.

Finally, with a focus on outlying fragments in a strewn field, we examine the velocities of the expelled bodies within each cluster (Figure 4.17(c)). Interestingly, the maximum velocities appear roughly consistent with the sum of the collective lateral velocities and center-of-mass offset, although there is no clear reason why this should be the case. The maximum lateral velocity of the survey (0.82) occurs in the lifting triplet of Figure 4.18(d) and is almost 2.5 times greater than the mean $\overline{V'_T}$, indicating that stable lifting arrangements may account for the highly ejected fragments noted in literature (see, e.g., Borovička and Kalenda (2003)). We also find a high concentration of exepelled spheres with $V'_{T,\max} \sim 0.7$ also arises, due mostly to shock surfing and paired travel, and an area-weighted average of 0.54.

4.4 Conclusions

A number of outstanding trends permeate the aerodynamic separation behavior of all small cluster configurations. Binary clusters invariably obey the dynamics dictated by the shock structure of the upstream sphere, although surface contact physics enables the previously unidentified stable lifting arrangement capable of producing far outlying members of a strewn field. Even among the high run-to-run variance exhibited, multi-sphere agglomerations instead reveal a division of governing aerodynamics into two phases, with mutual repulsion a critical component of the primary phase and subcluster interactions, such as those noted in the sphere-pair survey, dominant in the subsequent secondary phase. However, small clusters exhibit an obvious deviation from the idealized spherical cluster agglomeration, and the geometric idiosyncrasies of configurations such as tetrahedra greatly influence the resulting trajectories at varying attitudes. We have also discerned a correlation between the terminal lateral velocity of a fragment and its initial polar angle, which represents a statistical simplification in characterization of sphere-cluster separation.

Chapter 5: Equal Spheres: Intermediate Clusters

We now advance to clusters of intermediate population, that is, those numbering between five and nineteen spheres. Here, brief evaluations of two eight- and eleven-sphere experiments are accompanied by a comprehensive review of the thirteen-sphere simulation survey, which together demonstrate a growth in fragment dispersion with increasing population and a deepening division in the physics and statistics of the two separation phases. A summary of experiments with fourteen- and fifteen-sphere clusters, for which initial sphere positions were not obtainable, is omitted here, as the characteristics of such clusters are generally consistent with the other populations examined.

5.1 Eight-Sphere Experiments

The configurations considered to this point have demonstrated the prominence of both mutual repulsion and subcluster interactions in the separation dynamics of small sphere clusters. Doubling the sphere population to eight equal bodies, we can examine any changes in the relative importance of the active physical mechanisms. With less unoccupied volume than the less populous cases, the randomly constructed eight-sphere clusters form an intrinsically blunter geometry, which may be expected

to promote greater separation of the constituent bodies. At the same time, the larger number of initially shielded bodies may dictate the trajectories of those upstream solely by inertial/mechanical means. Note that these clusters, as well as all other experimental clusters of larger population, are composed of randomly positioned spheres, subject to the irregular packing process prior to a wind tunnel test. Thus, we present two exemplary experiments which illustrate the changing characteristics of sphere separation with increasing population.

Shot 8A, featuring an agglomeration with one body located further upstream than the rest, demonstrates different aerodynamic trends than have been observed thus far. The first panel of the thee-dimensional reconstruction (Figure 5.1(a)) shows two bodies (spheres 2 and 6) completely shielded from the freestream, with five others likely recipients of the bow-shock structure generated by sphere 1. Indeed, at $t' = 1.78$, these five exposed spheres are repelled from the system's center of mass, which is nearly coincident with sphere 1, while the spheres 2 and 6 remain bound to the wakes of spheres 1 and 4, respectively. As deduced from the lateral velocity timeseries of Figure 5.1(b), three bodies achieve aerodynamic independence at $t' = 2.5$, at which point the collective lateral velocity reaches an approximately constant value of 0.37. This plateau, therefore, denotes the transition from primary to secondary separation regimes, whereupon the volume spanned by the cluster has expanded by a factor of 2.3.

The following phase of separation is marked by the aerodynamic influence of sphere 1, which lies at least two radii upstream of all other bodies (aside from sphere 4). Most prominently, we find that spheres 2 and 3 have been captured by

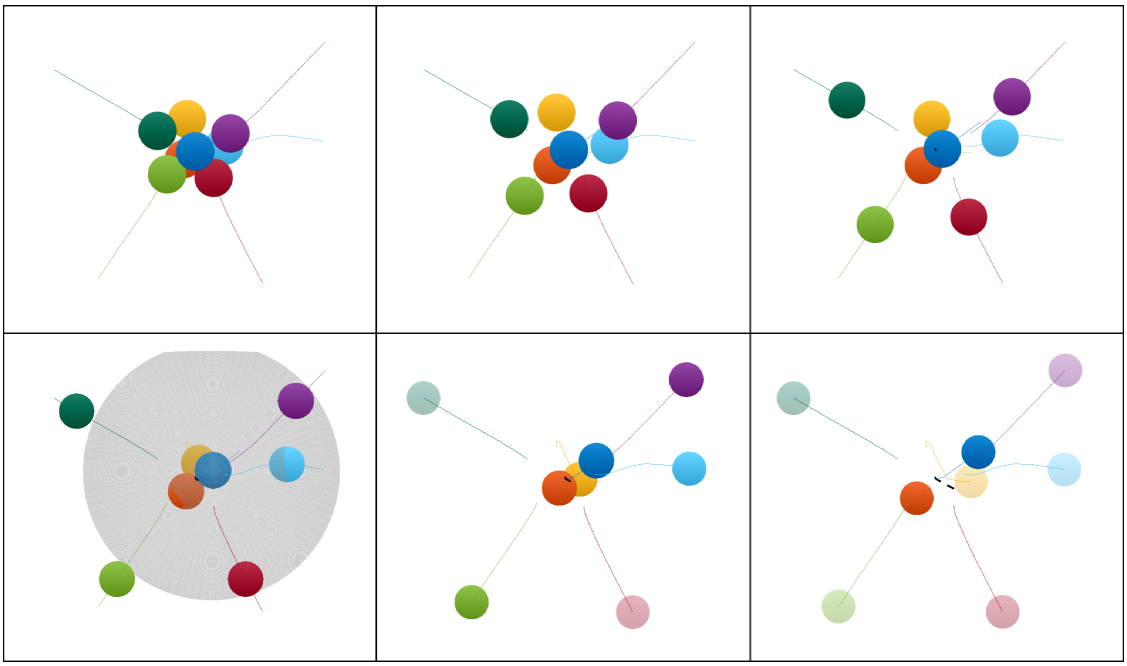

(a)

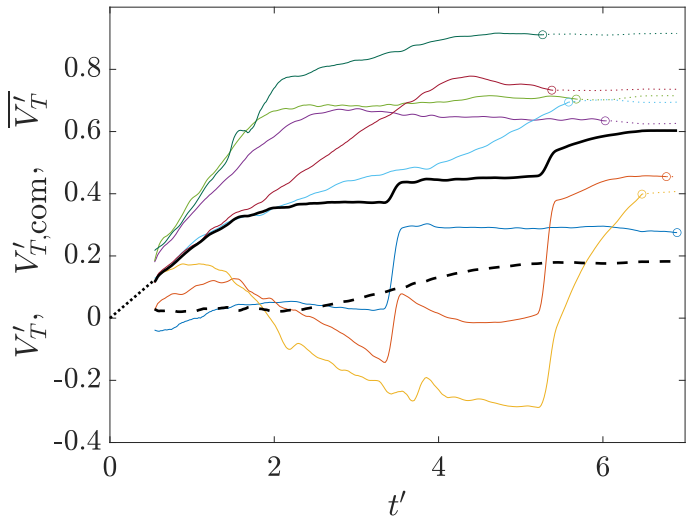

(b)

Figure 5.1: (a) Downstream reconstruction of shot 8A in increments of $1.24\tau_s$ (1.87 ms) beginning from $t' = 0.54$ and (b) Velocity profile of spheres in shot 8A. Computational shock surface generated by leading sphere shown at $t' = 4.26$. Sphere numbering by color: 1, blue; 2, red; 3, yellow; 4, purple; 5, light green; 6, cyan; 7, crimson; 8, dark green.

the attractive wake of sphere 1, forming a dense core of bodies along the primary axis of the cluster. The ensuing pair of collisions, occurring during the panel 4–5 and 5–6 interframe periods of Figure 5.1(a), aids in breaking up the cluster core, enhancing the collective lateral velocity by 16% and 20% at the obvious step-like discontinuities. Thus, these collisions effectively convert the kinetic energy resulting from relative streamwise velocity differences into lateral momentum. At the same time, spheres 6 and 7 commence extended shock surfing; sphere 7 escapes the influence of sphere 1 by $t' = 4.25$, likely due to a collision that pushes sphere 1 in the opposite direction, whereas sphere 6 continues to shock-surf until exiting the field of view. Such observations are consistent with the reconstructed shock profile of sphere 1 (extracted from an AMROC simulation of a single sphere at Mach 6) at $t = 4.26$, which shows the intersection of the bow shock with the surface of sphere 6, as well as its passage slightly downstream of sphere 7. Shock surfing has the added effect of shifting the center of mass away from the cluster's primary axis. From Figure 5.1(b), the center of mass diverges from its initial position near the point of primary–secondary phase shift, attaining a lateral velocity of 0.18 by the test's conclusion, and, from the final frame of Figure 5.1(a), is displaced in the direction of the two shock-surfing bodies. In any event, this experiment demonstrates both the augmented level of mutual repulsion accompanied by a greater cluster population and the persistence of secondary interactions through mechanisms such as shock surfing and collisional breakup.

Reconstructed in Figure 5.2(a), Shot 8B, on the other hand, exhibits a secondary separation phase of much diminished significance. In this blunter configura-

tion, a set of four upstream spheres forms a plane that is oriented almost directly into the freestream flow, and the resulting high internal pressures drive much of the cluster to impressive lateral velocities. From Figure 5.2(b), the primary separation phase constitutes 94% of the terminal collective lateral velocity (0.49) and is estimated to a comparatively brief duration of $\sim 2\tau_s$. In fact, the high bluntness of the configuration precludes any entrainment behavior, yielding a minimum lateral velocity of 0.27 at the end of primary separation. Also, in agreement with the initial polar angle dependence of lateral velocities from the four-sphere survey (Figure 4.15(a)), we find that the two most ejected bodies originated from polar angles of 96° and 73°, and the least expelled from 128°. The limited shock surfing that does occur arises later in the experiment (see spheres 2 and 8), and, despite its pronounced influence on the center of mass, its effect is only modestly transmitted to the final dispersion of the system.

As this experiment was conducted in the C3 camera arrangement, three-dimensional reconstruction errors are small enough to allow for force coefficient estimation, which is simply achieved by computing the finite difference of the velocity data in the same manner as described in Section 2.6. Thus, we present the transverse force coefficients centered about the system's primary axis (rather than the center of mass, which amplifies the measurement error), which display uncertainty levels of $\pm$ 0.03. The mean lateral force coefficient at the commencement of body tracking, 0.33, seems to originate from a constant state, with a deviation of 0.11 about this value. Interestingly, the body initially subjected to the greatest lateral force (sphere 2) is not the most expelled in the cluster but rather those

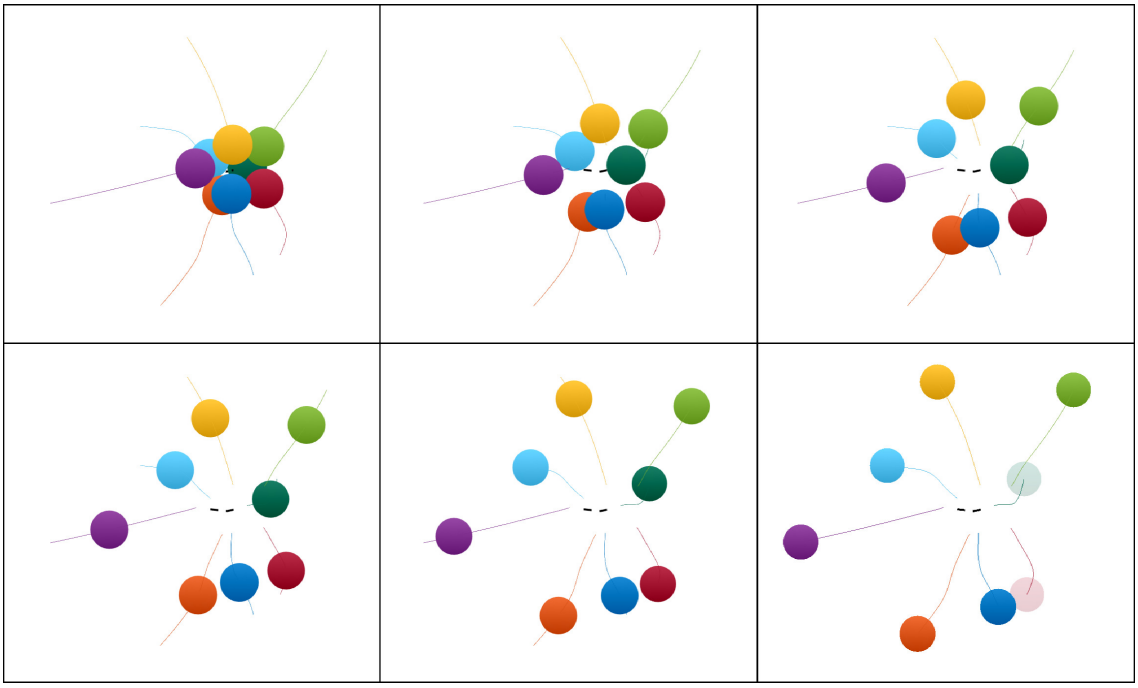

(a)

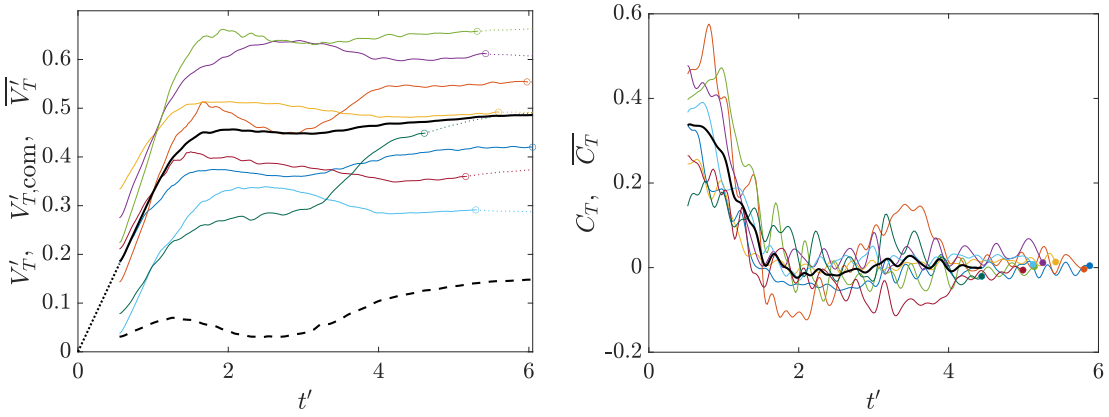

(b) (c)

Figure 5.2: ((a) Downstream reconstruction of shot 8B in increments of $0.96\tau_s$ (1.45 ms) beginning from $t' = 0.55$. (b) Lateral velocity and (c) lateral force coefficient timeseries of shot 8B. Sphere numbering by color: 1, blue; 2, red; 3, yellow; 4, purple; 5, light green; 6, cyan; 7, crimson; 8, dark green.

spheres whose lateral force coefficients decay more gradually. Comparing with Figure 5.2(b), we note that not all lateral velocities extrapolate to zero, indicating that certain aerodynamic interactions have occurred in the $\sim 0.5\tau_s$ between effective release and body tracking. For example, we might expect the lateral forces on sphere 3 to rise beyond their perceived maximum of 0.25, while sphere 6, predominantly shielded from the freestream flow, would experience near-zero transverse forces at release. Nonetheless, the mean force coefficient curve loosely resembles a half-Gaussian in appearance, an observation which may prove useful in defining a fragment separation model under an unsteady inflow.

5.2 Eleven-Sphere Experiments

Two experiments conducted with clusters of eleven spheres complement the experimental data taken from clusters of eight spheres. The clusters were constructed from randomly packed spheres and represent the most populous cluster for which sphere positions can be reliably traced back to test times preceding the termination of primary separation. The stereoscopic visualization of shot 11B, as well as the trajectory streamwise projections of both experiments (provided in Figures 5.4(a) and 5.4(b)), demonstrate the impressive lateral range achieved by the spheres over the $\sim 7\tau_s$ test durations. Indeed, the corresponding terminal collective lateral velocities reach values of 0.53 and 0.54 and, despite two (of five) eight-spheres tests with higher fragment dispersion, represent a notable enhancement to the mean separation behavior.

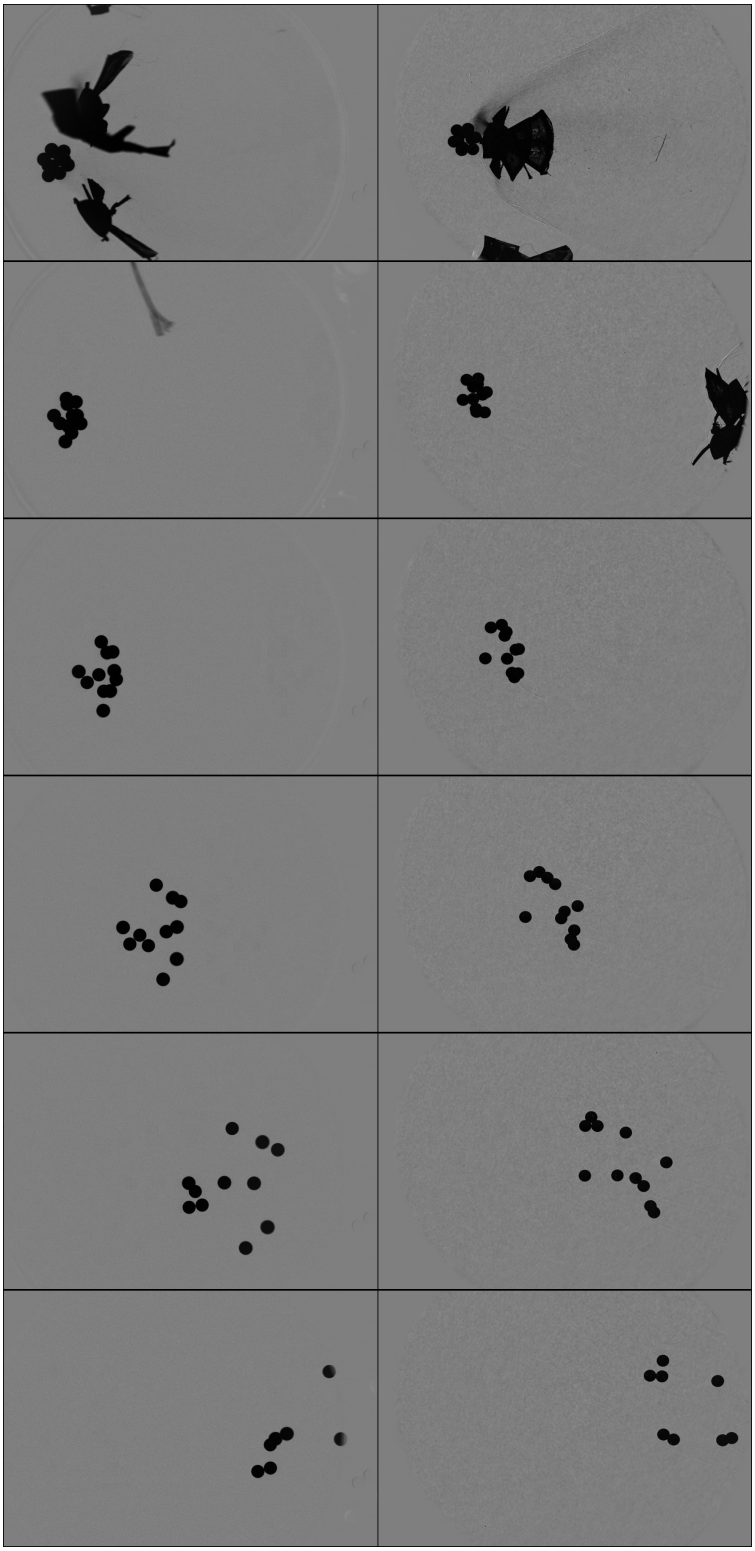

Figure 5.3: Separation sequence of shot 11B. Images taken from below (left column) and the side of the test section (right column) shown in intervals of $1.03\tau_s$ beginning at $t' = 1.58$

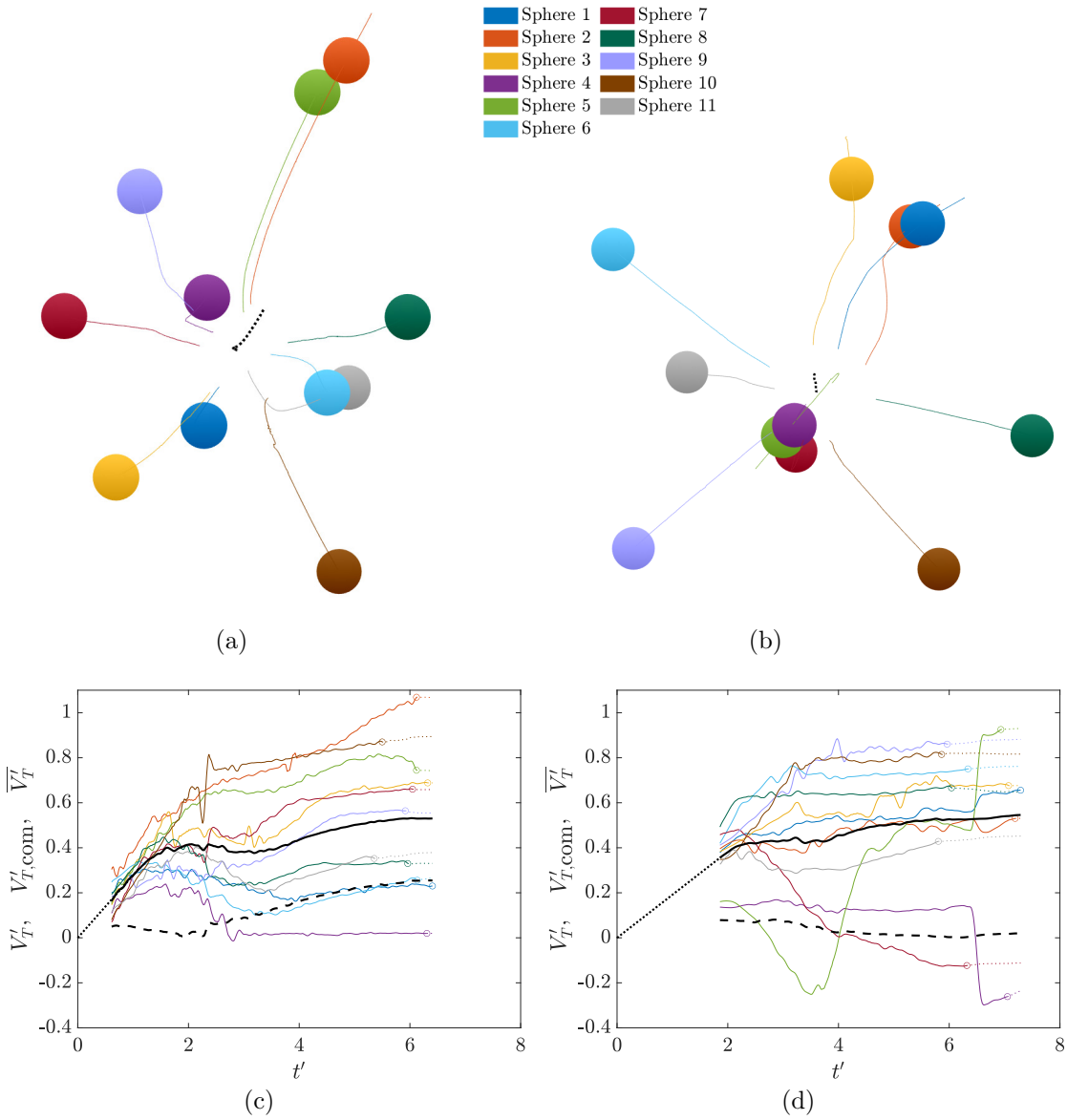

Figure 5.4: Downstream projection of sphere trajectories for shots (a) 11A and (b) 11B with center-of-mass path included in dotted black and instantaneous sphere positions provided at $t' = 5.63$ and $t' = 6.26$, respectively. Also, lateral separation velocities (colored solid), as well as center-of-mass offset (dashed black) and collective lateral velocity (solid black) with extrapolations to t_0' (dotted black), for (c) 11A and (d) 11B.

The details of each cluster's repulsion history (given in Figures 5.4(c) and 5.4(d)), however, reveal important differences in the means by which such values were obtained. In Shot 11A, we see that the lateral velocities of all bodies increase uniformly until $t' = 2$, through which point every sphere maintains contact with its immediate neighbor. Despite the reduction in V_T' manifested by some spheres, the collective lateral velocity continues to rise, peaking at $t' = 2.5$ and then remaining approximately constant for another $1.5\tau_s$. Based on the reduced mutual lift associated with the $\overline{V_T'}$ plateau at 0.4, we thus estimate a primary separation duration of $2.5\tau_s$. At the conclusion of this stage, the cluster has expanded laterally by a factor of 1.7. After $t' = 2.5$, the sphere motions are dominated by the subcluster interactions typical of the secondary separation stage, with five distinct subclusters (one of which comprises three spheres) emerging from the expanding agglomeration. Three of these assemblies form lifting bodies (as in Section 4.1) oriented towards the center of mass of the system, which is likely responsible for the sharp deceleration and subsequent minor dip in $\overline{V_T'}$. These inwardly directed subclusters, featuring trailing spheres that quickly roll upstream, cease contact after only a brief spell of modified transverse motion, and have all separated aerodynamically by $t' = 5$.

Nevertheless, one outwardly directed subcluster (spheres 2 and 5 at the top of Figure 5.4(a)) survives the incipient stages of secondary separation and achieves a prolonged state of lifting. The pair ceases surface contact at $t' = 5.1$ and continues to accrue lateral momentum before exiting the viewing volume at $t' = 6.2$. Over the course of their paired travel (starting from $t' = 2.1$), their global frame center-of-mass velocity is more than doubled, consequently shifting the total center-of-mass

velocity by 0.25 and increasing the collective lateral velocity of the cluster by 40% to a value of 0.53. Furthermore, the two spheres would appear sharply removed from the remainder of the cluster: if we consider a velocity reference point determined by the center-of-mass of 'core' spheres in the cluster, the resultant V_T' values of 0.94 and 1.27 for the pair, compared with a maximum (mean) of 0.72 (0.4) for the rest of the cluster, would register them as pronounced outliers in a strewn field. In addition to this pair, another, composed of the upstream sphere 6 and sphere 11 in its wake, is seemingly on course for collision beyond the test section and may affect the terminal cluster properties, but otherwise the remaining bodies are aerodynamically independent. Overall, shot 11A demonstrates both the elevated importance of the primary separation regime for more populous clusters and the enduring influence of subcluster interactions.

The trajectories of shot 11B, on the other hand, are much less marked by contact pairs than by wake entrainment and subsequent sphere collisions. The initial cluster arrangement in this experiment features one sphere (4) considerably further upstream than the rest and seems to dominate the dynamics of all nearby bodies. The lateral velocities of shot 11B in Figure 5.4(d), for instance, exhibit much different characteristics than 11A as a result of the leading sphere. The primary separation phase, which continues until $t' = 2.5$ as judged by the collective lateral velocity, indicates that spheres 5 and 7 experience modest amounts of initial repulsion before encountering attractive forces in the wake region of the principal sphere, shown slightly below center in Figure 5.4(b). The majority of bodies are more severely repulsed than those in 11A, achieving a mean lateral velocity of 0.49

by the end of primary separation. Consultation with the computed profile of the shock generated by the leader at $t' = 2.5$ reveals its intersection with five spheres, which seems to indicate that shock impingement enabled by the presence of a well-defined upstream body is responsible for the augmented separation of spheres not entrained in its wake.

One prominent aspect of the lateral velocities of shot 11B is the appearance of pronounced steps at $t' = 6.4$ in the profiles of the leading sphere (4) and one entrained in its wake (5). From the trajectories of these spheres, it is clear that they collide precisely at the moment of the velocity discontinuities, which facilitates the conversion of momentum from the streamwise to the lateral direction. Sphere 5 is deflected away from the center-of-mass, whereupon it directly achieves the highest lateral velocity in the cluster (0.93), although its position towards the core of the swarm in Figure 5.4(b) seemingly belies this observation. Sphere 4 is instead directed towards the center of the cluster with $V_T' = -0.3$, although one would expect its velocity to rise beyond the absolute value of this post-collision measurement following its closest approach to the center-of-mass. Despite the notable jumps in individual lateral velocities, the collective lateral velocity seemingly remains unaffected by the collision; however, assuming laterally inertial trajectories for all other bodies, the reversal of sphere 4's transverse velocity should account for an increase in $\overline{V_T'}$ of $\sim$0.05.

In general, the effect of collisions on the collective lateral velocity would be expected to depend nonlinearly on its severity: on one end of the spectrum, a gentle collision can result in paired lifting arrangements (as in shots 4B and 11A), while

an energetic collision can instantaneously enhance V_T' significantly (as in shot 8A), leaving an intermediate range in which collisions may be less important. Indeed, the red and yellow spheres in the upper right of Figure 5.4(b) suffer a collision of modest magnitude (streamwise approach velocity of 0.22) at $t' = 4.3$ that is barely perceptible in their lateral velocity profiles. Furthermore, the overall velocity increase would be expected to be highly sensitive to direction of collision-induced velocity change: keeping in mind that the center of mass of a colliding pair remains fixed in co-moving coordinates, a collision aligned with the sector between the total and local centers-of-mass would yield no lateral velocity increase (provided neither pre- nor post-collision V_T' values are negative), whereas a collision perpendicular to the same axis would add to the each sphere's lateral velocity a factor of $\sqrt{V_{T,\perp}'^2 + V_{T,0}'^2} - V_{T,0}$, where $V_{T,\perp}'$ denotes the perpendicular velocity added and $V_{T,0}'$ the velocity prior to collision. Despite the impressive scale of the collision-induced velocity jumps in shot 11B, their contribution to $\overline{V_T'}$ ($\sim$10%, extrapolated) is reduced from shot 8A, wherein the collisions constitute an average rise of 18%; this signifies the diminished impact of secondary interactions in more populous clusters.

5.3 Thirteen-Sphere Simulation Survey

Thus far, all clusters examined have been constructed such that every sphere has been partly exposed to the external flowfield. For close-packed clusters with thirteen or more spheres, however, at least one body must be located wholly on the interior (Huang and Yu, 2012), which may fundamentally alter the separation me-

chanics. Therefore, we now advance to a population of thirteen spheres — the next highest population after four with quasi-spherical face-centered cubic structure — and, as in the other computational surveys (see Sections 4.1 and 4.3), we employ the AMROC-DYNA3D suite to simulate the separation procedure of a thirteen-sphere cluster for a large selection of initial orientations. The base geometry is established by constructing a face-centered-cubic lattice outwards from a single central body, with the orientation of the lattice chosen such that a group of seven spheres forms a honeycomb-like pattern along the xy-plane with one vertex pointed directly upstream. We then vary the pitch and yaw of the cluster about the central body according to two distinct criteria: one half of the survey was selected from equally spaced points in the reduced parameter space of Section 4.3, while the remaining simulation attitudes were randomly sampled from a uniform distribution. Figure 5.5 gives a schematic of the base thirteen-sphere cluster configuration and geometric definitions. We note that spheres often exited the chosen computational fluid domain before the simulation had concluded, which prevents precise characterization of all terminal trajectories. While these bodies are occasionally still undergoing aerodynamic interactions, the majority of the cluster's lateral momentum has already been attained, so any marginal increases which would be gained downstream of the computational domain are of lesser concern overall. All pertinent simulation details can be found in Section 3.4.

First, to elucidate some of the separation behaviors characteristic of thirteen-sphere clusters, we present the results of two selected simulations. First, we analyze the trajectories and forces of spheres originating from a cluster rotated 136.8° in

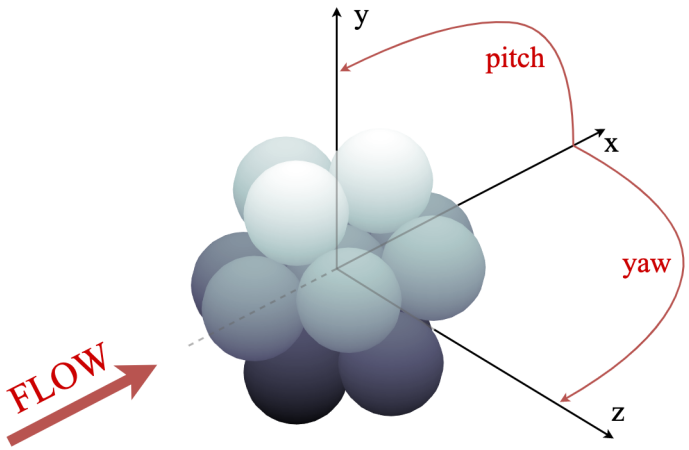

Figure 5.5: Rendering of thirteen-sphere cluster geometry with principal attitude shown.

pitch and $-141.1°$ in yaw from zero-incidence. From Figure 5.6, this configuration is highly blunted, with the most upstream four spheres producing a plane lying nearly normal to the primary axis. An additional five spheres partly exposed to the freestream form a plane behind the foremost layer, while four more are completely shielded further downstream. At the moment of sphere release, a common bow shock appears to encompass the entire cluster, with little evidence of shock impingement, and high inboard pressures occur on the surfaces of the upstream layer. The central body is likewise subjected to the high-pressure streamlines, but, owing to the symmetry of the cluster, these forces are predominately directed streamwise. As the cluster begins to separation, the upstream spheres are repelled under constant lateral forces ($C_T \sim 0.8$), separating enough to allow the shocked inflow to influence the motions of the initially shielded bodies, whose lateral force coefficients rise at $t' \sim 0.3$.

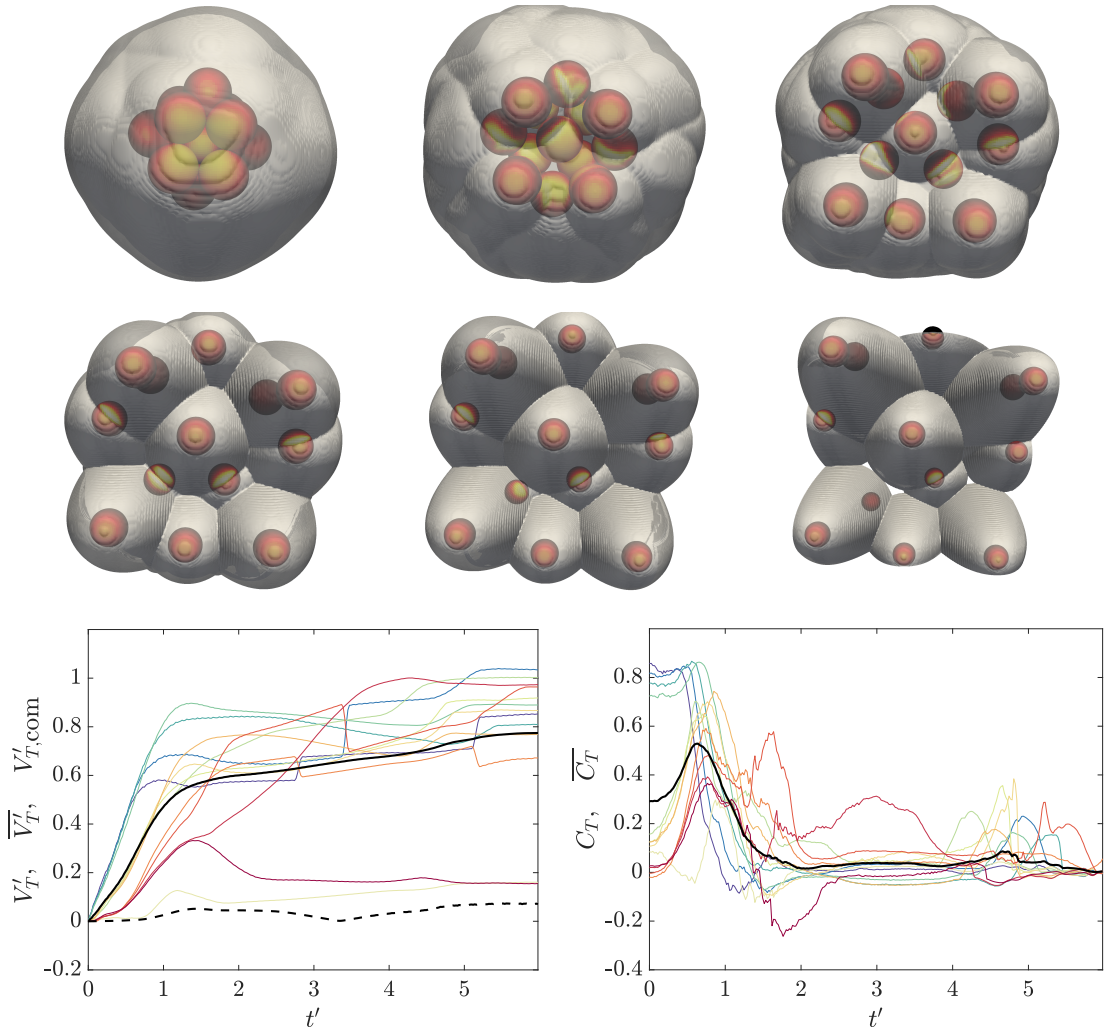

Figure 5.6: Downstream-projected trajectories of thirteen-body cluster at 136.8° pitch and 141.1° yaw, with spheres colored by surface pressure and translucent bow shocks extracted from pseudo-schlieren. Images shown in increments of $0.83\tau_s$ (1.67 ms).

By $t' = 0.7$ (immediately preceding frame 2), the internal mass flow rate ostensibly increases enough for the cluster to ingest the common bow shock, leading to its collapse into an intersecting set of bow shocks and the subsequent loss of lateral force on the upstream layer. As in frame 2 of the visualization, the ingested shock structure yields a series of impingements and reflections that propagate to all downstream bodies in the cluster (even those wholly eclipsed by upstream spheres), evident in the C_T maxima near $t' = 0.8$. This complex series of shocks is short-lived, however, as further division into independent shock systems progresses with increasing sphere spacing. The mean lateral force coefficient thus diminishes, reaching a minimum at $t' = 2$ and signifying the termination of the primary phase. At this point, the collective lateral velocity reaches a value of 0.60, and the most expelled spheres have originated from the upstream layer. The secondary phase begins between frames 3 and 4, which is marked by a more limited set of impinging shock interactions and the commencement of entrainment–collision sequences, manifest in the lateral velocity profiles of several bodies. These interactions all proceed in a manner consistent with expectations, that is, according to kinematics in the reference frame of the leading body of a given subcluster. Indeed, the computational visualizations of frames 5 and 6 reinforce the notion of independent subclusters bounded each by their own leader's bow shock. The collective lateral velocity rises to a terminal value of 0.77, a 28% increase from the end of primary separation, and the lateral center-of-mass velocity, 0.07, is only slightly offset from the primary axis. Overall, the separation of the initially blunt 136.8°-pitch/−141.1°-yaw cluster demonstrates the repulsive potential of an ingested shock structure, which itself forms a complex system of

impingements, reflections, and intersections during the primary separation phase.

The second representative simulation considers a much more slender geometry, oriented at $-0.1°$-pitch/$8.6°$-yaw to the freestream and displayed in snapshots in the uppermost panels of Figure 5.7. Here, a lone upstream sphere generates a bow shock that impinges on six downstream bodies, leaving an additional six bodies completely shielded from severe pressure loading. In contrast to the narrow bands of elevated pressure observed in more isolated shock impingement environments, broader regions of high pressure are apparent, resulting from the subsonic flow following sets of terminal normal shocks (see Figure 4.2, e.g., for a similar instance of this scenario). At the simulation's start, five of the exposed bodies exhibit significant lateral force coefficients — ~ 0.7 on average — while the remainder are subjected to modest aerodynamic repulsion. Inspection of the lateral velocity and force profiles reveals a discrepancy in the motions of three bodies (lines colored red); despite experiencing pressure loading substantially less than the mean through $t' \sim 0.5$, these spheres are expelled with speeds comparable to the collective lateral velocity, indicating that mechanical contact contributes to the cluster's break up. As in the previous case considered, the forces on the windward spheres diminish rapidly, reverting to the cluster mean by the frame 2. The transverse separation dynamics of the leeward bodies, on the other hand, is more complex, with shock impingement on select bodies commencing at $t' \sim 0.5$, subsiding thereafter, and reemerging at $t' \sim 2.0$, while other spheres remain in the aerodynamic shadow of the leading body for extended periods. After its secondary maximum near $t' = 1.7$, the mean lateral force coefficient vanishes at $t' = 2.4$, at which point the collective lateral velocity

reaches 0.57 and the secondary separation phase begins. During the secondary phase, a lifting pair (located WSW in frames 4 and 5 of Figure 5.7) represents the second-most ejected bodies of the cluster, after the sphere positioned within a triple-shock intersection towards the NW. Meanwhile, the cluster core persists through the simulation's end and remains to be disrupted by collisions. As a result of this ongoing interaction, the collective lateral velocity does not approach a constant value and is expected to exceed its final reading of 0.79, the highest recorded in the present survey.

Given the amplified importance of the primary separation phase in the separation of thirteen-sphere clusters, we find it prudent to examine the duration of and spatial expansion caused by its characteristic mutual repulsion. The concept of fragment decoupling timescales and radii, introduced by Passey and Melosh (1980), is not new, and its relevance to the primary separation statistics of the present work is reinforced by these historical explorations of the problem. To estimate the duration of primary separation in a given coupled simulation, we search for minima in the mean lateral force coefficient, $\overline{C_T}$, and select the earliest minimum for which the local value of $\overline{C_T}$ does not exceed 10% of its maximum. We note that a point of zero lateral force may instead be chosen if it occurs sooner than the identified minimum. Next, we compute the radius of sphere circumscribing all bodies at the selected time, which yields the magnitude of spatial expansion that enables aerodynamic decoupling.

Histograms of the primary separation timescale, t_p, and the decoupling radius, r_p, are presented in Figure 5.8. The resulting primary timescale values are not

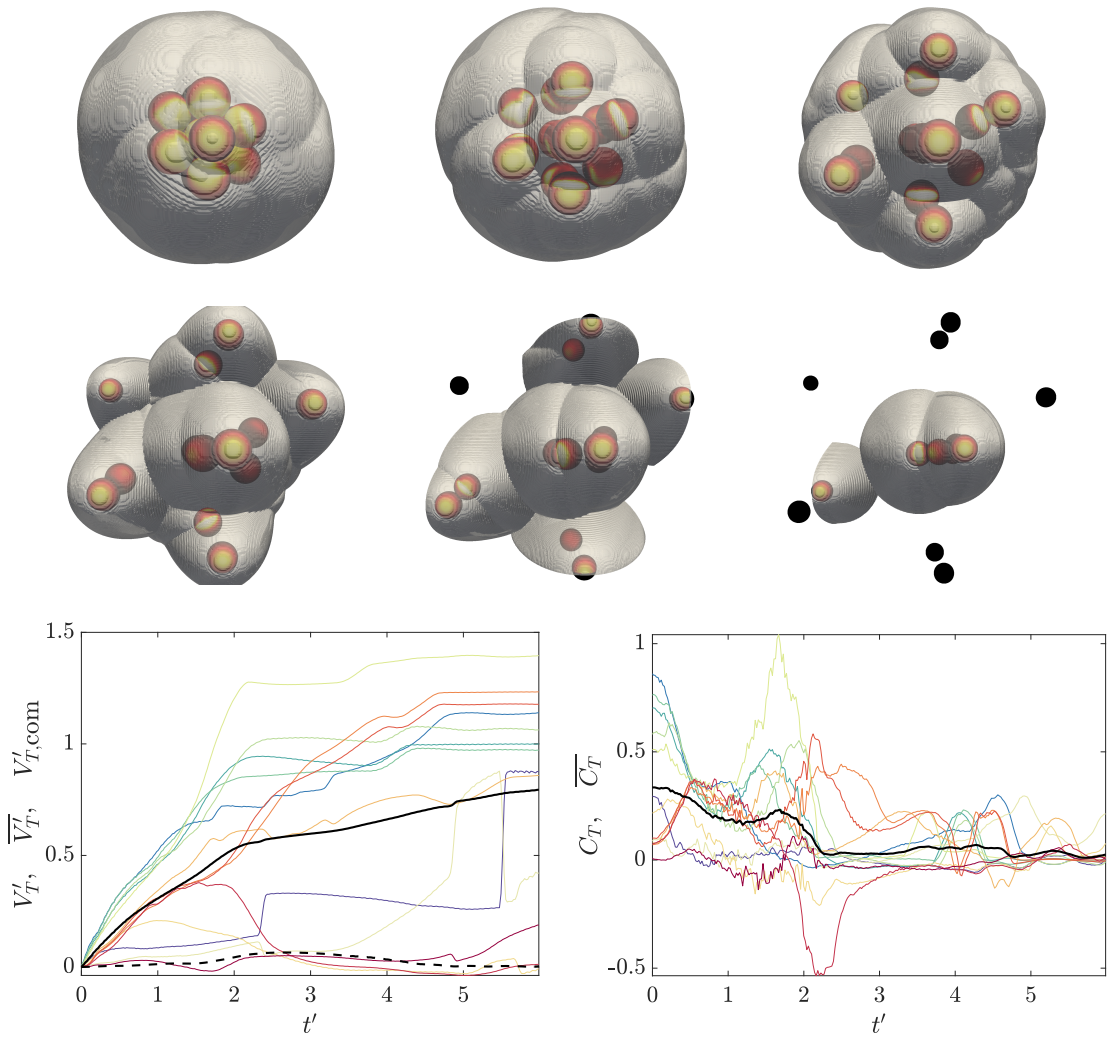

Figure 5.7: Downstream-projected trajectories of thirteen-body cluster at $-0.1°$ pitch and $8.6°$ yaw, with spheres colored by surface pressure and translucent bow shocks extracted from pseudo-schlieren. Images shown in increments of τ_s (2.0 ms).

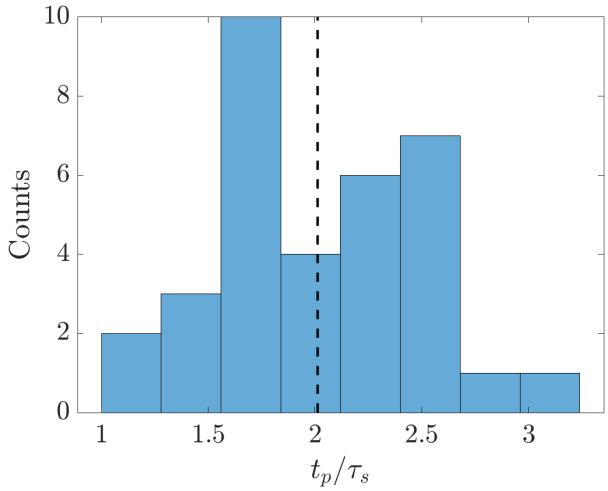

(a)

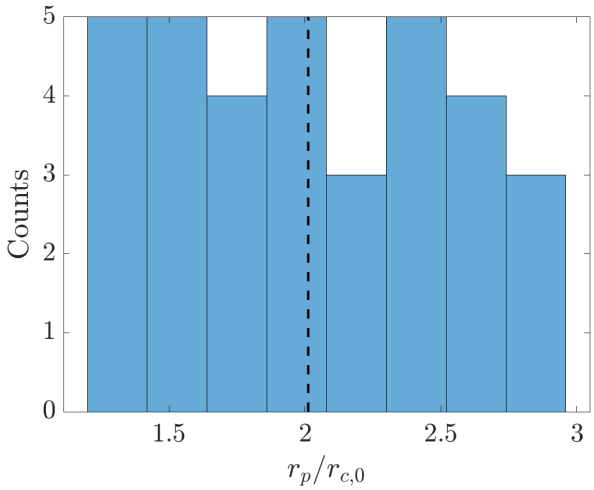

(b)

Figure 5.8: (a) Primary separation duration and (b) resulting radius for thirteen-sphere simulation survey.

well-characterized by familiar distribution curves; rather, we observe a prominent maximum at $\sim 1.7\tau_s$ and, with the exception of this peak, a monotonic increase in frequency from τ_s to $2.6\tau_s$, after which point long-duration interactions become rare. While the cause of the $\sim 1.7\tau_s$ peak is undetermined, it likely follows from geometric idiosyncrasies in the construction of the close-packed clusters. Additionally, the mean primary timescale of $2\tau_s$ represents a decrease from the eight-sphere experiments, in which primary separation lasts, on average, for $\sim 2.3\tau_s$. The decoupling radius, conversely, shows a nearly uniform frequency distribution, with a slight negative dependency detected. Furthermore, the extracted mean r_p of $2r_c$ is commensurate with the spatial extent of the eight-sphere clusters at the termination of the primary phase, possibly suggesting the insensitivity of this parameter to cluster composition. Interestingly, we find no evidence of a frequency maximum despite the prominence of the $1.7\tau_s$ peak in the primary timescale distribution.

From the visualizations of Figures 5.6 and 5.7, the intricate system of shocks driving the primary separation of thirteen-sphere clusters appears to be chaotic in nature and subject to the finer details of relative sphere motions. However, we found in Section 4.3 that the terminal lateral velocities of the four-sphere cluster constituents correlated strongly with their initial polar angles, and we endeavor to assess whether a similar statistically significant relationship exists for more populous clusters. Ignoring for the moment the kinematics of the central sphere, we bin all spheres in the survey by initial polar angle and calculate their transverse velocities through the termination of primary separation, which reveals emergent behaviors in each angular bin (see Figure 5.9(a)). In the 0°–15° group, the limited radial

range inhibits the generation of high-inboard-pressure regions and yields spheres that are gently pushed laterally and become inertial shortly after release. This bin largely consists of upstream bodies that shape later secondary interactions and, as such, tend to experience collisions near the phase transition point. Still relatively far upstream, the spheres of the 15°–30° bin are also subjected to temporally limited repulsion, but their increased radial positioning grants them additional lateral momentum. Moving toward higher polar angles, 30°–45° appears to be exposed to greater forces over a longer duration, resulting in lateral velocities of ~ 0.5.

The bin containing spheres located at θ_0 between 45° and 60° exhibits some degree of bi-modality in its lateral velocity profiles: both sudden and delayed repulsion are evident, although the bodies tend to approach similar velocities. For reference, this and the previous group contain the upstream spheres described in the first example simulation. In contrast to the smaller-angle bins, the velocity rise of 60°–75° is characterized by the presence of several inflection points indicating highly unsteady aerodynamics. As this bin is composed of external shock-receiving bodies (such as those in the second example simulation), the applied forces are highly sensitive to the motions of the upstream, shock-generating spheres. Bin 75°–90° contains highly variable trajectories that encompass a range of terminal behaviors including shock surfing, wake entrainment, and aerodynamic independence. Advancing to the leeward side of the cluster marks the transition to dynamics dominated by internal shock impingement following collapse of an initial bow shock. Indeed, the delayed onset of repulsion over 90°–105° is indicative of this particular phenomenon, although the final trajectories are marked by both independence and entrainment.

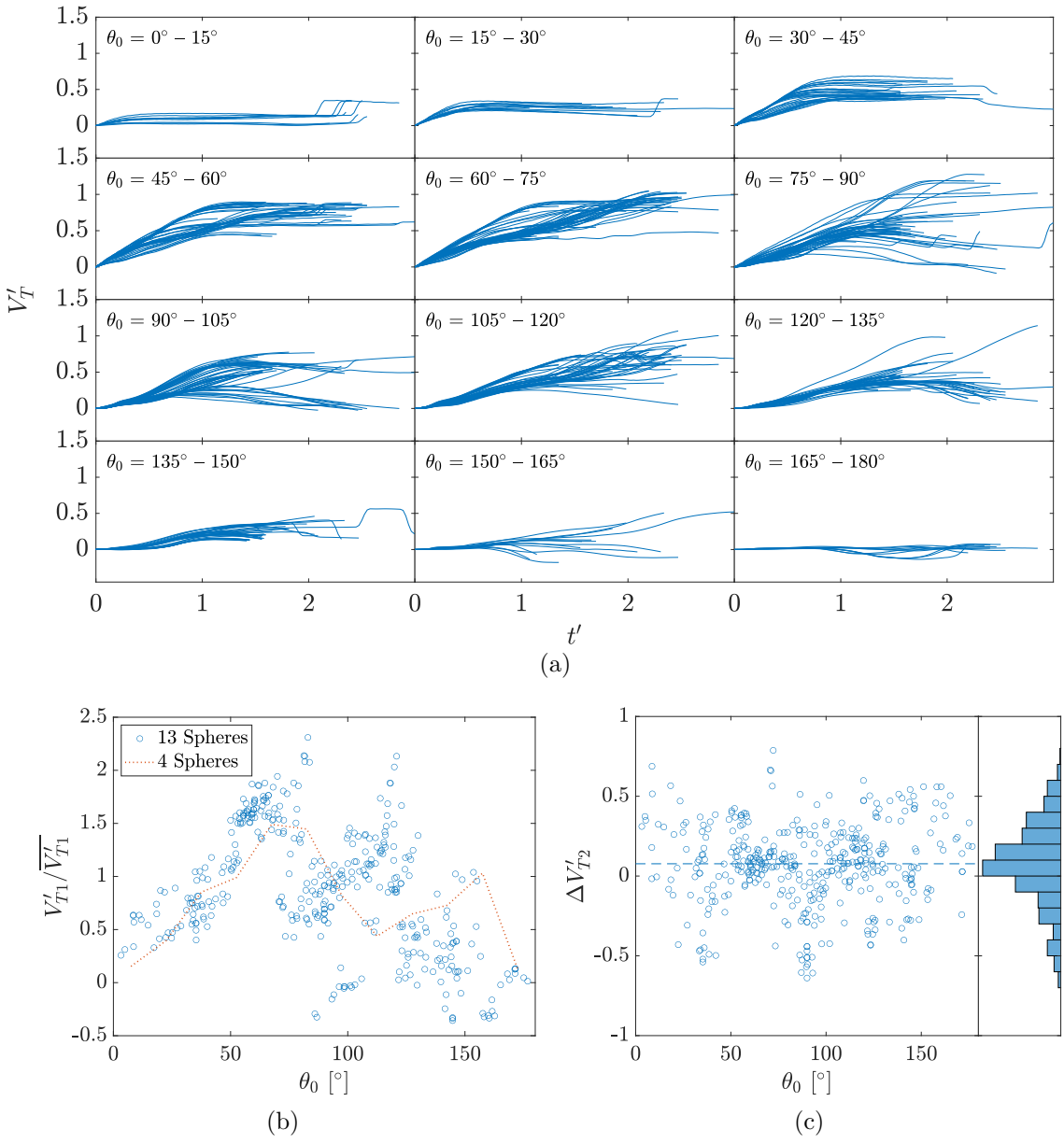

Figure 5.9: (a) Lateral velocity timeseries during primary phase binned by initial polar angle and (b) final primary-phase lateral velocity with initial polar angle, normalized by survey mean and compared with four-sphere survey correlation. (c) Lateral velocity accrued during secondary separation phase, with mean value denoted by dashed line and frequency distribution on right.

Lateral velocities at 105°–120° appear to increase throughout the primary phase, suggesting shock-surfing behavior, while spheres at 120°–135° adhere to the same tendency until $1.5\tau_s$, at which point the lateral forces seem to diminish considerably. Finally, at the rear of the formation (135°–180°), aerodynamically shielded spheres near the system's primary axis experience limited repulsion. In correspondence with the four-sphere computational survey, we again find that the complex aerodynamic phenomena promoting fragment dispersal can surprisingly be reduced to an approximate dependence on each sphere's initial positioning within a cluster.

We now compile the lateral velocities arising at the end of primary separation, V'_{T1}, and, in Figure 5.9(b), investigate the relationship with the initial polar angle of each sphere. For comparative purposes, we scale the these scattered values by the mean lateral velocity of the entire survey (0.55) and additionally include the measurements of each 15°-wide bin from the four-sphere survey of Section 4.3. It is immediately obvious that the sawtooth structure of the earlier velocity/polar-angle correlation is retained, despite the vast differences in the separation characteristics of the two populations. Both the four- and thirteen-sphere clusters exhibit a forward linear regime wherein the degree of expulsion is directly proportional to the initial polar angle of a body. Surprisingly, both datasets appear to reach maxima near 70°, corresponding to those sphere subjected to prolonged shock impingement, but the trends diverge at locations further downstream. For thirteen spheres, a precipitous drop in V'_{T1} occurs at 75°, whereas the four-sphere clusters possess a more gradual decline between 75° and 115°, effectively offsetting the downstream linear regimes by a significant margin. Such discrepancies point to differences in the un-

derlying physics; the downstream linear rise for four bodies (120°–160°) results from the inclination of such spheres to be adopted into a lifting pair arrangement, and, for thirteen spheres, the 75°–120° ascent represents the influence of internal shock impingements following collapse of the initial common bow shock. Even further downstream, aerodynamic shielding suppresses separation in both surveys. Thus, the well-defined correlation between initial polar angle and lateral velocity during primary separation may serve as the basis for reduced-order modeling of the fragmentation of arbitrary cluster configurations.

While the statistics of primary separation conform so closely to the various operating mechanisms over all polar angles, secondary separation proves a considerably less-ordered process. From Figure 5.9(c), in which we effectively repeat the above analysis for the secondary phase, the change in lateral velocity due to secondary separation, V'_{T2}, demonstrates no particular correlation with polar angle. The only visible features are the lack of radially inwards velocity changes near 0° and 65°, reflecting the on-axis positioning and severe expulsion, respectively, of spheres in the vicinity of those polar angles. Furthermore, the frequency distribution reduces to a function of approximately Gaussian form, asserting the stochastic nature of this interaction regime. Additionally, the positive mean value of 0.077 is consistent with the reduced impact of secondary separation with larger cluster populations, but the exceptionally large standard deviation (0.25) indicates that any sphere may undergo significant trajectory modifications after primary separation ceases. It is interesting, though not entirely surprising, that the primary phase, which is highly intricate in form, reduces to a tightly correlated relationship, while the secondary

phase, governed by relatively simple flight physics, results in a statistically random process. Given the lack of predictable order characterizing the secondary separation phase, we will, in the subsequent chapters of this work, consider all appreciable separation velocities to proceed from primary separation, upon which the randomness of the secondary phase is superposed.

Having established a clear delineation in resultant kinematics dictated by the distinct separation phases for individual sphere motions, we now turn to bulk cluster quantities and examine their dependence on the geometry's initial attitude. For the current base configuration, the asymmetry index of Equation 4.2 reduces to negligible value of order 10^{-7} (cf. the maximum of 0.32 for four spheres) and appears to exert no influence over cluster dynamics. Instead, we focus exclusively on the bluntness index, which has been slightly redefined to break a degeneracy between faces composed of three and four spheres:

$$B = \frac{1}{2}(\hat{n}_1 \cdot \langle -1, 0, 0 \rangle + \hat{n}_2 \cdot \langle -1, 0, 0 \rangle), \tag{5.1}$$

where unit-normals $\hat{n}_i$ have been sorted by the value of their $\hat{x}$-components. The bluntness index, now based on the orientation of the two most-exposed triangulated faces, varies between values of 0.8 and 1.0, with the sample clusters of Figure 5.10 illustrating the variation in appearance over a range of bluntness indices.

The collective lateral velocity, arguably the most important quantity sought after in this work, has been divided into its post-primary-phase and terminal values in Figure 5.11(a). Weak positive correlations with bluntness are discerned for both

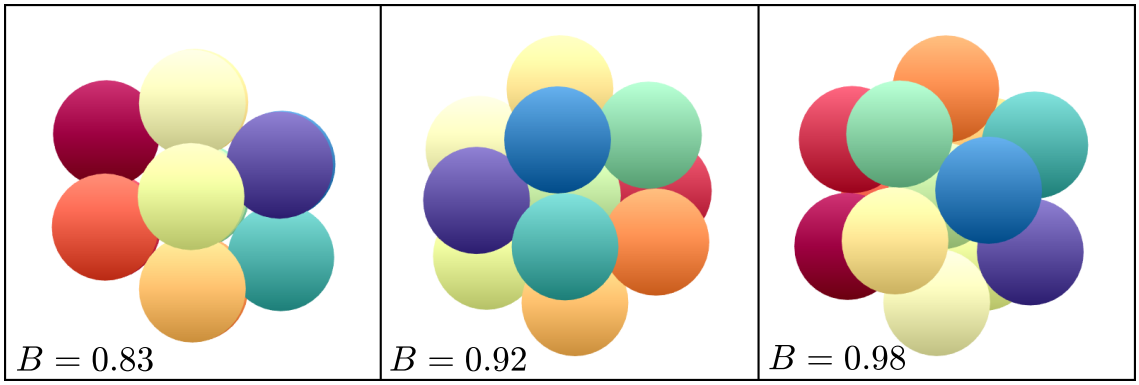

Figure 5.10: Sample clusters illustrating various bluntness indices.

epochs (removing from the terminal fit two outliers with near-zero overall lateral velocity), supporting the notion that an ingested bow shock can more effectively repel shielded bodies in a blunter configuration. The mean primary and terminal V_T' values of 0.474 and 0.551, respectively, are necessarily consistent with the mean secondary velocity enhancement of 0.077 (Figure 5.9(c)), which represents a 16% increase in lateral velocity over the survey. A closer examination of the vertical translation of datapoints reveals that clusters do not adhere to this criterion uniformly, however. While most agglomerations do experience enhanced separation after primary separation ceases, a handful approach near-zero values of $\overline{V_T'}$ due to inwardly directed lifting pairs (and triplets) and aided by rotational symmetries in the affected configurations near $B = 0.8$. While the permanent stability of these contracting clusters is doubtful, especially considering the eventual energetic collisions that may occur, they represent an interesting case in the resistance to separation when oriented bodies are involved, such as may occur in realistic fragmentation events. Overall, the difference between $\overline{V_{T1}'}$ and $\overline{V_{T2}'}$, in fact, possesses a Gaussian profile similar to Figure 5.9(c), albeit truncated at an upper limit of 0.23 and af-

fected by the noted outliers. Projecting these data along the figure abscissa, we find frequency histograms of unfamiliar form. The primary-phase velocities peak strongly at 0.52, whereas the terminal velocities show a strong skewness toward values above 0.55. Thus, we generally observe that the effects of cluster orientation on the collective lateral velocity are comparatively dulled as the agglomeration geometry more closely approximates the spherical form posited by the model problem, although some dependency is discerned. Given that the present population is relatively small, one might expect geometric effects to be entirely negligible for the larger clusters to be discussed in Chapter 6.

While a quantity of lesser overall importance for meteor disruption, the center-of-mass velocity shift can still hold significance for the precise location of a damage ellipse. As above, we plot the dependence of $V'_{T,\mathrm{com}}$ on the cluster's bluntness index for both primary and terminal epochs, with supplementary mean values and frequency histograms. As with the collective lateral velocity, the bluntness index correlates weakly with a cluster's center-of-mass offset for both epochs. This relationship likely follows from the combination of increased ejection of bodies from blunter configurations and the inevitability of subsequent wake entrainment in clusters of this population. The terminal center-of-mass velocity offset, however, shows some notable outliers, one of which occurs at $B = 0.090$ ($V'_{T,\mathrm{com}} = 0.22$) and is the result of an exceptional seven-body subcluster. The survey-wide mean value of $V'_{T,\mathrm{com}}$ rises from 0.058 to 0.083 over the secondary separation phase, constituting a 54% increase, which exceeds that experienced by the collective lateral velocity (16%). This dynamic is consistent with the previous observation that the center-of-

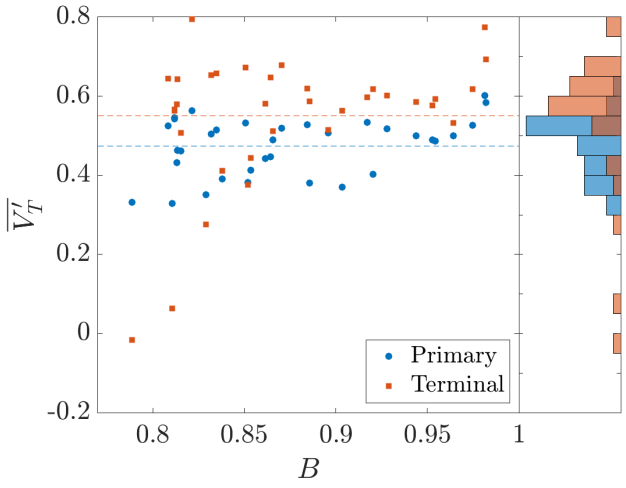

(a)

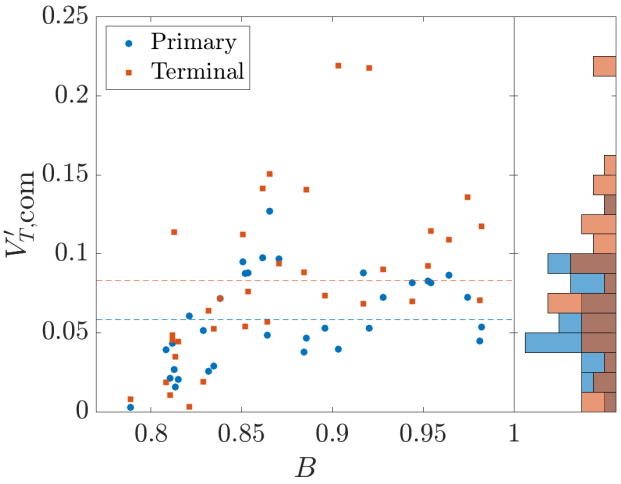

(b)

Figure 5.11: (a) Collective lateral velocity and (b) center-of-mass offset with bluntness index after primary and secondary phases. Frequency distributions of all quantities on right.

mass offset is typically driven by wake entrainment events, a common feature of the secondary phase, wherein massive subclusters draw the center of mass in their direction of propagation. Despite the loose organization of the center-of-mass velocity behaviors, the associated frequency profiles are not readily categorized into recognizable distributions. These incoherent distributions could be suggestive of the lack of statistical convergence in the survey, geometrical constraints of the base thirteen-sphere configuration, or the inherent properties of the center-of-mass motion itself. However, distinguishing between these possibilities is not possible at present. Nevertheless, the reduction in center-of-mass offset from the four-sphere survey (0.083 from 0.13) points to the bulk motion of more populous clusters aligning more closely with primary axis of their pre-fragmented trajectories.

One aspect of thirteen-sphere separation not yet considered is the presence of one body initial located at an internal position coincident with the cluster's center of mass. However, from an inspection of the cluster separation sequences, the central body occupies an important role in the dispersion of fragments, particularly in the secondary phase. Using the new definition of the bluntness index, B, we present the lateral velocity of the central body following both the primary and secondary separation regimes in Figure 5.12. It is immediately clear that the central sphere accrues minimal lateral momentum over the course of the primary phase, which makes sense considering the body's position and the approximate isotropic nature of primary separation. Although a least-squares fit wasn't conducted, a rough correlation during primary separation emerges, with minimal velocity at the bluntness limits and a potential maximum near the midpoint (0.87), while a peak

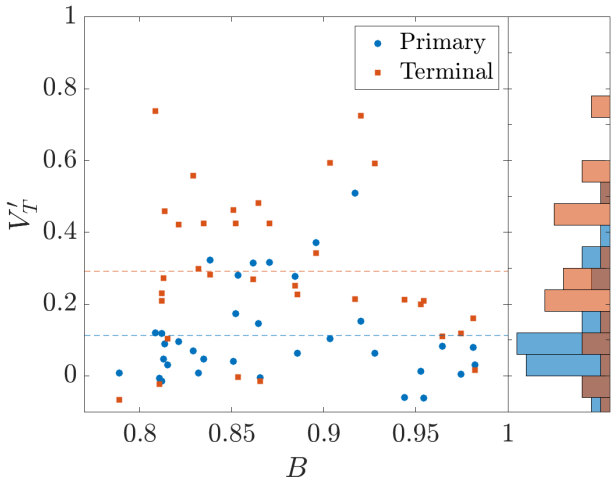

Figure 5.12: Primary and terminal separation velocities of internal spheres with frequency distribution on right.

in the frequency distribution appears to occur near $V_T' = 0.09$. The mean lateral velocity nearly triples between separation stages, rising from a modest value of 0.11 to 0.29, an indication of the sphere's augmented aerodynamic presence in subcluster interactions. The terminal lateral velocities of the central body show no evident dependence on the cluster's bluntness, and the frequency histogram similarly reveals no discernible trends.

In spite of the absence of obvious trends governing the central sphere's separation, its primary-phase separation velocity may serve as an important foundation for improved modeling of sphere trajectories from populous clusters. Because the polar angle correlation of Figure 5.9(b) is derived solely from bodies initially located in the external cluster layer, the dependence on a sphere's radial distance from the center of mass is effectively suppressed. In larger clusters, however, internal bodies can comprise a significant portion of an agglomeration's mass fraction, and this limited analysis effectively sets a benchmark for the separation properties of bodies

located at the very center of a sphere cluster.

Finally, we examine a practical question for risk prediction concerning the magnitude of atmospheric energy deposition during a fragmentation event. To assess the energy deposited by a separating thirteen-sphere cluster, we compute the mean aerodynamic force coefficient over the full survey, which is then equated with the work done on the flow. Thus, Figure 5.13 gives the temporal total force coefficient, $\overline{C_F}$, with standard deviation, as well as the drag coefficient for comparative purposes. The resulting force profiles are rather featureless; in particular, expectations of a dramatic overshoot beyond the nominal drag coefficient (~ 0.9), stemming from the prominent spikes in meteor lightcurves at disruption, do not materialize. Instead, the total forces are mostly due to aerodynamic drag, as opposed to the repulsive action, and remain approximately steady (to within 15%) over the simulated flight duration. The acute increase in radiative flux commonly observed in meteor events must then occur purely as a result of increased surface area following disruption into a greater number of bodies, as opposed to aerodynamic interference effects.

5.4 Conclusions

The separation dynamics of clusters numbering between five and nineteen bodies are characterized by a sharp division into primary and secondary phases, which are governed by mutual repulsion and subcluster interactions, respectively. A pair of experiments with eleven bodies exhibits the prolonged relevance of phenomena such as lifting sphere pairs and collisions, which can contribute to the appearance

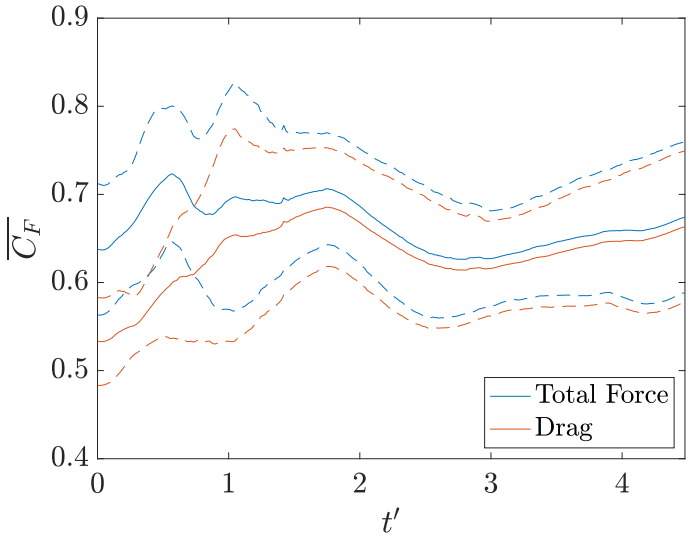

Figure 5.13: Temporal behavior of mean aerodynamic force coefficient as proxy for energy deposition. Dashed lines indicate the standard deviation over time.

of outlying fragments in a strewn field, while the main source of overall separation occurs in the short time following release into the freestream. From an examination of two exemplary thirteen-sphere simulations, the shock structures driving the primary phase are menacingly complex, but we later find that sphere kinematics at the point of phase transition are tightly correlated to the initial polar angle of each body. On the other hand, the comparatively simple physics of the secondary phase yield what appears to be a random normal process. The simulation survey also reinforces the notion that both subcluster interactions and geometric dependencies are of reduced influence in more populous clusters. Overall, the complexity of aerodynamic interactions in intermediate-sized clusters suggests that attempts to predict the exact motions of disrupted fragments are not worthwhile and focus should instead be given to the statistics of sphere kinematics, especially in light of our progression to even more populous clusters.

Chapter 6: Equal Spheres: Populous Clusters and Statistics

This chapter will examine the aerodynamic separation of the most populous equal-sphere clusters tested. Due to the amplified dependence on primary separation, which obfuscates the exact repulsion details, and a general inability to access the initial state of the agglomeration, we will present the findings of clusters numbering between twenty and one-hundred-fifteen bodies differently than those of previous chapters. First, a series of general observations will elucidate characteristics common to all populous clusters. The following segment will evaluate important statistical quantities extracted from all cluster populations, with discussion of the practical implications for meteor entry modeling.

At this point, we would like to remind the reader of the two suspension positions utilized in the free-flight experiments, one with the cluster initially visible within the field-of-view and one in an obscured location further upstream. As significant silhouette overlap renders body tracking unfeasible near the beginning of an test, most populous-cluster experiments were conducted with the spheres placed in the forward position, which promotes aerodynamic independence towards the end of visible flight. The downstream suspension position, on the other hand, allows for visualization and reduced-fidelity analysis of the opening stages of separation. The

data from both suspension positions will be used in a complementary manner to yield information about terminal kinematics and the initial repulsion experienced by the spheres.

6.1 General Observations

Before delving into the more detailed aspects of populous-cluster separation, we will present a qualitative overview of traits shared by all clusters considered. Figure 6.1, featuring images from shot 115D, visualizes the separation of spheres released from the downstream suspension position, with a schlieren apparatus in place of shadowgraph to emphasize flowfield features. In the first frame, the initial cluster, by this point slightly compressed in the streamwise direction, is exposed to the freestream flow after shell separation and establishes an encompassing bow shock; close inspection of the schlieren near the stagnation region reveals a short shock-standoff distance and a structure determined by the composition of smaller-scale bow shocks generated by the forward spheres. Much of the cluster remains in close proximity towards the start of the test, continuing to contract in the streamwise direction and expand laterally. Qualitatively, by the second frame, the conglomeration seems to achieve a somewhat triangular shape when viewed in projection, corresponding to a highly inclined cone in three dimensions. Such an arrangement might arise if the spheres near the cluster's lateral edge experience a larger streamwise pressure differential than those towards the center. Indeed, following the loss of surface contact, the higher sphere density at the cluster's core would be expected to

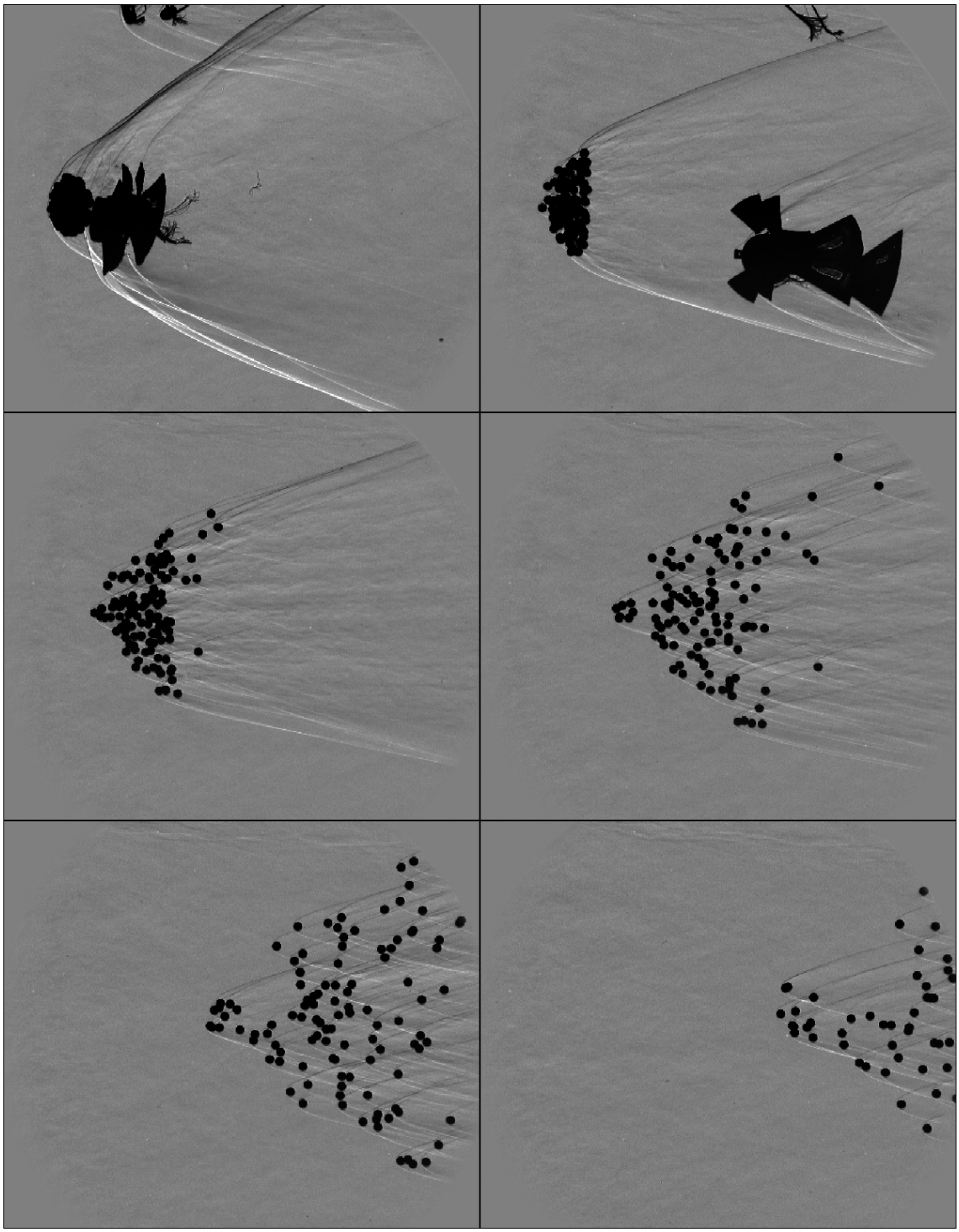

Figure 6.1: Schlieren images showing the separation sequence of shot 115D in increments of $0.84\tau_s$ (1.09 ms).

increase the base pressure on the leading bodies, while the presence of shock impingements further outboard would also contribute to the drag disparity. In the third and fourth frames, inter-sphere shock-waves begin to develop, possibly signaling the onset of the subclustering separation regime, and streamwise acceleration seems to overtake the initially acute lateral acceleration as the dominant kinematic trend. As the experiment progresses, the bodies separate further and exit the viewing volume, but a dense grouping of spheres persists near the remnants of the cluster's core.

Taking the observations from the above one-hundred-fifteen-sphere test as the expected separation procedure for populous equal-sphere clusters, we now work backwards to less populous agglomerations for comparison with this presumed standard. The shadowgraph visualization of fifty-two bodies separating from the downstream suspension position (Figure 6.2(a)) reveals a similar flattening of the cluster, arising from simultaneous streamwise compression and lateral expansion, although no evidence of extended shock surfing arises. Moreover, the ellipsoidal morphology transitions to a form of roughly triangular shape, as in 115D, though more highly inclined to the freestream, which may indicate differences in the separation timescales. Also, consultation of the video recording confirms that collisions assist in dispersing the core of upstream fragments, establishing that the qualitative trends of shot 52E are consistent with our understanding of populous-cluster separation. Shot 27E, on the other hand, demonstrates attributes that deviate from this model, as is shown in Figure 6.2(b). The cluster achieves neither the expected ellipsoidal appearance nor the triangular profile observed in more populous scenarios, instead maintaining a blunt forefront until frame 5 of the visualization. Collisions do occur

in the shadowgraph recording, aiding in the eventual dispersal of the dense core, but overall characteristics are not exactly reminiscent of the separation behaviors of more populous clusters, indicating that a transition may arise somewhere between twenty-seven and fifty-two equal bodies.

6.1.1 Primary Separation Attributes

Reviewing the thirteen-sphere simulations of Chapter 5, we found that primary separation was spurred by the impingement of intricate shock structures on exposed spheres downstream of the shock-generating body. Progressing to more populous clusters, we might expect a transition from composite shocks encompassing the cluster to a comparatively smoother morphology showing a reduction in impingement. Thus, we qualitatively investigate the results of a single simulation of fifty-seven spheres in Figure 6.3(a), which displays in increments of $0.28\tau_s$ the surface pressures (colored such that red corresponds to the freestream Pitot pressure and yellow/white anything higher) and computed shock profile of the separating cluster in downstream projection. The simulated cluster, composed of spheres arranged into a hexagonal close-packed lattice, represents a dense grouping of bodies with streamwise-aligned columns, which render it fairly resistant to separation, and is rotated to the most slender orientation possible, with a single sphere upstream of the rest. Immediately obvious in the surface pressure distributions of the first frame are numerous bands of pressure elevated beyond the stagnation value, corresponding to the locations of shock impingement on the spheres and noted by Edney (1968) as

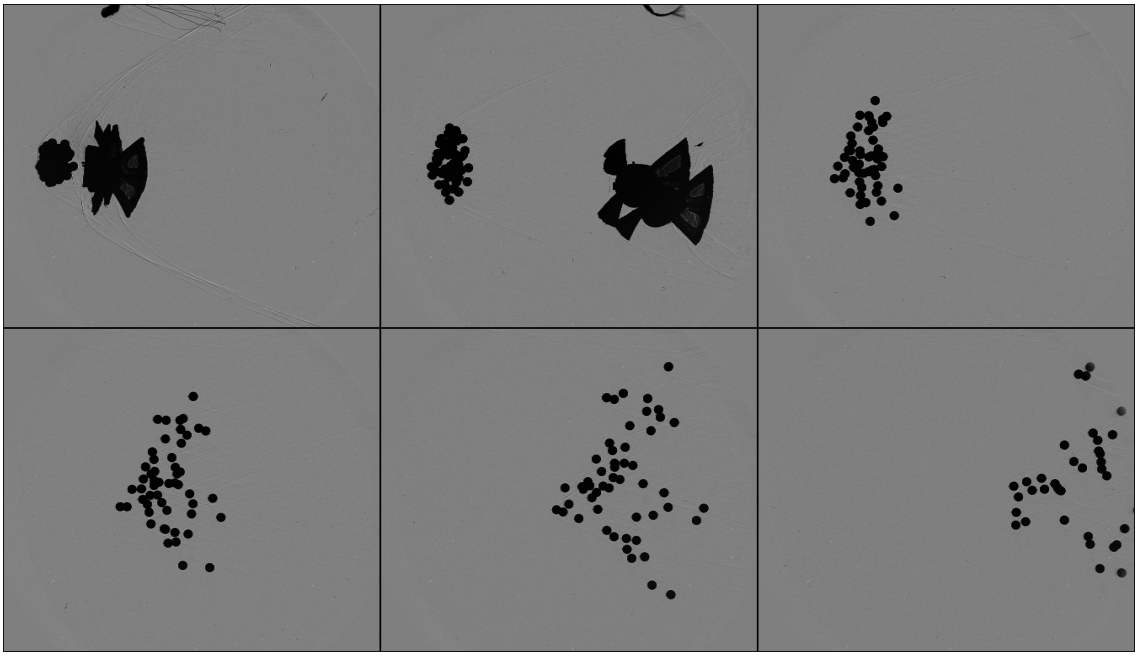

(a)

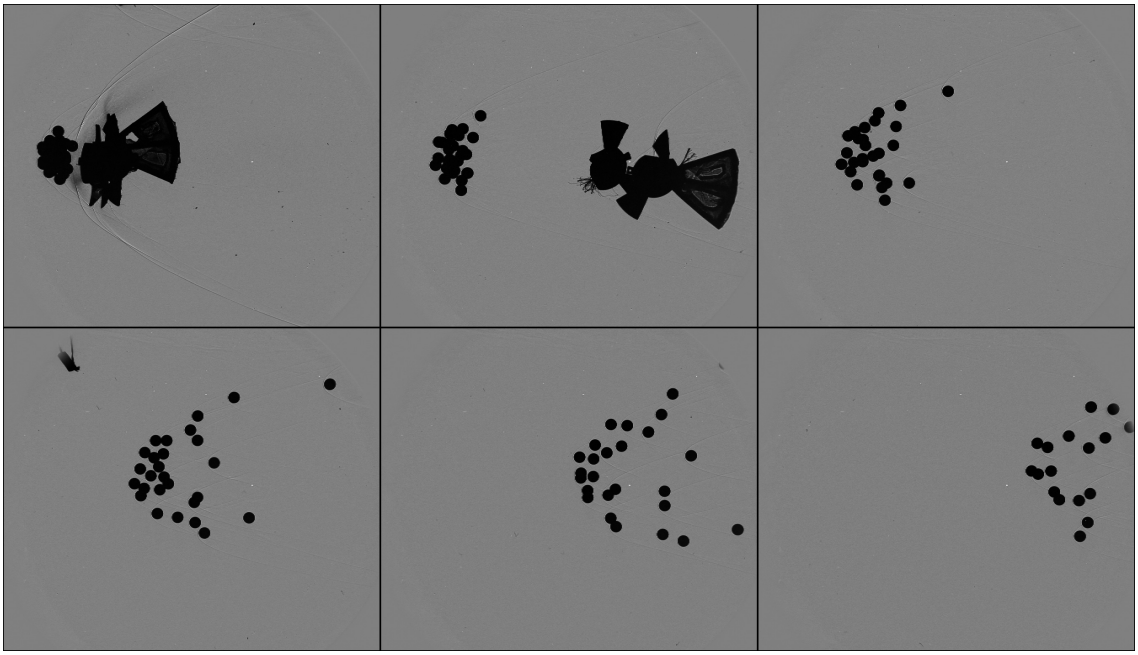

(b)

Figure 6.2: Shadowgraph sequences of shots (a) 52E and (b) 27E, with images shown in increments of $0.81\tau_s$ (1.14 ms) and $0.87\tau_s$ (1.23 ms), respectively.

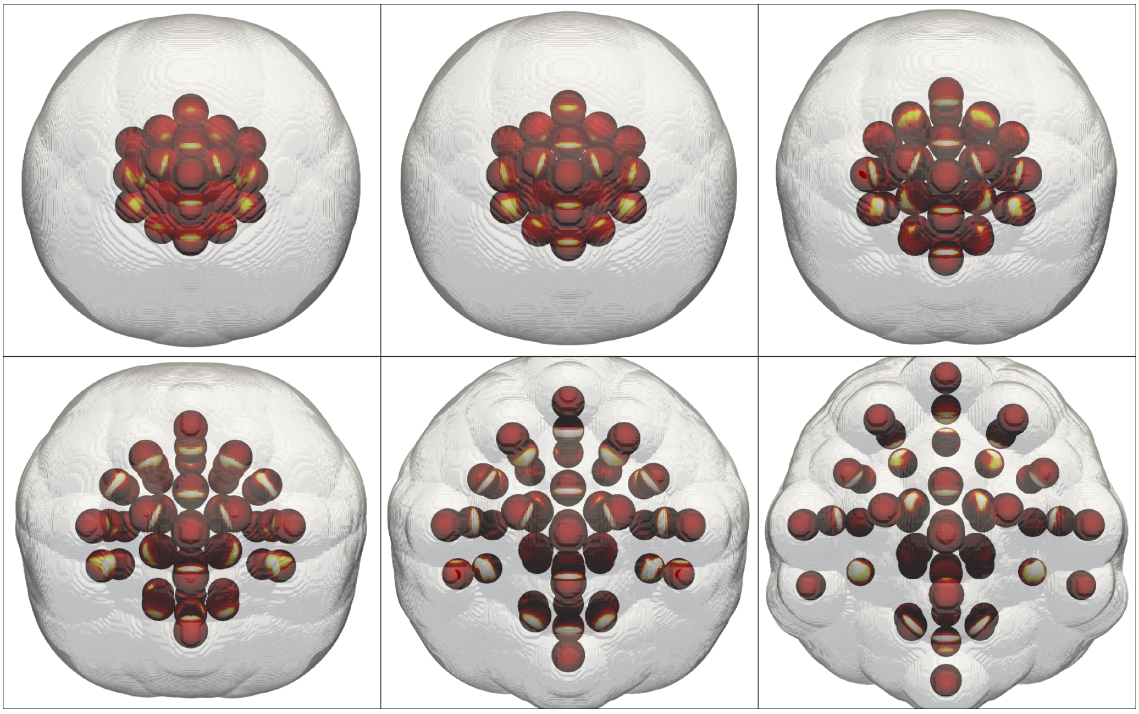

(a)

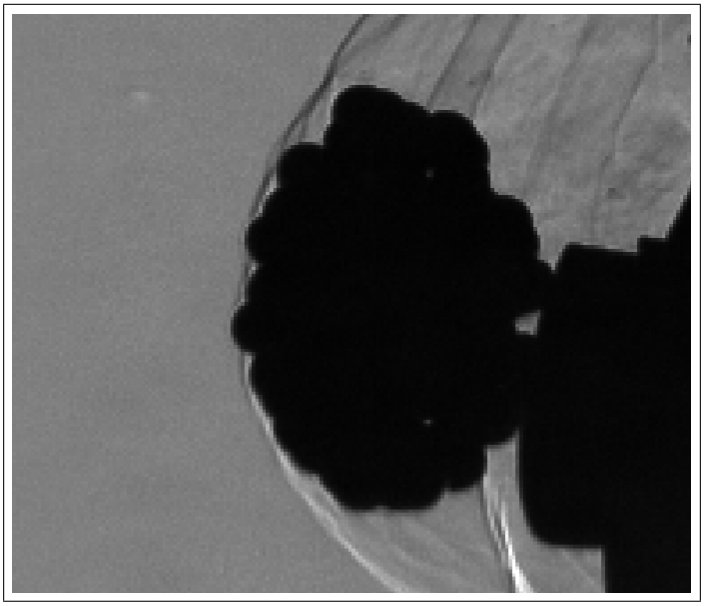

(b)

Figure 6.3: (a) Downstream-projected surface pressure and computed shock structures of a fifty-seven-sphere simulation in $0.28\tau_s$ increments and (b) zoomed schlieren image of shot 115D displaying bounding shock structure.

a standard feature of shock-shock interactions. Lateral expansion begins gradually, with little movement discernible between frames 1 and 2; pronounced acceleration arises later, particularly once the ingested shock amplifies the pressures experienced by the second and third sphere layers (from frame 4 onwards). The strength of the elevated pressure bands grows as the simulation progresses, which seems to arise from the increased streamwise separation between the receiver and generator bodies, decreasing both the wave angle and corresponding stagnation pressure loss. Additionally, the spatial extent of elevated pressure on a sphere's face is enlarged at later times, as evidenced by broad areas of high pressure on two bodies located SW and SE of center in frame 6. By the end of the simulation (which terminated prematurely when a CFL greater than 1 was encountered), a large collection of aerodynamically shaded spheres remains near the cluster's core, and are expected to separate by means of collisions at some later time. Marked by intense shock impingement/ingestion and a remnant core, the general fluid mechanical character of this larger cluster, is thus quite similar to the thirteen-sphere clusters inspected previously. The lattice-based structure of this cluster and its deviation from sphericity may influence the exact separation process, but the consistency of these separation traits across different populations highlight their wide influence in fragment dispersion generally.

Further qualitative information can be extracted from the flowfield features occurring in experiments of populous clusters. In Figure 6.3(b), the first frame of Figure 6.1 is reproduced in zoomed form to focus on the bow shock structure arising shortly after the bodies are released into the freestream. Near the midpoint of the

one-hundred-fifteen-sphere cluster's upwind face, the minute shock-standoff distance appears to span only one or two pixels, far less than expectations of a solid sphere of the same radius as the agglomeration (~ 14 pixels). As in the above simulation, the shock shape seems to be determined by individual spheres rather than the bulk obstacle presented by the cluster, with the density disturbance essentially following the contour of the sphere silhouettes. Presumably, at very high populations exists a limit at which reduced porosity and the absence of cavities on external faces (which effectively serve as expansions that decrease the shock angle) prompt the bow shock to adhere to the geometry of the spherical cluster, but it seems that, even for one-hundred-fifteen spheres, that threshold is beyond reach.

Quantitative information regarding both modifications to a swarm's shape and the duration of primary separation can be extracted from shadowgraph images of populous clusters even without computing full sphere trajectories. To demonstrate the analysis methodology and probe some of the relevant physics, we investigate the span of a thirty-six-sphere cluster in the orthographic-projected view, providing length-scales that are independent of object depth. For each frame after $t' = 0.17$, we calculate the minimum bounding box that contains all spheres except the one immediately expelled, as illustrated in Figure 6.4(a). The ratio of the cluster's lateral extent to its streamwise length serves as the flattening ratio and is accordingly provided in Figure 6.4(b). For the first $0.75\tau_s$, the cluster undergoes simultaneous rapid compression in the streamwise direction and expansion laterally, reaching an aspect ratio of 1.5. At this point, the spheres begin expanding slowly in the streamwise direction, decreasing the rate of flattening, while the transverse span approaches a

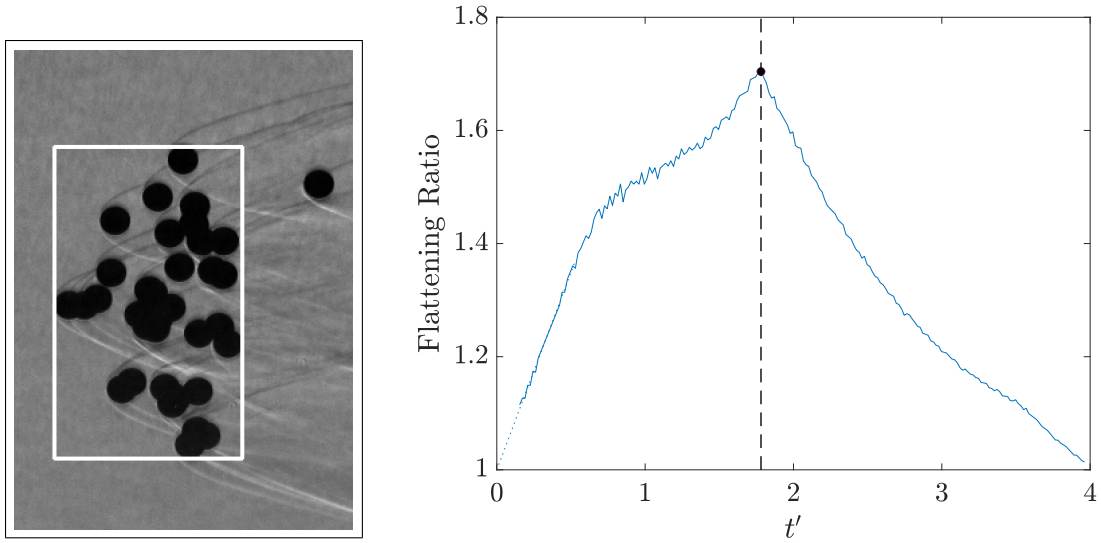

(a) (b)

Figure 6.4: (a) Minimum bounding box of shot 36A at $t' = 1.48$ (excluding highly expelled sphere) and (b) flattening ratio due to axial compression and lateral expansion, with posited end of primary separation denoted at critical point in curve.

constant velocity. Finally, at $t' = 1.8$, the increased streamwise acceleration of the outer spheres causes a critical point in the flattening ratio. Using the development of the flattening ratio as a proxy for identifying the stages of separation, we estimate that the primary separation phase gives way to subcluster interactions at the critical point of $t' = 1.8$ (in approximate temporal agreement with the appearance of oblique shocks in the wake region), by which time it has expanded to a lateral radius of $2.28r_c$. We additionally note that evaluation of thirteen-sphere cluster simulations using this method confirms the accuracy of this method of identifying the transition between separation stages.

6.1.2 Cluster-Core Collisions

From Figures 6.1 and 6.3(a), the retention of a core collection of spheres not expelled by shock dynamics is manifest even in the most populous clusters. In accordance with the typical terminal state of aerodynamically independent bodies, however, we would expect any dense cluster core to be dispersed eventually. As ascertained from visual inspection of shadowgraph videos and as noted in Section 5.3, collisions, in particular, contribute greatly to the separation of bodies entrained in the wake of a leader sphere. We, therefore, examine the kinematics of a representative cluster (shot 115E) that exhibits collisions and accordingly gauge their efficacy in dispersing the core. As shown in Figure 6.5(a), all bodies within a lateral distance of $10r_{\text{sph}}$ from the upstream-most sphere in the cluster are identified when body tracking commences ($t' = 2.8$) and designated as the core. This cluster core, composed of thirty-one spheres, appears to be grouped into several subclusters with a number of triplets on the periphery of the core are accompanied by extensive subclusters located towards the center and offset $5r_{\text{sph}}$ NE of the center. However, in the downstream visualization at $t' = 5$ (Figure 6.5(b)), the core spheres seem to have largely dispersed, with only a few bodies in close proximity to others when exiting the viewing volume.

To understand how this dispersal occurred, we inspect the lateral velocities of all bodies comprising the cluster core, labeling the spheres as either collisional or non-collisional according to an acceleration threshold. The velocities of the ten collisional bodies, highlighted in red in Figure 6.5(c), are marked by several ener-

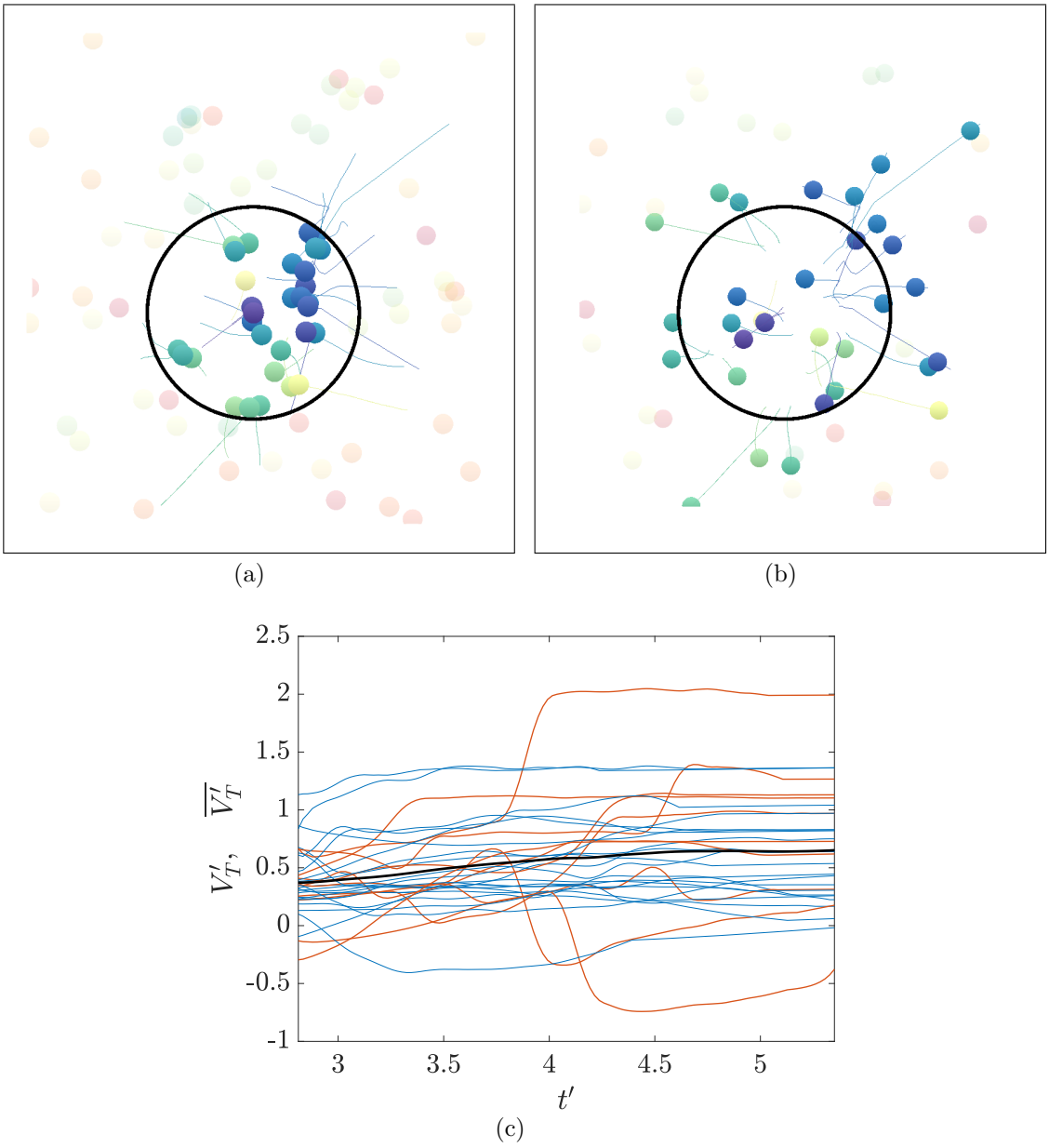

Figure 6.5: (a) Downstream-projected reconstruction of cluster core from shot 115E at $t' = 2.8$, with $10r_{\text{sph}}$ bounding radius from upstream-most body shown in black and trajectories emanating from current positions, and (b) the same graphic after core dispersal at $t' = 5$. (c) Lateral velocities of core spheres colored as follows: blue: non-collisional; red: collisional; black: mean.

getic impacts, whose magnitude is likely enhanced by the enlarged cluster size and the resultant increase in streamwise distance once entrainment begins. One notable event occurs at $t' = 3.75$, precipitating a $1.1\upsilon_s$ increase in the lateral velocity of one of the fragments; its partner sphere experiences a similar velocity differential, albeit directed towards the cluster center of mass, and, upon reaching a V_T' of 0.2 by the test's end, contributes to a lateral velocity increase of 46% for the pair. Overall, the mean lateral velocity of the core rises to 0.65 from 0.37, which is driven far more by the collisional spheres ($0.503\upsilon_s$ increase) than the non-collisional ($0.170\upsilon_s$ increase). As far as overall cluster separation is concerned, the collective lateral velocity grows by only 7.8% over the test duration, so the collisions are ultimately of minor importance to the total kinematics; this is consistent with previous observations of the diminished impact of secondary interactions in more populous agglomerations. In any case, the rapid deterioration of the cluster core is notable in the context of meteor entry, where prolonged propagation of massive clusters deep into the atmosphere would be stifled.

6.1.3 Highly Expelled Spheres

One outstanding question of high interest in meteoritics is the source of far outlying fragments in strewn fields (see, e.g., Laurence and Deiterding (2011)). Given the vast amount of kinematic data acquired in the equal-cluster campaign, we seek to identify the most expelled spheres of the more than $1,000$ bodies tracked and interpret the means by which they were so severely ejected. Thus, we accumulate all

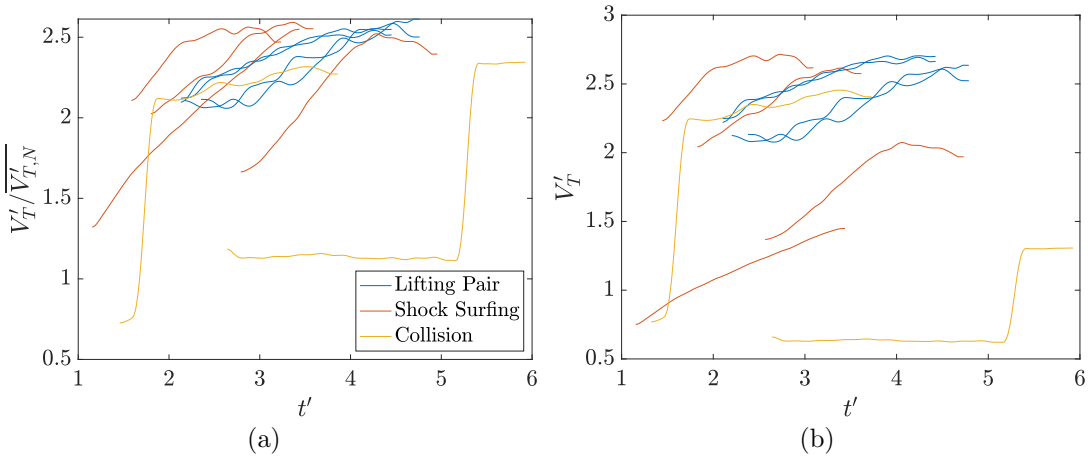

Figure 6.6: (a) Scaled and (b) unscaled lateral velocities of the most ejected spheres in the equal-cluster campaign classified by expulsion means.

terminal lateral velocities measured in the experimental campaign and scale each by the terminal $\overline{V_T'}$ for its population, $\overline{V_{T,N}'}$, before selecting the ten spheres demonstrating the greatest overall separation. Given that the somewhat fragmentary trajectory datasets cover only those periods in when overlap is not too restrictive and that the most ejected spheres are generally not obscured during their flight, we return to the stereoscopic images and utilize the body tracking routines of Chapter 1.5 to trace the motions of the selected bodies until the earliest possible time (usually at their entrance into the field-of-view, adding ∼50 frames).

At this point, we consult both the lateral velocity histories (Figure 6.6) and the three-dimensional reconstruction videos to determine the means by which each sphere was ejected, with classification into categories of lifting pairs, shock surfing, and collisions. We note that, while ten spheres were considered in this analysis, the presence of sphere pairs leaves only eight expulsion events responsible for the pictured velocity profiles, so, in our discussion, we will accordingly treat each pair

as a single unit. As the driving mechanism for four expulsion events, shock surfing constitutes the most prevalent type of interaction, while lifting pairs and collisions each occur twice. Despite the mean lateral velocity scaling introduced here, the intense ejection events chiefly arise in the most populous clusters: of the eight episodes considered, one transpired in a fourteen-sphere cluster, one in fifteen, one in fifty-two, two in ninty-nine, and three in one-hundred-fifteen. It is possible that this relationship is a function of the underlying fluid mechanics, but we find it more likely that the effectively limited sampling of smaller clusters prevents their equal representation here. Also, the unscaled lateral velocities (Figure 6.6(b)) surpasses V_T' values of 2.5, which far exceeds all measurements presented in related literature.

Given the reduced influence of subcluster interactions with increasing cluster population, one surprising discovery is that a collision serves as the source of expulsion for a sphere in shot 115A. The collision, visible at $t' = 1.75$ in the sphere's lateral velocity history, occurs a short time after the transition to secondary separation but involves another highly ejected body contacting the sphere of interest rather than an impact following attractive entrainment, so the mechanics are less aligned with the standard formula of subcluster interactions. Also unexpected is that the lifting pairs of shots 99A and 115B exhibit significantly lower lateral acceleration than the other expulsion categories, with their common lateral velocities appearing not to extrapolate back to negligible values at their effective release time. Examination of the shadowgraph/standard videos show that each pair was ejected in tandem during primary separation and, by chance, maintained surface contact at an appropriate alignment angle until independent flight could commence. Finally,

we find the colliding sphere at $t' = 5.25$, taken from a fourteen-sphere experiment, is the only ejection that unambiguously occurs as a result of subcluster interactions. Overall, shock surfing seems to be the preferred method of high lateral expulsion, but sphere pairs could comprise a larger proportion than indicated here if lifting bodies not identified here continue to accrue lateral momentum downstream of the visualization volume. However, in more realistic fragmentation scenarios, shock surfing with irregular fragments may be expected to arise more often (see, e.g., Li et al. (2015)), whereas paired lifting, potentially an idiosyncrasy of spheres, and collisional expulsion, which may instead induce further fragmentation, might not be so prominent as sources of highly expelled fragments.

6.1.4 Isotropy

To this point, we have treated the lateral velocity of sphere as a foundational quantity, but, more accurately, it is composed of the oriented expulsion of a body in the y- and z-directions. While one would not expect a separating cluster to display strongly preferential directional tendencies, the effects of subclustering (even if ephemeral) and slight non-sphericity of the initial agglomeration could conceivably introduce some degree of anisotropy to the arrangement of dispersed fragments. Therefore, to examine any directional correlations in equal-cluster separation, we discretize the terminal lateral velocity measurements of a chosen experiment into 10 azimuthal bins and determine the deviation of each grouping from the overall cluster mean, where a low variance would correspond to isotropic lateral expansion.

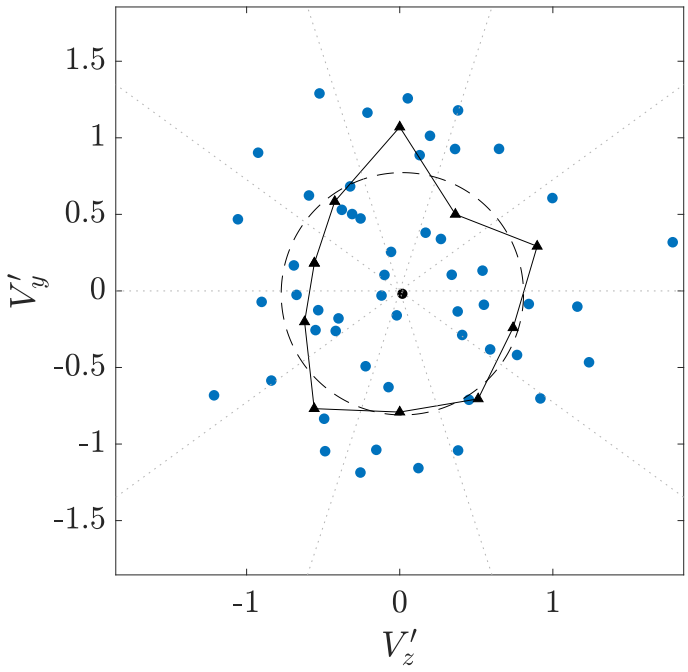

(a)

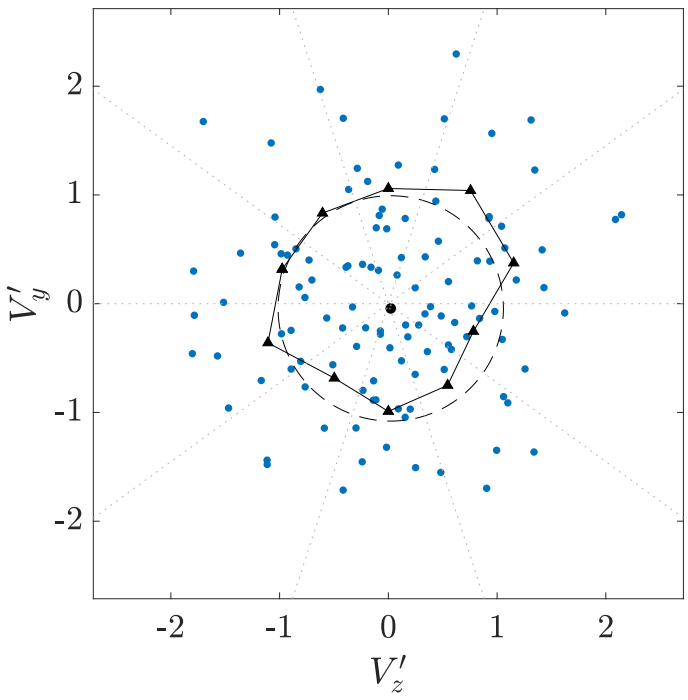

(b)

Figure 6.7: Azimuthal variance in terminal lateral velocity of shots (a) 52A and (b) 115A. Collective lateral velocity of cluster shown in dashed black and binned lateral velocity in solid black with triangular symbols.

Figure 6.7 thus presents the terminal velocities of shots 52A and 115A in zy-coordinates. Some subclusters and sizable voids appear to disrupt the overall homogeneity of the separation distribution, but the general impression is one of equal dispersion in all directions. More concretely, we supplement these velocities with the cluster's collective lateral velocity (dashed black) and the mean lateral velocity of each azimuthal bin (solid black with triangles), whose magnitude is denoted by the symbol's radial distance from the zy-origin. It is clear that both provided examples demonstrate a small amount deviation from isotropy on larger angular scales. In shot 52A, the large-scale velocity deficit located W of the primary axis seems to be associated with clustering at points further interior, potentially drawing bodies from adjacent bins and endowing the cluster with a slight N-S ejection bias. Shot 115A, on the other hand, exhibits a velocity deficit south of the cluster core, which instead stems from a dearth of high-ejection events in that general direction. The anisotropy of separation, as measured using the deviation from the mean, decreases from 0.211 to 0.139 between shots 52A and 115A, indicating an approach to isotropic expansion with increasing population. Such measurements are consistent with the mean anistropy indices for each cluster population, evaluating to 0.206 and 0.142 for fifty-two and one-hundred-fifteen spheres, respectively. Additionally, it should be noted that the lack of a persistent directional bias serves as indirect validation of the shell-based release mechanism introduced in Chapter 1.5.

6.2 Aggregate Statistics

6.2.1 Primary Separation Range and Duration

In the more populous clusters explored in the present study, the primary separation phase serves as the principal means of fragment dispersion. Therefore, understanding the characteristics of mutual repulsion with varying cluster populations is a critical component of deciphering meteor fragmentation. The particular quantities of interest here, the extent of lateral spreading at stage transition and the duration of primary separation, hold importance for a number of physical and practical reasons. The cluster span at the end of the primary phase effectively marks the radius at which the spheres aerodynamically decouple from one another. The primary separation timescale, on the other hand, relates to the efficiency of the hypersonic flow in moving mass, in addition to its use in determining the trajectory envelope of active separation (and thus the time-dependent dynamic pressure of inflow) during atmospheric descent.

To estimate the aforementioned properties, we employ three distinct methods which each depend on the source of data considered. In experiments of less populous clusters, the minimal obscuration encountered enables positional tracking at times shortly after release, so we compute as our separation metric the mean lateral force coefficient at each timestep. Fitting an error function to the lateral force profile, which helps moderate differentiation noise, we consider the time at which the error function reaches 95% of its final value to correspond to the end of primary

separation. For experiments of populous clusters suspended in the downstream position (for which sphere motions during primary separation are not available), the bounding box method of Section 6.1.1 serves to delimit the the primary phase from the secondary and gauge the lateral extent of the cluster. Given the approximate isotropy of sphere separation in large clusters (Section 6.1.4), the side-projected view should yield information characteristic of the cluster as a whole. Additionally, we include the primary separation statistics from the thirteen-sphere survey (Section 5.3), which were assessed by selecting minima in the mean lateral force coefficients extracted from the computation. This analysis, of course, relies on the inaccurate assumption of an instantaneous transition between dynamic regimes, but above methods reliably give results that yield an approximate delineation between the two.

We first explore the primary separation radius, r_p, over the test cases eligible for analysis, depicted in Figure 6.8(a). The resultant decoupling radii, each scaled by the initial cluster radius, form an weak relationship with cluster population. The separation radius, beginning from a minimum of 1.58 at four spheres, rises erratically before reaching a maximum of 2.26 at thirty-six spheres, whereupon a gradual decrease is evident. Despite the apparent trends, the uncertainty indicated by the 68% error bars of the 13-sphere simulations encompass the data from all other tests, which suggests that the observed scatter could simply be a manifestation of a process with high variance. Nonetheless, the cluster extent at stage transition remains within 20% of its mean value of 1.95, indicating that the decoupling radius is more or less constant for equal-sphere populations of the considered population

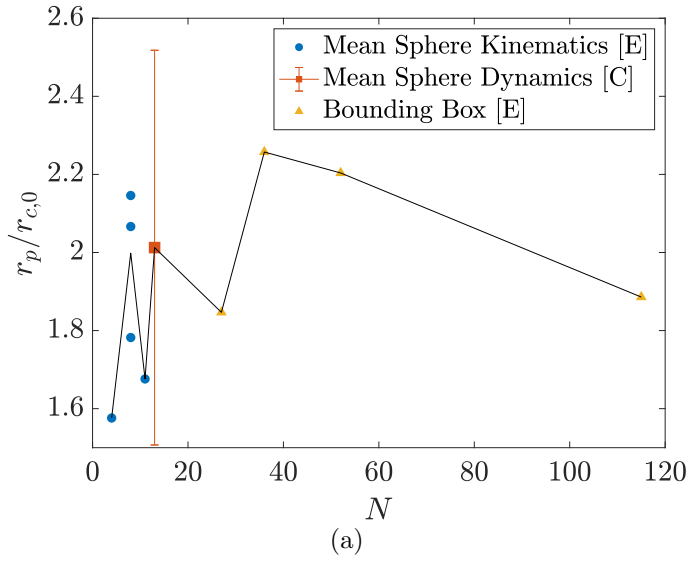

(a)

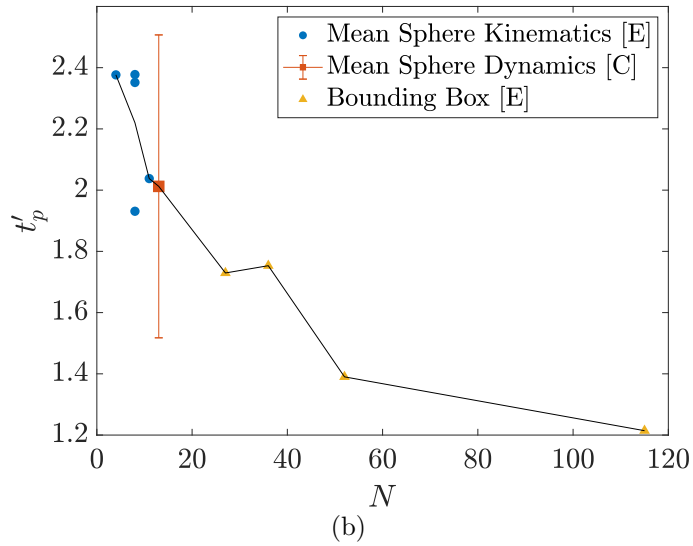

(b)

Figure 6.8: (a) Decoupling radius and (b) primary separation duration estimated using several techniques.

range.

The primary separation timescale, t'_p, on the other hand, adheres to a well-defined, monotonically decreasing trend, as shown in Figure 6.8(b). Falling from a maximum of $2.38\tau_s$, the separation timescale quickly diminishes to a value of $2.01\tau_s$ at a population of thirteen. For greater cluster populations, the separation timescale begins sloping downwards more gradually, reaching $1.21\tau_s$ at one-hundred-fifteen bodies and halving the separation timescale between the smallest and largest populations. The cause of such a dramatic decline at greater populations is likely due, at least in part, to the diminished sphere sizes relative to their parent clusters. However, normalizing the nondimensional time by the radius of the spheres rather than those of the clusters reveals that relative scale does not alone account the noted trend (in fact, we would expect a much steeper decline were this the case). Instead, it seems more likely that the reduced separation time is indicative of the enhanced efficiency of more populous clusters in distributing high pressure flow to its constituent spheres; specifically, because the forward spheres are able to spread laterally rapidly, bow shock ingestion may likewise occurs more quickly and produce shock impingement on the initially shielded bodies.

6.2.2 Lateral Velocity Distributions

The primary goal of the present work is to characterize fragment dispersion from a disrupted body at hypersonic conditions. Accordingly, the collective lateral velocity for a given cluster population serves as the preeminent metric for describ-

ing the magnitude of expulsion experienced by the constituent bodies. Through our investigation of small, intermediate, and populous clusters of equal-sized spheres, we have witnessed the development of the governing aerodynamics, proceeding from scenarios in which the leading sphere dictates the motions of all downstream to those the dominated by mutual repulsion and intricate shock formations. Transition to the primacy of the primary phase occurs at relatively small populations, with mutual repulsion clearly the foremost separation mechanism in the thirteen-sphere simulation survey. Notwithstanding any fundamental changes in the physics of aerodynamic sphere separation, the mean velocity measurements consistently indicate greater fragment dispersal at higher populations and a level of order belied by the apparent chaos visualized in wind-tunnel recordings. The exact relationship between the collective lateral velocity and cluster population is, perhaps, the most crucial aspect of the present work, providing a basis for constraining the behavior of a wide range of fragmentation events.

Thus, we present in Figure 6.9 the collective lateral velocities of all equal-sphere experiments for which suitably accurate kinematic data was obtained. As expected, the collective lateral velocity increases with cluster population. At first rising steeply from 0.22 (two spheres) and passing 0.5 (eight spheres) soon thereafter, $\overline{V_T'}$ begins to ascend more gradually, only surpassing a lateral velocity of 1.0 near a population of ninety-nine spheres. Comparing the spread in lateral velocity at certain populations, the variance in separation behavior seems to diminish with increasing cluster size, although at a slower rate than might have been expected. Given the well-defined structure constituted by the data, we endeavor to derive

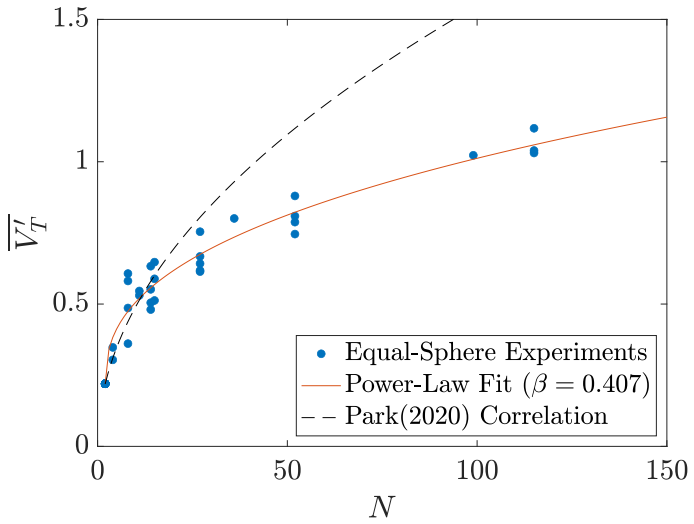

Figure 6.9: Collective lateral velocity with cluster population.

a curve-fit mathematically describing the observed correlation. The data closely resemble a power-law distribution, which is a functional relationship used to model many physical and mathematical processes:

$$\overline{V_T'}(N) = A(N-2)^{\beta} + \overline{V_T'}_{,N=2}, \tag{6.1}$$

where $N \geq 2$, β is the power-law index, A is the corresponding coefficient, and $\overline{V_T'}_{,N=2}$ forces consistency with the two-sphere separation behavior noted in Chapter 4 (excluding the lifting pair phenomenon).

The resultant curve (given in Figure 6.9) is defined by values $\beta = 0.407$, $A = 0.123$ and fits the data remarkably well overall. Some points of note do exist, however. First, the collective lateral velocity fit does not capture the considerable range of fragment dispersion that can occur at a given population. In the thirteen-sphere simulation survey, for instance, a 30.5% standard deviation in the collective lateral velocity was measured, which, according to the power-law fit, would effec-

tively span cluster populations from four to thirty-four spheres. The sample size of experiments at different populations is too small to accurately characterize the variance in collective lateral velocity, however. Additionally, the power-law description of sphere separation necessarily diverges as the high population limit is approached, which is a nonphysical result, as will be shown in the dust-cloud experiments of Chapter 8. Therefore, the power-law relationship is expected to break down for larger equal-sphere clusters than those tested in the present work. Indeed, as the number of bodies in an agglomeration grows, both the cluster porosity and the effective aerodynamic footprint of a single sphere diminish; with less mass ingested and expansions of reduced magnitude between bodies, the bow-shock standoff distance would grow to a point that shock impingement on exposed spheres would cease, undoubtedly altering the physics of separation. At that undetermined population, an asymptote or turnover in the functional relationship might arise, invalidating the use of a power-law fit. Nevertheless, the present curve fit provides an excellent basis for estimating the lateral spread of fragmented clusters for the population range tested.

Sources in free-flight separation literature generally recognize the importance of cluster population in fragment dispersion but have never explored the subject in a comprehensive manner. Thus, we now review historical values of V_T' from relevant sources and compare with the present results. As values cited in the literature are often reported in terms of separation coefficient, C, and in reference to the cross-range width of the swarm, we modify the values for consistency with the definitions used in the present work. Artemieva and Shuvalov (2001) simulated the motions

of equal hemicylinders to obtain a lateral separation velocity of 0.22, in very close agreement with the two-sphere simulations of Chapter 4. Additionally, the same authors numerically simulated the breakup of thirteen cubic fragments to find a $\overline{V_T'}$ of $\sim$ 0.5; this is slightly less than that predicted by the power-law relation, but the general consistency between the separation characteristics of spheres and moderately nonspherical bodies may signal a broader range of applicability for the power-law relationship. In their theoretical model of dusty debris separation, Hills and Goda (1993) posited that a dimensionless lateral velocity of 1.87, much larger than any value attained here, would describe the maximum radius of an expanding cloud. However, by appeal to Figure 6.6, the maximum-to-mean expulsion ratio of $\sim$2.5 instead places this estimate in the vicinity of thirty-eight equal bodies, which is somewhat surprising given that the governing physics are likely to be completely dissimilar. Finally, Park and Park (2020), from free-flight experiments of separating sphere rings (up to $N = 6$), proposed a square-root law for the collective lateral velocity, which is also plotted in Figure 6.9. The Park correlation shows close agreement with the small- and intermediate-cluster populations but diverges sharply from the present measurements above populations of twenty. As with all other historical estimates of $\overline{V_T'}$, a collective dearth of experimental and computational data prevented a composite characterization of the terminal separation kinematics.

From a modeling standpoint, a more important inquiry might be the expected velocity of a sphere when separating from a cluster of a given population. Therefore, we set out to evaluate the lateral velocity distributions of spheres originating from various cluster populations. To achieve robust statistics, we pool all mea-

sured velocities by cluster population, effectively stacking frequency distributions of individual experiments; five experiments populate the distribution for $N = 27$, four for $N = 52$, one for $N = 99$, and three for $N = 115$. Additionally, to any negative terminal velocities are assigned their absolute values, as such bodies will inevitably attain positive separation velocities following a closest approach to the center of mass. The probability density functions (PDFs) of lateral velocity for the selected cluster populations are thus presented in Figure 6.10. The convergence of the PDFs clearly depends on the sample size offered by a certain population, as the distribution of $N = 115$ appears far smoother than for $N = 27$. Notable are the shifting distribution peaks shifts towards higher values with increasing population, in agreement with expectations from the collective lateral velocity trend of Figure 6.9. Furthermore, the PDFs appear to vanish near values of zero in the largest clusters, but residual subclustering during visible flight may prevent such a tendency for twenty-seven spheres.

The probability density functions closely resemble the Rayleigh distribution, which is a single-parameter family of curves used, coincidentally, in studies of munitions ballistics (Williams, 1997), as well as other branches of physics, and whose PDF is defined as:

$$f_r(V_T'; \sigma_r) = \frac{V_T'}{\sigma_r^2} e^{-V_T'^2/(2\sigma_r^2)}, \tag{6.2}$$

where σ_r is known as the scale parameter. Thus, we provide in Figure 6.10 the best-fit Rayleigh curve for each stacked dataset, along with the scale parameter and the confidence with which the null hypothesis can be rejected, as computed

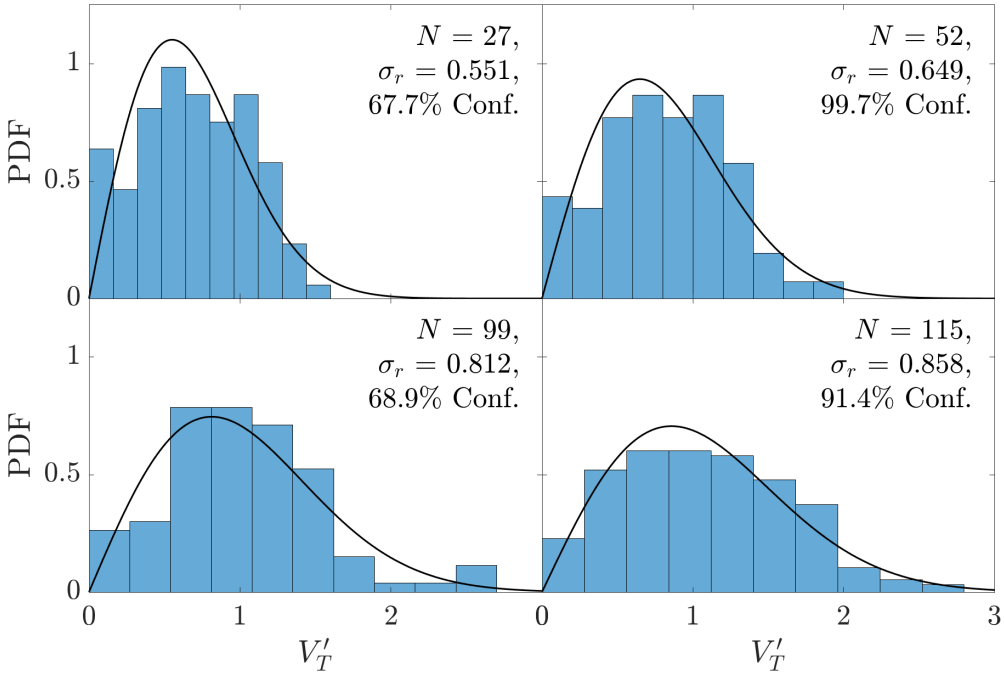

Figure 6.10: Probability density functions of lateral velocity for several cluster popoulations with best-fit Rayleigh distributions superposed.

using Pearson's χ^2 goodness-of-fit test (Pearson, 1900). The Rayleigh fits conform to the stacked data quite well, although the confidence level varies between cluster populations. A minimum confidence of 67.7% arises for twenty-seven spheres; as discussed previously, differences in the development of cluster kinematics likely prevent this set from completely dispersing the bodies. On the other hand, populations of $N = 52$ and 115 exhibit close agreement with the Rayleigh PDF, achieving confidence levels of 99.7% and 91.4%, respectively. We note also that the Rayleigh distribution is still consistent with the frequency distributions of isolated experiments but with the reduced confidence of a smaller sample size, as demonstrated by the single ninety-nine-sphere test. Aside from the noted exceptions, the Rayleigh distribution describes the data very well over a range of cluster populations.

Given the high fidelity provided by the Rayleigh distribution in describing the lateral separation of equal spheres from compact clusters, we now have a basis for modeling fragment dispersion velocities form agglomerations of any population. The scale parameter, the lone variable describing the Rayleigh distribution, is linked with the mean value by the relation:

$$\overline{V_T'} = \sigma_r \sqrt{\frac{\pi}{2}}, \tag{6.3}$$

enabling the selection of an exact Rayleigh curve by evaluation of the power-law fit to the collective lateral velocity (Equation 6.1 and Figure 6.9). At this point, a set of lateral velocities can be generated from a random realization of the Rayleigh distribution with the desired scale parameter, forming a simple statistical model

for an expanding swarm of equal-sized fragments, with far more physical grounding than existing models of meteor fragmentation aerodynamics.

Finally, we briefly assess the statistics of the lateral offset to the center-of-mass velocity that generally results from subcluster interactions. As noted in Chapter 5, the center-of-mass offset, $V'_{T,\mathrm{com}}$, tends to decrease with increasing cluster population, a finding supported by the experimental $V'_{T,\mathrm{com}}$ measurements given in Figure 6.11. The smaller populations exhibit high variance in the center-of-mass offset, ranging from 0.09 to 0.23 for the eight-sphere clusters, while increased consistency and lower overall offsets feature at greater populations. We do note, however, that at $N = 115$, one anomalously high offset occurs, possibly due to shell asymmetry during the release process. The general appearance of the data mimics that of a power law, so we perform a least-squares fit with a function of the form:

$$V'_{T,\mathrm{com}}(N) = AN^{\beta}. \tag{6.4}$$

Here, the parameters $\beta = -0.436$ and $A = 10.66$ give the best-fit power law, which is presented atop the experimental data in Figure 6.11. While the power law seems to slightly overestimate the degree of center-of-mass offset between populations of twenty and fifty, the curve provides an altogether accurate representation of the trends across a range cluster sizes and is consistent with expectations of asymptotic behavior in the high-population limit.

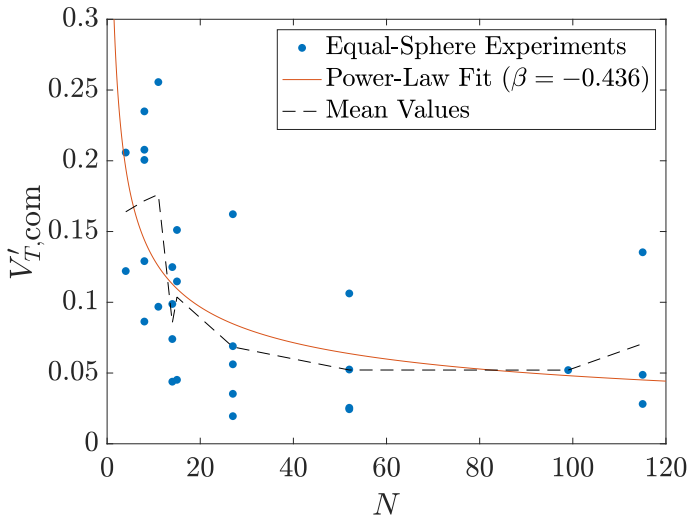

Figure 6.11: Center-of-mass lateral offset with cluster population.

6.3 Conclusions

In this chapter, we found that large clusters are marked by the dominance of seemingly random shock impingements in the primary separation process, accounting for half of the highest expulsion events observed. At the same time, cluster collisions help to disperse dense subclusters that coalesce near the formation's core, although the overall contribution of these collisions to the terminal lateral kinematics is modest. Nevertheless, the resulting cluster dynamics appear well-ordered, with isotropic expansion typical of all clusters with fifty-two or more bodies. Exploring pertinent statistical quantities across all equal-cluster populations reinforces the order emerging from the ostensible chaos of populous-cluster separation. Employing several methods to estimate the delineation between separation phases showed that, while the aerodynamic decoupling radius remains approximately constant, the separation timescale decreases markedly in populous clusters. The collective lateral velocity demonstrates a monotonic rise with cluster population and is fit well by

a power-law function with index $\sim$0.4. Furthermore, investigating the lateral velocity distributions of certain cluster populations showed close agreement with the Rayleigh distribution, serving as a basis for modeling the lateral expansion of equal clusters of any population.

Chapter 7: Unequal-Sphere Clusters

It is well known that meteoroids do not fragments into clusters of equal-sized bodies. Thus, in this progression to the second phase of the present study, we hope to achieve a more accurate characterization of realistic meteor disruption events by investigating clusters with unequal spheres, in accordance with the model problem described in Chapter 1.

Unequal-sphere clusters are expected to introduce several phenomena observed in studies of different-sized sphere pairs but inaccessible to clusters of equal spheres. While it occurred occasionally in the equal-sphere phase of this work, extended shock surfing has been shown to increase in severity when the bodies involved are of differing scales (Laurence et al., 2012). For instance, the lateral velocity of a shock-surfing fragment can rise by a factor of 8 between radius ratios of 1 and 0.25, so the maximum lateral velocities attained here should be appreciably higher than those measured previously. While flight through the wake of an upstream body inevitably leads to entrainment and collisional separation for equal spheres, Register et al. (2020) have noted the existence of far wake trajectories in their aerodynamic-database-derived flight simulations of unequal sphere-pairs. In the far wake, a region bounded by the bow-shock and viscosity-dominated near wake, the reduced length-

scale of smaller bodies can allow for positive streamwise acceleration (relative to the flow-generating sphere) even in a flow regime of modest dynamic pressure. Marwege et al. (2018) showed, however, that entrainment can still occur for unequal spheres in the far wake, with implied high sensitivity to the radius ratio and proximity of the secondary body to the low-momentum core that survives downstream. In the context of equal spheres, a potentially stable arrangement in which the bodies are in continual contact near an alignment angle of 140° was identified. A similar instance of persistent contact for a radius ratio of 1/6 was highlighted by Register et al. (2020), with stable contact conditions likely to exist for all intervening radius ratios. While the secondary fragment in the aforementioned simulation maintains a position further forward, near $\theta = 113°$, it is substantially less exposed to the freestream flow; relative to the equal-sphere case demonstrating shock impingement, the aerodynamic shielding reduces the bulk lateral (and streamwise) acceleration, yielding an essentially lift-free contact pair for sufficiently small radius ratios. Finally, due to the diminished attractive acceleration of a small sphere entrained in the near wake of one larger, commensurately reduced relative velocities may be expected to occur at the point of collision, which could plausibly prevent the dispersal of the fragments. However, to the author's knowledge, such drafting arrangements have been postulated (as in Register et al. (2020)) but not directly observed (outside of particle image velocimetry systems). The emergence of these mechanisms would thus signal a dichotomy between the enhanced ejection of shock-surfing spheres and the additional mass retained by a wake-generating fragment, leading to interesting questions regarding the ultimate kinematic trends of unequal-sphere clusters.

The separation of unequal-sphere clusters is investigated solely through experiments. Therefore, we will first review the details of the experimental configurations in further depth. Similar to the template of Chapter 6, this chapter will continue with a discussion of general observations and a presentation of statistical findings before concluding with the proposal of a statistical separation model. We note that, aside from shock surfing, no comprehensive study of the above phenomena (with specific emphasis on the effects of radius ratio) has been conducted. As these mechanisms tend to arise naturally in unequal-cluster experiments, one could investigate the details of each interaction type through its serendipitous appearances, but exploration of the fluid mechanical minutiae is beyond the scope of the present work. Instead, we focus on the resulting statistical properties of clusters subject to such fluid-structure physics.

7.1 Cluster Parameters and Sizing Considerations

Approaching the problem of unequal-cluster separation in a reducible manner requires adoption of a suitable parameterization. Meteorite size distributions are typically found to adhere to power-law distributions (Hartmann, 1969), and, while the fragments recovered on the ground necessarily obey a size distribution distinct from that of fragments at the moment of atmospheric disruption, one might still expect a power law to describe airborne fragmentation adequately. The functional form of the fragment size distribution (FSD) employed in this work is a truncated

power law with variable exponent index, α:

$$p(r) = Ar^{-\alpha}, \tag{7.1}$$

where A is a normalization constant dependent on α and the cluster population, N. For consistency with equal-sphere experiments, we fix the cluster population to fifty-two bodies, which was deemed an appropriate size to allow for some measure convergence in cluster selections while preventing overly burdensome body tracking. We note that assessments of meteorite FSDs generally place α close to a value of 5 (Hartmann, 1969), with the survey of Betzler and Borges (2020) suggesting ground-recovery power-law indices of $\sim$5.8 for ordinary chondrites and $\sim$4.6 for iron-type impactors. However, the atmospheric entry simulations of Appendix A establishes that an airburst power-law index varying between 1 and 5 effectively brackets the spectrum of recovered meteorites, with an α of $\sim$3.5 found to provide best agreement with chondritic fragments. Indeed, steepening of the FSD following disruption might be expected given the preferential ablation of larger bodies that descend deeper into the atmosphere. In any case, we select power-law indices of 1, 2, 3, 4, and 5 for generation of the cluster compositions used in experimental testing. As shown in Figure 7.1(a), this choice of α range spans both 'heavy' and 'light' distributions, wherein the majority of the cluster mass is contained in the largest and smallest fragments, respectively, and is centered about $\alpha = 3$, which represents equal mass fraction for all fragment sizes. An additional discriminating attribute between 'heavy' and 'light' clusters lies in the probability distribution of

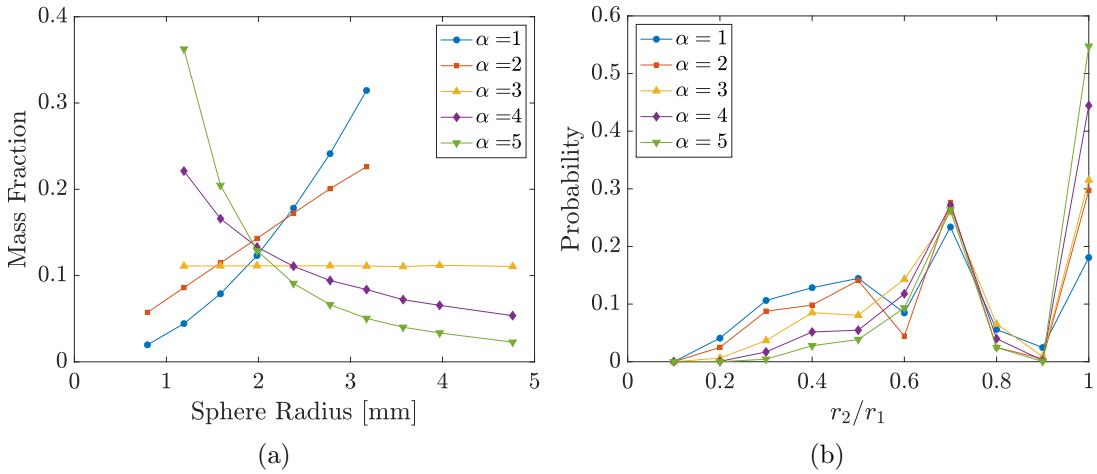

(a) (b)

Figure 7.1: (a) Mass fraction of the prescribed sphere sizes and (b) radius-ratio probabilities averaged over 1,000 realizations for $N = 52$.

the sphere-pair radius ratios (Figure 7.1(b)): for the selected cluster population, 'heavy' clusters favor sphere-pair combinations with one body twice to thrice as large as its partner, while equal-sized pairs tend to dominate the composition of 'light' clusters. As will be shown in Section 7.3, such pair-size characteristics are of high consequence for the ultimate separation behaviors observed experimentally.

The selection of sphere sizes constitutes a trade-off among experimental length-scale, shell interference, and packing efficiency considerations. The principal constraints are the preservation a minimum-to-maximum radius ratio of 0.25 and a shell radius between 6.0 and 9.0 mm, which maintains a sufficiently small characteristic length scale compared to the streamwise extent of the field-of-view while eschewing the undesired shell interference that can afflict less massive clusters. In jointly sizing the admissible shell and sphere radii, we additionally impose a packing efficiency restriction, assisting in the generation of a viable cluster, whereby the mean cluster-to-shell volume ratio of a given power-law index must evaluate to 0.55, a

slight increase from the optimal packing efficiency of fifty-two equal spheres (Huang and Yu, 2012). Thus, iterating on both the suspension shell and sphere sizes, we assumed the following collection of sphere radii (all in mm), determined in part by vendor stock: 0.79, 1.19, 1.59, 1.98, 2.38, 2.78, 3.18, 3.57, 3.97, and 4.76. The exact selection of spheres available for cluster generation varies among the power-law indices, however, and can be discerned from Figure 7.1(a). Additionally, as was given in Table 2.2 of Chapter 1.5, the chosen shell radii in order of ascending α are 8.75 mm, 7.20 mm, 8.95 mm, 7.60 mm, and 6.80 mm.

The realization of a collection of spheres according to a particular power-law index is a straightforward process. After partitioning the appropriate cumulative density function into bins dictated by the corresponding sphere pool, the evaluation and sorting of N random realizations of the uniform distribution indicate the chosen sphere sizes. For a cluster to be considered valid, its packing efficiency (i.e., the ratio of summed sphere and shell volumes) must fall within 10% of 0.55, as exceptional cluster realizations can result in under-filled or unphysically over-packed agglomerations. Clearly, both porosity and mass are not conserved for clusters constructed from the same α, indicating high variability in separation behavior. An additional source of variability is the manner in which spheres are loaded into their suspension apparatus; for example, a large sphere in an upstream location would result in high mass retention whereas a downstream positioning of the same body would tend to encourage increased fragment dispersal. Therefore, great care is taken to ensure that spheres of all sizes are distributed evenly and randomly throughout. One consequence of the steep power-law indices and limited cluster population is

the low probability of selecting the largest spheres for $\alpha = 3, 4, 5$, which can produce agglomerations without the largest bodies of the selection pool. Despite the minimum-to-maximum radius ratio not evaluating to 0.25 in such configurations, the prescribed $r_{\min}/r_{\max}$ is still upheld in a statistical sense. Finally, noting the high variability in unequal-cluster separation, the four upstream-suspended tests conducted for each power-law index are too few for true statistical convergence of the aerodynamic behaviors but give an approximate sense of the overall trends.

Some practical differences arise in the experimentation of equal- and unequal-clusters as well. Most notably, the level of obscuration during eclipse events is of greater magnitude for unequal-clusters; the duration of silhouette overlap is generally shorter, requiring only a second-order positional interpolation to satisfactorily rectify tracking errors, but the occasional extended occultation yields high reconstruction errors for the affected bodies, particularly those that draft in a crowded wake. Additionally, pronounced disparities in the streamwise accelerations of variously sized bodies causes spheres to enter and exit the field-of-view at dramatically different times, requiring large-scale extrapolations to compute the cluster center-of-mass at late epochs. Typically, spheres that exit the viewing volume early have already achieved aerodynamic independence, but errors in center-of-mass estimation necessarily arise when interacting bodies can no longer be tracked. Finally, for compactness of notation, we note that the collective lateral velocity, $\overline{V_T'}$, is implicitly interpreted as a mass-weighted quantity throughout.

7.2 General Observations

A basic understanding of the qualitative aspects of unequal-cluster separation is required before interpretation of the ultimate separation trends is possible, so we first begin with a discussion of the general appearance of two tests initially suspended in the downstream position. As the clusters are visible in the shadowgraph view soon after flow arrival, an approximate assessment of the fluid dynamic state of the arrangement helps to explain some of the observed behavior. Additionally, certain details are supported by features apparent in the vertical camera view, which is omitted here. As these clusters are not likely to reach their terminal state from the downstream suspension position, we did not extract sphere trajectories, so all analysis is qualitative, though informative, in nature.

The separation sequence of shot 2E-U in Figure 7.2 demonstrates the high variation in body sizes stemming from the realization of an $\alpha = 2$ power-law cluster. In particular, this 'heavy' cluster, shown in steps of $0.90\tau_s$, is composed such that 8% of the bodies constitute 50% of the mass, leaving a great number of minor fragments that provide a smaller contribution to the overall kinematics. In contrast to the complex shock structures imaged in the equal-cluster experiments, examination of the first panel reveals that the bow shock is generated by only a few larger spheres. In a fluid dynamic sense, one might expect the advanced onset of shock ingestion but with a higher degree of aerodynamic shielding. Moreover, consultation of the vertical camera view shows that smaller bodies initially occupying the gaps between those larger spheres had already vacated their forward positions before the

capture of the first presented frame, indicating that the shock ingestion process is already ongoing. This initial still also pictures two bodies isolated from the rest of the agglomeration; visually tracing their trajectories downstream, one continues to accelerate, presumably surfing the shock generated by the dispersing cluster, while the other maintains an approximately constant streamwise velocity, apparently drawn into a far-wake trajectory. As separation progresses (frame 2), lateral expansion of the cluster is evident, but the axial compression characteristic of equal-sized clusters is absent. After frame 2, however, dramatic streamwise growth of the cluster is manifest in the considerable displacement of small bodies (specifically, those of the two smallest radii) between frames 2 and 3, possibly marking the transition to secondary separation. On the other hand, several spheres achieve delayed separation (between frames 3 and 4) to similar velocities following brief travel through the near-wake region of a larger sphere. While the smallest spheres are carried far downstream of the cluster core, significant subclusters begin to develop upstream, rendering the cluster comparatively blunted in shape overall. Of note is a subcluster emerging at the bottom of frame 4 which appears to endure intact until exiting the field-of-view. The spheres composing this subset are not in continual contact, so this formation would seem to correspond to the conjectured drafting phenomenon (although a large body drafting in the wake of one smaller seems a transient arrangement). Meanwhile, spheres in the vicinity of the central subcluster experience collisions and subsequent repulsive shock impingement, leaving only a non-contacting sphere pair with radius ratio 0.67 remaining. On the whole, the severe ejection of the smallest bodies and mass retention of the largest are features characteristic of configurations near $\alpha = 2$.

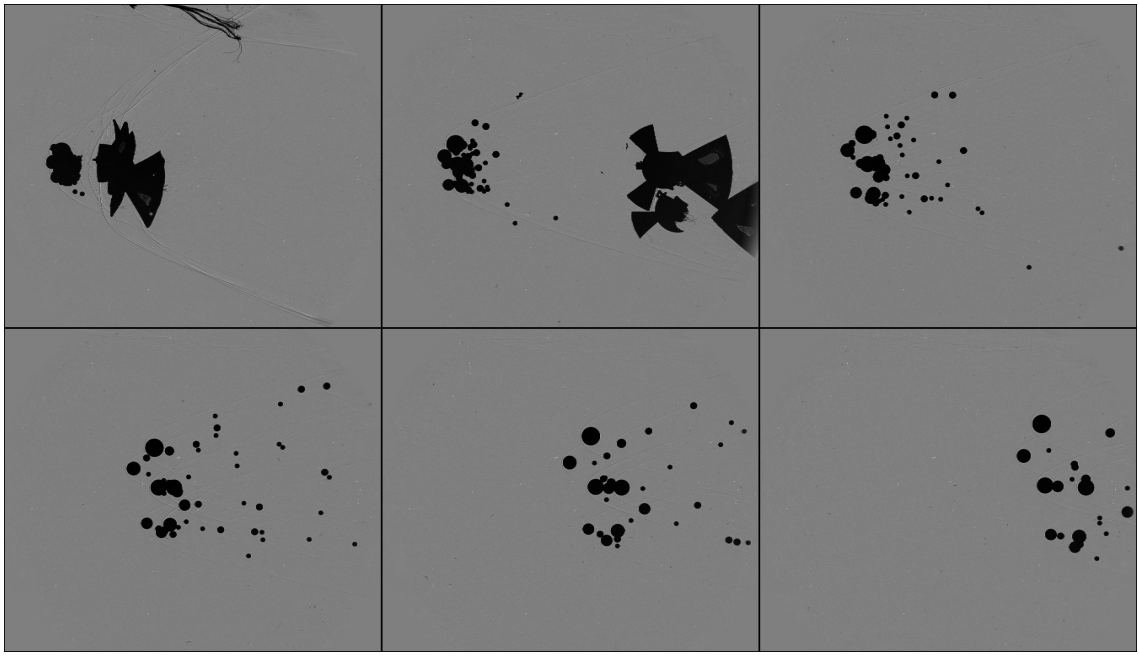

Figure 7.2: Shadowgraph images showing the separation sequence of shot 2E-U in increments of $0.90\tau_s$ (1.20 ms)

At $\alpha = 5$, the cluster of shot 5E-U (Figure 7.3) is composed of one large body accompanied by an abundance of secondary spheres. In accordance with the theoretical mass fractions of Figure 7.1(a), roughly 60% of the total mass is contained in the two smallest denominations of sphere radius, implying that a partial return to the dynamics of equal-sphere separation is likely. The first frame of the sequence diverges from expectations, however, as an isolated upstream body alone produces the governing bow shock. The video recording reveals that this sphere was thrust upstream from its initial position, seemingly under the influence of a back pressure briefly in excess of the freestream Pitot pressure. Despite the outboard translation of shock impingement induced by this sphere's upstream motion, the remainder of the cluster obeys the standard lateral-expansion/axial-compression sequence commonly

witnessed in the equal-cluster experiments of Chapter 6, although its transition from ellipsoidal to conical form may be hastened by the presence of a large upstream body. One important distinction between equal- and unequal-clusters regards the notion of aerodynamic independence: here, the highly ejected spheres rapidly escape the influence of the largest fragment, but, traveling along a laterally inertial trajectory, they will eventually accrue enough streamwise velocity to again traverse the primary bow shock far downstream. This re-entry may occur so far downstream that the shock has diminished in strength to a Mach wave and the forces (outside of the turbulent inner-wake) are similar to those experienced in the freestream. Beginning in frame 4, a subcluster traveling in the near wake of the primary body is discernible. Together, the six spheres drawn into this drafting configuration constitute a mass 27% that of the primary body, effectively enhancing the inertia of the subcluster and, in the context of meteor entry, allowing it penetrate further into the atmosphere. These drafting bodies frequently collide with each other, but the low impact velocities prevent the spheres from venturing far beyond the viscous near wake region. The eventual state of the drafting subcluster is unknown, so the stability characteristics of such arrangements cannot be gauged. In any case, this $\alpha = 2$ cluster shows markedly different attributes from the $\alpha = 5$ example, with shades of equal-sphere separation blended with distinct unequal-cluster phenomena such as near-wake drafting.

We now review the reconstructed trajectories and velocities of shot 3A-U, shown both in Figure 7.4. As with all other unequal-cluster experiments for which sphere motions were extracted, the agglomeration was initially suspended in the

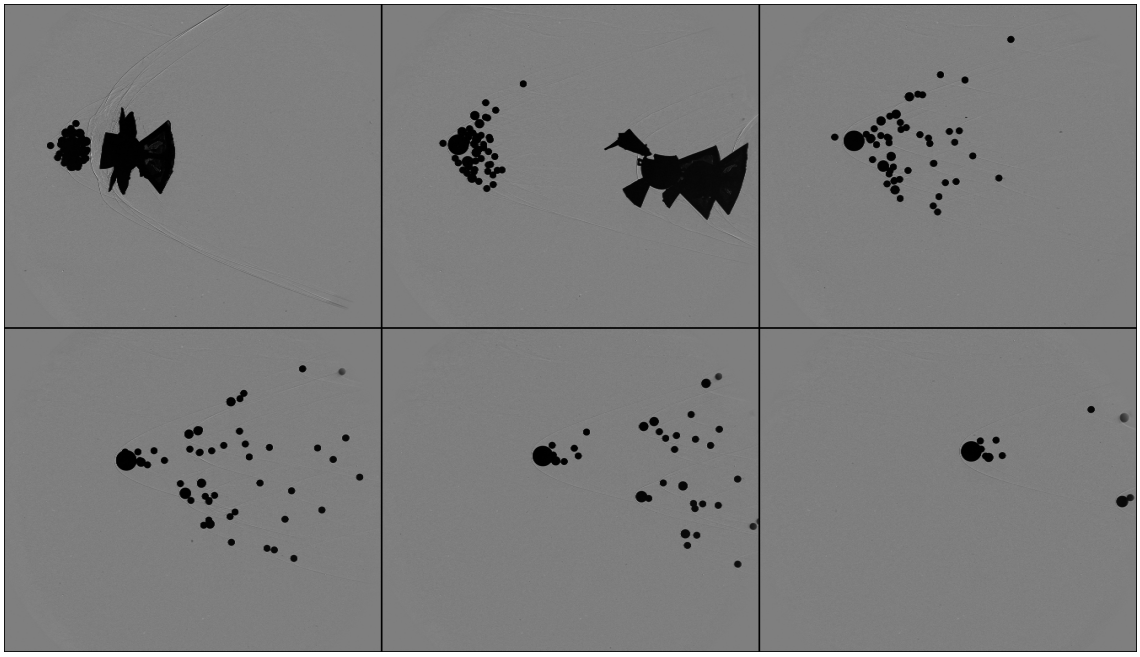

Figure 7.3: Shadowgraph images showing the separation sequence of shot 5E-U in increments of $0.95\tau_s$ (1.2 ms)

upstream position to encourage ample separation over the visible flight envelope. The dynamics occurring prior to the spheres' entrance into the test section are thus undetermined, but inferences regarding the primary separation phase can be drawn from the available data. The downstream reconstruction of the sphere motions is rather chaotic in appearance, so we will highlight selected features, corresponding mainly to the mechanics representative of unequal-cluster separation. Sphere 1, located NW in frame 3 of Figure 7.4(a), demonstrates highly delayed, yet markedly severe, repulsion: after traveling at a constant lateral velocity of 1.1, this small sphere ($r/r_{\max} = 0.25$) is suddenly accelerated at $t' = 3$, reaching a V_T' of 2.25 before exiting the test section only $0.75\tau_s$ later. With a multitude of shock-generating candidates, it is difficult to diagnose the exact source of this notable shock-surfing event, but consultation of the shadowgraph recording reveals that the most probable

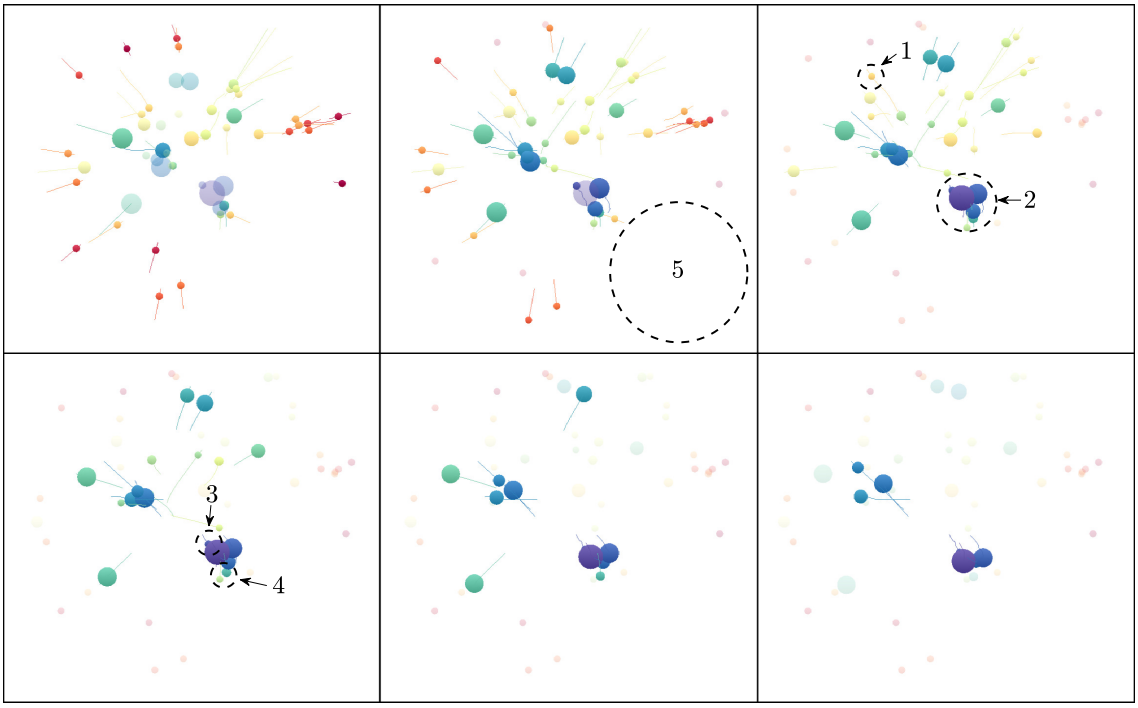

(a)

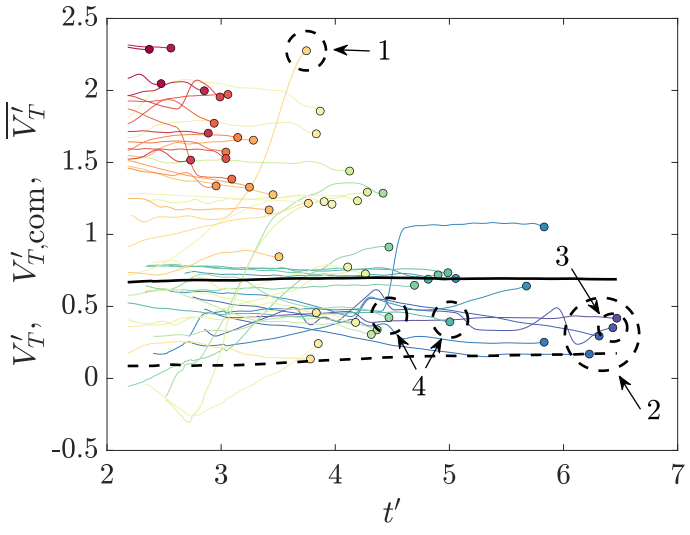

(b)

Figure 7.4: (a) Downstream-projected trajectory reconstruction of shot 3A-U shown in increments of $0.64\tau_s$ (1.06 ms) and (b) corresponding lateral velocity histories with colored lines representing individual sphere trajectories, the solid black line giving the collective lateral velocity, and the dashed black line showing the center-of-mass velocity offset. Additionally, common annotations label features of keen interest.

culprit is itself accelerating laterally, yielding a shock-surfing cascade of sorts. Label 2 (located SE in frame 3) represents a massive subcluster containing spheres of five different sizes and constituting 30% of the total mass of the initial agglomeration. One of the secondary spheres (label 3 in frame 4) is a shielded fragment in nearly continual contact with the leading sphere (the distance between bodies never exceeds 25% of the radius of the smaller). Meanwhile, two additional bodies (label 4 in frame 4) are accelerated streamwise but resist lateral ejection, as is manifest in the equivalence of their final lateral velocities with those upstream. Moreover, they exit the viewing volume much sooner than the rest, terminally swept into the far wake region of the upstream subcluster. The remainder of the clustered spheres occupy the free-shear layer region of the primary's near wake, occasionally colliding with one another and never quite resolving their eventual trajectories. Finally, label 5 (SE in frame 2) indicates a region devoid of highly expelled spheres, most likely explained by the presence of the larger spheres of the aforementioned subcluster, which shield the smaller, more ejection-prone bodies from shock impingement during primary separation and subsequently produce attractive wake effects in the secondary phase. Despite the large quantity of mass retained by this subcluster, the center of mass of the full system is shifted sharply NW at $0.17v_s$, possibly signifying an anticorrelation between the formation of subclusters and lateral center-of-mass motion.

Overall, the collective lateral velocity of the cluster remains fairly constant throughout the experiment, maintaining a value near 0.68. Thus, regardless of the impressive degree of subclustering detected here, primary separation continues to serve as the dominate mode driving separation. In spite of the lack of positional

data earlier in the cluster's flight, the velocity history of the cluster reveals that duration of primary separation is likely comparable to, or at least not conspicuously longer than, that of fifty-two equal spheres ($\sim 1.4\tau_s$).

Finally, Figure 7.5 presents the lateral velocities of the most highly expelled spheres over the entire unequal-cluster survey. These severely ejected bodies overwhelmingly occur in 'heavy' clusters — $\alpha = 1, 2$ — but the apparent bias may follow from practical considerations in cluster construction. To keep both the cluster population and minimum-to-maximum sphere radius ratio fixed for all power-law indices, the size of the suspension shell must be modified, resulting in a monotonic increase in $r_{\min}/r_c$ with α and potentially contributing to the augmented repulsion of the smallest bodies in 'heavy' clusters. A closer examination of the velocity histories reveals that the majority of extreme ejection events appear to follow shock-surfing trajectories, suppressing lifting pairs and collisions as sources of intense repulsion, in contrast to the behaviors noted for equal clusters. Two events without the signature velocity increase of extended shock-surfing instead point to acute initial repulsion on short timescales. The expulsions of interest occur upstream of the experimental field-of-view, however, so characterization of the dynamics producing such intense lateral acceleration ($\sim 3v_s$ per τ_s) is not possible. Nonetheless, the highly ejected spheres highlight the role of shock surfing as the primary source of outlying fragments in unequal clusters.

The maximum lateral velocities approaching 3.5 are, by far, higher than any estimates of the separation coefficient in related literature. However, in their analysis of the Morávka airburst, Borovička and Kalenda (2003) note that certain fragments

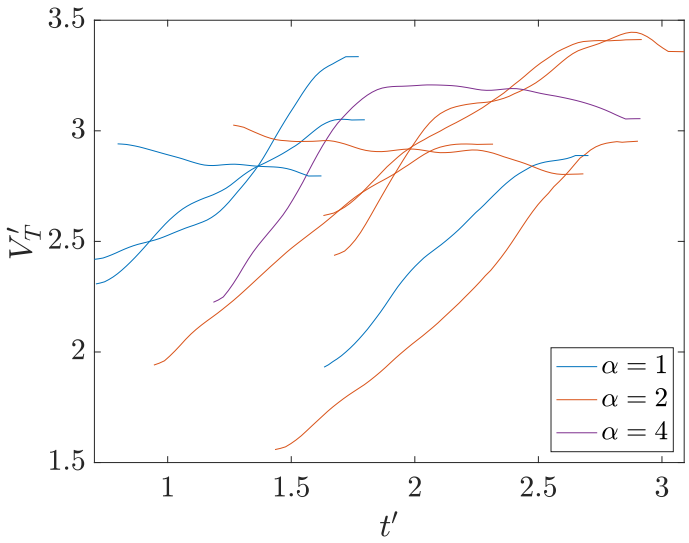

Figure 7.5: Lateral velocities of the most ejected spheres in the unequal-cluster survey.

were expelled with velocities one order of magnitude greater than those expected, equating with a V_T' of $\sim$10. The present measurements, therefore, cannot account for such severe repulsion, although, were the unequal-cluster experiments examining separation from clusters more populous than fifty-two bodies, the anticipated value of $V_{T,\max}'$ would be enhanced. Moreover, the present results can be considered analogous to solitary fragmentation events, so successive disruption during an expelled fragment's descent could conceivably produce separation velocities consistent with the observations of Borovička and Kalenda (2003).

7.3 Aggregate Statistics

In light of the competing effects of augmented expulsion and subcluster mass retention, a critical question is whether unequal-sphere clusters experience greater overall separation than their equal-sphere counterparts. We now consider the ter-

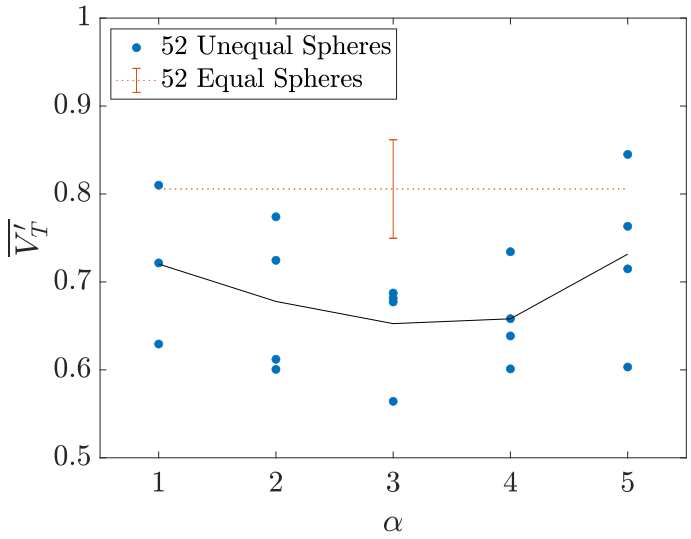

Figure 7.6: Terminal mass-weighted collective lateral velocity of unequal-sphere clusters compared with fifty-two bodies from equal-cluster survey. Mean values for each power-law index indicated in black.

minal (mass-weighted) collective lateral velocities of the present survey with the power-law index from which each cluster was generated (Figure 7.6). Clearly, unequal clusters do not disperse their fragments as effectively, as only two experiments exceed the mean value of the equal-sphere configuration (0.81) and the majority lie beyond its lower standard deviation. Additionally, the variance in $\overline{V_T'}$ for a particular power-law index is far greater than that of the equal clusters, which likely reflects the strong dependence on the random positions of the initial close-packed arrangement. The obvious conclusion for the reduction in fragment dispersal is that mass retention effects (such as in Figure 7.4) overwhelm the enhanced ejection of the smallest spheres, with moderate differences arising between the distinct groups of power-law clusters. Beginning from roughly equivalent values at $\alpha = 1$ and 5 (0.72 and 0.73, respectively), the collective lateral velocity reaches a minimum of 0.65 at $\alpha = 3$. For the expected power-law index of ~ 3.5 for ordinary chondrite impactors,

this roughly equates to a 19% decrease in the terminal lateral momentum, enough to considerably influence the extent of the ground damage ellipse. That $\overline{V_T'}$ values at $\alpha = 1$ and 5 begin to approach to the equal-cluster value is consistent with the reversion to equal-sphere compositions in the high $|\alpha|$ limit (still far removed from the range of α considered), but the physics driving the observed separation statistics require further investigation.

Due to the pronounced influence of subcluster mass retention on the characteristics of unequal-cluster separation, we now probe the clustering properties of all unequal configurations. To identify a free-flight subcluster we employ the following methodology: operating over all combinations of sphere pairs, we construct the computational bow-shock profile of the upstream body at the final timestep for which the downstream is visible and determine their relative positions and velocities; the pair is considered a subcluster if the downstream body is smaller than the upstream (preventing lifting sphere pairs among other arrangements), resides inside the bow shock of the primary, and possesses a leading-sphere-referenced lateral velocity no larger than 0.1. Generally, the presence of populous subclusters will foster a complex hierarchy of dependency, so a simple recursive routine is then utilized to merge and establish the principal sphere of the appropriate subclusters. By manual inspection of a significant subset of results, this methodology proved capable of associating spheres in drafting, continual contact, and far-wake arrangements. We also note that all subsequently calculated subcluster masses, m_{sub}, exclude the contribution of the principal body, whose trajectory is unlikely to be altered substantially by the subsidiary spheres.

To assess the dependence of subcluster mass on power-law index, we sum the masses of all subclusters in each experiment, which are then plotted against α in Figure 7.7(a). While the level of mass retention for each cluster type is highly variable, a clear trend emerges wherein the amount of retained mass diminishes with increasing distance from the maximum m_{sub}/m_c at $\alpha = 3$. Additionally, we present in Figure 7.7(b) the relationship between the collective lateral velocity of a cluster and the total amount of retained mass. In general agreement with the observed lateral momentum deficit of Figure 7.6, we observe a weak negative correlation between $\overline{V_T'}$ and m_{sub} with a slope of -0.56. Indeed, the test with the highest mass retention (0.23, $\alpha = 3$) demonstrates the lowest collective lateral velocity of the unequal-cluster survey (0.57). Due to limited sample sizes, however, no well-defined correlation exists within each cluster class (with the exception of $\alpha = 4$); such a trend only emerges when all data are stacked, indicative of the high variability inherent to configurations of this type. Additionally, the imprecise nature of the relationship is reinforced by the inconsistency between the equal-sphere value of $\overline{V_T'}$ and that to which the linear extrapolates at $m_{\text{sub}} = 0$. Nevertheless, the suppression of fragment dispersal generally appears to result from increased subclustering. Combined with the findings of Figure 7.7(a), this trend confirms that the source of reduced fragment dispersal is indeed subcluster effects.

The question remains, however, why certain power-law clusters are more likely to retain mass than others. To address this problem, we focus on the radius-ratio, r_2/r_1 with $r_1 > r_2$, of all entrainment pairs in the identified subclusters. Figure 7.8(a) thus presents the stacked frequency distributions of r_2/r_1 at each power-

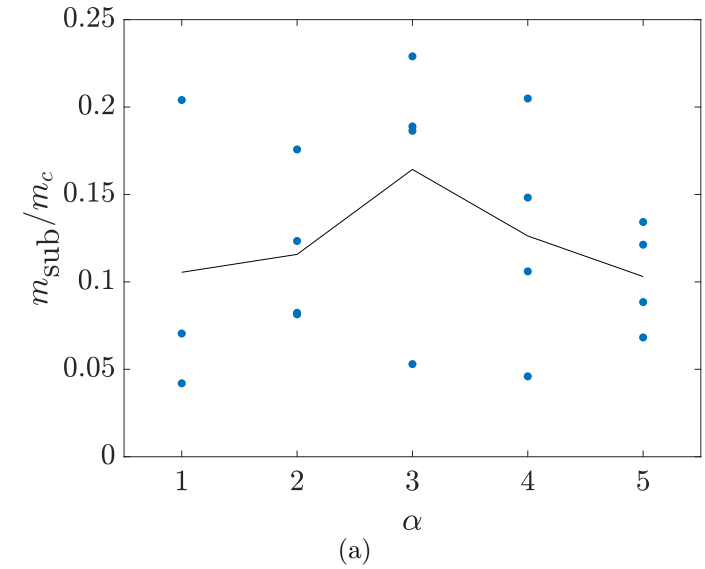

(a)

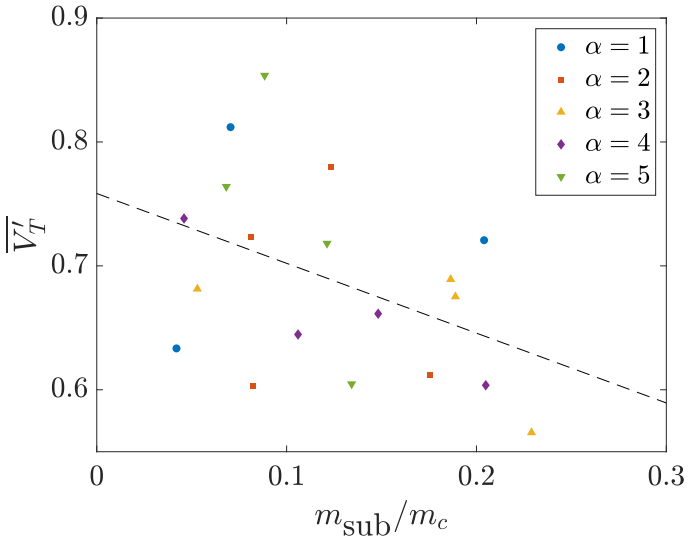

(b)

Figure 7.7: (a) Dependence of collective lateral velocity on subcluster mass, with linear fit shown in dashed black, and (b) the mass retained at each power-law index.

law index to determine whether certain radius ratios are preferred for mass retention. The frequency distribution of entrainment appears somewhat flat between 0.3 and 0.7, with a mean of 0.53 and standard deviation of 0.175. As might be expected, the radius-ratio dependence of entrainment counts is not constant across the various cluster types investigated. In accordance with the probabilities of Figure 7.1(b), the configurations with $\alpha = 1, 2$ posses a larger share of disparate-sized subclusters ($r_2/r_1 < 0.5$) than the higher power-law indices, while clusters with $\alpha = 4, 5$ constitute the greatest number of events for $r_2/r_1 > 0.55$, despite exhibiting pairing probabilities roughly equivalent to the other arrangements. The greatest number of entrained spheres, however, occurs in the $\alpha = 3$ configuration, which exhibits the high entrainment below $r_2/r_1 = 0.5$ and more modest subclustering for bodies of comparable size. However, we notice that the aggregate r_2/r_1 distribution does not mirror the radius-ratio probabilities of Figure 7.1(b) exactly, indicating that the underlying fluid mechanics of mass entrainment are indeed partial to certain radius ratios. In particular, when we to scale Figure 7.8(a) by the radius-ratio probabilities, as is presented in Figure 7.8(b), the $r_2/r_1 = 0.3, 0.9$ bins appear highly over-represented, and incoherent scatter arises between 0.3 and 0.8. The preferential retention of smaller bodies seems a natural result given their susceptibility to form drafting subclusters (see, e.g., Figure 7.3), while the prevalence of subclusters composed of pairs with $r_2/r_1 \approx 0.9$ is slightly surprising, possibly indicating an increase in pairing probability due to continual contact between bodies of comparable size.

The number of spheres sorted by entrainment radius ratio, however, is not

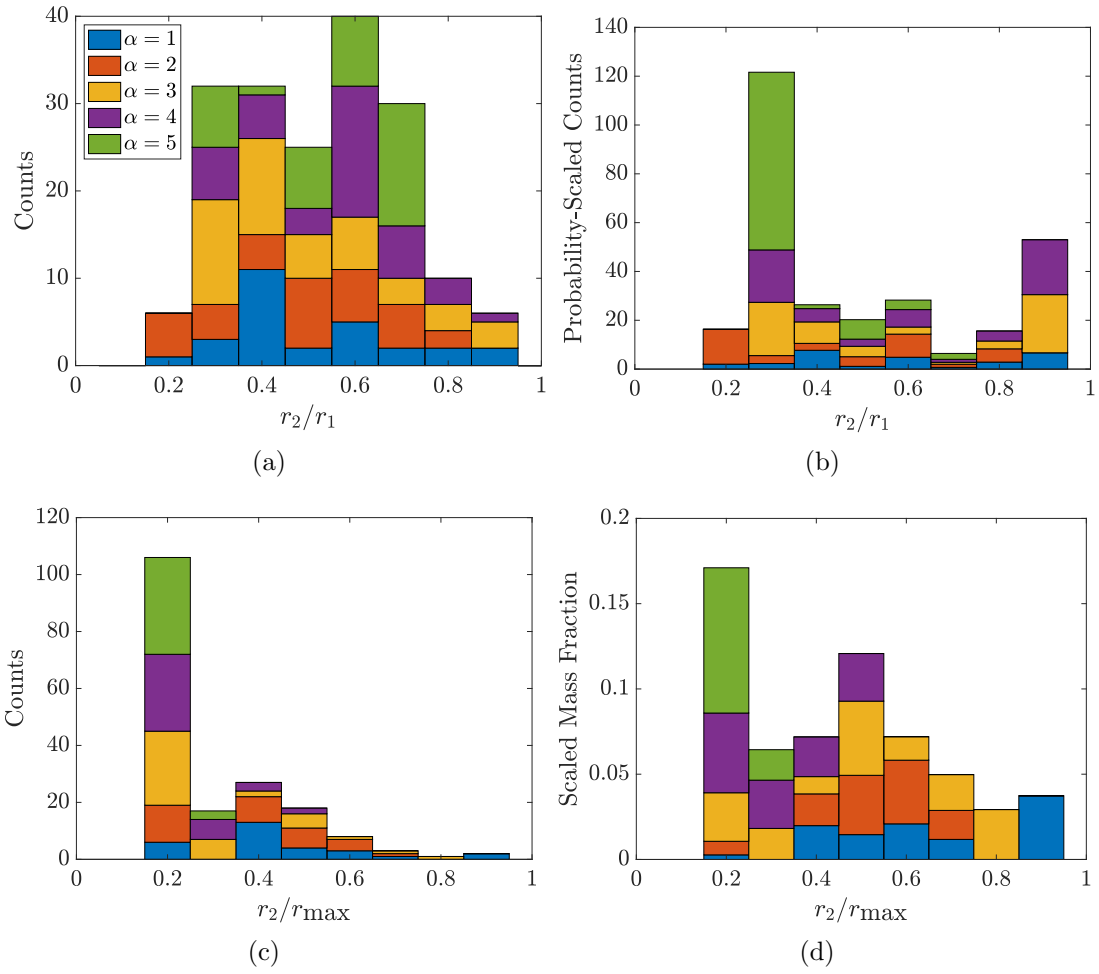

Figure 7.8: (a) The frequency distribution of entrainment grouped by radius ratio and (b) the same figure reproduced with mass-fraction scaling.

quite as important dynamically to the total subcluster mass, so we instead present in Figure 7.8(c) the frequency distributions of $r_2/r_{\max}$, that is, the radii of the subclustered spheres scaled by the maximum radius allowed for that power law. The transition between this and Figure7.8(a) highlights the overwhelming presence of small bodies in the subcluster statistics. For $\alpha = 1$ and 2, the subcluster radius ratios were already biased to small values ($r_2/r_1 < 0.5$), so the corresponding $r_2/r_{\max}$ distributions remain unchanged comparatively. Meanwhile, at $\alpha = 4$ and 5, the low probability of selecting large bodies means that most entrainment events, especially those near $r_2/r_1 \sim 0.6$–0.7, are actually composed of less-massive spheres, which is obvious from the $r_2/r_{\max}$ distributions, wherein most of the events counts are confined to the smallest bin. Now, we scale these frequency distributions by the appropriate fragment masses to highlight the impact on the overall separation properties (Figure 7.8(d)). At $\alpha = 1, 2$, smaller bodies constitute an insignificant fraction of a cluster's total mass, so the entrainment bias towards $r_2/r_{\max} < 0.5$ reduces their effective mass retention, despite the enhanced contribution of higher-mass pairs. While the smallest bodies occupy a great portion of the cluster mass at power-law indices of $\alpha = 4$ and 5, each individual entrainment event contributes little to the overall pattern of mass dispersal. Furthermore, 7.1(b) shows that clusters at $\alpha = 4$ and 5 have the greatest shares of equal-sized spheres, which are not considered in the subcluster identification routine. Finally, the $\alpha = 3$ configuration is subject to a constant mass-fraction for all sphere radii (Figure 7.1(a)), which seems to encourage mass retention over the full spectrum of sphere sizes, which is possibly responsible for the observed maximum in mass retention at this power-law

index. Thus, the point of transition from 'heavy' to 'light' clusters thus serves as the critical point in the mass-retention behavior of unequal clusters.

In the context of trajectory modeling, a task of foremost importance is constraining the dispersion velocities for all sizes of spheres. In the equal-cluster scenario, the lateral velocities of all spheres are described well by a Rayleigh distribution with a population-dependent scaling parameter, but, for the present cluster arrangements, smaller bodies are ejected far more severely than those larger, so a single Rayleigh distribution is unlikely to provide an accurate representation of a cluster's separation behavior. Instead, we decompose clusters of the same power-law index into groups of common sphere size and inspect the lateral velocity distributions of each subset. Figure 7.9(a), depicting the lateral velocity counts for three selected sphere sizes over all experiments at $\alpha = 3$, reveals that each radius group roughly conforms to a Rayleigh distribution of unique scaling, although the agreement is not perfect. The degree of correspondence between a V_T' frequency distribution and its best-fit Rayleigh curve varies with the population of the specified radius subset, with the insufficient occurrences of larger bodies preventing convergence of the underlying distribution. Notwithstanding the limitations posed by incomplete sampling of certain sphere radii, the lateral velocities of all other power-law indices show the same approximate agreement with a decomposed family of Rayleigh distributions, which is illustrated in Figure 7.10(a) for the three subsets of smallest r_2/r_1. As discussed previously in Chapter 6, the Rayleigh PDF, subject only to a single parameter, scales directly with the mean value of the set considered, and, therefore, the mean lateral velocity of each radius group, $\overline{V_{T,r}'}$, determines the the correspond-

ing Rayleigh scale. Indeed, presenting a set of size-binned mean lateral velocities in Figure 7.9(b), we find that $\overline{V'_{T,r}}$ for a power-law index of 3 roughly follows a decaying exponential dependence with sphere radius, as do the other power-law indices shown instead in Figure 7.10(b). The exponential fit depicted, of the form

$$\overline{V'_{T,r}} = ae^{-br/r_{\max}}, \tag{7.2}$$

yields the values $a = 1.89$ and $b = 2.01$.

Simply using the direct exponential fits of $\overline{V'_{T,r}}$ to scale the Rayeigh PDFs yields results characteristic of the observed collective lateral velocities (Figure 7.11(c)), but excessive deviation from the mean is exhibited by certain power-law clusters. Both the Rayleigh and exponential fits to $\alpha = 2$ in Figure 7.10, for example, are subject to high scatter in the lateral velocity data and exhibit lower confidence overall. Cognizant of the moderate deficiencies in the Rayleigh description of unequal-sphere separation and seeking a serviceable representation of fragment velocities, we relax our constraints on the exponential fits to $\overline{V'_{T,r}}$ and instead prioritize consistency with the statistics at each power-law index. For fitting purposes, we now introduce a new variable, the scaled lateral momentum, $(m/m_c)V'_T$; for any choice of α, the mean value of this quantity's PDF, multiplied by the cluster population, gives the expected collective lateral velocity. Furthermore, this formulation of lateral expansion in unequal-sphere clusters removes the mass–velocity degeneracy in momentum measurement. Thus, employing a nonlinear least-squares fitting routine and allowing the two exponential parameters to float, we minimize for each α the difference

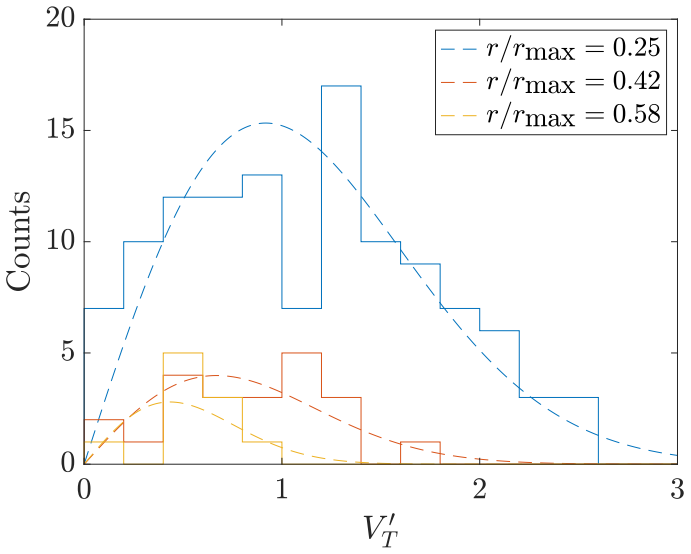

(a)

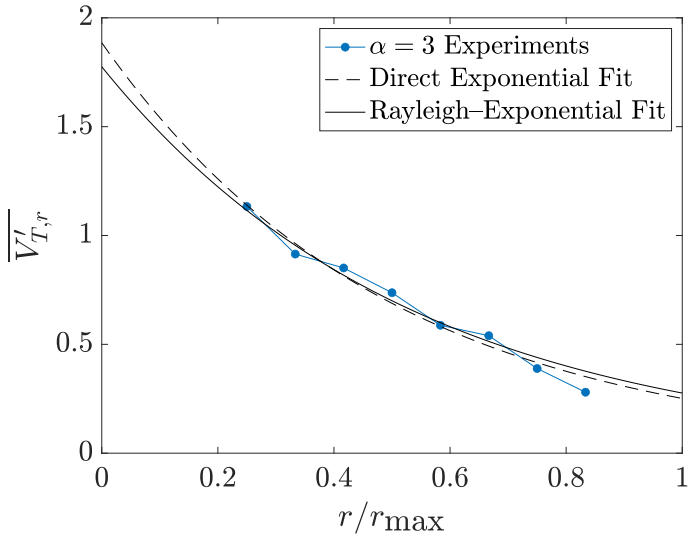

(b)

Figure 7.9: (a) Examples of decomposed Rayleigh distributions, with best fit shown in dashed lines, and (b) exponential fits to the mean lateral velocity with sphere radius ratio, both at $\alpha = 3$.

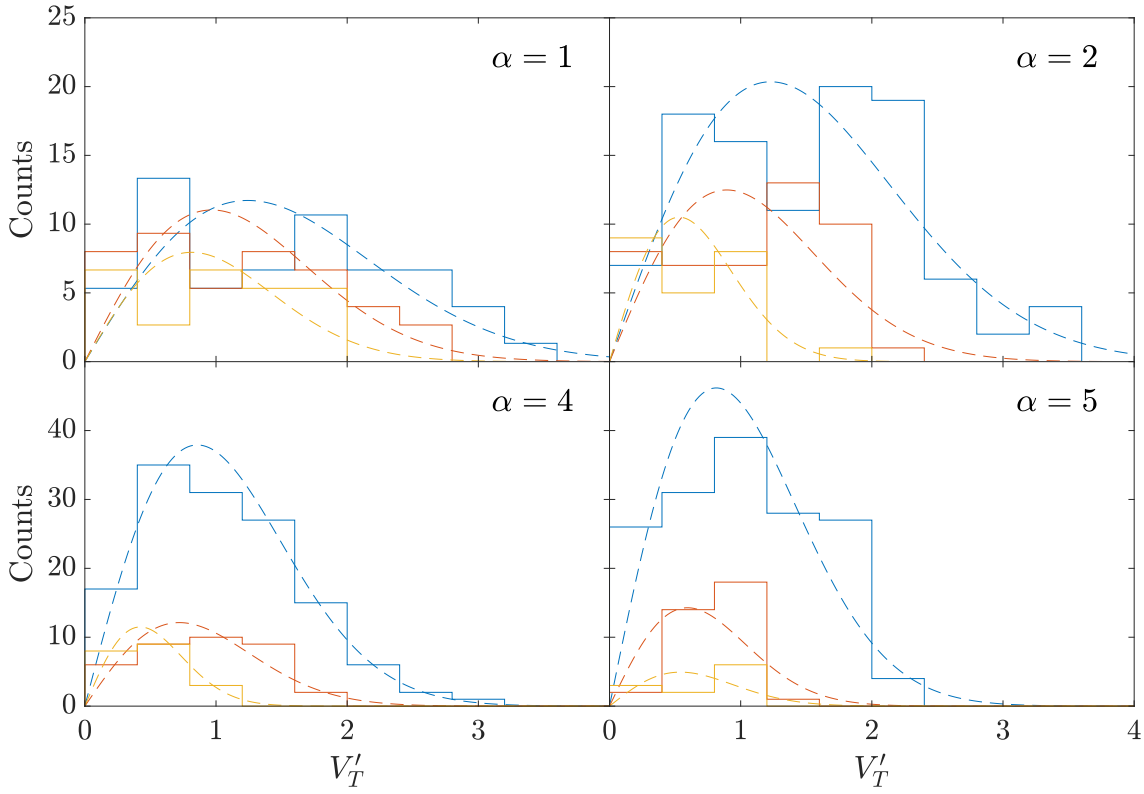

(a)

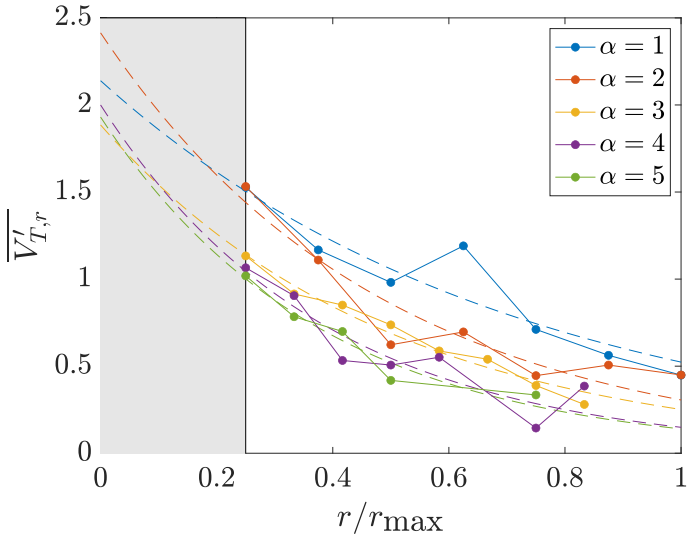

(b)

Figure 7.10: (a) Decomposed Rayleigh fits (dashed lines) for clusters of $\alpha = 1$, 2, 4, and 5. Data taken from three bins of smallest r_2/r_1. (b) Mean lateral velocity within each bin and associated exponential fits.

between the experimental PDF of the scaled lateral momentum and the composite PDF as constructed from the decomposed Rayleigh distributions, scaled according to an exponential function. Mathematically, the Rayleigh–exponential PDF fit to the experimental data, f_{re}, is formed from Equations 6.2, 6.3, 7.1, and 7.2, and can be written as:

$$f_{re}((m/m_c)V_T') = \frac{\pi}{2}\frac{(m/m_c)V_T'}{a^2}\frac{1}{\sum_i r_i^{-\alpha}} \cdot \sum_i \frac{r_i^{-\alpha}}{(m_i/m_c)^2}\exp\left\{-\frac{\pi}{4}\frac{((m/m_c)V_T')^2 e^{2b(r/r_{\max})_i}}{(m_i/m_c)^2 a^2} + 2b(r/r_{\max})_i\right\}, \tag{7.3}$$

where the summation index, i, accounts for all sphere sizes for a given power law and exponential terms a and b are the free parameters initialized using the direct exponential fit.

Continuing with the $\alpha = 3$ example, the modeled mean and standard deviation of the collective lateral velocity in Figure 7.11(a) closely conform to the experimental values (accompanied by only modest alteration to the exponential fit in Figure 7.9(b)), but the Rayleigh–exponential model does result in some discrepancies between the measured and fitted lateral momentum PDFs. Presented in semi-log scaling and with sphere radius increasing from upper-left to lower-right, Figure 7.11(a) reveals, in residual near the plot's upper left, that much of the modeling error is derived from inadequacies in the PDFs of the two smallest sphere sizes; an overestimate of the data near $(m/m_c)V_T' \sim 0.005$ and an underestimate at 0.017 mark the largest deviations but appear to offset one another, yielding close agreement in mass-weighted lateral velocity (0.01% error). Additionally, beyond

$(m/m_c)V_T' \sim 0.05$, the experimental PDF is sparsely populated, so the lateral momentum tail may not be well constrained. Regardless, the agreement between the measured and modeled PDFs is close enough to justify use of this methodology in constraining the separation behavior of unequal clusters.

Modified according to the above PDF-matching routine, the best-fit exponential functions tend decay more slowly than their direct-fit counterparts, with slight downwards translation of the curve, as in Figure 7.9(b). Altogether, the fitted exponentials are displaced downwards with increasing power-law index over the valid radius-ratio domain (0.25 – 1), which is depicted in Figure 7.11(b). Considering the minimum in $\overline{V_T'}$ at $\alpha = 3$, the tendency for higher expulsion of all spheres in lower-α configurations may seem counterintuitive. This apparent contradiction, though, is rectified by recalling the mass fraction constituted by each fragment size; at $\alpha = 1$, the total cluster mass is overwhelmingly composed of larger bodies (hence the 'heavy' designation), which lie on the lower end of the curve, whereas, at $\alpha = 5$, the smaller bodies with higher $\overline{V_{T,r}'}$ predominate. At intermediate values, the combination of the two effects yields the well-described $\alpha = 3$ minimum, while the right and left extrema of $\alpha = 1$ and 5, respectively, begin to approach the theoretical limit of equal-sphere kinematics from below and above.

Finally, in Figure 7.11(c), we compare the modeled collective lateral velocities with those measured experimentally, where the error bars are computed from 10,000 power-law realizations, each with lateral velocities computed according to the Rayleigh–exponential process. While the effects of implementing the above fitting routine appear modest, the $\overline{V_T'}$ estimates match the experimental data better than

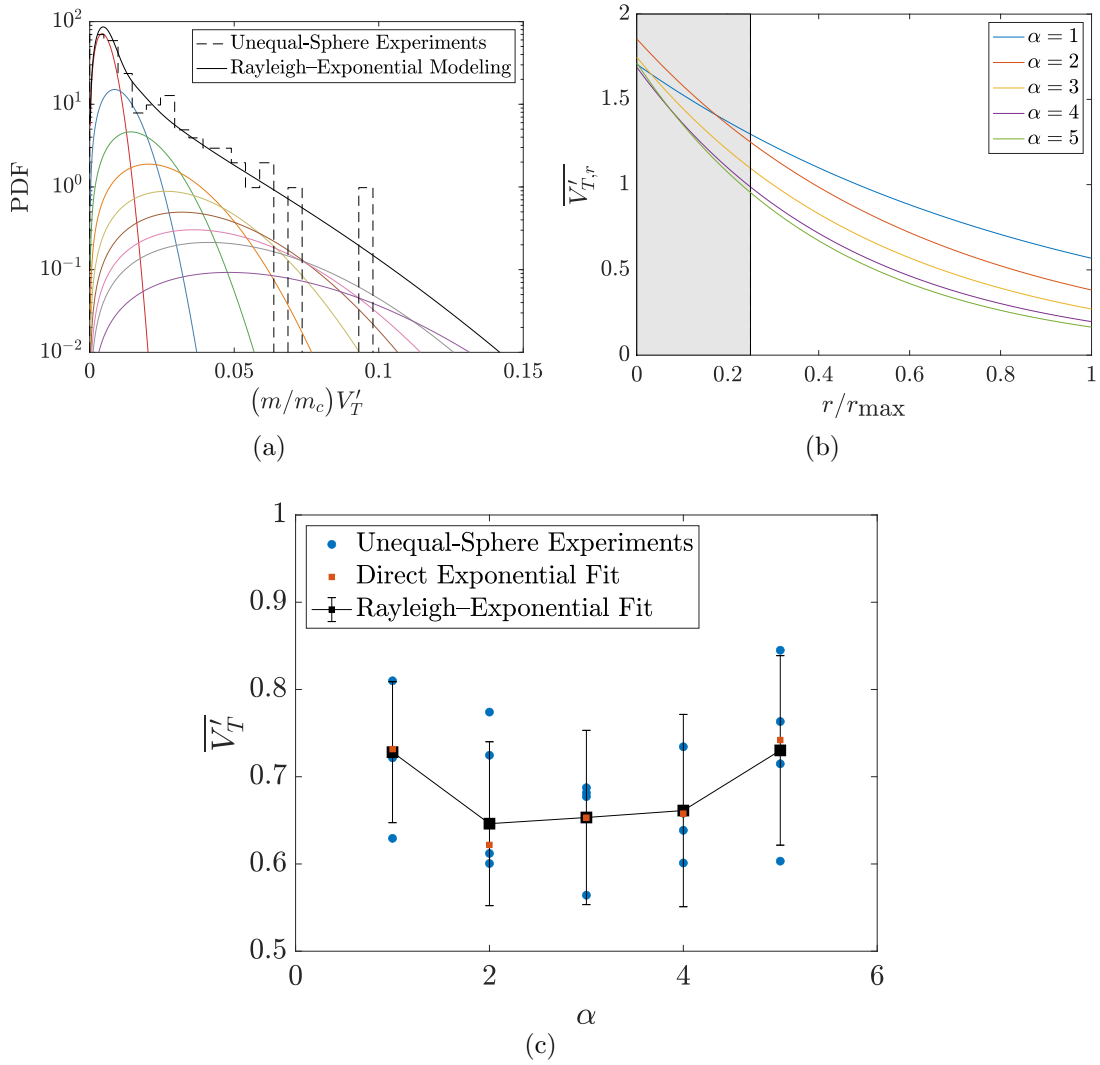

Figure 7.11: (a) Comparison of lateral momentum PDFs from experiments and Rayleigh–exponential model. Colored curves indicate spheres of increasing size moving from upper-left to lower-right and individual PDFs are scaled by power-law probabilities. (b) Optimized exponential functions as derived from PDF-fitting routine, with the invalid $r/r_{\max} < 0.25$ region indicated in gray, and (c) comparison of Rayleigh–exponential collective lateral velocities with experiments.

those computed using the direct exponential fit. At $\alpha = 2$, however, neither method suitably estimates the average collective lateral velocity, stemming from either inaccuracies in the Rayleigh decomposition at that power-law index or unconverged statistics. The measured and modeled standard deviations are also in rough agreement, with the exception of overestimates at $\alpha = 3, 4$. This methodology thus yields close agreement with the statistics of the experimental dataset and can be justifiably employed for prediction of the dispersal of fragmented bodies transiting the atmosphere. One should remain aware, however, of the effects of limited sample sizes on the fidelity of the Rayleigh–exponential description of unequal-sphere separation, which can be alleviated only by further extensive testing.

7.4 Separation Modeling

Now with a operational description of the lateral velocities of spheres separating from a number of unequal-cluster power-law indices (where equal-sphere clusters are generalized as realizations of power laws at indices $\pm\infty$), we can predict, in a statistical manner, fragment dispersion given only a cluster population, N, and power-law index, α. First, we note that the Rayleigh–exponential fits of Section 7.3 are particular to populations of fifty-two spheres only. Thus, for closure of the vast parameter space, this modeling approach considers the effects of population and fragment size distribution to be separable, an assumption which cannot be verified using the existing data but may be expected to produce reasonably accurate results for larger populations in which primary separation chiefly dictates the magnitude

α	a	b
1	1.30	0.82
2	1.25	1.19
3	1.10	1.40
4	0.99	1.61
5	0.95	1.76
$\pm\infty$	$\overline{V'_T}_{,N=52} = 0.82$	0

Table 7.1: Exponential parameters for unequal-sphere lateral velocity fit

of mutual repulsion. Furthermore, the exponential fits to the size-dependent lateral velocities of Section 7.3 rely on a minimum-to-maximum radius ratio of 0.25, which will not be applicable to clusters with different ranges of fragment size. To account for this requirement, we introduce a linear scaling to transform the radius-ratio domain to [0, 1], which, in turn, modifies the exponential parameters of Equation 7.2: $a \rightarrow ae^{-b/4}$ and $b \rightarrow 3b/4$. Such a transformation might not be physically consistent, but it forces the $\overline{V'_T}$ values of more populous unequal clusters to remain less than the corresponding equal-cluster value, which essentially upholds the critical finding of Section 7.3. Further testing with different radius ratios would help inform the physically appropriate method of introducing a radius scaling. The best-fit exponential parameters for each power-law are thus given in Table 7.1. When non-integer values of α are desired, linear interpolation between the listed values is performed (extrapolation beyond the tested range has not yet been implemented).

The general process for predicting the lateral velocity of a disrupted body of predetermined N and α is thus formulated as follows:

1. Generate a set of spherical fragments according to the power law:

$$p(r) = Ar^{-\alpha}, \tag{7.4}$$

where A is the normalization constant. At this stage, using mass conservation considerations, one also determines the $r_{\min}$ and $r_{\max}$ values needed to scale the radius ratio.

2. For all selected spheres, compute the mean lateral velocity specific to that radius using the exponential fit:

$$\overline{V'_{T,r}} = ae^{-br_s}, \tag{7.5}$$

where a and b are functions of α made available in Table 7.1 and the normalized radius, r_s, is defined as:

$$r_s = \frac{r - r_{\min}}{r_{\max} - r_{\min}}. \tag{7.6}$$

3. Obtain lateral velocities for individual spheres by sampling the corresponding Rayleigh distributions, which are scaled according to $\overline{V'_{T,r}}$:

$$p(V'_T|\overline{V'_{T,r}}) = \frac{\pi}{2}\frac{V'_T}{\overline{V'_{T,r}}^2}e^{-\pi V'^2_T/(4\overline{V'_{T,r}}^2)}. \tag{7.7}$$

4. To account for population effects, scale all V'_T by the collective lateral velocity expected at that population:

$$V'_T \rightarrow V'_T\frac{\overline{V'_{T,N}}}{\overline{V'_{T,N=52}}}, \tag{7.8}$$

where $\overline{V'_{T,N}}$ is governed by the power-law relation

$$\overline{V'_{T,N}} = A(N-2)^{\beta} + \overline{V'_{T,N=2}}, \tag{7.9}$$

with A and β values of 0.123 and 0.407, respectively, and $\overline{V'_{T,N=2}}$ set to 0.22 (see Section 4.1).

5. Finally, appealing to the isotropy of populous equal-sphere clusters, the separation azimuth for all fragments is established by sampling the uniform distribution on $[0,\ 2\pi]$.

This simple stochastic process can be used to generate randomized lateral velocities representative of clusters of the desired class and population. To demonstrate the new capabilities afforded by our statistical modeling approach, we provide two examples of zy-velocity distributions in Figure 7.12. In the first, forty equal-sized spheres separate with a collective lateral velocity of 0.63, while the second shows the dispersion of two-hundred fragments generated from a power-law index of 3. Such results can be used to seed the lateral velocities of fragments at the moment of atmospheric disruption prior to simulating the remainder of their flight to the ground, enabling investigation of ground damage characteristics for various selections of impactor class. Examining trends in strewn field formation is beyond the scope of the current work, however, and is left open for future studies.

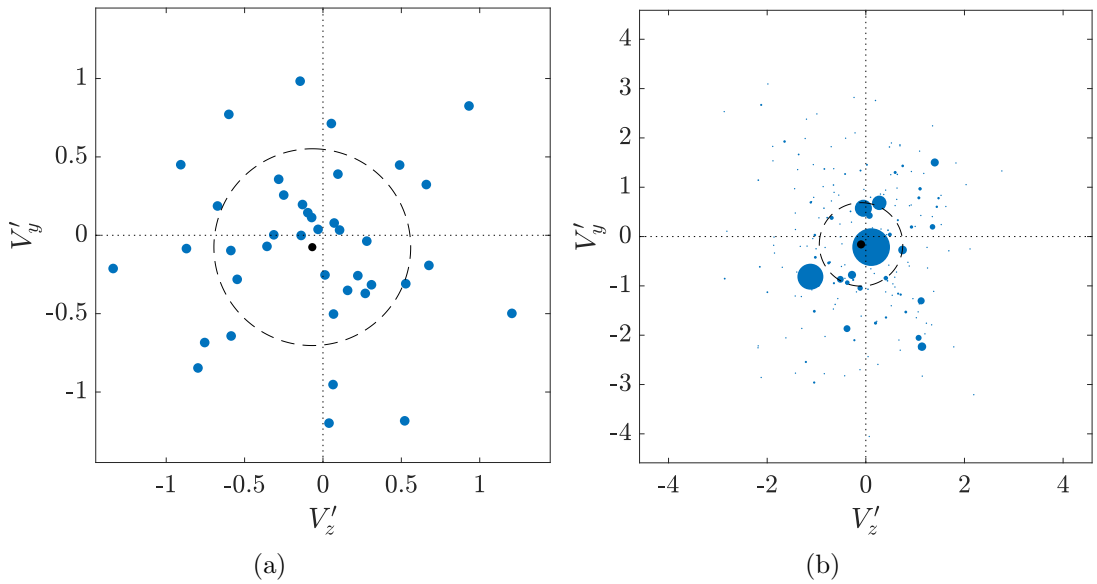

Figure 7.12: Sample lateral velocities from (a) forty equal spheres and (b) two-hundred spheres from $\alpha = 3$ power law, as generated by the Rayleigh–exponential model with population scaling.

7.5 Conclusions

In this chapter, qualitative observations of several free-flight wind tunnel tests demonstrated the stark differences between the present unequal-cluster scenario and the equal clusters of previous chapters. Additionally, the trajectories of an experiment at a power-law index 3 was examined in detail, revealing the presence of phenomena such as drafting, shielded contact, and far-wake flight, which were not attainable in equal-sphere configurations. Despite the highly enhanced ejection of the smallest bodies, coalescence of subclusters proved a dominant aerodynamic mechanism, behind only initial mutual repulsion. The persistence of subclusters throughout the separation process was found to inhibit the overall dispersal of spheres, with the amount of retained mass correlated to the mass-weighted collective lateral ve-

locity. Due most likely to its equal distribution of mass in fragments of all sizes, the power-law index of 3 exhibited the highest degree of subclustering and minimal fragment dispersal, whereas α values of 1 and 5 appeared to mark a transition toward the behavior of equal-sphere clusters. The resemblance of both the size-based lateral-velocity subsets to the Rayleigh distribution and the mean lateral velocities to the exponential function prompted the adoption of a statistical separation model wherein the overall fragment dispersal is decomposed into distinct Rayleigh distributions, scaled each by a radius-ratio-dependent exponential function. This model of fragment separation can thus be employed to predict the lateral separation velocities of any cluster composition (within the scope of the model problem), which may be of considerable use for ground damage risk assessment.

Chapter 8: Dusty Debris

Having fulfilled the primary objectives of the model problem of discrete fragmentation, we now advance to an entirely different class of disruption phenomenon. As the name suggests, the rubble pile impactors that form the an appeciable fraction of the Solar System's identified potentially hazardous objects possess negligible internal strength (Walsh, 2018) and are expected to respond to high-speed flows far differently than their airburst meteor counterparts. Rather than catastrophically fragmenting at a particular altitude, debris clouds should instead experience continuous deformation over a range of altitudes. The problem of dusty debris separation has been recognized as significant for decades, but all efforts to characterize its behavior and model the risks posed have been purely theoretical in nature and lacking in empirical support (Chyba et al., 1993; Hills and Goda, 1993). As an addendum to the core of the present work and as an analogy for rubble pile impactors, we extend the experimental methodology of Chapter 1.5 to clusters composed of a fine powder and interpret the results in the framework of mass depletion and energy deposition.

The dusty debris experiments were an unplanned supplement to the primary wind tunnel campaign and, therefore, were conducted with a material already on hand rather than another acquired for this purpose. Specifically, the cornstarch baby

powder which coated the 3D-printed models to mitigate adhesion to spheres was repurposed as the dusty debris of interest. The powder was lightly packed into a 13.9-mm-diameter suspension/release shell rolled by 45° to minimize dust spillage onto the lower window, which supported both unimpeded vertical visualization and the integrity of the dust pile's spherical structure. To resolve the fine fluid and granular details of these clusters, we converted the shadowgraph camera of arrangement C2 to high-resolution mode, which quadruples the number of available pixels at the expense of the system's acquisition rate, reduced to 9.4 kfps here. Given the ad hoc nature of the setup, certain quantities such as the cluster mass and particle size distribution were not measured prior to experimentation, leaving these parameters subject to approximate estimation during later analysis.

As is standard, this chapter will begin with general qualitative observations of two tests demonstrating distinct characteristics before introducing an analysis technique enabling assessment the cloud's mass at each image of the experiment. Next, a new atmospheric energy deposition model founded on mass depletion considerations is proposed and evaluated, with emphasis on implications for ground damage risk. Finally, a single hybrid-separation experiment, serving as the closest approximation to an actual disruption event in this work, will be briefly investigated.

8.1 General Observations

The currently accepted description of dusty debris at hypersonic conditions is one of a rapidly flattening cloud, compressed under the burden of a profound stream-

wise pressure differential and extending laterally to compensate (Chyba et al., 1993; Hills and Goda, 1993). This 'pancake' or 'liquid drop' model of dusty debris is instantly refuted by a cursory examination of Figure 8.1, which instead presents a shadowgraph view of a cloud that largely resists expansion (similar to the experiment of Schultz (2008)). The debris cloud of shot PB, following a transient event suspected to stem from shell separation (frames 1 and 2), spawns an elongated trail of dust behind its upwind hemispherical cap and ejects a smaller fraction of particulate into the outlying regions nearer the bounding bow shock. In fact, the lack of expulsion by shock surfing is somewhat surprising, but a closer examination of the particle front reveals a bow shock offset far enough to prevent individual grains from accessing shock impingement states. By frame 3, the well-established dusty tail extends beyond the visualization volume, reaching a length of at least 14 initial cloud radii, and seems to decline in grain density downstream, although precise estimation of line-of-sight particulate abundance is not possible in the present arrangement. Through frames 3 and 4, the particle front maintains a steady, smooth appearance, but later, (frames 5 and 6) minor disturbances modify the cloud's upwind contour and propagate laterally downstream. As the powder exits the field-of-view, its inferred frontal area remains comparable to that observed at the beginning of the experiment, strongly reinforcing the notion of a cloud resistant to lateral spreading. As will be discussed in Section 8.3, the resistance to flattening may allow the impactor to penetrate much further into the atmosphere than the existing models allow, which would drastically alter the ground risks posed.

The extended dusty wake and resistance to lateral separation exhibited by

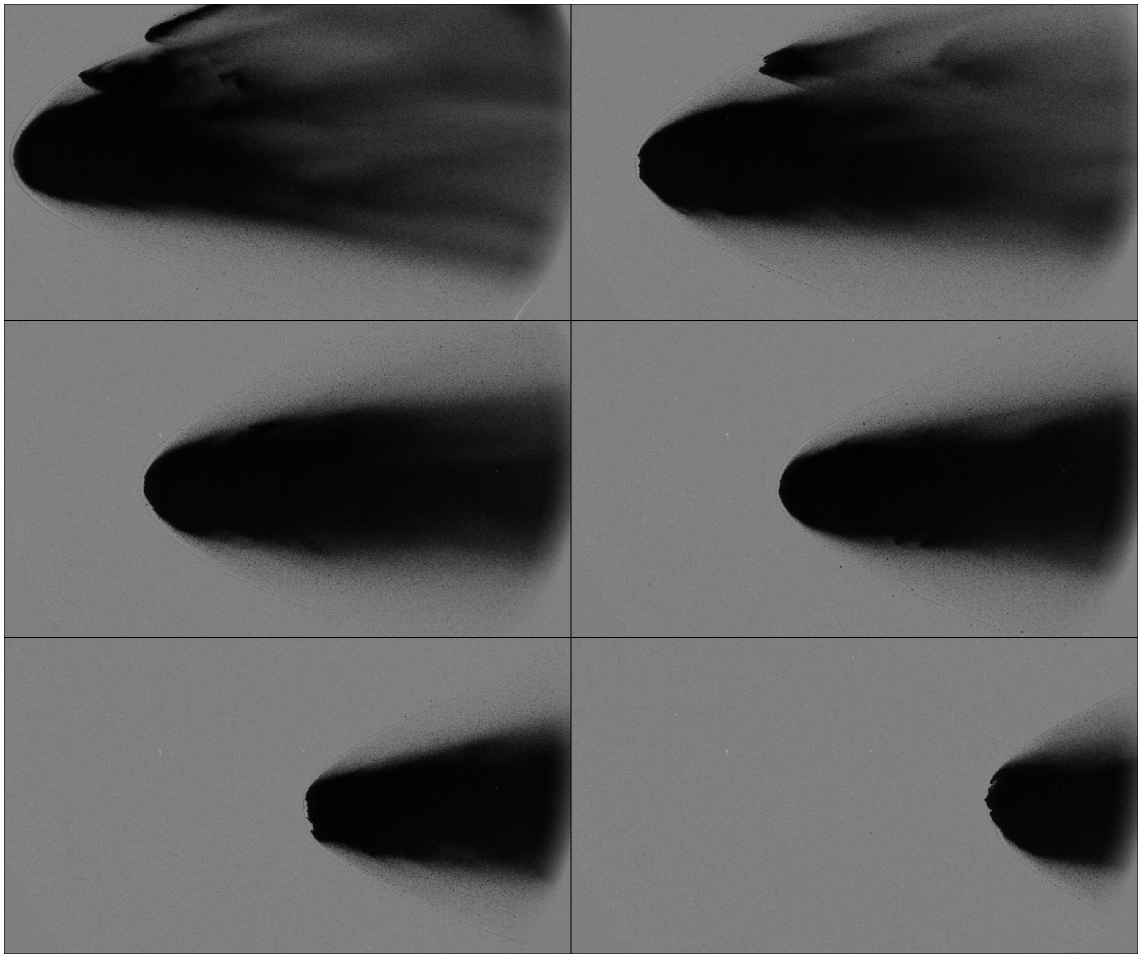

Figure 8.1: Shadowgraph sequence of shot PB, with images shown in increments of $0.48\tau_s$ (0.62 ms).

present debris cloud are unexpected behaviors that necessitate a reevaluation of the fluid physics governing such scenarios. The fundamental tenet of the existing debris expansion models is the intense streamwise pressure differential across the cloud, which is effectively unopposed by expansion-influenced forces on the cloud's flanks. In this scenario, the resulting flattening then increases the frontal area of the cloud, which intensifies the compressive forces and leads to runaway lateral expansion. However, in approximate agreement with the less-accepted 'needle' interpretation of fragmentation (Schultz, 2008), the exact opposite behavior is observed in Fig-

ure 8.1, suggesting that inwardly directed outboard forces balance the streamwise compression. The conception of aerodynamic forces in the existing models relies on a definition of the pressure distribution dictated by the contours of an impermeable flow-generating body, whereas the debris cloud more realistically allows for some degree of through-flow. Thus, we engage in a brief thought experiment to decipher the propagation of porosity effects onto the overall cloud dynamics. Consider the pressure distribution on the surface of an impermeable blunt body in high-speed flow: the streamline that follows the surface contour originates from a region immediately adjacent to the stagnation streamline, and because entropy is conserved along streamlines, the stagnation pressure is essentially equivalent to the freestream Pitot pressure, providing an upper bound on the static pressure over the windward surface of the body. If porosity is allowed, on the other hand, we can imagine that some fraction of the flow along every streamline is ingested into the body, and subsequently is decelerated to near-stagnation conditions; progressing further away from the primary axis, the stagnation pressure would then be increasingly governed by streamlines that transit weaker portions of the bow shock, through which irreversible losses are reduced. The result would thus be the presence of outwardly directed static- stagnation-pressure gradient on the body's exterior and interior, respectively. Returning to the problem at hand, a stagnation pressure gradient oriented outwards from the cloud's primary axis could be capable of balancing the compressive action of the streamwise pressure differential and, therefore, inducing the constancy in the spanwise extent of the cloud. Additionally, outboard fragments, acting more as individual particles than members of a swarm, would tend to

be propelled downstream, which is consistent with the extended trail of particulate in the wake. Of course, this analysis is, at best, highly approximate in nature but may help to comprehend the major discrepancy between the present observations and existing models.

Another important facet of the cloud's resistance to flattening is the implied transition from the inevitable separation behavior of discrete fragment swarms. Recalling the power law relating the lateral extent of a cluster to its population, the separation velocity diverges in the high population limit, which is clearly inconsistent with the compactness of the cloud in shot PB. Examining the shadowgraph images of incipiently released populous clusters (see, Figure 6.3(b), for example) and debris clouds, obvious differences in the shock structures emerge. The bow shock encompassing the cluster of shot 115D, for instance, exhibits a short standoff distance and follows the outline of the cluster's silhouette, appearing to impinge on every exposed sphere. Further offset from the particle front, the shock of shot PB possess a smooth profile, reminiscent of a sphere-generated bow shock, with impingement structures noticeably absent. As discussed extensively in Chapters 4–6, shock impingement is chiefly responsible the primary phase of fragment separation, so it almost seems intuitive that an arrangement lacking such features would resist lateral expansion. The question of interest, then, is at what cluster population shock impingement ceases to occur and the power-law correlation of Chapter 6 loses its validity. To roughly estimate the population at which separation begins to be suppressed, we assume that the transition between behaviors occurs when the expected shock-standoff distance is equal to the sphere radius. After performing some simple

calculations involving cluster porosity in equal-sphere clusters, we find a population threshold of 385 for Mach-6 flow; in the high Mach number limit, this instead evaluates to 510. If, on the other hand, the sphere diameter serves as the appropriate shock-standoff threshold, these estimates rise to $\sim 3,000$ and $\sim 5,000$, respectively. The power-law relation, therefore, might sustain its validity to much higher populations than those considered in the discrete-fragment portion of this study, allowing for values of $\overline{V_T'}$ approaching 1.8 (or, for the alternate transition definition, 4.1) for realistic entry Mach numbers.

The visualization of shot PB indicate that debris clouds dissipate by means of continuous mass loss to the elongated tail, but other experiments provide evidence for discrete shedding modes that may accelerate the mass depletion process. The best example of discrete shedding comes from the shot PE, with the relevant portion of the experiment (and accompanying annotations) shown in the zoomed shadowgraph sequence of Figure 8.2. Note that we omit discussion of the uppermost feature, which appears to be a shell-separation artifact. Pictured penetrating the particle front in frame 1, a large grain is propelled into the shock layer, displacing the bow shock upstream and drawing nearby particles into its wake (frame 2). At $\sim 300\mu$m in mean diameter (~ 5 pixels in the present camera view), the grain of interest is far more massive than the surrounding particulate, and the combination of its high inertia and low drag in the cloud's interior likely bring it to the front of the accelerating swarm. By frame 3, the bow shock is transformed to a highly inclined conical shock which impinges on regions of dust further outboard and persists beyond the point at which the large grain reunites with the cloud (frames 4–5). The shocked

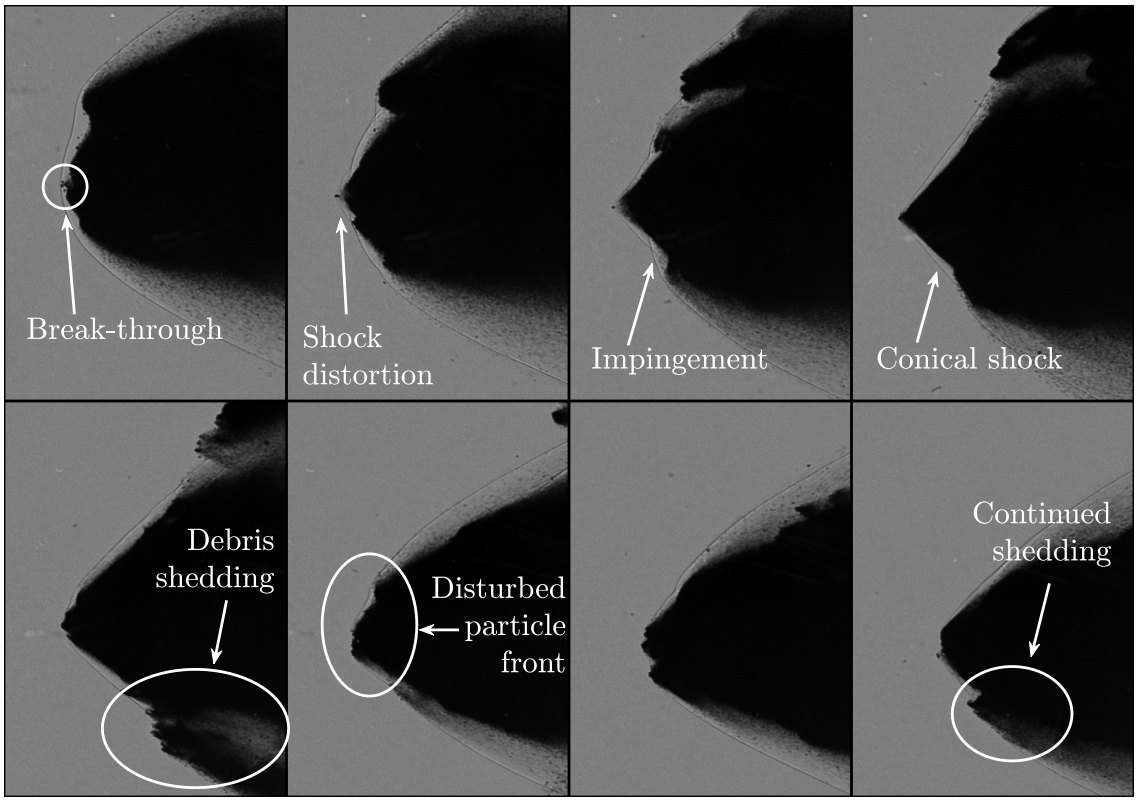

Figure 8.2: Zoomed shadowgraph sequence of shot PE, with images in increments of $0.12\tau_s$ (0.21 ms) and annotations describing important features in the lower half of each frame. Image column shifted by 45 pixels between frames to focus on affected portion of viewing volume.

regions of dust, presumably forming a ring-like structure, appear to accelerate substantially in the lateral direction, which is manifested in enhanced spanwise range of the cloud in frame 5. The cloud quickly reverts to its nominal width after the shedding event passes (frame 6), but the upstream particle front remains severely disturbed, spawning additionally smaller-scale shedding events, such as that visible below center in frames 7 and 8. Stabilization of the particle front after a period of agitation could be achievable, as in the epoch after shell separation transients in shot PB, but such a state seems beyond reach for the current experiment.

While the present propelled-grain-induced shedding incident is the most sig-

nificant of the campaign, many other smaller-scale events occur, always initiated by the inertial motions of a larger grain into the shock layer. The primary implication for the presence of discrete shedding events is the acceleration of the mass depletion process, principally due to perpetuated shedding on a destabilized particle front. We note that the prevalence and magnitude of discrete shedding events is potentially strongly dependent on the particle size distribution of powder employed. For example, a powder with a non-negligible probability of massive fragments would be expected to result in similar unstable behavior, whereas a uniform particulate might exhibit near stability throughout its flight. Unfortunately, the present Johnson & Johnson cornstarch-based baby powder has no published particle size distribution, so, barring future sedimentation measurements, these results cannot be confidently related to the dynamics of other types of debris clouds. Indeed, the purported sensitivity to powder properties highlights the need for meticulous selection of debris material with close attention to the particle size distribution.

Three additional dusty debris experiments were conducted, with one deemed unreliable due to inadequate separation of the suspension shell from the cloud. Of the clouds appearing the two viable tests, one closely resembles the quasi-stable arrangement of shot PB, while the other, in a manner similar to shot PE, exhibits rapid mass loss in the form of discrete shedding events. From this limited exploration of dusty debris clouds at hypersonic conditions, it thus appears that the two identified mechanisms of continuous and discrete particulate shedding dominate the dynamics of such systems, although, with all clusters formed from a presumably uniform powder sample, it is unclear what causes one particular behavior to take

precedence during an experiment.

8.2 Mass Depletion

In the standard model of atmospheric energy deposition, the majority of the energy transfer results from the mass reduction induced by ablation processes. In the current setting, however, the lack of a principal solid object renders the concept of ablation ill-defined, so the critical task in characterizing the risk posed by dusty debris impactors is instead constraining the deterioration timescales of a particular debris cloud, which allows for prediction of the rate of mass loss. Therefore, we introduce a methodology for estimation of the debris cloud's mass based on standard image processing techniques and simple aerodynamic arguments. The following routine is applicable only to debris clouds with well-ordered particle fronts, as in Figure 8.1, for reasons both practical and physical. First, we argue, based on the resistance to shape change of the debris cloud in shots PB and PD (not shown), that a debris cloud is aerodynamically self-similar; that is, its effective drag coefficient remains constant over its flight. Under steady inflow conditions and this assumed drag coefficient, the cloud's frontal area and acceleration — both quantities measurable from shadowgraph imagery — fully constrain the mass of the cluster at any time. Estimating the acceleration is straightforward: we cross-correlate between successive images the grayscale values of 50 pixel rows centered about the front of the cloud, which yields a streamwise offset in the cloud's position following an averaging of the 50 correlation lags. Dividing by both the known lengthscale conversion

and sampling interval, we obtain the velocity of the particle front, which is then finite-differentiated for acceleration using a three-point central scheme. We note that, because of the dispersed nature of the configuration, the notion of cloud acceleration is not well defined, but, assuming that much of the energy transfer occurs along the particle front, this kinematic quantity should be dynamically relevant in the energy deposition process.

Conversely, determination of the effective frontal area is a more involved process, as the lateral edges of the cloud grow downstream and lack a definitive boundary. Discerning similarities between the shape of the cloud's shock and that of a hypersonic sphere (as in Figure 8.3), we employ the analogy of a surrogate sphere generating the same bow shock as the debris cloud to constrain the frontal area. First, we must identify the pixel coordinates of the cloud's bow shock, a process conducted in several stages. Two sets of Canny filters (Canny, 1986) are combined to produce a binary image of the edges of intermediate strength in the shadowgraph, which excludes many of the strong edge pixels near the particle front. Input from the user establishes the edges associated with the bow shock, shown in light blue in Figure 8.3, with edges only as far downstream as the aft of the surrogate sphere typically selected. At this point, a nonlinear least-squares routine minimizes the difference between the observed shock coordinates and those modeled from a Mach-6 AMROC simulation of a stationary sphere, which is additionally illustrated by the red lines and circle in Figure 8.3. The frontal area of the best-fit surrogate sphere,

A_s, is then used in the relation for cluster mass:

$$m_c = \frac{\frac{1}{2}\rho_\infty (u_\infty - v_c)^2 A_s C_D}{a_c}, \tag{8.1}$$

where m_c, v_c, and a_c represent the mass, velocity, and acceleration of the cloud, respectively. Additionally of note in Figure 8.3 is the reduced shock-standoff distance of the cloud relative to the surrogate sphere, indicating that the porosity of the cloud does indeed allow for ingestion of the post-shock flow, as discussed in Section 8.1.

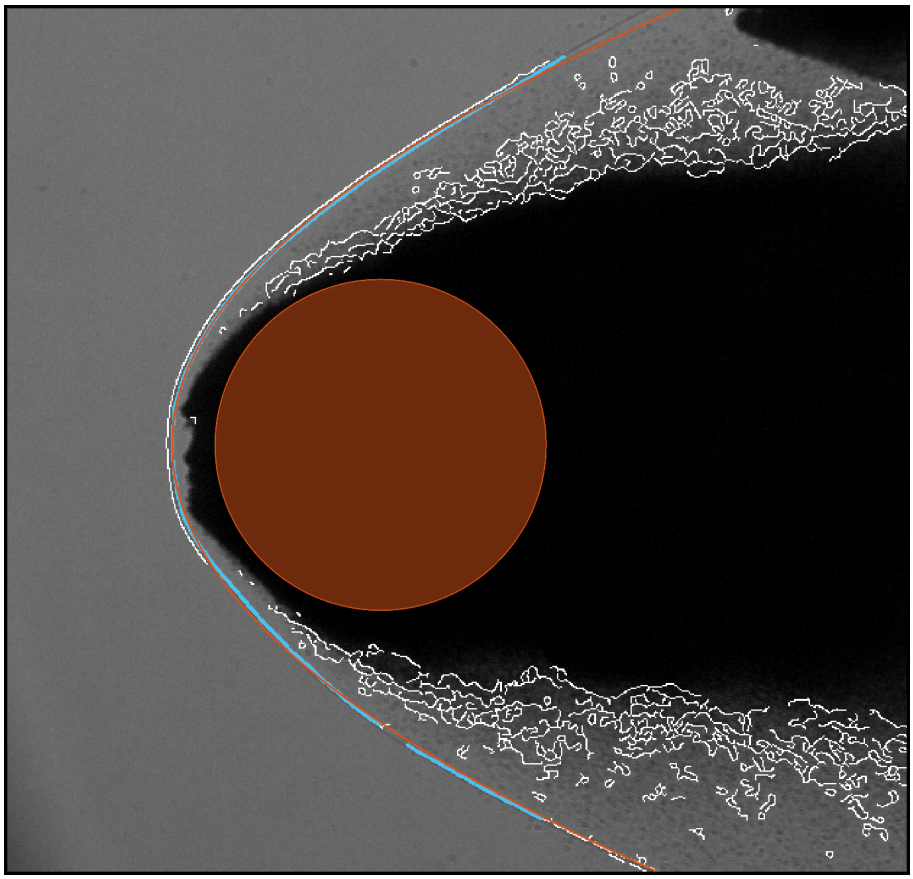

Figure 8.3: Shadowgraph image of shot PB demonstrating surrogate sphere fitting methodology. Intermediate-strength edges overplotted in white, user-selected bow shock pixels in light blue, and the fitted sphere and computational bow shock in red.

In Figure 8.4, the temporal development of the cloud mass from shot PB

demonstrates an appreciable degree of variability but, overall, appears to follow an exponential relationship. Here, the initial cluster mass, m_0, is estimated from a typical bulk density of loosely packed powder (700 kg/m^3, Rojas et al. (2012)), and the release time is chosen as the frame in which the shells have separated from the debris in the vertical camera view. Furthermore, in the absence of a concrete characterization of the aerodynamics of this configuration, we assume a drag coefficient of unity. The logarithmic decrement of the mass loss history, which removes the dependence on the tunable parameters, is too noisy to constrain the mass depletion timescale (it evaluates to 4–8τ_s for different subsets of $\overline{m^{i+1}/m^i}$), so we opt for an exponential fit of form:

$$\frac{m}{m_0} = Ae^{-t/\tau_d}, \tag{8.2}$$

where A is a generic scaling coefficient and τ_d the mass depletion timescale. Shown atop the cloud's mass history in Figure 8.4, the fitted exponential function with time constant $\tau_d = 4.43\tau_s$ nearly extrapolates to the initial mass at time-zero (i.e., $A \sim 1$), which loosely verifies the viability of the relationship. Of course, this particular function is sensitive to the drag and packing density parameters chosen, but, forcing $A = 1$ in the fit and letting each parameter vary by 20%, we find a range of τ_d values spanning roughly $\pm 1\tau_s$. Additionally, we find that the radius of the surrogate sphere is $\sim$ 50% greater than that computed from a spherical arrangement of the cloud's mass at its initial bulk density, which will be of use in the following section. Despite the uncertainty associated with this assessment of

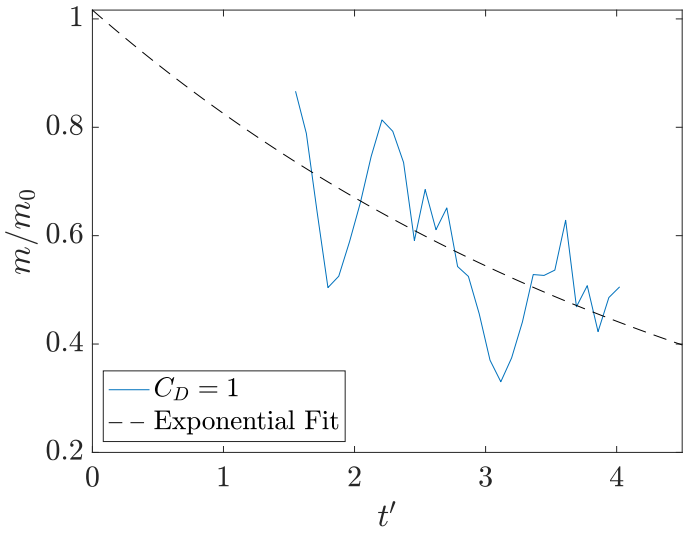

Figure 8.4: Mass of debris cloud in shot PB, assuming a drag coefficient of 1. Exponential fit with $\tau_d = 4.43\tau_s$ shown in dashed black.

the decay constant (additional testing would help constrain this value), the present exponential fit can form the basis of a new approach for modeling the atmospheric energy deposition of rubble-pile-type impactors.

8.3 Energy Deposition Modeling

The exponential mass loss of dusty debris clouds represents a major modification to the physics of atmospheric entry that will undoubtedly alter the modeling of energy deposited over a wide range of altitudes. To demonstrate the expected energy transfer of such impactors, we employ the standard trajectory equations

of Opik (2004):

$$\begin{aligned}
\frac{\mathrm{d}V}{\mathrm{d}t} &= \frac{\frac{1}{2}\rho_a V^2 C_D A_s}{m} - g\sin\theta, \\
\frac{\mathrm{d}\theta}{\mathrm{d}t} &= \left(\frac{V}{r_E + h} - \frac{g}{V}\right)\cos\theta, \\
\frac{\mathrm{d}m}{\mathrm{d}t} &= -\frac{1}{2}\rho_a V^3 \sigma_{ab} C_D A_s, \\
g &= g_0\left(\frac{r_E}{r_E + h}\right)^2,
\end{aligned} \tag{8.3}$$

where g and g_0 represent gravitational acceleration in the atmosphere and on the ground, respectively, σ_{ab} is the ablation coefficient, r_E is Earth's radius, h is the impactor's altitude, θ is its angle of travel above horizontal, and the freestream quantities ρ_∞ and u_∞ have been replaced by the time-dependent terms ρ_a and V, respectively. Introducing into this framework the physics of debris clouds, we replace the ablative mass loss relation with the ordinary differential equation form of the exponential decay from Equation 8.2:

$$\begin{aligned}
\dot{m} &= -\frac{1}{\tau_d} m, \quad \text{where} \\
\tau_d &= 4.43\sqrt{\frac{\rho_c}{\rho_a}}\frac{r_c}{V}.
\end{aligned} \tag{8.4}$$

Additionally, r_c is computed by scaling up the radius of the cloud by 50%, in accordance with the correlation observed in Section 8.2. Considering that only a single test was used to define the present mass-loss model, a critical assumption here involves the use of a dimensionless timescale referencing the effective radius of the cloud (using the surrogate sphere definition and corrective scaling) and its initial bulk density. Such a nondimensionalization is well-suited to discrete fragmen-

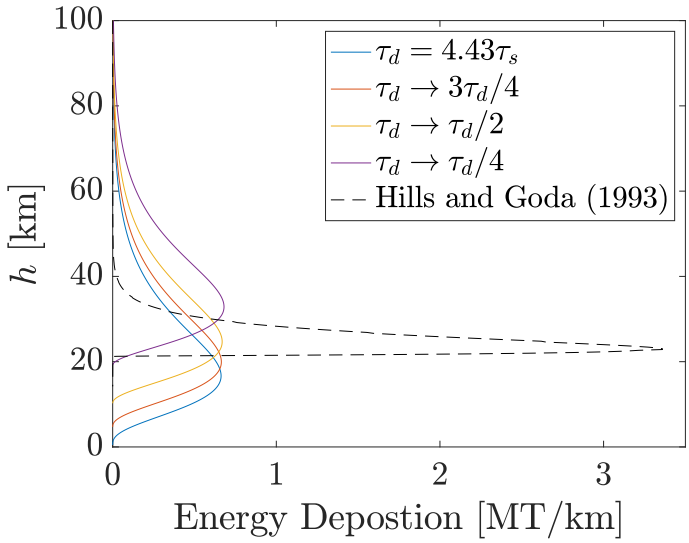

Figure 8.5: Atmospheric energy deposition of a rubble-pile impactor with the following parameters under differing mass loss models: $V_0 = 30$ km/s, $r_{cl,0} = 30$ m, $\theta_0 = 45°$, and $\rho_{cl,0} = 1500$ km/m^3.

tation problems but, in the context of dusty debris, requires confirmation though additional testing. Likewise, our measurement of the mass depletion time constant ($4.43\tau_s$) possesses a high degree of uncertainty, especially with potential acceleration of cloud deterioration by discrete mass shedding events and the accompanying particle front destabilization. Nonetheless, the present data represent a suitable first step to the observationally constrained energy deposition of debris clouds.

First, a comparison with the existing 'pancake' model of Hills and Goda (1993) is fitting. The baseline scenario considers an 30-m impactor of bulk density 1500 kg/m^3 entering the atmosphere at a velocity of 30 km/s and inclination angle of 45°, with the drag coefficient fixed to a value of unity and the ablation coefficient (for the pancake model) to 10^{-8} s^2/m^2 (Bronshten, 2012). Substantial differences in the deposited energy predicted by each model are manifest in the Figure 8.5 . As might be expected, the debris cloud's resistance to spreading allows it penetrate

much further into the atmosphere, lowering the altitude of peak energy from 23 km to 16 km. Meanwhile, the onset of mass shedding occurs at higher altitudes, reaching non-negligible energy transfer (5% of peak) at 60 km, approximately 20 km above the same threshold for the pancake model. Also an anticipated consequence of the cloud's morphology is the drastic reduction in peak energy, which represents a fivefold decrease from the pancake model and obscured the meaning of a unique burst altitude. Despite the reduced severity of energy deposition, the proposed model predicts an increased risk of ground damage with appreciable energy transfer sustained down to altitudes of 2 km. Uncertainty in the mass depletion constant, τ_d, induced by discrete shedding behavior may mitigate some of this risk, however. Assessing the energy deposition under several variations of the time constant (biased to shorter depletion timescales), we find that entire curve is shifted considerably upwards, and, in the case of $\tau_d \rightarrow \tau_d/4$ lies almost entirely above the prediction of Hills and Goda (1993). In any case, the empirically constrained debris cloud model signifies an exceptional modification to the behavior expected of rubble pile bodies transiting Earth's atmosphere.

Having established a general understanding of the behavior of dusty debris impactors during atmospheric transit, we seek to evaluate the sensitivity of these characteristics to variations in the principal entry parameters: initial velocity, radius, inclination angle, and bulk density. Thus, in Figure 8.6, we give the energy deposition of debris clouds under selected conditions, with the baseline case of Figure 8.5 highlighted in solid black. The most surprising result is that the altitude dependence of energy deposition is completely insensitive to changes in entry veloc-

ity, as the heights of peak deposition (16 km) and complete deterioration (2 km) are identical for all scenarios. Such a finding stands in stark contrast to the model of Hills and Goda (1993), which predicts a strong dependence of burst altitude on an object's initial velocity. Alterations to the radius and bulk density parameters likewise represent changes to an impactor's initial kinetic energy, but the modification to the energy deposition profile is far more significant. For example, a 15-m meteroid fully deteriorates at an altitude of 12 km, whereas an impactor of initial radius 35 meters survives to the ground intact. Also, as might be surmised, the entry of an impactor at a shallower angle increases the path length per unit height, which in turn causes the debris cloud to dissipate at higher altitudes; the shift between peak-energy altitudes of 13 km and 26 km for 75° and 15° entries, respectively, reinforce this notion. Overall, however, the proposed model for dusty debris entry is highlighted by the penetration of an impactor deeper into the atmosphere and the associated heightened risk of ground damage.

8.4 Hybrid Separation

Many documented airbust events are characterized by fragmentation of a consolidated impactor into both discrete fragments and an abundance of dusty debris (Borovička and Kalenda, 2003; McCord et al., 1995; McIntosh and Douglas, 1968; Popova et al., 2013), combining components from all preceding investigations. To establish a foundation for interpreting such scenarios, we conducted a single experiment with both fifteen equal-sized spheres and cornstarch baby powder, and

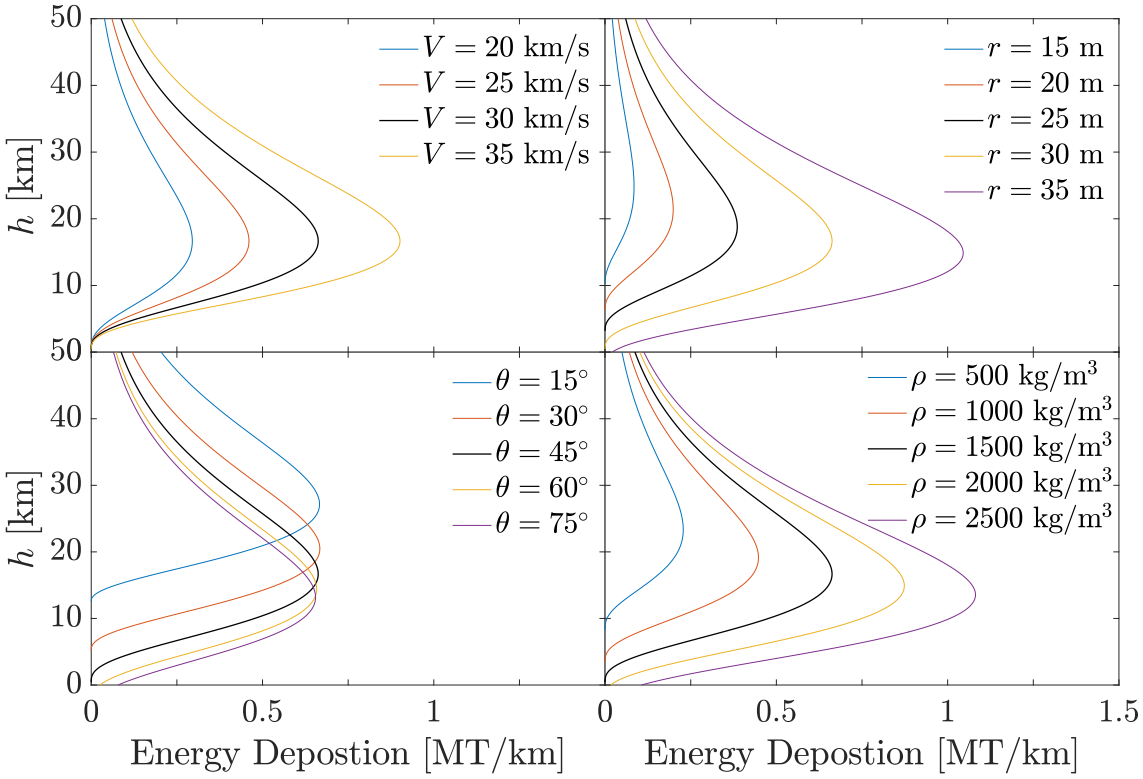

Figure 8.6: Parametric variation of primary entry variables for energy deposition of dusty debris impactors. Values corresponding to baseline case of Figure 8.5 shown in solid black.

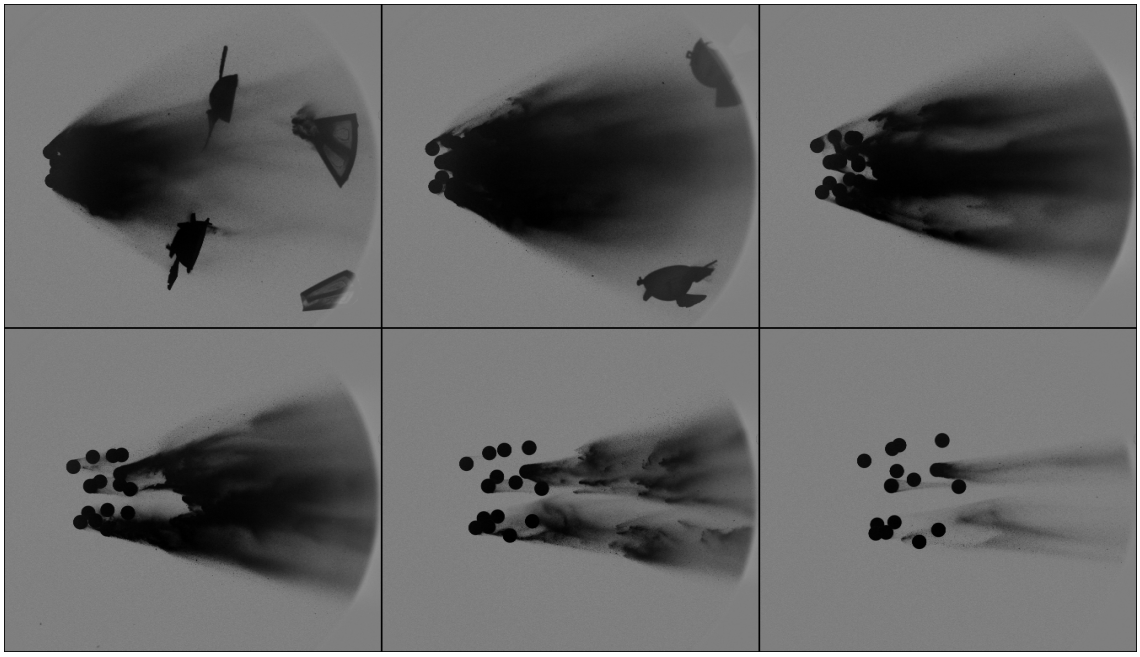

Figure 8.7: Separation sequence of hybrid cluster in shot 15P with standard-camera images shown in increments of $0.44\tau_s$ (0.78 ms).

tracked the motions of the spheres once unobscured by dust. The side view of shot 15P (so designated due to the presence of the powder) is thus presented in Figure 8.7. The dusty debris, estimated to account for $\sim$1/3 of the cluster's mass, thoroughly encompasses the spheres in frame 1 ($t' = 0.42$) but is rapidly transported downstream, as the forward bodies are fully visible in frame 2. As the test progresses, the dust is increasingly confined to the wake regions of certain spheres (frames 4 and 5) and is soon entirely swept downstream, barring a wake-entrained accumulation that seems to recirculate within the wake of one sphere for the duration of its flight.

The interplay between the dusty debris and spheres introduces interesting modifications to the behaviors diagnosed throughout this work. In Section 8.1, the presence of abnormally large grains appeared to accelerate the cloud mass depletion process, and, in a similar manner, the large spheres suppress the hemispherical

particle front that enables quasi-stable propagation in a hypersonic flowfield. In this particular configuration, the mode of dust cloud deterioration seems simpler: the spheres, of higher overall inertia, channel the dust into lanes between bodies, from which it is subsequently convected into the wake region. From the visualization of Figure 8.7, the dust is almost entirely swept downstream by $t' = 2.2$, far sooner than would be expected for the previous debris clouds. The influence of the dust on the kinematics of the spheres is notable as well. Inspection of the reconstructed sphere trajectories (omitted here) reveals a conspicuous absence of bodies in the vicinity of the system's primary axis, generally a standard feature of equal-sphere clusters of intermediate population. Indeed, the collective lateral velocity of the spheres ($\sim$ 0.70) surpasses the $\overline{V_T'}$ of all other fifteen-sphere experiments, lying $\sim 1.7\sigma$ beyond the average value of the other experiments (0.58). The role of the dust, it appears, would be to assist in repelling all spheres from the center of the agglomeration. Of course, such a proposition cannot be confirmed from a single experiment, but characterization of the potential enhancement to the lateral spread of fragments constitutes a critical problem for future studies.

8.5 Conclusions

Observations of a fine powder in a hypersonic flow have uncovered major inaccuracies in the existing model of dusty debris impactors. In particular, a nearly hemispherical particle front resists flattening and lateral spreading in favor of expulsion of outboard particles into an extended tail. However, the presence of large

grains can induce discrete shedding events and the general destabilization of the particle front, potentially accelerating mass depletion. Nevertheless, analysis of the kinematics and morphology of the narrow dust column allowed for estimation of the exponential mass depletion timescale, which itself formed the basis of a new model of energy deposition. Limited modeling efforts demonstrated that impactors of a dusty debris composition penetrate much deeper into the atmosphere than predicted by the existing model, which may elevate the risk of ground damage. Finally, the investigation of a single hybrid separation experiment revealed details of the interaction between equal spheres and dusty debris, with enhanced lateral separation and accelerated dust shedding possible consequences.

Chapter 9: Conclusions

Meteor impacts are a perpetual threat to humanity and, in the size range of astronomical objects that strike Earth most frequently, almost universally result in catastrophic fragmentation that generates blast waves, impact craters, thermal radiation, and other assorted hazards. The physics of meteoroid fragmentation, however, are poorly characterized, especially the during epoch of aerodynamic separation following structural detachment. Existing models of fragment dispersal have been founded on either unrealistic physical arguments or the dynamics of sphere pairs, the latter of which is unlikely to accurately model the populous swarms commonly observed. Thus, the need for a physically consistent description of meteor disruption based on observations of fragment-cluster aerodynamics is manifest.

Throughout the present work, we adhered to a model problem of meteor fragmentation in which a cluster of close-packed spheres is released instantaneously into a steady hypersonic flow. While this representation of aerodynamic separation is quite simplified from actual airburst events, many of the assumptions therein introduced only minor inaccuracies and have beem frequently employed in related works. With the population and fragment size distribution of a cluster hypothesized to strongly influence the separation attributes of a disrupted body, we accord-

ingly examined the dynamics and statistics of agglomerations composed of varying populations of equal- and unequal-sized spheres. Ancillary investigations of rubble-pile-type impactors, which are posited to shed mass continually rather than in discrete airbursts, relaxed the constraints of the model problem and explored debris-cloud propagation at hypersonic conditions. A complementary experimental/computational approach allowed us to address many outstanding questions impeding adequate characterization and prediction of meteor fragmentation events.

All experiments consisted of sphere/dust clusters released into the Mach-6 freestream of the UMD HyperTERP shock tunnel and a stereoscopic visualization system imaging the free-flying objects. The use of a short-duration hypersonic facility with negligible start-up transients, in tandem with a reliable suspension/release system, allowed for approximation of the instantaneous release stipulated by the model problem. Experimentation, in particular, constituted an efficient method of exploring a large parameter space, particularly with varying fragment sizes, large cluster populations, and repeated testing at each condition required. The high complexity of the experiments necessitated the development of novel optical body-tracking and camera-calibration techniques, which together enabled accurate reconstruction of the three-dimensional motions of all imaged spheres.

The computational component of the present study, on the other hand, provided precise control of attitude parameters for a well-studied subset of equal-sphere configurations and truly instantaneous release into a Mach-20 freestream. The coupled CFD/FEA tool of choice was AMROC/DYNA3D; AMROC, an inviscid flow solver on an adaptively refined Cartesian mesh, transmitted computed surface pres-

sures to the nonlinear finite element solver DYNA3D, which, in turn, solved for the displacements of each constituent body. The numerical methodology was both verified in a grid-refinement study and validated from a matched experiment and computation of a four-sphere cluster. Parametric variation of the orientations of two-, four-, and thirteen-equal-sphere clusters, in addition to a single fifty-seven-sphere case, formed the foundation of the computational approach.

At small clusters population, computations of equal-sized sphere pairs revealed a previously unidentified phenomenon wherein two bodies in continual mechanical contact oscillate about a stable angle-of-attack equilibrium and achieve anomalously high lateral velocities. From inspection of the experimental and computational lateral velocities of four-sphere clusters, separation procedure could be divided into two stages: mutual repulsion from a common center and subsequent subcluster interactions dictated by the influence of an upstream body. A reduced parameterization of geometric properties of such agglomerations helped to identify the dependence of collective separation attributes on the apparent bluntness and asymmetry of an agglomeration.

Moving to clusters of intermediate population, the primary phase showed greater influence over the terminal trajectories of the constituent spheres, although the effects of lifting pairs and collisions persisted. From analysis of thirteen-sphere simulations, we found that the bow-shock system driving primary separation was incredibly complex, composed of impingements, intersections, and reflections, but also that the sphere kinematics at the point of stage transition were tightly correlated to the initial polar angle of each body. Conversely, the comparatively simple physics of

the secondary phase yielded what appeared a normally distributed random process with slight positive bias. The staggering complexity of the aerodynamic interactions at these populations suggested that attempts to model fragment separation should focus on the statistics of sphere kinematics.

The most populous clusters of equal spheres, likewise, were chiefly dispersed by seemingly random shock impingements, although collisions helped to disperse dense subclusters that coalesced near the formation's core. Statistical examination of the revealed numerous findings of high interest for modeling purposes. First, the aerodynamic decoupling radius remained approximately constant at an expansion ratio of two, whereas the separation timescale decreased markedly with population. Next, the collective lateral velocity demonstrated a monotonic rise with population and was fit well by a power-law function with index $\sim$0.4. Finally, the lateral velocity distributions of the most populous cluster configurations showed close agreement with the Rayleigh distribution.

Qualitative observations of unequal-cluster experiments demonstrated stark differences between the equal-sphere clusters and more realistic fragmentation scenarios. In particular, certain phenomena, such as drafting, shielded contact, and far-wake flight, were identified as particular to unequal-clusters, while the most highly expelled spheres attained lateral velocities 40% higher than their equal-cluster counterparts. Despite the highly enhanced ejection of the smallest bodies, the coalescence of subclusters proved a dominant aerodynamic mechanism, suppressing the overall dispersal of spheres and limiting the collective lateral velocities achieved. The resemblance of both the size-based lateral-velocity subsets to the Rayleigh distribution

and the mean lateral velocities to the exponential function prompted the adoption of a statistical separation model constituted by a combined Rayleigh–exponential function, which enabled generation of random lateral velocities for spheres of any cluster class and population.

Finally, a limited experimental investigation of hypersonic debris clouds showed major discrepancies with the accepted models of dusty debris impactors. Namely, the steady hemispherical particle front largely resisted flattening and lateral spread in favor of shedding outboard particles into an extended wake. However, the presence of large grains within the cloud contributed to discrete shedding events, which appeared to destabilize the particle front and accelerate mass loss. The application of simple image processing routines allowed for estimation of the mass depletion rate in clouds unaffected by discrete shedding; the exponential mass-loss fit formed the basis of a new energy deposition model which demonstrated that impactors of a dusty debris composition penetrate much deeper into the atmosphere than predicted by the existing models, elevating the risk of ground damage.

Several aspects of this work constitute critical contributions to the field of planetary defense. Most notably, the statistical model of fragment dispersal for arbitrary cluster compositions enables ground footprint prediction of disrupted meteors. Thus, using the capabilities afforded by this model, the extent and magnitude of damage zones can be assessed for variations in both kinematic and fragmentation parameters, which, in turn, may inform impact mitigation strategies. Additionally, we have, to some extent, reconciled the conundrum of the highly expelled fragments observed in certain meteor falls. These shock-surfing bodies are posited to originate

from populous fragment swarms and may require at least two fragmentation events during atmospheric transit to reach the maximum recorded velocities. Finally, our experimental platform overcame the severe practical limitations that typically hinder the study of rubble-pile-type impacts. These (mostly qualitative) observations anchor a new model for the atmospheric energy transfer experienced by weakly bound impactors and highlight the enhanced hazards posed by such objects. Overall, the physical mechanisms identified in this work form a knowledge base for understanding the complex interactions that occur in more realistic scenarios, enabling future studies that can better constrain meteor fragmentation.

Suggested future studies of aerodynamic separation of fragmented bodies predominantly involve relaxing the constraints of the present model problem, which naturally increases the complexity of the considered scenario and mostly limits the recommendations to various experimental free-flight configurations in the same general framework. Discarding the two primary simplifications of the current work, the exploration of nonspherical bodies within nonspherical clusters would constitute a geometric generalization more representative of observed astronomical bodies and recovered meteorites. Commencing with ellipsoids before progressing to more irregular shapes would be advised. Additional modifications to the model problem would include further testing of hybrid dust/fragment clusters, as well as observation of flow-induced disruption of friable materials in unsteady-inflow facilities. Certain components of the present work merit further investigation in their own right; for example, clusters composed of powders of desired fragment-size distributions would assist in characterizing mass depletion in debris clouds, while the expected transi-

tion from lateral expansion to streamwise elongation at high population could be gauged by experimentation with microspheres. Finally, an obvious extension of the present work is the undertaking of a Monte Carlo survey of atmospheric entry to assess the hazards posed by the models proposed herein.

Appendix A: Power-Law Fragmentation

As introduced in the model problem introduced in Chapter 1 and examined in the experiments of Chapter 7, we form clusters of unequal-sized spheres by realization of a power-law relation between the size of a fragment and its probability of selection:

$$p(r) = Ar^{-\alpha}, \tag{A.1}$$

where α is the power-law index and A a normalization constant. Under this scheme, we vary the power-law index of the probability (while holding fixed the cluster population number and minimum-to-maximum fragment size ratio) to explore the kinematic statistics for a range of cluster types. While a rational way to proceed without any knowledge of the actual meteor fragment-size distribution (FSD), it would be beneficial to support these assumptions with some physical grounding. We thus turn to the work of Betzler and Borges (2020), who compiled a database of recovered meteorites (distinct from airborne fragments) and fit statistical distributions to the various categories of fall; they find that the q-stretched exponential distribution, a three-parameter family of functions, replicates all variety of mass spectra well. At high masses, the q-stretched exponential roughly reverts to a power law, whose index evaluates to $\sim$5.8 for ordinary chondrites and $\sim$4.6 for iron-type im-

pactors. These best-fit distributions form the basis for the best available constraints on meteor fragmentation, serving as an indirect representation of the atmospheric FSD.

Our methods for identifying the appropriate range of power-law indices for air-burt fragmentation, then, rely on simulating the passage disrupted meteors through the atmosphere for selected entry parameters and comparing the final assortment of meteorites to the distributions of (Betzler and Borges, 2020). We employ a simple atmospheric transit model (Opik, 2004) to simulate the motions of individual bodies, where aerodynamic drag, gravity, and ablation serve as the primary drivers for the ballistic trajectories achieved:

$$\begin{aligned}
\frac{\mathrm{d}V}{\mathrm{d}t} &= \frac{\frac{1}{2}\rho_a V^2 C_D A_s}{m} - g\sin\theta, \\
\frac{\mathrm{d}\theta}{\mathrm{d}t} &= \left(\frac{V}{r_E + h} - \frac{g}{V}\right)\cos\theta, \\
\frac{\mathrm{d}m}{\mathrm{d}t} &= -\frac{1}{2}\rho_a V^3 \sigma_{ab} C_D A_s, \\
g &= g_0\left(\frac{r_E}{r_E + h}\right)^2,
\end{aligned} \tag{A.2}$$

where m is the fragment's mass, V its velocity, A_s its frontal area, ρ_a is the density at altitude h, C_D is the drag coefficient, g and g_0 represent gravitational acceleration in the atmosphere and on the ground, respectively, σ_{ab} is the ablation coefficient, r_E is Earth's radius, and θ is its angle of travel above horizontal. Additionally, a Weibull (1939) scaling law is adopted to model the increasing compressive strength of smaller fragments after a breakup event is initiated (once the stagnation pressure exceeds

the strength of a given body):

$$S = S_0 \left(\frac{m}{m_0} \right)^{-\alpha_s}, \tag{A.3}$$

where S and S_0 are the material strengths of the new and original fragments, respectively, m_0 the parent mass, and α_s the strength-scaling exponent. The system constants governing fragmentation are values typical of chondritic meteoroids (Wheeler et al., 2017): $S_0 = 1.5$ MPa, $\alpha_s = 0.35$, $\rho_m = 3300$ kg/m^3, $\sigma_{ab} = 5 \times 10^{-9}$ kg/J, and $C_D = 1$. The fragment population of a disrupted parent body is then selected according to the following process: first, the number of bodies is selected from a Poisson distribution centered about a user-defined mean of 300 children fragments; then, a randomly designated amount of mass given by a normal distribution is lost to dusty debris (20 +/- 10%); finally, the masses of the children bodies are determined by a random sampling from the specified power-law distribution (Equation A.1), where the lower and upper limits of the distribution are chosen such that mass continuity is ensured. This new population of fragments simply inherits the kinematic properties of the progenitor body, and the equations of motion are integrated numerically until either ground impact or subsequent airborne breakup. While this constitutes a nondeterministic algorithm, any given entry simulation can produce in excess of 1,000,000 meteorites, so we consider the statistics suitably converged. Other entry parameters governing the characteristics of the initial impactor are set to typical values to define a benchmark case (20 km/s, 20 m initial radius, 45° entry angle).

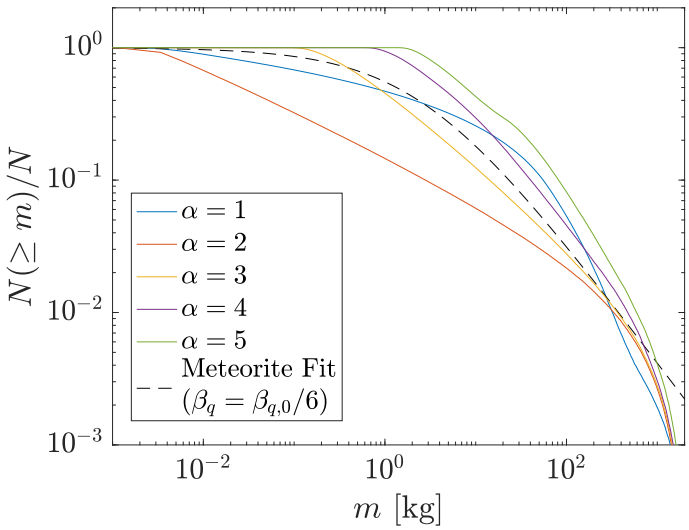

Figure A.1: Simulated meteorite fragment-size distributions for varying power-law indices compared with the Betzler and Borges (2020) fit of compiled ordinary chondrites recovered in the field.

We thus examine the effect of the fragmentation power-law index on the fragment-size distribution of all bodies on the ground. The metric for comparing the simulation results with the recovered meteorite sample is the complementary cumulative density function of mass (rather than radius, the parameter dictating cluster generation probabilities). As is provided in Figure A.1, the power-law indices of 1, 2, 3, 4, and 5 all show some deviation from Betzler and Borge's ordinary chondrite fit (which has been shifted horizontally to match the data), with some appearing to adhere to the general shape more closely than others. From the overall level of agreement observed here, the power-law description of meteor fragmentation seems consistent with recovered meteorite statistics, which provides support for the experimental strategy. In the intermediate mass range (1 kg $< m <$ 100 kg), the fit of Betzler and Borge falls between power-law indices of 3 and 4, seemingly corresponding to an airborne fragmentation index of $\alpha = 3.5$, which represents a

marked decrease from the power-law decay of 5.8 for chondritic meteorites. Indeed, steepening of the FSD following disruption might be expected given the preferential ablation of larger bodies that descend deeper into the atmosphere. In any case, α value ranging from 1 to 5 bracket the meteorite FSD, so we find our use of these power-law indices in generating unequal-sphere clusters justified.

Bibliography

D. G. Altman and J. M. Bland. Standard deviations and standard errors. *British Medical Journal*, 331:903, 2005. https://doi.org/10.1136/bmj.331.7521.903.

L. W. Alvarez, W. Alvarez, F. Asaro, and H. V. Michel. Extraterrestrial cause for the Cretaceous-Tertiary extinction. *Science*, 208(4448):1095–1108, 1980. https://doi.org/10.1126/science.208.4448.1095.

J. D. Anderson. *Hypersonic and high temperature gas dynamics*. AIAA, 2000. https://doi.org/10.2514/4.105142.

N. Artemieva and V. Shuvalov. Interaction of Shock Waves during the Passage of a Disrupted Meteoroid through the Atmosphere. *Shock Waves*, 5:359–367, 1996. https://doi.org/10.1007/BF02434011.

N. Artemieva and V. Shuvalov. Motion of a Fragmented Meteoroid through the Planetary Atmosphere. *Journal of Geophysical Research*, 106(E2), 2001. https://doi.org/10.1029/2000JE001264.

A. S. Betzler and E. P. Borges. Mass distributions of meteorites. *Monthly Notices of the Royal Astronomical Society*, 493(3):4058–4064, 2020. https://doi.org/10.1093/mnras/staa521.

P. A. Bland and N. A. Artemieva. Efficient disruption of small asteroids by Earth's atmosphere. *Nature*, 424(6946):288–291, 2003. https://doi.org/10.1038/nature01757.

J. Borovička and P. Kalenda. The Morávka meteorite fall: 4. Meteoroid dynamics and fragmentation in the atmosphere. *Meteoritics & Planetary Science*, 38(7):1023–1043, 2003. https://doi.org/10.1111/j.1945-5100.2003.tb00296.x.

J. Borovička, P. Spurnỳ, P. Kalenda, and E. Tagliaferri. The Morávka meteorite fall: 1. Description of the events and determination of the fireball trajectory and orbit from video records. *Meteoritics & Planetary Science*, 38(7):975–987, 2003. https://doi.org/10.1111/j.1945-5100.2003.tb00293.x.

J. Borovička, P. Spurnỳ, P. Brown, P. Wiegert, P. Kalenda, D. Clark, and L. Shrbenỳ. The trajectory, structure and origin of the Chelyabinsk asteroidal impactor. *Nature*, 503(7475):235–237, 2013a. https://doi.org/10.1038/nature12671.

J. Borovička, J. Tóth, A. Igaz, P. Spurnỳ, P. Kalenda, Jakub Haloda, Ján S., L. Kornoš, E. Silber, P. Brown, and M. Husárik. The Košice meteorite fall: Atmospheric trajectory, fragmentation, and orbit. *Meteoritics & Planetary Science*, 48 (10):1757–1779, 2013b. https://doi.org/10.1111/maps.12078.

V. A. Bronshten. *Physics of meteoric phenomena*, volume 22. Springer Science & Business Media, 2012.

P. G. Brown, J. D. Assink, L. Astiz, R. Blaauw, M. B. Boslough, J. Borovička, N. Brachet, D. Brown, M. Campbell-Brown, L. Ceranna, W. Cooke, C. de Groot-Hedlin, D. P. Drob, W. Edwards, L. G. Evers, M. Garces, J. Gill, M. Hedlin, A. Kingery, G. Laske, A. Le Pichon, P. Mialle, D. E. Moser, A. Saffer, E. Silber, P. Smets, R. E. Spalding, P. Spurnỳ, E. Tagliaferri, D. Uren, R. J. Weryk, R. Whitaker, and Z. Krzeminski. A 500-kiloton airburst over Chelyabinsk and an enhanced hazard from small impactors. *Nature*, 503(7475):238–241, 2013. https://doi.org/10.1038/nature12741.

C. S. Butler and S. J. Laurence. HyperTERP: A newly commissioned hypersonic shock tunnel at the University of Maryland. *AIAA Aviation Forum*, June 2019. https://doi.org/10.2514/6.2019-2860. AIAA Paper 2019-2860.

C. S. Butler, T. J. Whalen, C. E. Sousa, and S. J. Laurence. Dynamics of a spherical body shedding from a hypersonic ramp. Part 2. Viscous flow. *Journal of Fluid Mechanics*, 906, 2021. https://doi.org/10.1017/jfm.2020.757.

J. Canny. A Computational Approach to Edge Detection. *IEEE Transactions on Pattern Analysis and Machine Intelligence*, PAMI-8(6):679–698, November 1986. https://doi.org/10.1109/TPAMI.1986.4767851.

Z. Ceplecha, J. Borovička, W. G. Elford, D. O. ReVelle, R. L. Hawkes, V. Porubčan, and M. Šimek. Meteor phenomena and bodies. *Space Science Reviews*, 84(3):327–471, 1998. https://doi.org/10.1023/A:1005069928850.

Y. B. Chu and X. Y. Lu. Characteristics of unsteady type IV shock/shock interaction. *Shock Waves*, 22(3):225–235, 2012. https://doi.org/10.1007/s00193-012-0366-y.

C. Chyba, P. Thomas, and K. Zahnle. The 1908 Tunguska Explosion; Atmospheric Distruption of a Stony Asteroid. *Nature*, 361, January 1993. https://doi.org/10.1038/361040a0.

R. Deiterding. A Parallel Adaptive Method for Simulating Shock-Induced Combustion with Detailed Chemical Kinetics in Complex Domains. *Computers and*

Structures, 87:769–783, 2009. https://doi.org/10.1016/j.compstruc.2008.11.007.

R. Deiterding and S. Wood. Parallel Adaptive Fluid–Structure Interaction Simulation of Explosions Impacting on Building Structures. *Computers and Structures*, 88:719–729, 2013. https://doi.org/10.1016/j.compfluid.2013.05.009.

B. E. Edney. Effects of shock impingement on the heat transfer around blunt bodies. *AIAA Journal*, 6(1):15–21, 1968. https://doi.org/10.2514/3.4435.

P. Farinella, L. Foschini, Ch. Froeschlé, R. Gonczi, T. J. Jopek, G. Longo, and P. Michel. Probable asteroidal origin of the Tunguska Cosmic Body. *Astronomy & Astrophysics*, 377(3):1081–1097, 2001. https://doi.org/10.1051/0004-6361:20011054.

A. Fujiwara, J. Kawaguchi, D. K. Yeomans, M. Abe, T. Mukai, T. Okada, J. Saito, H. Yano, M. Yoshikawa, D. J. Scheeres, O. Barnouin-Jha, A. F. Cheng, H. Demura, R. W. Gaskell, N. Hirata, H. Ikeda, T. Kominato, H. Miyamoto, A. M. Nakamura, R. Nakamura, S. Sasaki, and K. Uesugi. The Rubble-Pile Asteroid Itokawa as Observed by Hayabusa. *Science*, 312(5778):1330–1334, 2006. https://doi.org/10.1126/science.1125841.

E. Gnos, B. A. Hofmann, M. A. Halawani, Y. Tarabulsi, M. Hakeem, M. Al Shanti, N. D. Greber, S. Holm, C. Alwmark, R. C. Greenwood, and K. Ramseyer. The Wabar impact craters, Saudi Arabia, revisited. *Meteoritics & Planetary Science*, 48(10):2000–2014, 2013. https://doi.org/10.1111/maps.12218.

T. Y. Gorazdovskij. The explosion dynamics of the Tunguska meteorite in the light of effects of an experimental regolith explosion. *Problems of Meteoritics. The problem of the Tunguska Meteorite*, pages 74–82, 1976.

N. N. Gorkavyi, T. A. Taidakova, E. A. Provornikova, I. N. Gorkavyi, and M. M. Akhmetvaleev. Aerosol plume after the Chelyabinsk bolide. *Solar system research*, 47(4):275–279, 2013. https://doi.org/10.1134/S003809461304014X.

I. Halliday, A. A. Griffin, and A. T. Blackwell. Detailed data for 259 fireballs from the Canadian camera network and inferences concerning the influx of large meteoroids. *Meteoritics & Planetary Science*, 31(2):185–217, 1996. https://doi.org/10.1111/j.1945-5100.1996.tb02014.x.

J. Hallquist and J. I. Jin. A nonlinear explicit three-dimensional finite element code for solid and structural mechanics. Technical Report UCRL-MA-107254, Lawrence Livermore National Laboratory, 2005.

W. K. Hartmann. Terrestrial, lunar, and interplanetary rock fragmentation. *Icarus*, 10(2):201–213, 1969. https://doi.org/10.1016/0019-1035(69)90022-0.

J. G. Hills and M. P. Goda. The Fragmentation of Small Asteroids in the Atmosphere. *The Astronomical Journal*, 105(3):1114–1144, 1993. https://doi.org/10.1086/116499.

W. Q. Huang and L. Yu. Serial Symmetrical Relocation Algorithm for the Equal Sphere Packing Problem. 2012. https://arxiv.org/abs/1202.4149.

C. O. Johnston and E. C. Stern. A model for thermal radiation from the Tunguska airburst. *Icarus*, 327:48–59, 2019. https://doi.org/10.1016/j.icarus.2019.01.028.

L. Kresak. The Tunguska object-A fragment of Comet Encke. *Bulletin of the Astronomical Institutes of Czechoslovakia*, 29:129–134, 1978.

E. L. Krinov. Fragmentation of the Sikhote-Alin meteoritic body. *Meteoritics*, 9(3): 255–262, 1974. https://doi.org/10.1111/j.1945-5100.1974.tb00081.x.

B. Lang and M. Kowalski. On the possible number of mass fragments from Pultusk meteorite shower, 1868. *Meteoritics*, 6, 1971. https://doi.org/10.1111/j.1945-5100.1971.tb00106.x.

S. Laurence and R. Deiterding. Shock-Wave Surfing. *Journal of Fluid Mechanics*, 676:396–431, 2011. https://doi.org/10.1017/jfm.2011.57.

S. Laurence and S. Karl. An Improved Visualization-Based Force-Measurement Technique for Short-Duration Hypersonic Facilities. *Experiments in Fluids*, 48: 949:965, 2010. https://doi.org/10.1007/s00348-009-0780-9.

S. Laurence, R. Deiterding, and H. Hornung. Proximal Bodies in Hypersonic Flow. *Journal of Fluid Mechanics*, 590:209–237, 2007. https://doi.org/10.1017/S0022112007007987.

S. Laurence, N. Parziale, and R. Deiterding. Dynamical Separation of Spherical Bodies in Supersonic Flow. *Journal of Fluid Mechanics*, 713:159–182, 2012. https://doi.org/10.1017/jfm.2012.453.

S. J. Laurence. On tracking the motion of rigid bodies through edge detection and least-squares fitting. *Experiments in Fluids*, 52:387–401, 2012. https://doi.org/10.1007/s00348-011-1228-6.

S. J. Laurence and H. G. Hornung. Image-based force and moment measurement in hypersonic facilities. *Experiments in Fluids*, 46:343–353, 2009. https://doi.org/10.1007/s00348-008-0565-6.

T. Li, J. Sui, S. Gong, and C. Wu. Dynamical Separation of Rigid Bodies in Supersonic Flow. *Technological Sciences*, 58(12), 2015. https://doi.org/10.1007/s11431-015-5966-1.

A. Marwege, S. Willems, A. Gülhan, M. Aftosmis, and E. Stern. Superposition Method for Force Estimations on Bodies in Supersonic and Hypersonic Flows. *Journal of Spacecraft and Rockets*, 55(5), 2018. https://doi.org/10.2514/1.A34128.

D. L. Mathias, L. F. Wheeler, and J. L. Dotson. A probabilistic asteroid impact risk model: assessment of sub-300 m impacts. *Icarus*, 337:106–119, 2017. https://doi.org/10.1016/j.icarus.2017.02.009.

S. P. Mauch. *Efficient algorithms for solving static Hamilton–Jacobi equations*. PhD thesis, California Institute of Technology, 2003.

T. B. McCord, J. Morris, D. Persing, E. Tagliaferri, C. Jacobs, R. Spalding, L. Grady, and R. Schmidt. Detection of a meteoroid entry into the Earth's atmosphere on February 1, 1994. *Journal of Geophysical Research: Planets*, 100(E2): 3245–3249, 1995. https://doi.org/10.1029/94JE02802.

B. A. McIntosh and J. A. V. Douglas. The Fireball of April 25, 1966. II, Photographic Observations and Orbit Determination. *Journal of the Royal Astronomical Society of Canada*, 62:55, 1968.

S. McMullan and G. S. Collins. Uncertainty quantification in continuous fragmentation airburst models. *Icarus*, 327:19–35, 2019. https://doi.org/10.1016/j.icarus.2019.02.013.

B. K. Mishra and R. K. Rajamani. The discrete element method for the simulation of ball mills. *Applied Mathematical Modelling*, 16(11):598–604, 1992. https://doi.org/10.1016/0307-904X(92)90035-2.

N. R. Mudford, S. O'Byrne, A. Neely, D. Buttsworth, and S. Balage. Hypersonic Wind-Tunnel Free-Flying Experiments with Onboard Instrumentation. *Journal of Spacecraft and Rockets*, 52(1):231–242, 2015. https://doi.org/10.2514/1.A32887.

J. Nelder and R. Mead. A Simplex Method for Function Minimization. *The Computer Journal*, 7(4), 1965. https://doi.org/10.1093/comjnl/7.4.308.

E. J. Opik. *Physics of meteor flight in the atmosphere*. Courier Corporation, 2004.

C. Park and J. D Brown. Fragmentation and spreading of a meteor-like object. *The Astronomical Journal*, 144(6):184, 2012. https://doi.org/10.1088/0004-6256/144/6/184.

S. Park and G. Park. Separation process of multi-spheres in hypersonic flow. *Advances in Space Research*, 65(1):392–406, 2020. https://doi.org/10.1016/j.asr.2019.10.009.

Q. Passey and H. Melosh. Effects of Atmospheric Breakup on Crater Field Formation. *Icarus*, 42:211–233, 1980. https://doi.org/10.1016/0019-1035(80)90072-X.

K. Pearson. On the criterion that a given system of deviations from the probable in the case of a correlated system of variables is such that it can be reasonably supposed to have arisen from random sampling. *The London, Edinburgh, and Dublin Philosophical Magazine and Journal of Science*, 50(302):157–175, 1900. https://doi.org/10.1080/14786440009463897.

Olga P. Popova, Peter Jenniskens, Vacheslav Emel'yanenko, Anna Kartashova, Eugeny Biryukov, Sergey Khaibrakhmanov, Valery Shuvalov, Yurij Rybnov, Alexandr Dudorov, Victor I. Grokhovsky, Dmitry D. Badyukov, Qing-Zhu Yin, Peter S. Gural, Jim Albers, Mikael Granvik, Läslo G. Evers, Jacob Kuiper, Vladimir Kharlamov, Andrey Solovyov, Yuri S. Rusakov, Stanislav Korotkiy, Ilya Serdyuk, Alexander V. Korochantsev, Michail Yu. Larionov, Dmitry Glazachev, Alexander E. Mayer, Galen Gisler, Sergei V. Gladkovsky, Josh Wimpenny, Matthew E. Sanborn, Akane Yamakawa, Kenneth L. Verosub, Douglas J. Rowland, Sarah Roeske, Nicholas W. Botto, Jon M. Friedrich, Michael E. Zolensky, Loan Le, Daniel Ross, Karen Ziegler, Tomoki Nakamura, Insu Ahn, Jong Ik Lee, Qin Zhou, Xian-Hua Li, Qiu-Li Li, Yu Liu, Guo-Qiang Tang, Takahiro Hiroi, Derek Sears, Ilya A. Weinstein, Alexander S. Vokhmintsev, Alexei V. Ishchenko, Phillipe Schmitt-Kopplin, Norbert Hertkorn, Keisuke Nagao, K. Haba, Makiko, Mutsumi Komatsu, and Takashi Mikouchi. Chelyabinsk Airburst, Damage Assessment, Meteorite Recovery, and Characterization. *Science*, 342(6162), 2013. https://doi.org/10.1126/science.1242642.

Y. Prevereaud. *Contribution à la Modélisation de la Rentrée Atmosphérique des Débris Spatiaux*. PhD thesis, Institut Supérieur de l'Aéronautique et de l'Espace, July 2014.

P. Register, D. Mathias, and L. Wheeler. Asteroid fragmentation approaches for modeling atmospheric energy deposition. *Icarus*, 284:157–166, 2017. https://doi.org/10.1016/j.icarus.2016.11.020.

P. J. Register, M. J. Aftosmis, E. C. Stern, Brock J. M., P. M. Seltner, S. Willems, A. Guelhan, and D. L. Mathias. Interactions between asteroid fragments during atmospheric entry. *Icarus*, 337(113468), 2020. https://doi.org/10.1016/j.icarus.2019.113468.

J. Rojas, Y. Uribe, and A. Zuluaga. Powder and compaction characteristics of pregelatinized starches. *Die Pharmazie-An International Journal of Pharmaceutical Sciences*, 67(6):513–517, 2012. https://doi.org/10.1691/ph.2012.1118.

C. M. Rumpf, H. G. Lewis, and P. M. Atkinson. Asteroid impact effects and their immediate hazards for human populations. *Geophysical Research Letters*, 44(8):3433–3440, 2017. https://doi.org/10.1002/2017GL073191.

P. Scheirich, J. Ďurech, P. Pravec, M. Kozubal, R. Dantowitz, M. Kaasalainen, A. Betzler, P. Beltrame, G. Muler, P. Birtwhistle, and F. Kugel. The shape and rotation of asteroid 2008 TC3. *Meteoritics & Planetary Science*, 45(10-11): 1804–1811, 2010. https://doi.org/10.1111/j.1945-5100.2010.01146.x.

P. H. Schultz. "Needle Model" for Surviving Entry: Implications of the Carancas Impact. *Asteroids, Comets, Meteors 2008*, 1405:8342, 2008.

CE Sousa, Ralf Deiterding, and Stuart J Laurence. Dynamics of a spherical body shedding from a hypersonic ramp. Part 1. Inviscid flow. *Journal of Fluid Mechanics*, 906, 2021. https://doi.org/10.1017/jfm.2020.756.

W. Starshak, C. Butler, and S. Laurence. Optical Free-Flight Measurements using GPU-Accelerated Computer Graphics. *AIAA Space Forum*, September 2018. https://doi.org/10.2514/6.2018-5385. AIAA Paper 2018-5385.

W. C. Starshak and S. J. Laurence. Computer-Graphics-Based Optical Tracking for Hypersonic Free-Flight Experiments. *AIAA Journal*, pages 1–14, 2021. https://doi.org/10.2514/1.J060017.

S. Sugita, R. Honda, T. Morota, S. Kameda, H. Sawada, E. Tatsumi, M. Yamada, C. Honda, Y. Yokota, T. Kouyama, N. Sakatani, K. Ogawa, H. Suzuki, T. Okada, N. Namiki, S. Tanaka, Y. Iijima, K. Yoshioka, M. Hayakawa, Y. Cho, M. Matsuoka, N. Hirata, N. Hirata, H. Miyamoto, D. Domingue, M. Hirabayashi, T. Nakamura, T. Hiroi, T. Michikami, P. Michel, R.-L. Ballouz, O. S. Barnouin, C. M. Ernst, S. E. Schröder, H. Kikuchi, R. Hemmi, G. Komatsu, T. Fukuhara, M. Taguchi, T. Arai, H. Senshu, H. Demura, Y. Ogawa, Y. Shimaki, T. Sekiguchi, T. G. Müller, A. Hagermann, T. Mizuno, H. Noda, K. Matsumoto, R. Yamada, Y. Ishihara, H. Ikeda, H. Araki, K. Yamamoto, S. Abe, F. Yoshida, A. Higuchi, S. Sasaki, S. Oshigami, S. Tsuruta, K. Asari, S. Tazawa, M. Shizugami, J. Kimura, T. Otsubo, H. Yabuta, S. Hasegawa, M. Ishiguro, S. Tachibana, E. Palmer, R. Gaskell, L. Le Corre, R. Jaumann, K. Otto, N. Schmitz, P. A. Abell, M. A. Barucci, M. E. Zolensky, F. Vilas, F. Thuillet, C. Sugimoto, N. Takaki, Y. Suzuki, H. Kamiyoshihara, M. Okada, K. Nagata, M. Fujimoto, M. Yoshikawa, Y. Yamamoto, K. Shirai, R. Noguchi, N. Ogawa, F. Terui, S. Kikuchi, T. Yamaguchi, Y. Oki, Y. Takao, H. Takeuchi, G. Ono, Y. Mimasu, K. Yoshikawa, T. Takahashi, Y. Takei, A. Fujii, C. Hirose, S. Nakazawa, S. Hosoda, O. Mori, T. Shimada, S. Soldini, T. Iwata, M. Abe, H. Yano, R. Tsukizaki, M. Ozaki, K. Nishiyama, T. Saiki, S. Watanabe, and Y. Tsuda. The geomorphology, color, and thermal properties of Ryugu: Implications for parent-body processes. *Science*, 364(6437), 2019. https://doi.org/10.1126/science.aaw0422.

V. V. Svetsov and I. V Nemtchinov. Disintegration of Large Meteoroids in Earth's Atmosphere: Theoretical Models. *Icarus*, 116:131–153, 1995. https://doi.org/10.1006/icar.1995.1116.

H. Tanno, T. Komero, K. Sato, K. Itoh, M. Takahashi, K. Fujita, S. Laurence, and K. Hannemann. Free-Flight Force Measurement Technique in Shock Tunnel. *AIAA Aerospace Sciences Meeting*, January 2012. https://doi.org/10.2514/6.2012-1241. AIAA Paper 2012-1241.

B. Triggs, McLauchlan P. F., Hartley R. I., and Fitzgibbon A. W. Bundle Adjustment – A Modern Synthesis. *Vision Algorithms: Theory and Practice*, 1883, 2000. https://doi.org/10.1007/3-540-44480-7_21.

V. I. Tsvetkov. Sikhote-Alin meteorite shower: fragmentation, scattering, trajectory, orbit. *Meteoritika*, 46:3–10, 1987. https://doi.org/10.1007/BF00130888.

W. G. Vincenti and C. H. Kruger. Introduction to physical gas dynamics. *Introduction to physical gas dynamics*, 1965.

K. J. Walsh. Rubble Pile Asteroids. *Annual Review of Astronomy and Astrophysics*, 56(1):593–624, 2018. https://doi.org/10.1146/annurev-astro-081817-052013.

W. Weibull. A statistical theory of strength of materials. *IVB-Handl.*, 1939.

T. J. Whalen and S. J. Laurence. Experiments on the separation of sphere clusters in hypersonic flow. *Experiments in Fluids*, 62(4):1–19, 2021. https://doi.org/10.1007/s00348-021-03157-z.

T. J. Whalen, S. J. Laurence, and R. Deiterding. A Numerical Investigation of Clustered Spheres Separating in Mach 20 Flow. *AIAA Aviation Forum*, June 2020. https://doi.org/10.2514/6.2020-2970. AIAA Paper 2020-2970.

L. Wheeler, P. Register, and D. Mathias. A Fragment-Cloud Model for Asteroid Breakup and Atmospheric Energy Deposition. *Icarus*, 295:149–169, 2017. https://doi.org/10.1016/j.icarus.2017.02.011.

C. E. Williams. A Comparison of Circular Error Probable Estimators for Small Samples. Technical report, AIR FORCE INST OF TECH WRIGHT-PATTERSON AFB OH SCHOOL OF ENGINEERING, 1997.